

Analysis Note

2 Measurement of D^0 azimuthal anisotropy in Au+Au Collisions at $\sqrt{s_{\text{NN}}} = 200$ GeV

Xiaolong Chen (xlchen89@mail.ustc.edu.cn),¹ Xin Dong (xdong@lbl.gov),²
 Liang He (he202@purdue.edu),³ Michael Lomnitz (mlomnitz@kent.edu),^{4,2}
 Long Ma (malong@sinap.ac.cn),^{5,2} Mustafa Mustafa (mmustafa@lbl.gov),²
 Hao Qiu (hqiu@lbl.gov),² and Guannan Xie (xgn1992@mail.ustc.edu.cn)^{1,2}

¹*University of Science & Technology of China, Hefei 230026, China*

²*Lawrence Berkeley National Laboratory, Berkeley, California 94720, USA*

³Purdue University, West Lafayette, Indiana 47907, USA

⁴Kent State University, Kent, Ohio 44242, USA

⁵*Shanghai Institute of Applied Physics, Shanghai 201800, China*

(Dated: February 19, 2016)

Contents

15	Goal	4
16	Datasets and event selections	5
17	Datasets	5
18	Trigger and event selection	5
19	Centrality definition	5
20	Trigger efficiency	6
21	D^0 reconstruction	8
22	Daughter selection	8
23	Geometrical cuts tuning with TMVA	9
24	D^0 signals	18
25	KF vertex	20
26	Mixed event background	28
27	Correlated background "bump" from other D meson decay channels	31
28	Double mis-PID	35
29	v_2 calculation with event plane method	44
30	Event plane reconstruction	44
31	Obtain D^0 yield in different $\Delta\phi$ bins and fit v_2	47
32	Systematic errors for the event plane method	52
33	Results from the event plane method	54
34	Correlation v_2	56
35	Acceptance correction	57
36	$\Delta\eta$ between D^0 (hadron) to hadron	57
37	Reference hadron v_2	59
38	Background subtraction	60
39	Statistic error	62
40	Systematic uncertainties for correlation method	65
41	Results from the correlation method	66

42	common systematic uncertainties	68
43	Non-flow	68
44	B feed-down contribution to D^0	72
45	Result and discussion	79
46	Appendix	84
47	Event plane method plots for different p_T bins	84

48

GOAL

49 The goal of this analysis is to measure the second order Fourier coefficient v_2 of the azimuthal
50 distribution of D^0 production in 200 GeV Au+Au collisions. If we define ϕ and Ψ as the azimuthal
51 angle of D^0 and the second order harmonic plane of particles in the event respectively, v_2 can be
52 obtained using the following equation: $A(1 + 2v_2\cos(2(\phi - \Psi)))$, where A is a free constant.
53 By measuring $D^0 v_2$ we can study charm flow and the interaction between charm quark and the
54 medium, and study the properties of the QGP medium.

Trigger ID	description
450050	vpdmb-5-p-nobsmd-hlt
450060	vpdmb-5-p-nobsmd-hlt
450005	vpdmb-5-p-nobsmd
450015	vpdmb-5-p-nobsmd
450025	vpdmb-5-p-nobsmd
450014	VPDMB-5-p-nobsmd
450024	VPDMB-5-p-nobsmd

TABLE I: Trigger ID used in the analysis

55

DATASETS AND EVENT SELECTIONS

56

Datasets

57 This analysis is based on the AuAu collisions at $\sqrt{s_{\text{NN}}}=200$ GeV collected by the STAR ex-
 58 periment during the 2014 run. It is the first year of physics running the new STAR Heavy Flavor
 59 Trackter Detector. The data is processed with SL15c library. The analysis uses picoDst which is
 60 produced from MuDst. Details of picoDst can be found at

61 <http://rnc.lbl.gov/~xdong/SoftHadron/picoDst.html>

62

Trigger and event selection

63 In this analysis, a minimum-bias trigger, denoted as "vpdmb-5-p-nobsmd" and "vpdmb-5-p-
 64 nobsmd-hlt", is used. The event selection used in this analysis is

65 • $|\text{primary vertex in z direction}| < 6 \text{ cm}$

66 • $|\text{primary vertex z} - \text{vpdVz}| < 3 \text{ cm}$

67 vpdVz is the vertex z position calculated from time difference measured by two sides of VPD.

68 After cuts, a total of 1077 M events are used for the analysis.

69

Centrality definition

70 The centrality for RUN14 200GeV AuAu minBias sample is based on gRefMult, which is
 71 defined as the number of global tracks within $|\eta| < 0.5$, with some correction according to primary

centrality(%)	gRefMult
80-100	<10
75-80	10-14
70-75	14-21
65-70	21-29
60-65	29-40
55-60	40-54
50-55	54-71
45-50	71-92
40-45	92-116
35-40	116-145
30-35	145-179
25-30	179-218
20-25	218-263
15-20	263-315
10-15	315-373
5-10	373-441
0-5	>441

TABLE II: Centrality defintion based on gRefMult

72 vertex z and luminosity. The centrality definition according to the corrected gRefMult is listed in
 73 Table II. There is a specific STAR maker (StRefmultCorr) to calculate centrality. More details
 74 about the centrality definition can be found in
 75 <http://www.star.bnl.gov/protected/heavy/xgn1992/Centrality/>
 76 Run2014/VPDMB5/index.html

77 **Trigger efficiency**

78 The VPD minbias trigger has a trigger effciency that are lower for periheral events. To do the
 79 measurement without centrality bias, a weight proportional to inverse trigger efficiency is applied.
 80 The weight as a function of corrected gRefMult is shown in Fig. 1.

81 There is an additional weight to deal with different centrality distributions for different vertex
 82 z, due to VPD vertex z resolution for different centralities. Central events have more particles,
 83 better VPD signal, and better VPD vertex z resolution. So they are easier to pass VPD vertex z
 84 cuts (± 5 cm). This creates a bias towards central events near the VPD vertex z cuts, and this bias
 85 is different for different vertex z. This can be corrected also by a weight.

86 Both these 2 weights are taken care of by the StRefmultCorr. More details can also be found

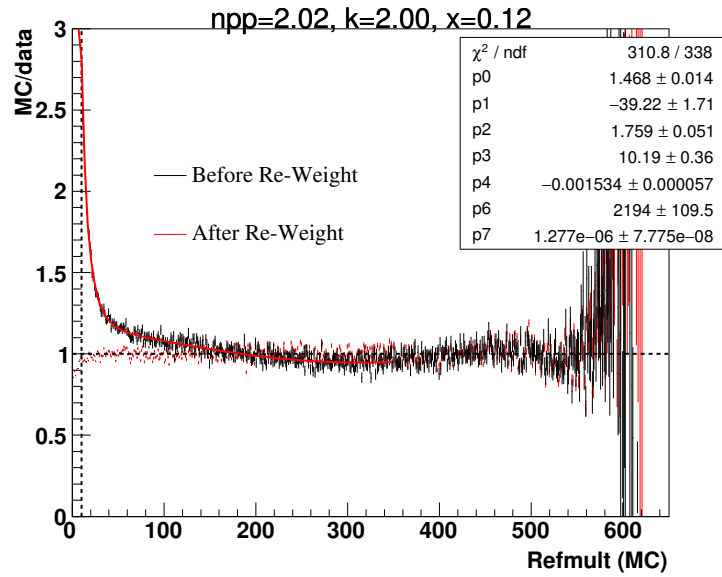


FIG. 1: MC/data gRefmult distribution before and after VPD minbias trigger efficiency correction. The red line fit function is the correction reweight function.

87 here.

88 <http://www.star.bnl.gov/protected/heavy/xgn1992/Centrality/>
 89 Run2014/VPDMD5/index.html

90

 D^0 RECONSTRUCTION

91 D^0 and \bar{D}^0 are reconstructed through the $K \mp \pi \pm$ channel. In the following we will describe the
 92 daughter selection, the geometry cuts and how they are obtained through the TMVA tuning. We will
 93 show the D^0 signals for different p_T bins. We will also discuss some related topics: the primary
 94 vertex reconstructed by the Kalman Filter algorithm with better quality than the STAR default, the
 95 mixed event to reconstruct the combinatorial background, and the correlated background source
 96 shown as a 'bump' at invariant mass lower than the D^0 .

97

Daughter selection

98 daughter track selection:

- 99 • global tracks
- 100 • $p_T > 0.6 GeV/c$
- 101 • $|\eta| < 1$
- 102 • $nHitsFit \geq 20$, in TPC
- 103 • at least one hit in every layer of PXL and IST

104 pion PID:

- 105 • $|nSigmaPion| < 3.0$, based on TPC dE/dx
- 106 • If TOF is available: $|\frac{1}{\beta} - \frac{1}{\beta_{exp}}| < 0.03$

107 kaon PID:

- 108 • $|nSigmaKaon| < 2.0$, based on TPC dE/dx
- 109 • If TOF is available: $|\frac{1}{\beta} - \frac{1}{\beta_{exp}}| < 0.03$

110

Geometrical cuts tuning with TMVA

111 The secondary vertex is reconstructed with selected Kaon and Pion global tracks. In this anal-
 112 ysis, the middle point on the Distance of the Closest Approach between two daughter tracks is
 113 considered as the secondary decay vertex of the candidate D^0 . As shown in Fig. 2, 5 geometrical
 114 variables are chosen to select D^0 and reject combinatorial background, which is dominated by a
 115 pair of tracks directly from the primary vertex: decay length (the distance between the decay ver-
 116 tex and PV), DCA between the 2 daughters, DCA between the reconstructed D^0 flying path and
 117 PV, DCA between the π track and PV, and DCA between the K track and PV. The cuts on these
 118 variables are optimized by the Toolkit for Multivariate Data Analysis (TMVA) package. They
 119 change according to the D^0 candidate p_T in order to have the best significance in all the covered
 120 p_T range. Additionally there is a $\cos(\theta) > 0$ cut to make sure the decay vertex relative to the
 121 primary vertex is roughly in the same direction as the momentum.

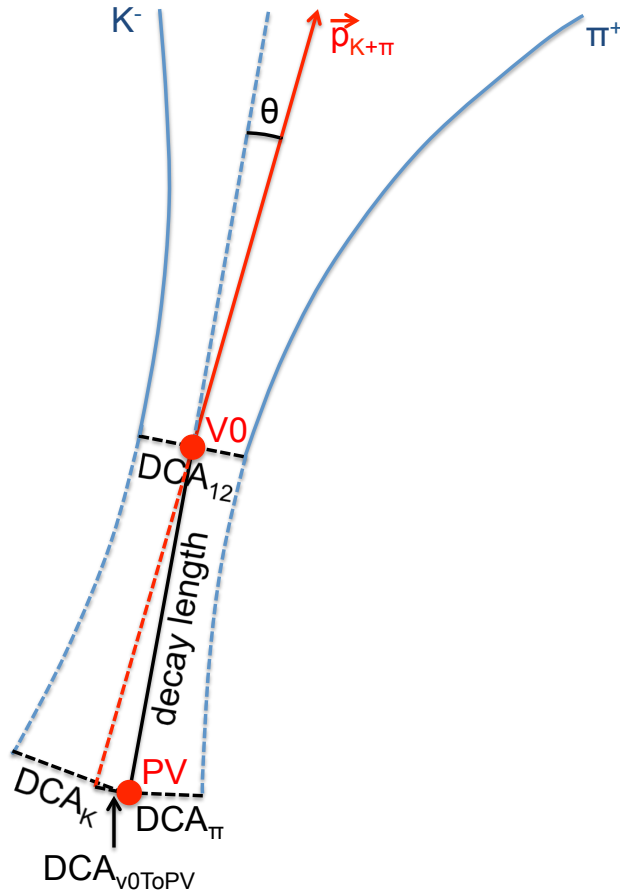


FIG. 2: D^0 decay topology variables

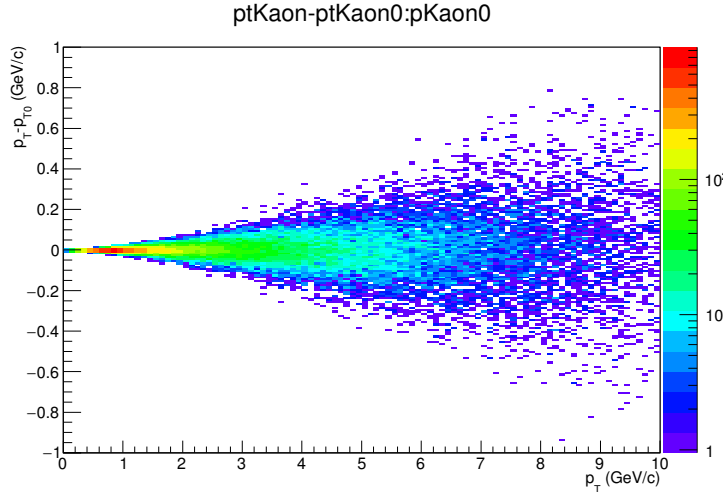


FIG. 3: p_T smearing vs. p_T for D^0 daughter kaons

122 The TMVA need signal and background sample to train. The signal sample is obtained from
 123 a toy simulation and the background sample is from real data like sign pairs in D^0 mass window
 124 and un-like sign pairs in side bands.

125 In the toy simulation for D^0 signals, the D^0 decays, and then the daughters' momentum and
 126 position are smeared according to detector response. The daughters' acceptance and reconstruction
 127 efficiency is also considered. Fig. 3 shows p_T smearing vs. p_T for D^0 daughter kaons. The
 128 smearing $\sigma = p_T(0.6 + 0.38p_T)/100$, which is a rough estimation. For geometry cuts simulation,
 129 the p_T resolution is not very important. It only makes the D^0 peak width more realistic as shown
 130 in Fig. 4.

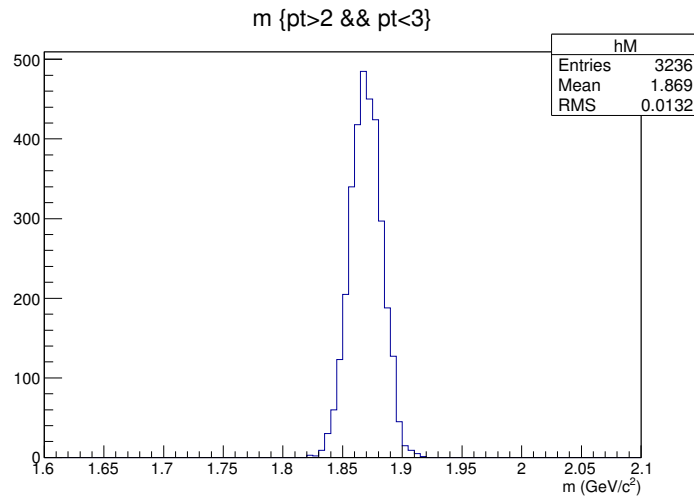


FIG. 4: reconstructed D^0 mass from toy simulation for p_T 2-3 GeV/c

131 The position smearing need to be precise to reproduce the behavior of the real data, so that the
 132 effects of geometry cuts are reproduced realistically. In the toy simulation the position resolution
 133 has 2 parts: a) due to hit error, including pixel size, vibration, and alignment, which is a constant
 134 contribution; and b) due to multiple Coulomb scattering, whose angular dispersion is described
 135 as a function of p : $13.6\text{MeV}/(\beta cp)z\sqrt{x/X_0}(1 + 0.038\ln(x/X_0))$, where z is the charge of the
 136 particle (=1 for most particles produced in STAR), x is the thickness of the material and X_0 is
 137 the radiation length to the material. The parameters for position smearing in the toy simulation
 138 (constant for hit error effect and $\sqrt{x/X_0}(1 + 0.038\ln(x/X_0))$) are calibrated using DCA position
 139 resolution vs. p from real data, as shown in Fig. 5. For data the PID is done with TPC dE/dx and
 140 TOF. The agreement is very good after calibration for $p_T > 0.6 \text{ GeV}/c$ used for this analysis. The
 141 discrepancy at very low p could be a bin width effect due to the decreasing p spectrum, and / or
 142 wrong mass in tracker (always assuming π mass) when dealing with energy loss.

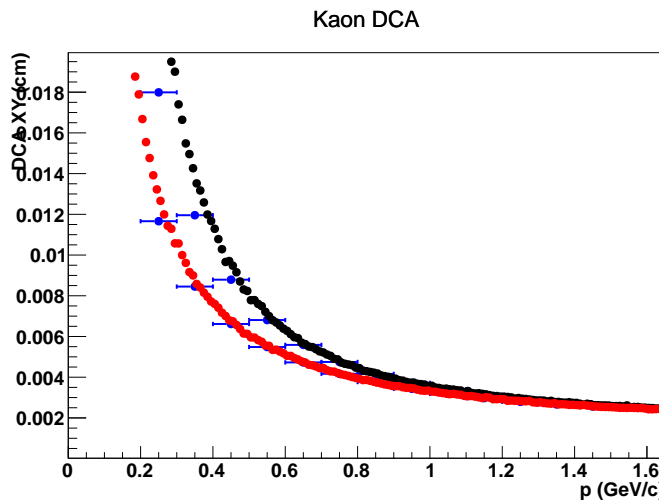


FIG. 5: comparison of simulated position resolution (DCA XY) vs. p for kaon (black), pion (red) and data measurements (blue)

143 The D^0 daughter efficiency includes TPC efficiency from embedding (<https://drupal.star.bnl.gov/STAR/starsimrequests/2013/nov/07/vpdmb-d0d0bar-pp-200-gev-run12>) and HFT efficiency from simulation scaled
 144 to real data measured HFT track / TPC track ratio, as shown in Fig. 6. At low p_T , many tracks
 145 match to wrong HFT hits. So the scale is to match the simulated efficiency to the HFT ratio at
 146 high p_T .

149 For some other selection methods rather than cuts, the TMVA could be trained to identify D^0
 150 according to kinetic information like invariant mass rather than geometry information due to the

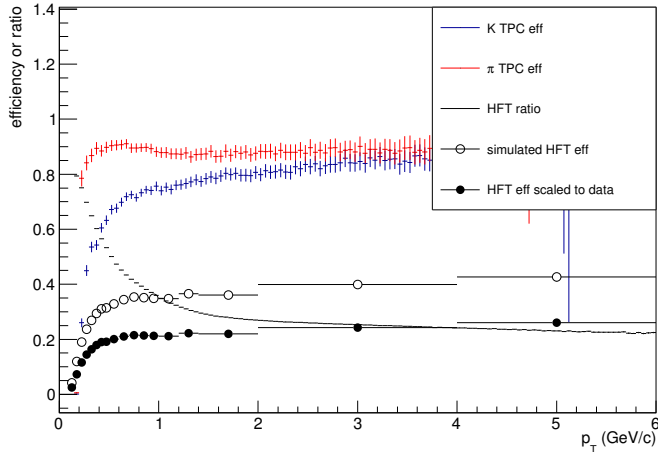


FIG. 6: pion, Kaon TPC reconstruction efficiency from embedding, HFT ratio (HFT track / TPC track) from data and HFT efficiency from simulation, and scaled HFT efficiency to match the HFT ratio from data.

decay. This will create a fake signal, which is not what we want. To avoid this, a mass that has the same distribution with the background sample for TMVA training is assigned to D^0 in the toy simulation. Fig. 7 and Fig. 8 show background (side band and same sign) invariant mass distribution from data and modified simulated signal invariant mass distribution respectively. The latter matches the earlier, so TMVA will not be trained to identify D^0 according to the invariant mass. This signal mass modification is not necessary for training of rectangular cuts used in this analysis, but intended only for future analyses which might use kinematic info and other selection methods in TMVA.

The toy simulation use flat p_T input from 0 to 10 GeV/c. Fig. 9 shows the outcome D^0 p_T distribution after considering detector acceptance and efficiency. When used for TMVA training, the entries are weighted by a function fit to the measured D^0 p_T spectrum (Phys. Rev. Lett. 113 (2014) 142301), and the yield is scaled to what is expected for the whole data set of 1.3 B events.

The background from real data naturally has the real p_T distribution. However, in order to have enough statistics from low to high p_T , while keep the tree file size and the CPU time for training acceptable, the low p_T part is randomly sampled to form a flat distribution below 3 GeV/c. Fig. 10 shows background p_T distribution with (black) and without (blue) random sample. When used for TMVA training, the sample is weighted back to orginal distribution. Only part of the Run 14 data is sampled for background in TMVA training, so the background yield is scaled to the whole data set of 1.3 B events.

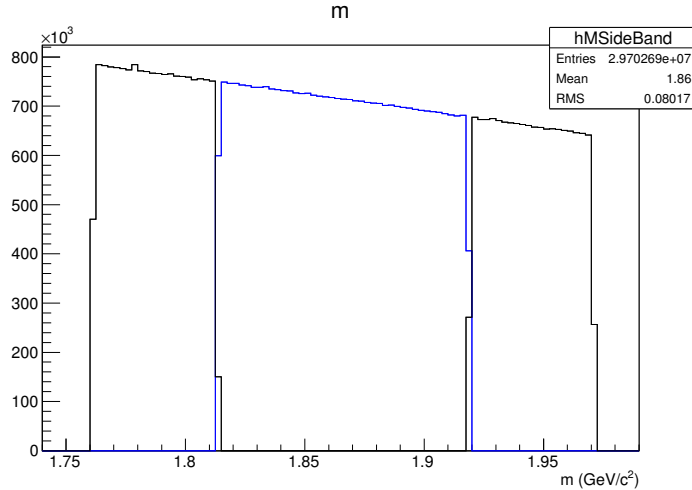


FIG. 7: background invariant mass distribution for side bands (black) and same sign (blue) from real data

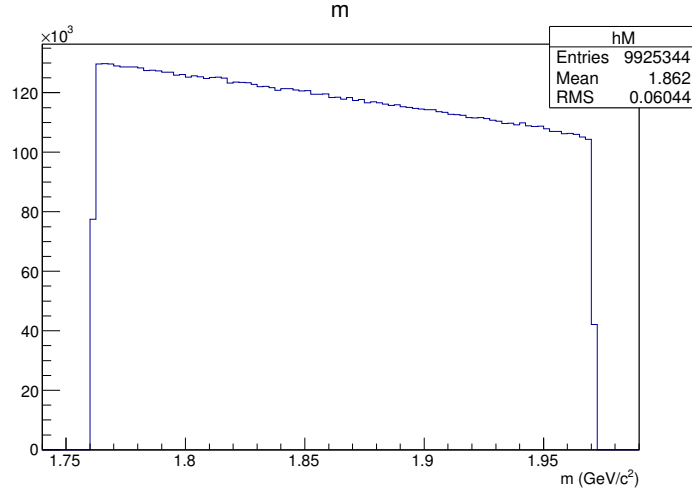
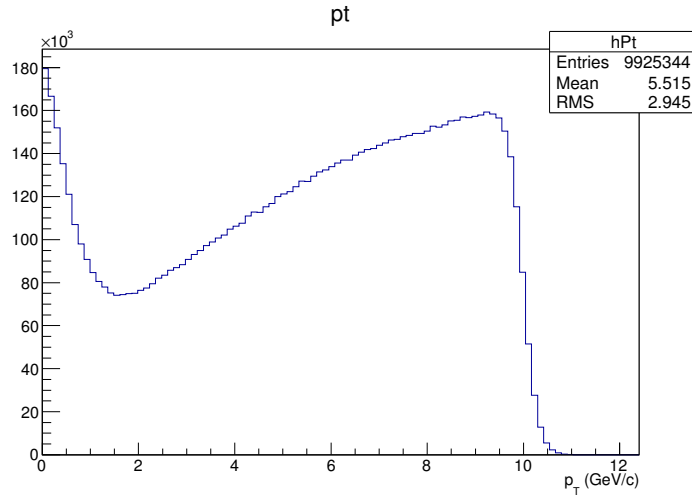
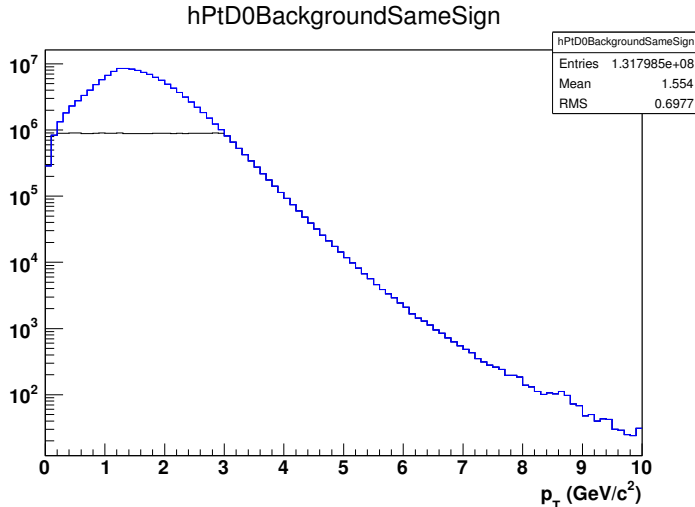


FIG. 8: modified simulated D^0 invariant mass to match background invariant mass distribution

Fig. 11 shows distributions of the 5 geometry variables for signal (blue) and background (red) plotted by the TMVA, for candidates p_T between 2 and 3 GeV/c.

The 'cuts' option of TMVA is used to tune D^0 cuts. This option randomly sample different cut sets in the variable space, calculate signal and background efficiency for each cut set. Then it chooses one cut set with lowest background efficiency for a certain 1% signal efficiency bin. We can then pick the cut set with the best significance according to the signal and background yield corresponding to the whole data set of 1.3 B events. Fig. 12 shows the lowest background efficiency, significance and so on vs. signal efficiency for p_T between 2 and 3 GeV/c. We can see that as cuts get tighter, signal and background efficiency both decrease, but background efficiency

FIG. 9: simulated D^0 p_T distributionFIG. 10: background p_T distribution with (black) and without (blue) random sample

179 decrease much faster. The best significance for 1.3 B events is around signal efficiency of 10%.
 180 However, because the background efficiency is too low, there are a lot of fluctuations for the
 181 significance.

182 We can solve the problem by having loose cuts on the 5 variables before putting into TMVA
 183 training. So a majority of background is rejected by the loose cuts, and the left sample is more
 184 sensitive to the best cuts region. In this way with the same sample size the cut tuning is more
 185 precise. The loose cuts can be obtained also with TMVA training, requiring higher signal efficiency
 186 than the best significance, for example, 60% signal efficiency in Fig. 12. And this procedure can
 187 be repeated to tighten the cuts step by step, until the statistics around the best significance region

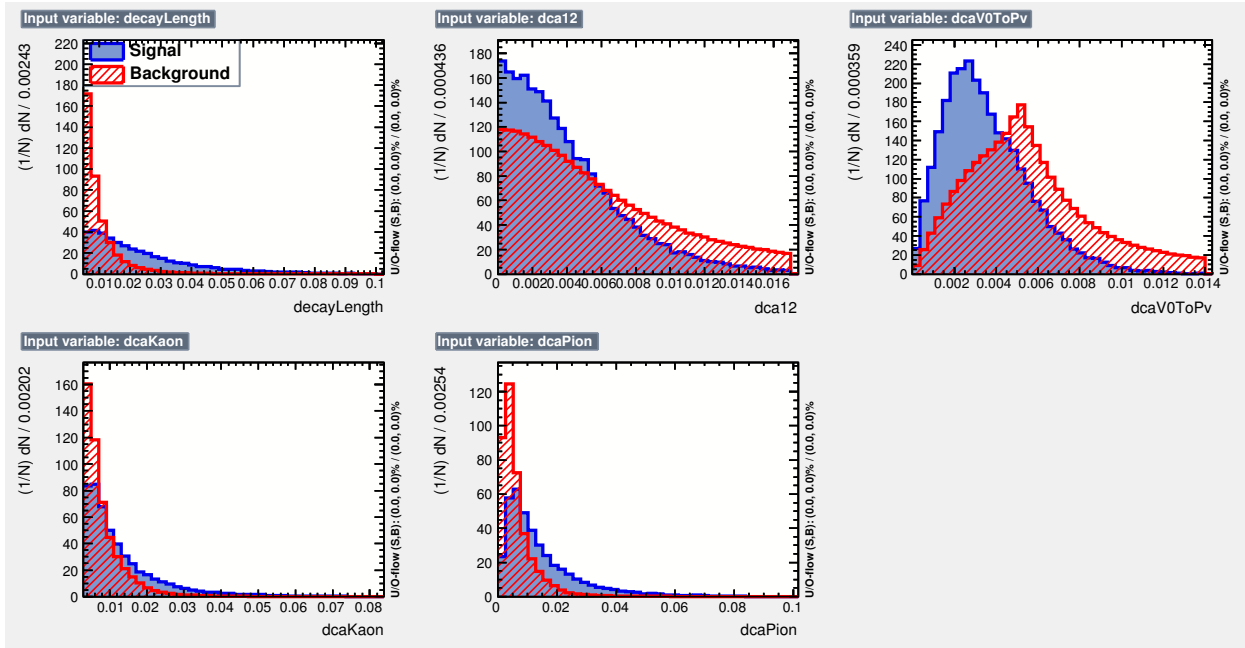


FIG. 11: distributions of the 5 geometry variables for signal (blue) and background (red)

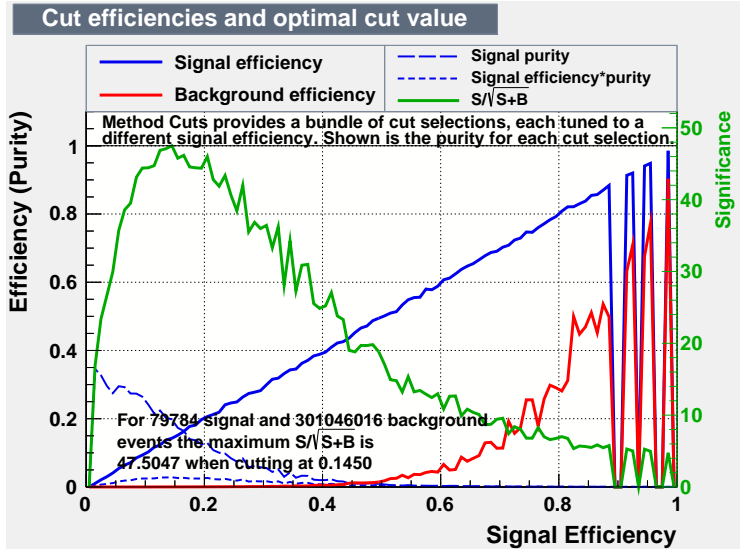


FIG. 12: signal efficiency, lowest background efficiency, significance and so on vs. signal efficiency

is good. Fig. 13 shows the same lowest background efficiency, significance and so on vs. signal efficiency plot, in the last step of tuning. The cuts with the best significance is the result of the TMVA tuning.

The result of the geometry cuts tuned for best significance are shown in Table III. These are the standard cuts used in the D^0 reconstruction to calculate v_2 central value.

For v_2 systematics estimation, another 2 sets of geometry cuts are tuned with TMVA, with

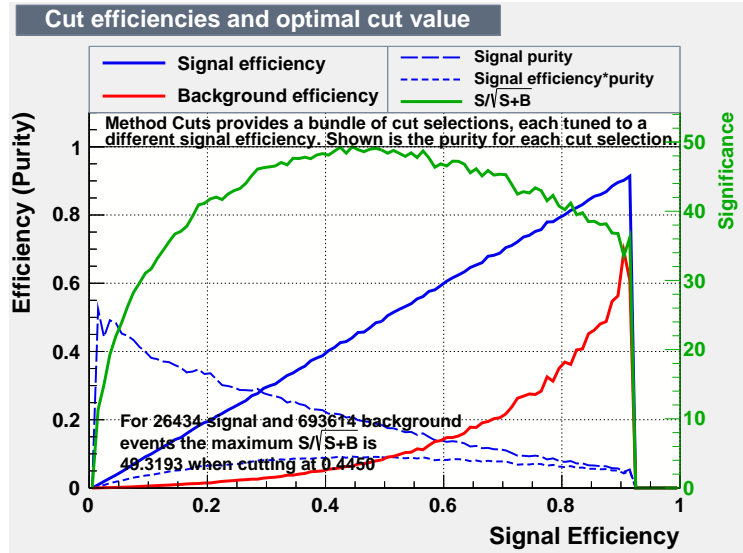


FIG. 13: signal efficiency, lowest background efficiency, significance and so on vs. signal efficiency

¹⁹⁴ 50% and 150% D^0 efficiency relative to the standard cuts. They do not give the overall best D^0
¹⁹⁵ significance, but for the certain D^0 efficiency, they are still the cuts with the lowest background
¹⁹⁶ efficiency and best D^0 significance. As shown in Fig. 13, with 50% and 150% D^0 efficiency
¹⁹⁷ relative to the standard cuts, their significance is still about 80% of the standard cuts with the
¹⁹⁸ overall best significance. These 2 cuts sets are listed in Table IV and V.

TABLE III: Standard geometrical cuts for different $D^0 p_T$.

$D^0 p_T$ (GeV/c)	0-1	1-2	2-3	3-5	5-10
decay length (μm) >	145	181	212	247	259
DCA between 2 daughters (μm) <	84	66	57	50	60
DCA between D^0 and PV (μm) <	61	49	38	38	40
DCA between π and PV (μm) >	110	111	86	81	62
DCA between K and PV (μm) >	103	91	95	79	58

TABLE IV: Tight geometrical cuts for different $D^0 p_T$.

$D^0 p_T$ (GeV/c)	0-1	1-2	2-3	3-5	5-10
decay length (μm) >	144	204	242	245	300
DCA between 2 daughters (μm) <	69	48	44	49	47
DCA between D^0 and PV (μm) <	44	36	31	26	32
DCA between π and PV (μm) >	120	102	118	109	96
DCA between K and PV (μm) >	119	110	109	106	80

TABLE V: Loose geometrical cuts for different $D^0 p_T$.

$D^0 p_T$ (GeV/c)	0-1	1-2	2-3	3-5	5-10
decay length (μm) >	110	168	187	199	180
DCA between 2 daughters (μm) <	77	78	74	68	66
DCA between D^0 and PV (μm) <	72	53	47	42	62
DCA between π and PV (μm) >	92	78	86	65	47
DCA between K and PV (μm) >	105	68	80	66	41

199

 D^0 signals

200 Fig. 14 is the invariant mass of $K\pi$ after topological cuts. The different panels are for different
 201 p_T bins. The red histograms are like-sign pair and blue histograms are mixed event to be explained
 202 later. The primary vertex used here is fit using the Kalman Filter (KF) algorithm, with more details
 203 in the following sub-section. There are some correlated background in the foreground, making it
 204 higher than the like-sign and mixed event background outside the D^0 peak region. They may be
 205 constituted of the “bump” at lower invariant mass region from other decay channels of D mesons
 206 and a shoulder below the D^0 peak from double mis-PID (K identified as π while π identified as
 207 K), which are described in later sub-sections.

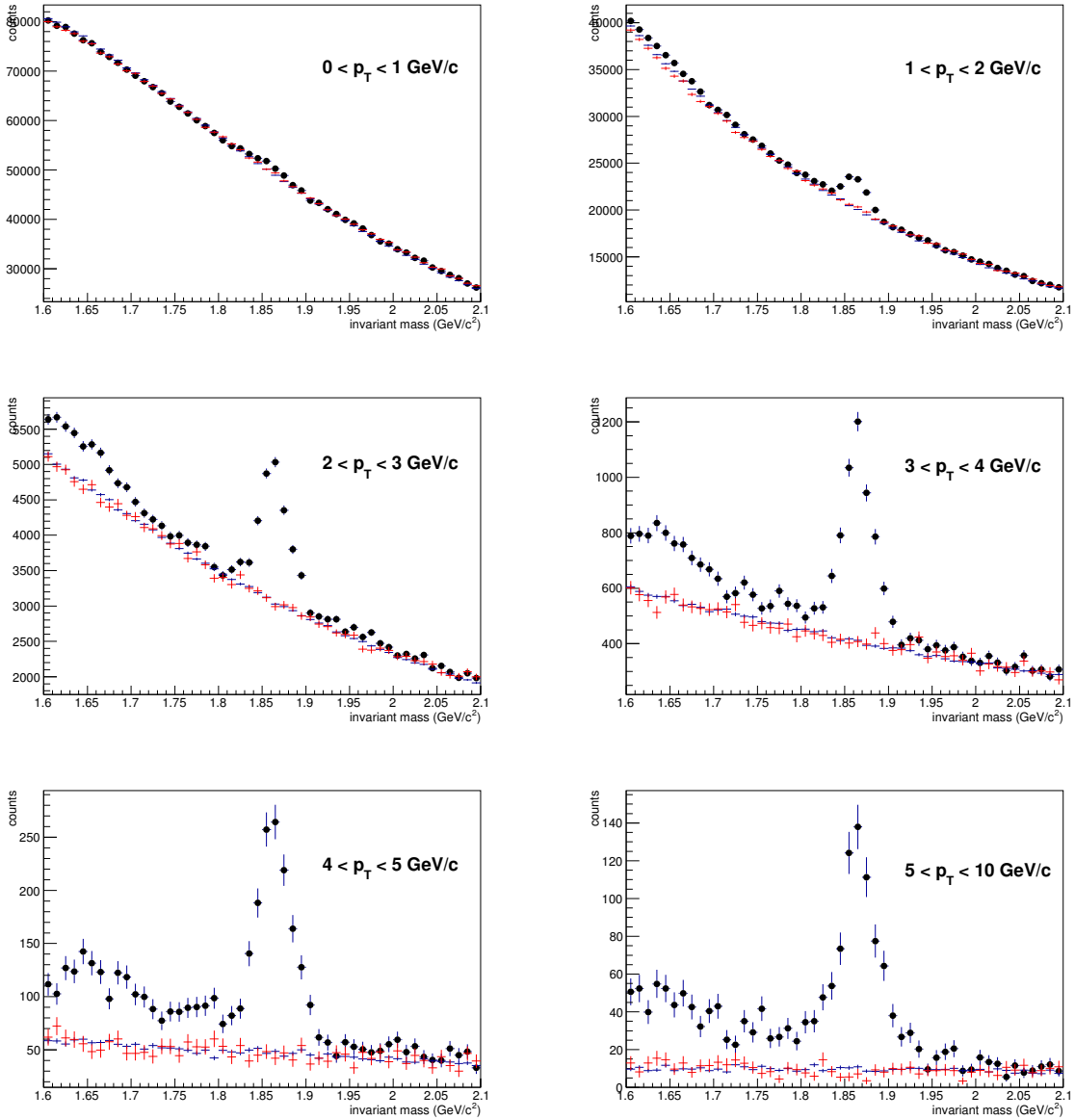


FIG. 14: invariant mass of $K\pi$ with D^0 signals after topological cut for different p_T bins. The red histograms are like-sign pair and blue histograms are mixed event.

208

KF vertex

209 The D^0 reconstruction depend on very precise geometry cuts related to both the secondary and
 210 the primary vertices. It has been found that the vertex resolution for peripheral events is improved
 211 when using the Kalman Filter (KF) algorithm as opposed to the STAR default vertex using Minuit
 212 algorithm. In this section we summarize our studies on this.

213 The default vertexing algorithm in Au+Au collisions at STAR uses Minuit. In this study we
 214 select the highest ranking vertex from the MuDsts' that has

$$|V_z| < 100. \text{ cm}$$

$$|V_z - V_z\{VPD\}| < 3. \text{ cm}$$

215 We further apply a $|V_z| < 6. \text{ cm}$ cut on the vertex. We re-fit the vertex of the selected events
 216 using the KF algorithm (notice that this implies that we compare KF and Minuit on an identical
 217 set of events). For the KF vertex we use the following track cuts:

$$|\text{DCA}(\text{pVtx})| < 3. \text{ cm}$$

$$\text{number-of-fit-points} \geq 20$$

218 where pVtx is the Minuit primary vertex, number-of-fit-points includes both TPC and HFT fit
 219 points. These cuts are very close to those used by the Minuit vertexing algorithm at STAR.

220 We first show the impact of the two algorithms vertex resolution on the D^0 reconstruction
 221 efficiency. Around 537M events were used for this comparison, the D^0 topological cuts are tuned
 222 by TMVA mentioned above. Fig.15 shows the D^0 signal in MinBias centrality, it is clear that the
 223 total counts and significance are higher using KF vertex.

224 Fig.16 and Fig.17 compare the signal in p_T -bins in 0-80% and 40-80% centralities, respectively.
 225 The improvement of KF vertex is clear in all p_T bins and, as expected, is more significant in
 226 peripheral collisions.

227 Fig.18 compares the counts and significance from KF vertex and Minuit for most peripheral,
 228 most central and MinBias centralities. Again, from these comparison we can see that KF vertex
 229 gives better significance especially in the peripheral collisions.

230 We also systematically studied the KF vertex resolution and Minuit Vertex resolution.

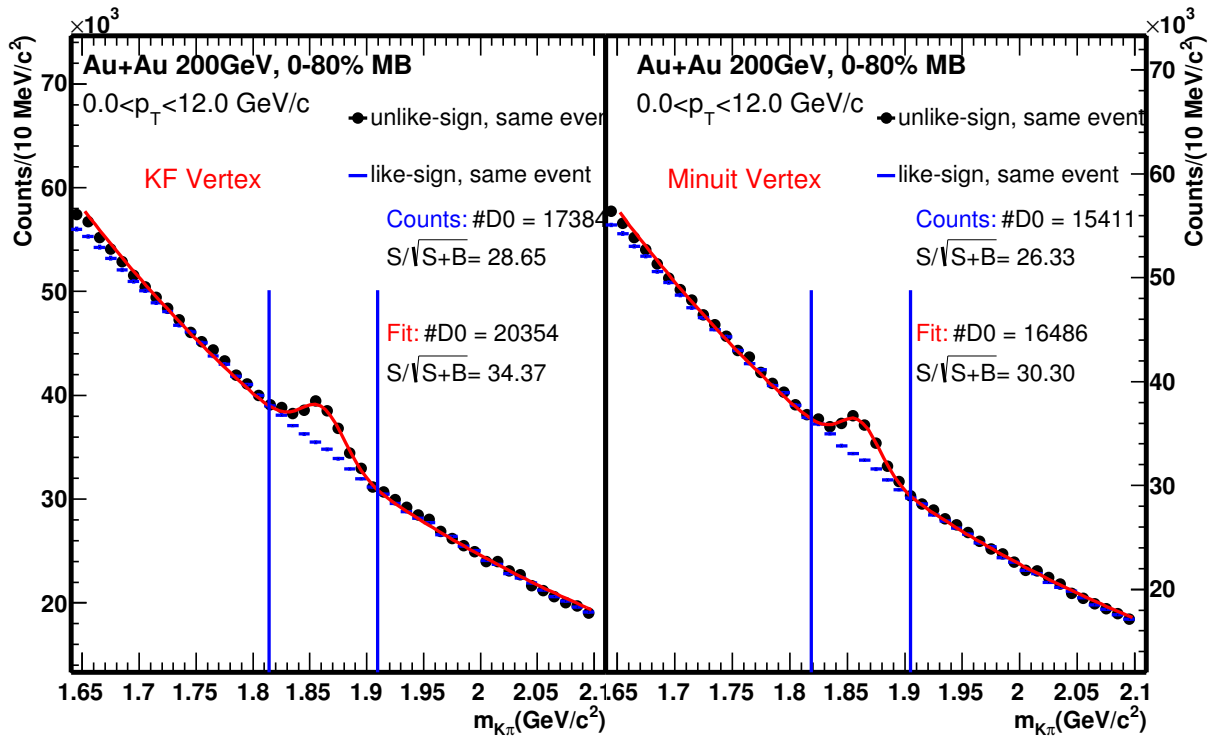


FIG. 15: Invariant mass spectrum of $K\pi$ pairs for KF vertex (left) and Minuit vertex (right). The black points are unlike sign pairs with the D^0 signal; The blue solid lines show the like sign and red line are gaus+exp fit respectively.

In real data, we don't know where the collision happens in reality. To study primary vertex resolution, we divide tracks in the event randomly into 2 sub-events, and reconstruct primary vertices for these 2 sub-events separately. Figure 19 shows vertex x difference between 2 random sub-events for KF and Minuit, comparing with MC simulation, for different multiplicity ranges. By comparing the RMS, we can see that the KF resolution is better than Minuit for real data. The MC simulation can reproduce the data except the most central's tail in real data. This tail makes it difficult to use RMS as a good representative of the resolution, so we use the Full width at half maximum (FWHM) to summarize the comparison in 3 dimensions, as shown in Fig.20.

The FWHM well represents the width of the major peak, but another important information is how large is the tail, i.e., the 2 sub-event vertices are far from each other and one has to be wrong. Figure 21 shows the ratio of reconstructed vertices within 100 μm from each other, in X, Y, and Z dimension, for KF and Minuit. We can see that for real data the ratio of KF vertex within 100 μm is higher than Minuit, meaning KF 'fail' less than Minuit. The KF ratio also gets close to unit in the most central collisions.

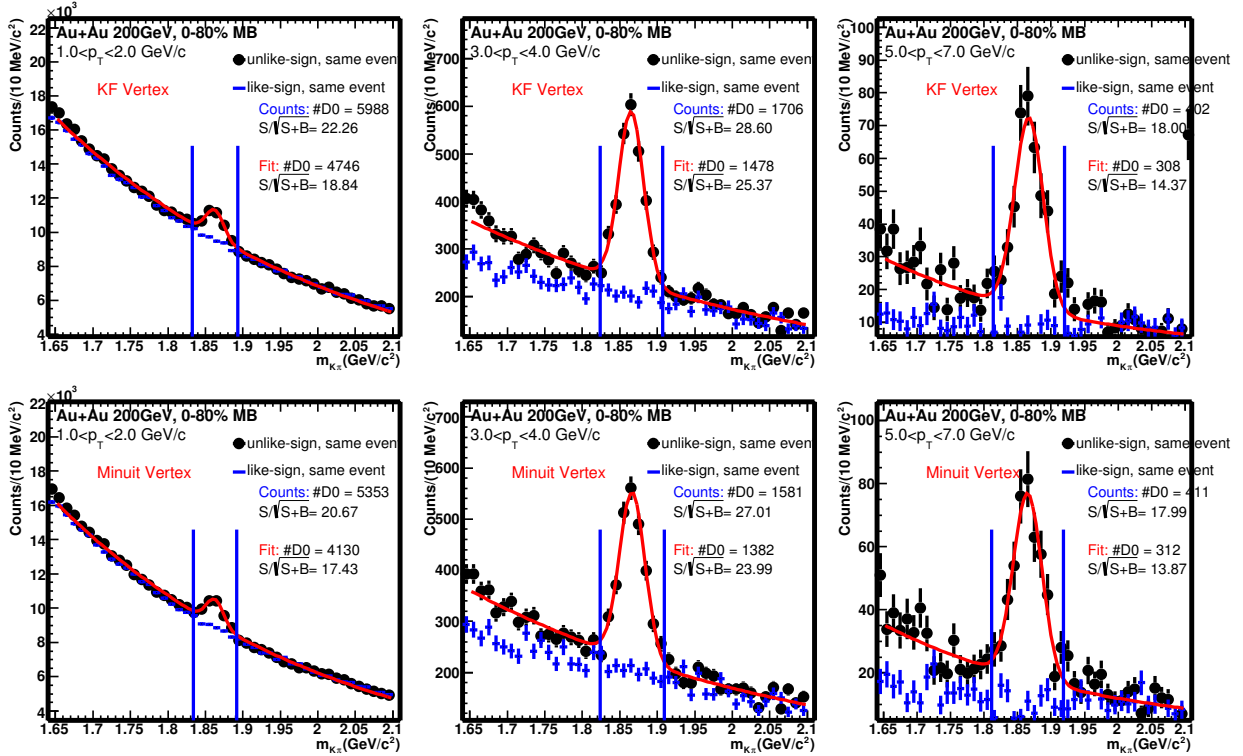


FIG. 16: Invariant mass spectrum of $K\pi$ pairs for KF vertex (top) and Minuit vertex (bottom). Different centrality(0-80%) and transverse momentum range.

245 In general the KF always works better than Minuit for primary vertex reconstruction. In this
 246 analysis, a KF primary is always reconstructed and used, including the D^0 signals in Fig.14 shown
 247 before.

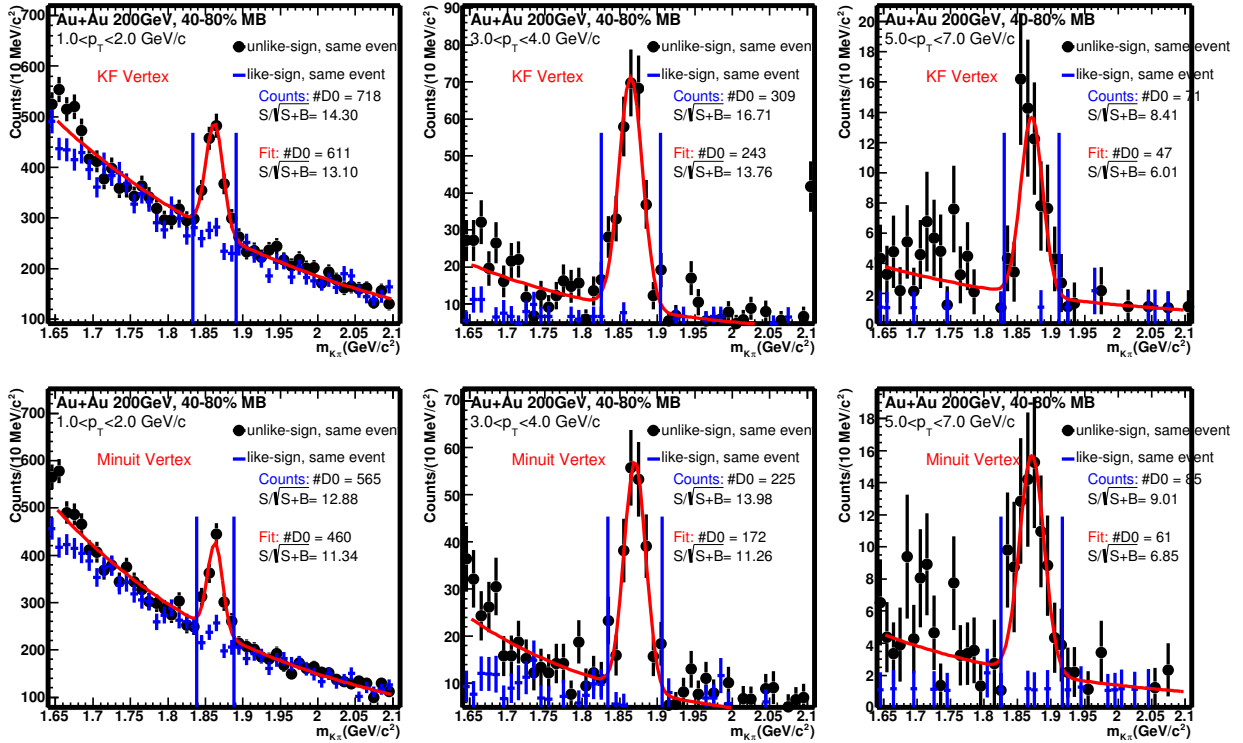


FIG. 17: Invariant mass spectrum of $K\pi$ pairs for KF vertex (top) and Minuit vertex (bottom). Different centrality(40-80%) and transverse momentum range.

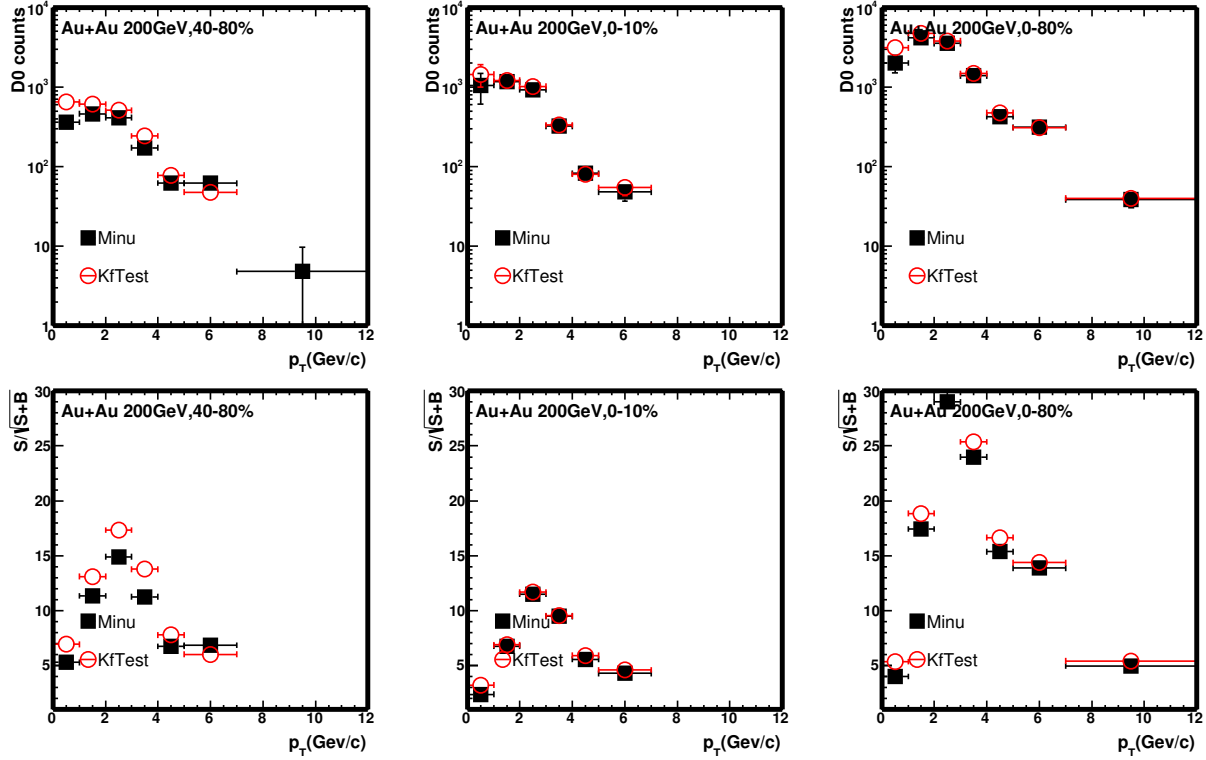


FIG. 18: D^0 counts (top) and significance (bottom) for KF and Minuit vertex comparison from different centrality and transverse momentum range.

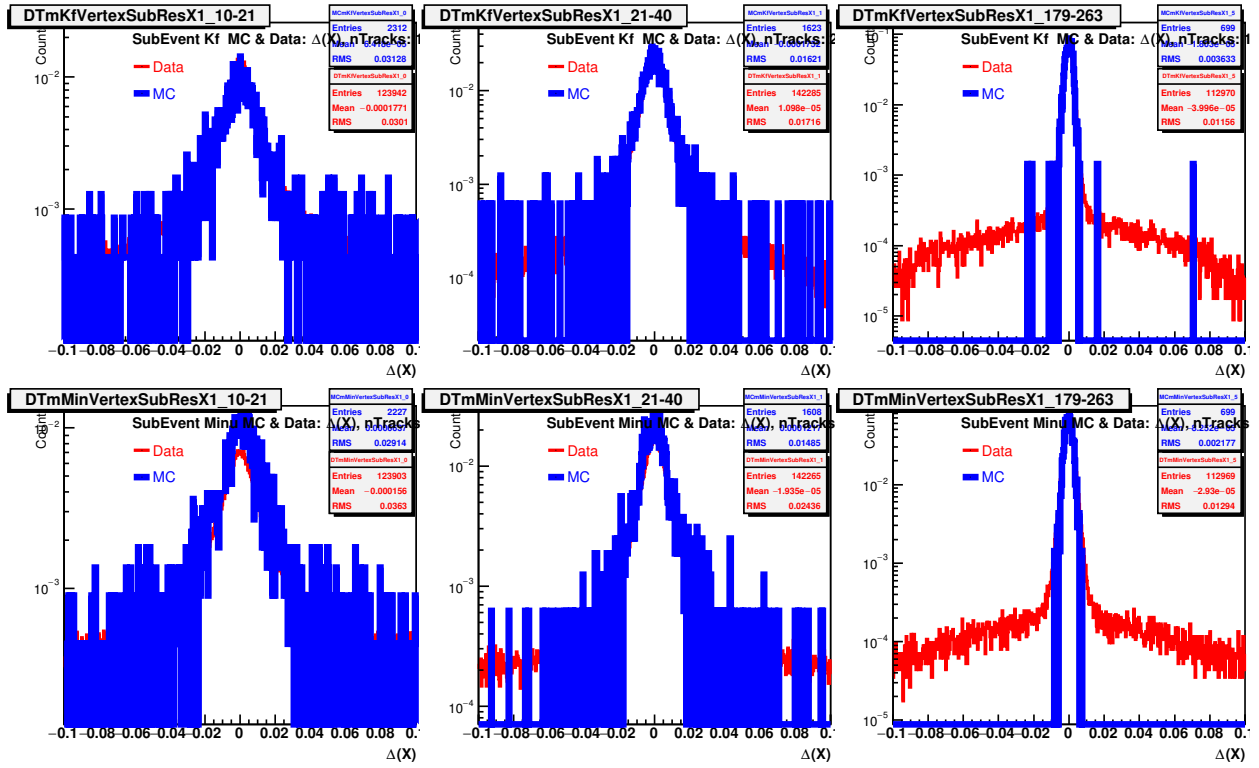


FIG. 19: Sub-event vertex(X) difference for KF (top) and Minuit (bottom), also comparison with MC simulation separately. Left to Right is from peripheral to central events.

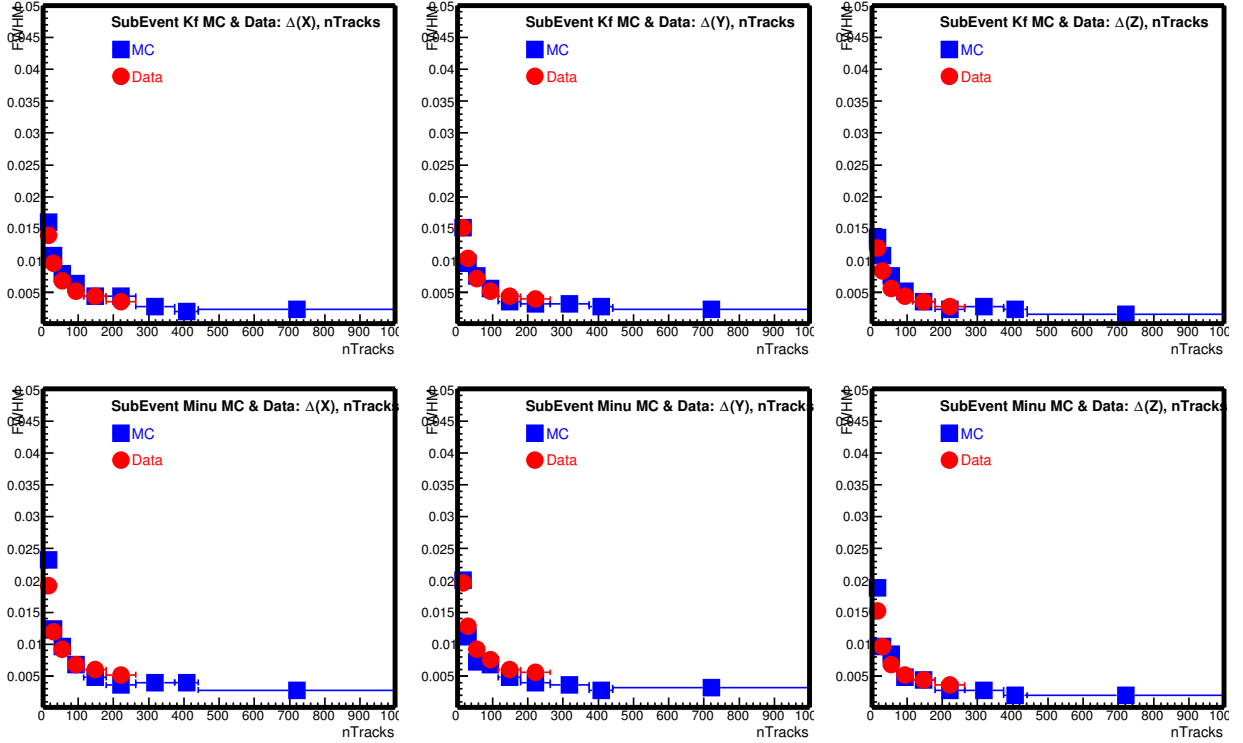


FIG. 20: Sub-event vertex difference Full Width at Half Maximum (FWHM) for KF (top) and Minuit (bottom), also comparison with MC simulation, for X, Y, and Z directions from left to right panels.

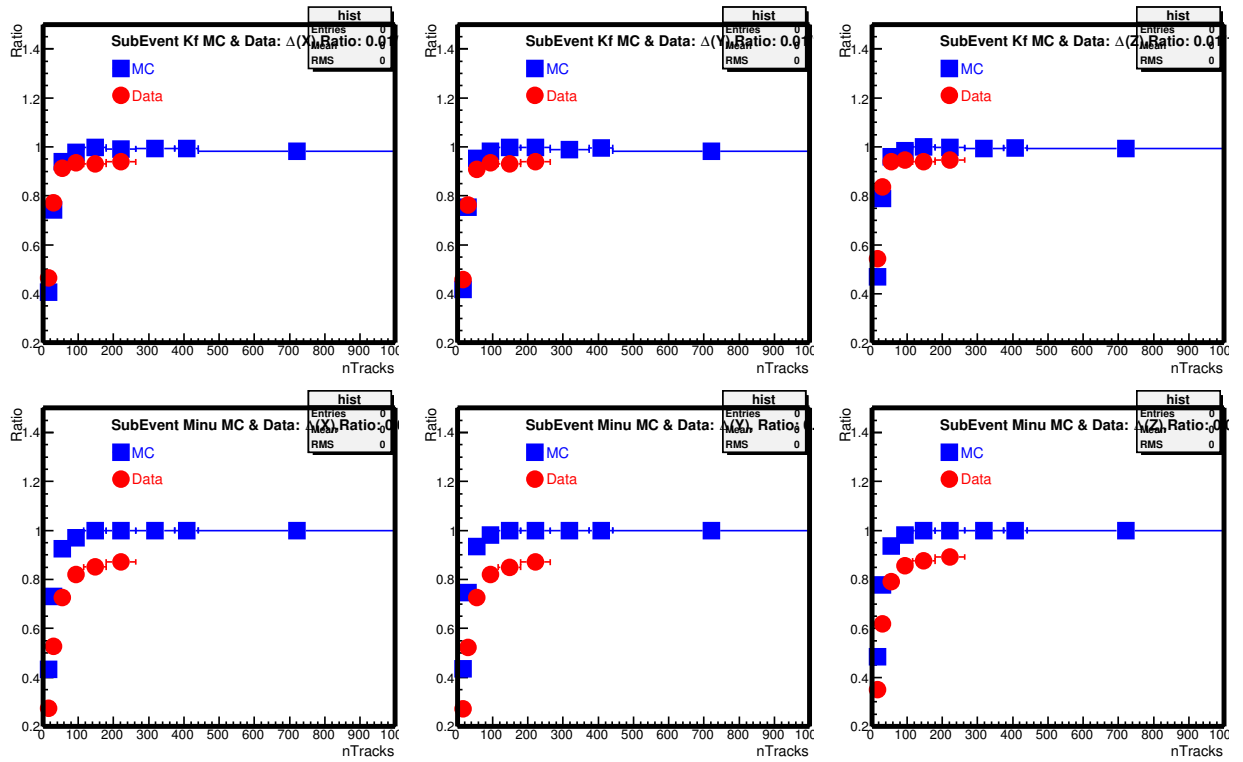


FIG. 21: Ratio of reconstructed sub-event vertices within $100 \mu\text{m}$ from each other for KF (top) and Minuit (bottom), also comparison with MC simulation, for X, Y, and Z directions from left to right panels.

248

Mixed event background

249 There are several established procedures to statistically describe the contribution of the un-
 250 correlated background to the foreground when studying particle reconstruction. In particular, all
 251 correlations between particles can be broken by mixing tracks from different events with the added
 252 benefit of improved statistical precision as a single event can be mixed with many others.

253 To construct the mixed event background it is important to combine events with some degree of
 254 similarity, and as such events are classified according to the position of the primary vertex (PV)
 255 along the beam-line, their centrality class and the orientation of the event plane. Ten bins of
 256 equal width were used for both the event plane ($\Psi \in [-\pi, \pi]$) and the position of the primary
 257 vertex ($V_z \in [-6, 6]$), as well as nine centrality classes between 0-80%, for a total of 900 event
 258 "categories".

259 Given that events must be read and mixed over several files, each event is saved to an associated
 260 buffer after being categorized, and due to memory and speed considerations only the relevant
 261 information from a given event and its associated tracks are saved. Table VI summarizes the
 important information saved to the event buffers:

StMixerTrack	StMixerEvent
Origin	PV Origin
Momentum	Magnetic Field
Q-Vector	Event Plane
Track information	Array of mixer tracks Array of indices to identified pions Array of indices to identified kaons

TABLE VI: Summary of information saved to the event buffer for mixing

262

263 Each mixer track, as they were dubbed, occupies roughly 90 bytes of memory and contains
 264 the necessary information to reconstruct the track, its orientation relative to the event plane (used
 265 for the v_2 analysis) as well as other track information such as charge, PID according to different
 266 detectors, etc. which is encoded in the binary representation of a short variable.

267 In the current implementation studying $D^0 \rightarrow K\pi$ reconstruction, only pions and kaons were
 268 identified and the position of their associated tracks in the array of mixer tracks is saved for quick
 269 access. To illustrate the advantage lets assume a simple scenario in which two events, both with
 270 identical number of kaons N_K and pions N_π , are to be mixed. If we were to simply loop over all
 271 tracks in each event in search of pair candidates the total number of loops is:

$$N^2 = N_K^2 + N_\pi^2 + 2N_K N_\pi \quad (1)$$

272 On the other hand, assuming that pions and kaons have already been identified, then the number
273 of loops is reduced to:

$$N_K N_\pi + N_\pi N_k = 2N_K N_\pi < N^2 \quad (2)$$

274 To illustrate the improvement in performance we can assume a somewhat average distribution
275 of produced particles, such that: $N_\pi = 0.8N$ and $N_K = 0.2N$. In this case the difference between
276 both procedures is more than a factor of three $2N_K N_\pi \simeq 0.32N^2$.

277 A quick calculation is useful to estimate the memory required to save and mix the events. As
278 mentioned previously, each track occupies ~ 90 bytes of memory; assuming an average of a
279 thousand tracks per event, each event will occupy ~ 90 kilobytes. Considering 11 events per
280 buffer(so each event can be mixed with 10 others) and 900 categories, a total of roughly 0.9
281 megabytes of memory is required, well within allowances for most processors either at PDSF or
282 RCF.

283

284 Once the buffer has been filled the pions from the first event are combined with kaons from the
285 rest of the events in the buffer, considering both like-sign and unlike-sign combinations. In the
286 first iteration the pions and kaons from the same event are combined to produce the foreground
287 (unlike-sign) as well the same event like-sign background. In order to apply the topological cuts to
288 the background, the second event is moved during the mixing such that the position of the primary
289 vertex in both coincides.

290 Once the mixing has been completed, the first event is removed from the buffer leaving space
291 for another event to be added at the end. Figure 22 shows the invariant mass distribution for the
292 foreground and three different uncorrelated backgrounds: same event like-sign, mixed event like-
293 sign and mixed event unlike-sign in three p_T bins. Both mixed event backgrounds have been scaled
294 to the foreground using the integration range $m_{K\pi} \in [2, 2.1] \text{GeV}/c^2$.

295 There is good agreement between the three descriptions of the combinatorial background and
296 they appear to provide an adequate description in the vicinity of the D^0 signal and, as was to be
297 expected, the mixed event backgrounds have improved statistical precision.

298 It is interesting to observe the presence of an "excess" in the foreground, relative to all of the

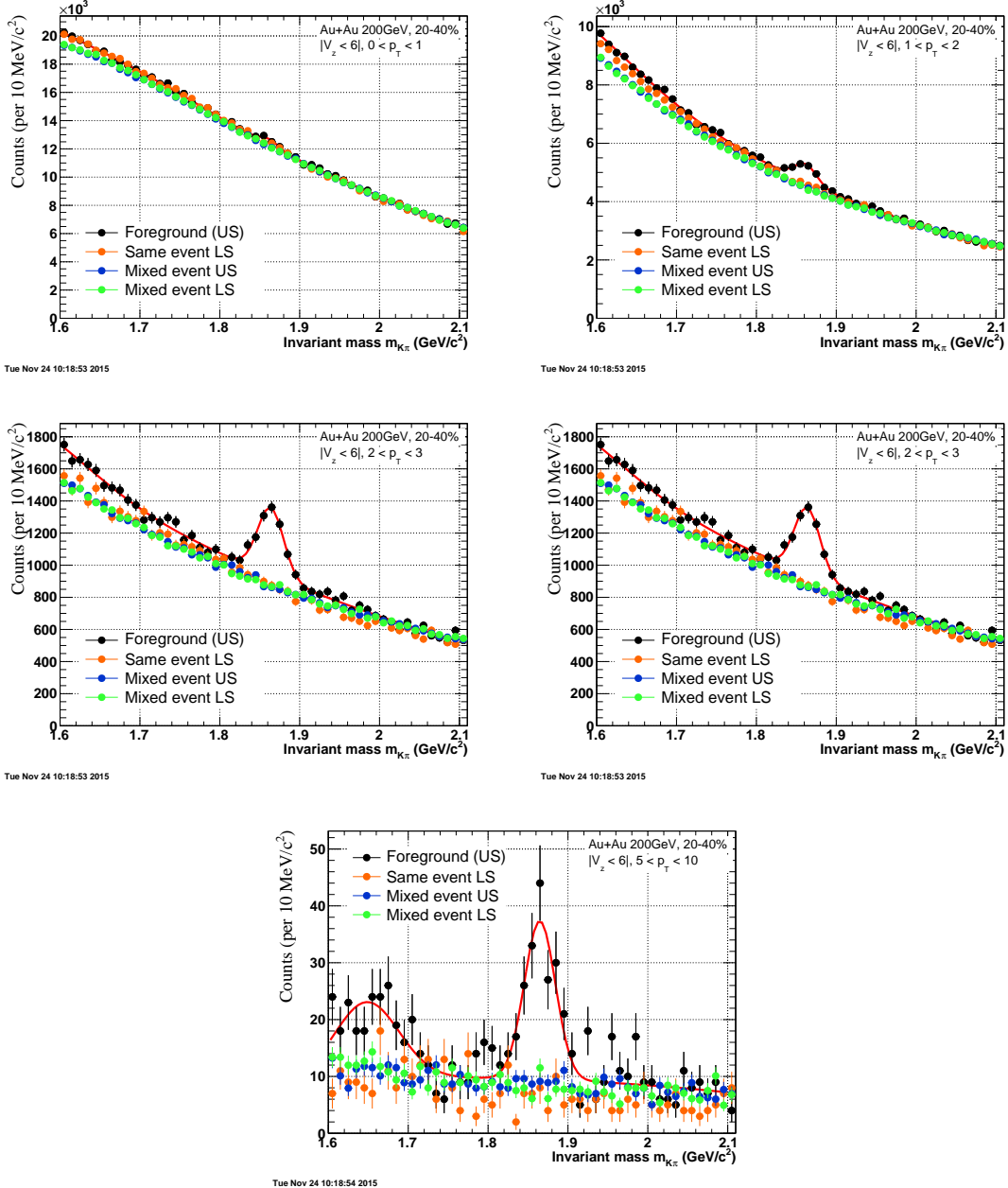


FIG. 22: Invariant mass distribution for foreground and three descriptions of combinatorial background in 5 p_T bins

background curves, below roughly $1.75 \text{ GeV}/c^2$. This so called bump was investigated using the Data Driven Fast Simulator, and will be covered briefly in the following section.

301 **Correlated background "bump" from other D meson decay channels**

302 In order to study other possible contributions to the observed D^0 background, a cocktail of
 303 particle decays were generated with realistic p_T distributions (from published D^0 data) and flat η
 304 and ϕ distributions, which were then decayed using a simple MonteCarlo simulation and sampling
 305 distributions obtained from data and embedding.

306 Once the particles are decayed, the daughter momentum and the distance of closest approach
 307 (DCA) to the primary vertex (PV) are smeared according to distributions obtained from data.

308 Pion-kaon pairs are formed from the decays using the topological cuts optimized for D^0 recon-
 309 struction to study the contributions that fall within the invariant mass spectrum studied. The finite
 310 probability of double mis-PID, where a pion is confused with a kaon and vice a versa, was also
 311 included in this study by sampling TPC dE/dx distributions from data.

312 The contributions to the invariant mass spectrum from the following D^0 and D^\pm decays were
 313 included in a qualitative study of the correlated background:

- 314 • $D^0 \rightarrow K^- \pi^+$ (B.R. 0.039)
- 315 • $D^0 \rightarrow K^- \pi^+ \pi^0$ (B.R. 0.011)
- 316 • $D^0 \rightarrow K^- \rho^+ \rightarrow K^- \pi^+ \pi^0$ (B.R. 0.108)
- 317 • $D^0 \rightarrow K^{*-} \pi^+ \rightarrow K^- \pi^+ \pi^0$ (B.R. 0.007)
- 318 • $D^+ \rightarrow K^- \pi^+ \pi^+$ (B.R. 0.073×0.415)

319 The charm fragmentation ratio used is the following from ZEUS Collaboration (arXiv:hep-
 320 ex/0508019 - Table 4):

- 321 • $f(c \rightarrow D^+) = 0.217$
- 322 • $f(c \rightarrow D^0) = 0.523$
- 323 • $f(c \rightarrow D_s^+) = 0.095$
- 324 • $f(c \rightarrow_c^+) = 0.144$
- 325 • $f(c \rightarrow D^+) = 0.200$

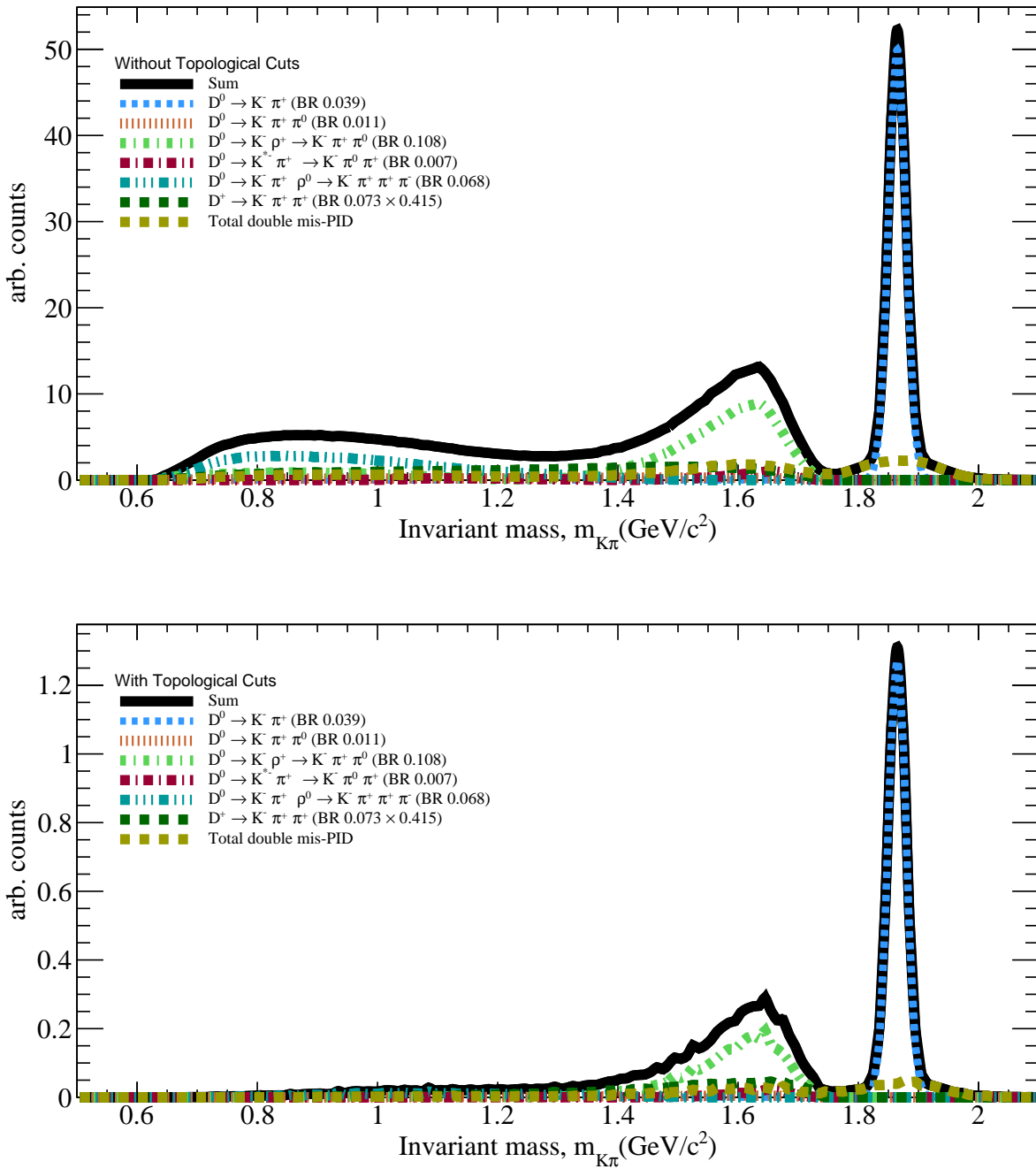


FIG. 23: Simulated contribution to the invariant mass spectrum from cocktail

326 Figure 23 shows the invariant mass spectrum obtained from the cocktail after scaling by the
 327 branching ratio for different decays as well as the fragmentation ratio for the different charmed
 328 meson species.

329 The spectrum is shown before and after the $D^0 \rightarrow K\pi$ topological cuts have been applied.
 330 It is clear that the contributions from correlated background can, at least in part, account for the

331 enhancement observed below roughly $1.7\text{GeV}/c^2$.

332 The cocktail simulation was then scaled by fitting the amplitude of the D^0 peak obtained from
333 fast simulator to the signal observed in data, and the cocktail was then added to the mixed event
334 background. Figure 24 shows a comparison between the invariant mass distribution obtained from
335 data and the spectrum obtained by combining the mixed event background and the results from
336 the data driven fast simulator.

337 The inclusion of correlated background sources can qualitatively describe the foreground ob-
338 served, reproducing the location of the bump structure albeit underestimating the degree of en-
339 hancement itself. Furthermore, there is likely a finite contribution to the observed bump originating
340 from jet correlations which should be included to improve on the description of the background.

341 It should also be noted that the studies presented here were done with an early version of the
342 fast simulator which only included the p_T and centrality dependence of sampled distributions,
343 revisiting the studies with more differential distributions should improve on these results.

344 Nonetheless, the results provide confidence in a qualitative understanding on the sources of the
345 correlated background and, what is more, suggest that the contribution from these source in the D^0
346 signal range is dominated by double mis-PID, and is nearly negligible as shown in the following
347 sub-section.

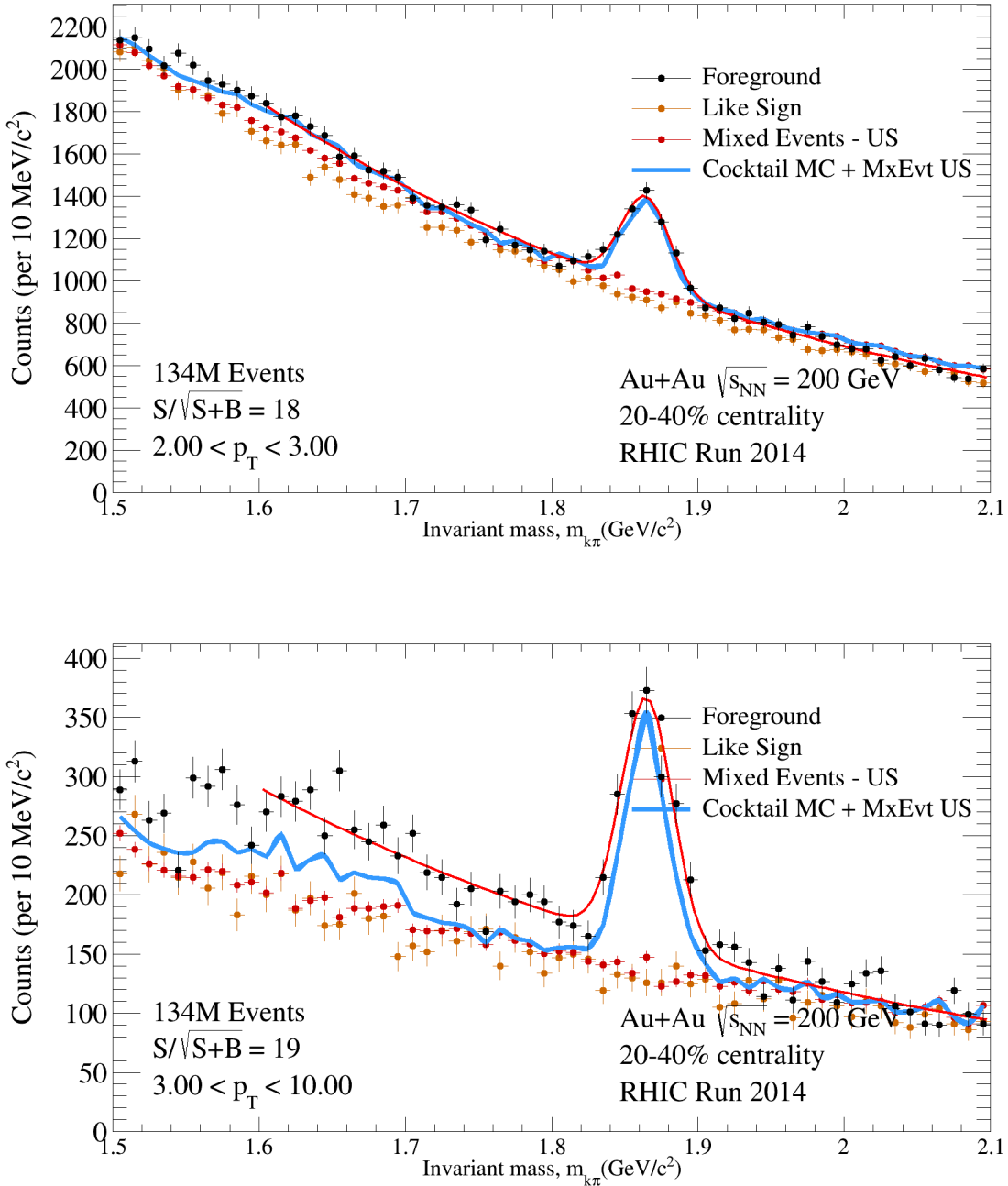


FIG. 24: Comparison of $K\pi$ invariant mass distribution for unlike-sign (US) foreground, like-sign combinatorial background, unlike-sign (US) mixed events combinatorial background, and unlike-sign (US) mixed events combinatorial background + toy montecarlo cocktail for correlated background, for two p_T ranges

348

Double mis-PID

349 D^0 candidates are reconstructed with pairing K^- and π^+ candidate tracks. When D^0 daughter
 350 K^- is misidentified as a π^- while the other daughter π^+ is misidentified as a K^+ , the resulting
 351 pair $K^+\pi^-$ will enter into the distribution for reconstructing $\overline{D^0}$. Although the mass assignments
 352 are wrong, the pair $K^+\pi^-$ invariant mass will be still peak around the D^0 region with typically
 353 a broader distribution compared to the real signal. When counting the final D^0 candidates, these
 354 within the mass selection window will be counted twice. (See also study in previous STAR open
 355 charm hadron measurements - STAR notes below).

356 <https://drupal.star.bnl.gov/STAR/starnotes/private/psn0594>

357 <https://drupal.star.bnl.gov/STAR/starnotes/private/psn0550>

358 The double counting issue will certainly affect the obtained D^0 raw yields. In the v_2 analysis,
 359 since the doubly counted candidates are still coming from D^0 , this issue should not affect the
 360 obtained central value of v_2 . However, the statistical errors could be slightly off.

361 The double counting probability estimation need a precise determination of the PID variable
 362 distributions, $n\sigma_X$ from dE/dx and $1/\beta$ from TOF. For dE/dx calculation, we tried two methods

363 1) Select pure pion and proton samples from weak decays (K^S , Λ)

364 2) Look at the single particle distributions directly and perform multi-component fit in the
 365 region where the dE/dx bands can be separated out.

366 Figure 25 shows the reconstructed $\pi\pi$ (left) and $p\pi$ (right) invariant mass distributions from
 367 unlike-sign and like-sign pairs in $1.0 < p_T < 1.1$ GeV/c and top 0-10% central Au+Au collisions.
 368 The weak particle peaks are prominent. We use unlike-sign subtract like-sign around the peak
 369 region to select clean weak decays and make dE/dx $n\sigma_X$ distributions for the pion and proton
 370 daughters.

371 In the distributions shown below, distributions from top 0-10% central collisions are usually
 372 shown as examples if not specified.

373 These $n\sigma_X$ distributions are fit to simple gaussian functions to obtain the mean and width values
 374 vs. particle momentum which is shown in Figure 26

375 Figure 27 shows extracted $n\sigma_X$ mean values from single particle dE/dx distributions directly.
 376 Results from the region beyond the dE/dx identification capability are not so reliable (kaons above
 377 0.4 GeV/c and protons above 0.8 GeV/c).

378 Figure 28 summarized the extracted $n\sigma_X$ mean values vs. $\beta\gamma$ for both methods discussed above.

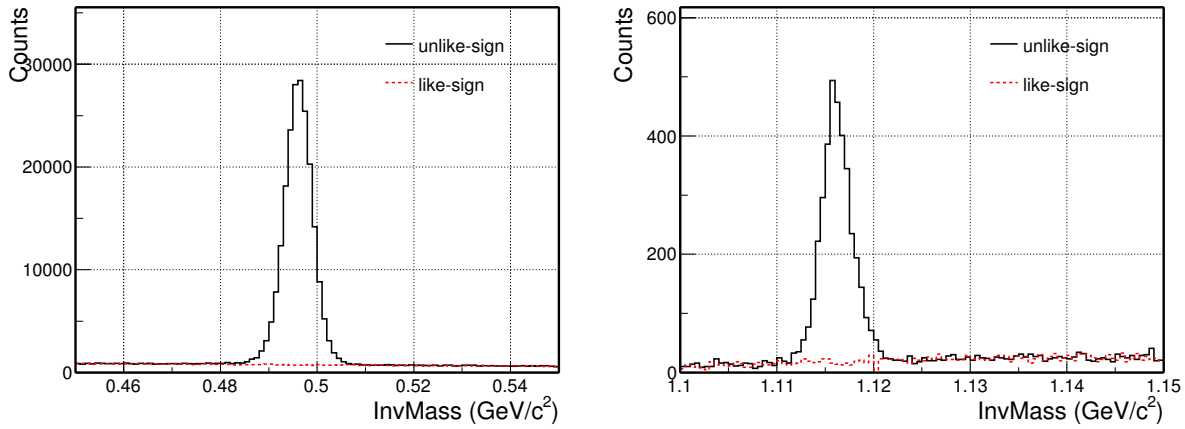


FIG. 25: Top 0-10% central Au+Au collisions and $1.0 < p_T < 1.1 \text{ GeV}/c$: $\pi\pi$ (left) and $p\pi$ (right) invariant mass distributions from unlike-sign and like-sign pairs.

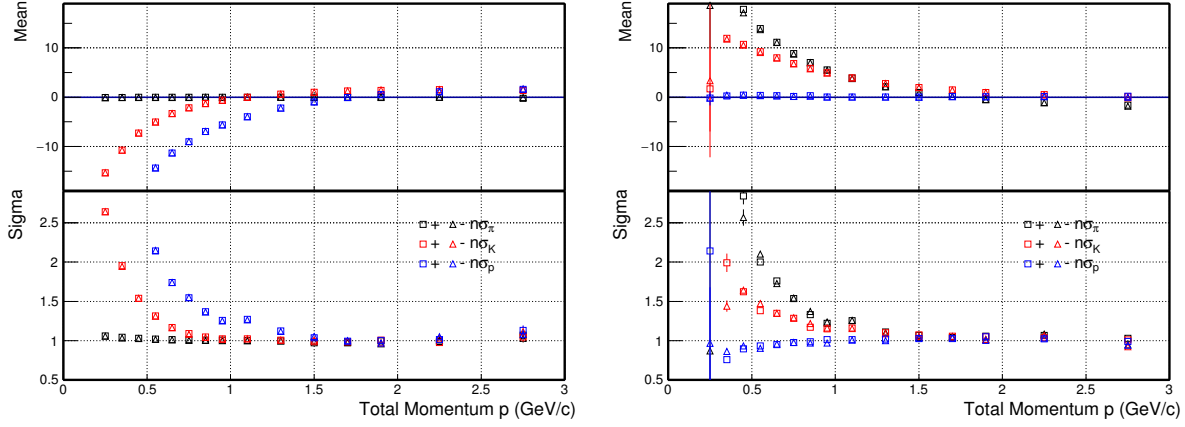


FIG. 26: Top 0-10% central Au+Au collisions: extracted $n\sigma_X$ mean values for (left) pions from K_S decays and (right) protons from Λ decays. Black, red, and blue markers are for $n\sigma_\pi$, $n\sigma_K$, and $n\sigma_p$ respectively. Squares and triangles are for positive and negative particles respectively.

379 It looks good that in the overlapping region between different particles and different methods, the
 380 results look consistent. The dashed blue lines are parametrized function fits to the data points.
 381 These will be used to estimated the mis-identification probability.

382 The hybrid PID also involves the TOF detector. We also estimated the TOF PID variable $1/\beta$
 383 distributions and TOF matching/PID efficiency. Figure 29 shows the fit results on the mean and
 384 width values for $1/\beta - 1/\beta_{expected}$ distributions vs. particle momentum for different particles.
 385 Similar as dE/dx , results in the region beyond the TOF PID are not reliable. We use results which
 386 are safe in PID for later analysis, which are $p < 1.5 \text{ GeV}/c$ for pions, $p < 1 \text{ GeV}/c$ and kaons
 387 and $p < 2 \text{ GeV}/c$ for protons. It is good to see the mean and width values are quite stable in
 388 a broad momentum region. At very low momentum, the multiple scattering effect will increase

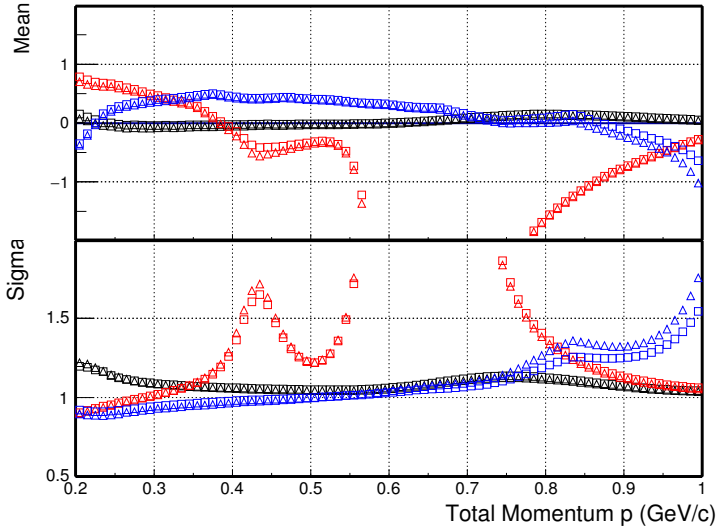


FIG. 27: Top 0-10% central Au+Au collisions: extracted $n\sigma_X$ mean values from single particle dE/dx distributions directly, for π (black), K (red) and proton (blue). Results from the region beyond the dE/dx identification capability are not so reliable.

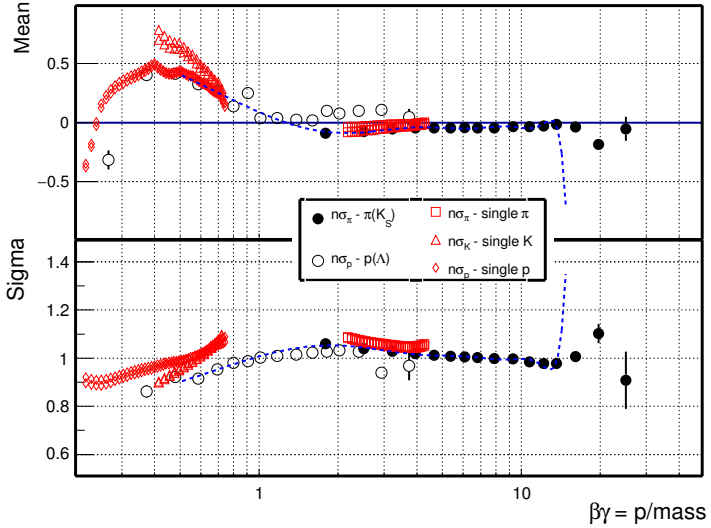


FIG. 28: Top 0-10% central Au+Au collisions: extracted $n\sigma_X$ mean values vs. $\beta\gamma$ for both methods discussed in the text.

momentum resolution and $1/\beta - 1/\beta_{expected}$ spread, and track energy loss will also shift the mean of $1/\beta - 1/\beta_{expected}$ away from 0. But these will not affect the study here since tracks with $p_T < 0.6$ GeV/c are not used for D^0 reconstruction.

TOF matching and PID efficiencies were evaluated with a standard method by selecting candidate tracks using TPC dE/dx PID and look at the TOF response. Figure 30 shows TOF matching and valid β efficiencies vs. p_T for particles identified with dE/dx selection. The open symbols

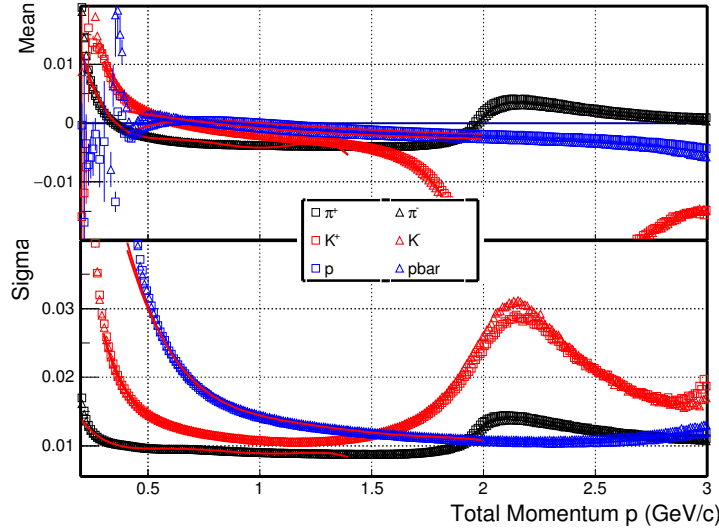


FIG. 29: Top 0-10% central Au+Au collisions: extracted $1/\beta - 1/\beta_{expected}$ mean and width values vs. particle momentum for pions, kaons and protons. Results for pions and kaons at $p > 1.5$ GeV/c are beyond the TOF PID capability. The fit results are not reliable.

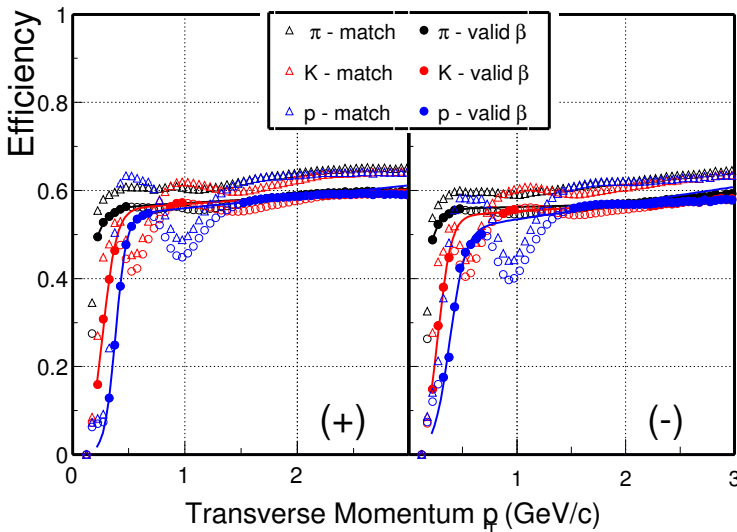


FIG. 30: Top 0-10% central Au+Au collisions: TOF matching and valid β efficiencies vs. p_T for particles identified with dE/dx selection. The open symbols indicate the regions where their dE/dx bands cross so there are quite some contaminations in the dE/dx selection.

395 indicate the regions where their dE/dx bands cross so there are quite some contaminations in
 396 the dE/dx selection. Function fits were conducted to the solid data points to parametrize these
 397 distributions for later calculations.

398 With all these at hand, we can evaluate the hybrid PID efficiency which is shown in Figure 31.
 399 The advantage of the hybrid method is to keep the highest efficiency as one sees from the plot.
 400 The mis-identification probability for pion and kaon daughters can be also evaluated, as shown in

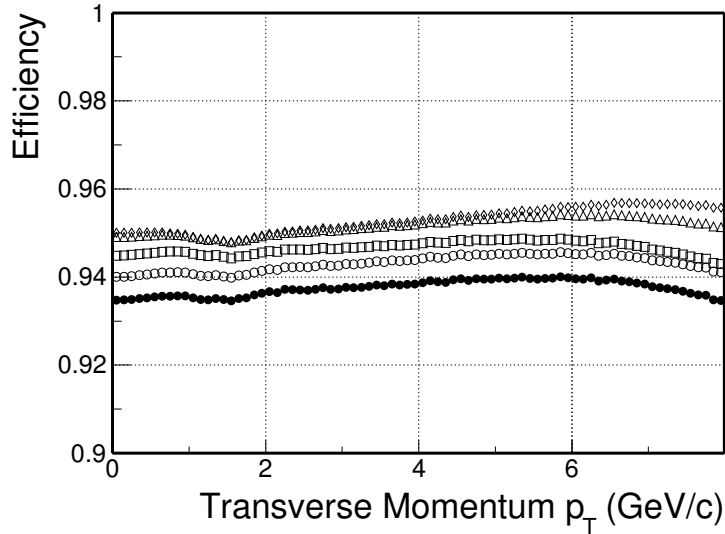


FIG. 31: The combined PID cut efficiency with the hybrid PID method for 0-10% (black solid symbols) to 60-80% (open diamonds) collisions.

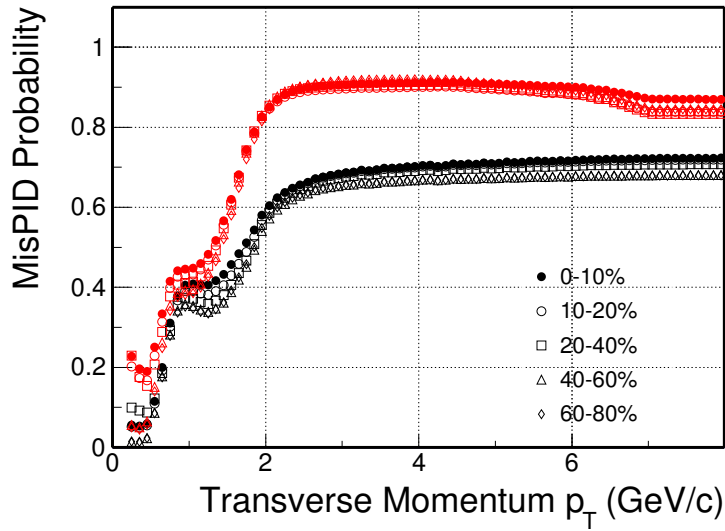


FIG. 32: Particle misidentification probability for kaons (red) and pions (black) from different centrality bins in Au+Au collisions.

⁴⁰¹ Figure 32.

⁴⁰² With the misidentification probability, we can reconstruct the invariant mass distributions from
⁴⁰³ doubly mis-PID. The momentum resolution for pion and kaon tracks are chosen to fit to the D^0
⁴⁰⁴ signal peak. Figure 33 and Figure 34 show these distributions compared to the signal distributions
⁴⁰⁵ in different D^0 p_T regions. The distributions are normalized to the input real D^0 signals.

⁴⁰⁶ Figure 35 shows the final estimated double-counting contribution to the real signal with two
⁴⁰⁷ different calculation methods. The black symbols show the result from directly counting the entries

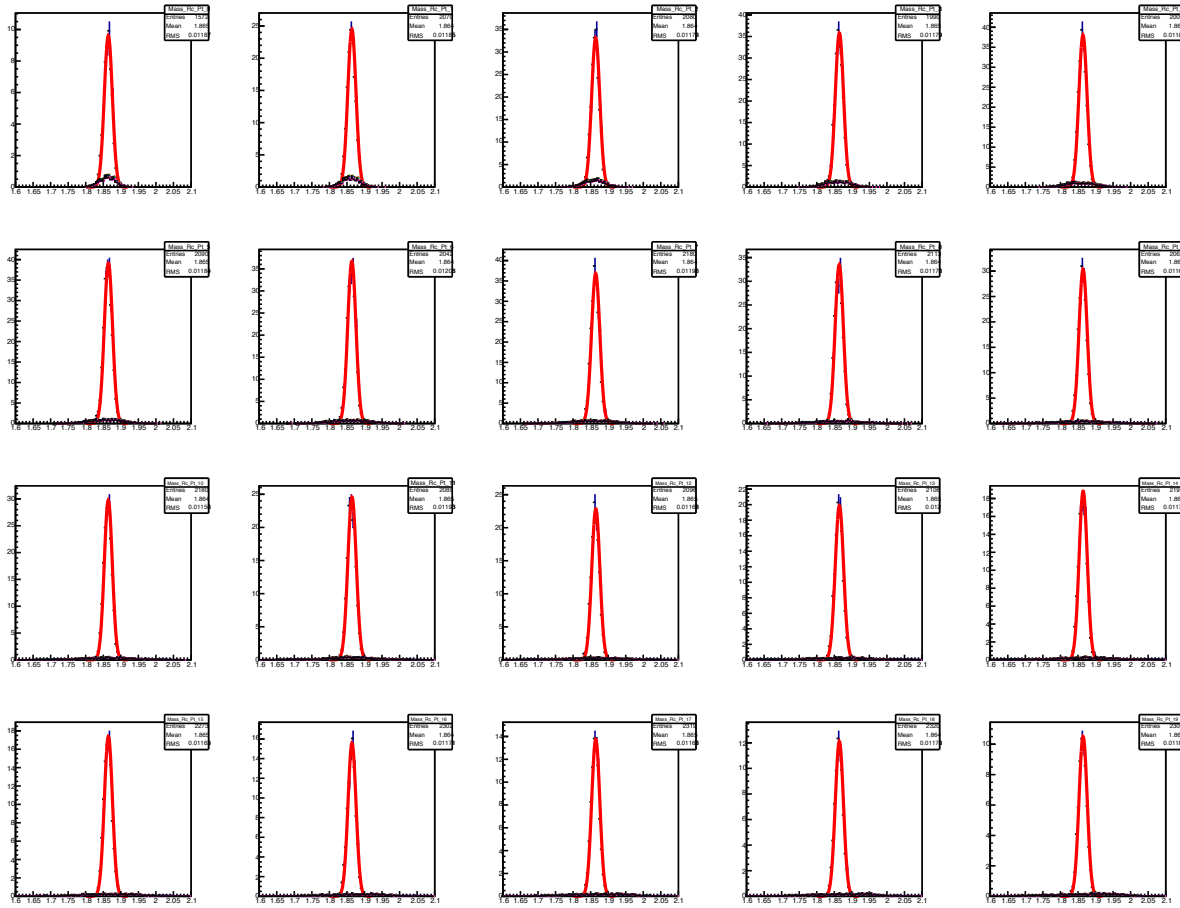


FIG. 33: Reconstructed $K\pi$ invariant mass distributions from clean PID and doubly mis-identification. The relative magnitude is fixed according to the realistic mis-identification probability. From top left to bottom right shows the distributions in p_T bins 0-0.1 GeV/ c , 0.1-0.2 GeV/ c , ..., 1.9-2.0 GeV/ c .

408 within 2.5σ of the D^0 mass window. In real data analysis, we used the side-band distributions to
 409 normalize our fit or estimate our background. The blue data points show the result by subtracting
 410 also the side-band distributions with the same mass window selection as in event plane method v_2
 411 calculation.

412 In the v_2 analysis, the doubly counted candidates are still coming from D^0 , and there is no
 413 reason that the double counting ratio is different at different ϕ relative to the harmonic plane of the
 414 event. Thus the double counting issue should not affect the obtained central value of v_2 . However,
 415 the statistical errors could be slightly off, because the 2 counts are not independent but are treated
 416 as independent when calculating v_2 statistic errors.

417 Assuming there is no combinatorial background. Let's define the D^0 signal yield as S , and
 418 that a portion P_{SS} of signal has a double mis-PID count in the signal region, and a portion

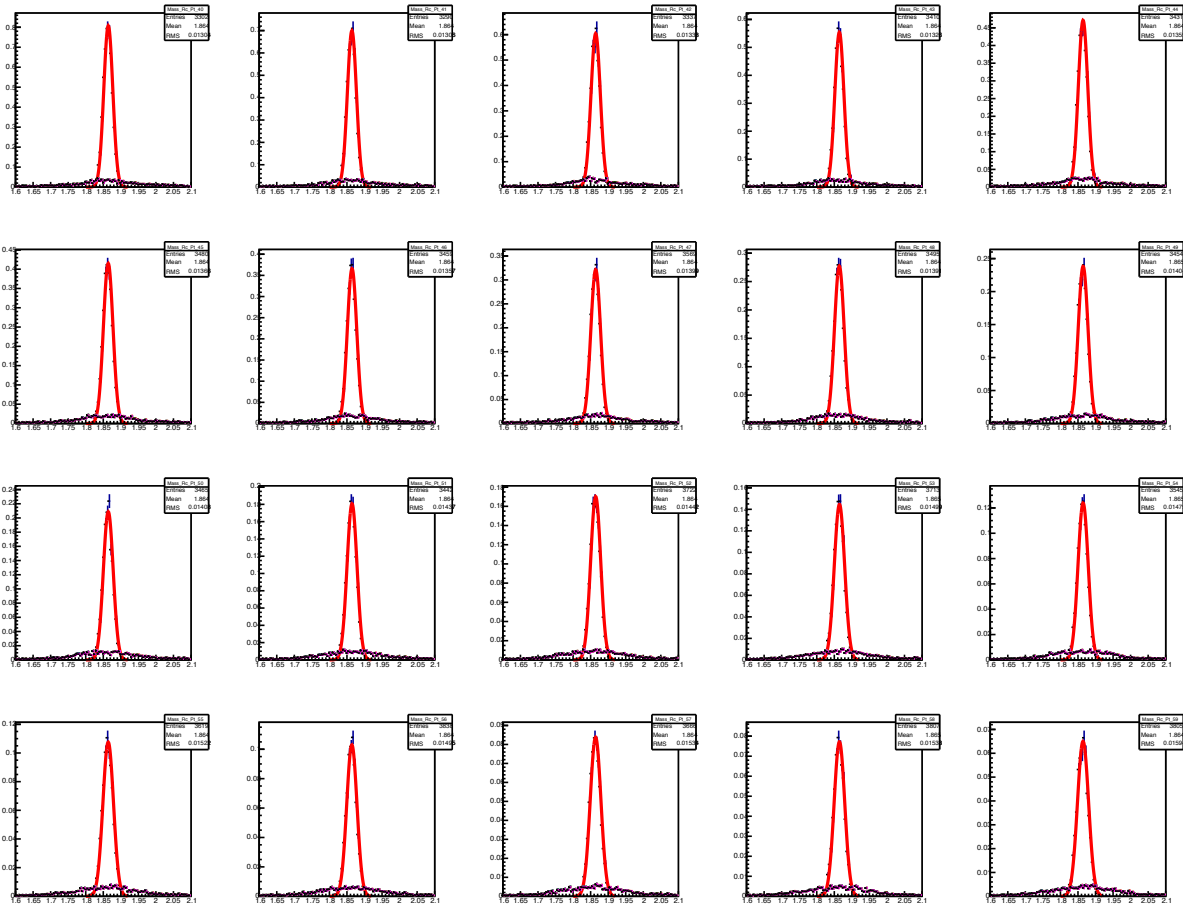


FIG. 34: Reconstructed $K\pi$ invariant mass distributions from clean PID and doubly mis-identification. The relative magnitude is fixed according to the realistic mis-identification probability. From top left to bottom right shows the distributions in p_T bins 4-4.1 GeV/ c , 4.1-4.2 GeV/ c , ..., 5.9-6.0 GeV/ c .

419 P_{SB} of signal has a double mis-PID count in the side band region. Then the measured D^0
 420 yield will be $S(1 + P_{SS} - (\Delta m_S / \Delta m_B)P_{SB}) = S(1 + P_{SS} - P_{SB}/2)$, with the statistic error
 421 $\sqrt{S(1 + P_{SS} - (\Delta m_S / \Delta m_B)P_{SB})} = \sqrt{S(1 + P_{SS} - P_{SB}/2)} \approx \sqrt{S}(1 + P_{SS}/2 - P_{SB}/4)$. Here
 422 $\Delta m_S = 0.09$ GeV/ c^2 and $\Delta m_B = 0.18$ GeV/ c^2 are widths for signal and side band invariant mass
 423 regions respectively. $\Delta m_S / \Delta m_B = 1/2$ is the scale used in v_2 analysis when subtracting side
 424 band background. The approximation is done with $P_{SS} \ll 1$ and $P_{SB} \ll 1$. In reality, there are
 425 3 independent samples of D^0 : a) those counted once $S(1 - P_{SS} - P_{SB}) \pm \sqrt{S(1 - P_{SS} - P_{SB})}$; b)
 426 those counted twice with double mis-PID entry in the signal region $SP_{SS} \pm \sqrt{SP_{SS}}$; c) those with
 427 double mis-PID entry in the side band region $SP_{SB} \pm \sqrt{SP_{SB}}$. When calculating the raw yield,
 428 component b) has a weight of 2, and component c) has a weight of $1 - \Delta m_S / \Delta m_B = 1/2$. The
 429 real total statistic error is $\sqrt{S(1 - P_{SS} - P_{SB} + 2^2 P_{SS} + (1 - \Delta m_S / \Delta m_B)^2 P_{SB})} \approx \sqrt{S}(1 +$

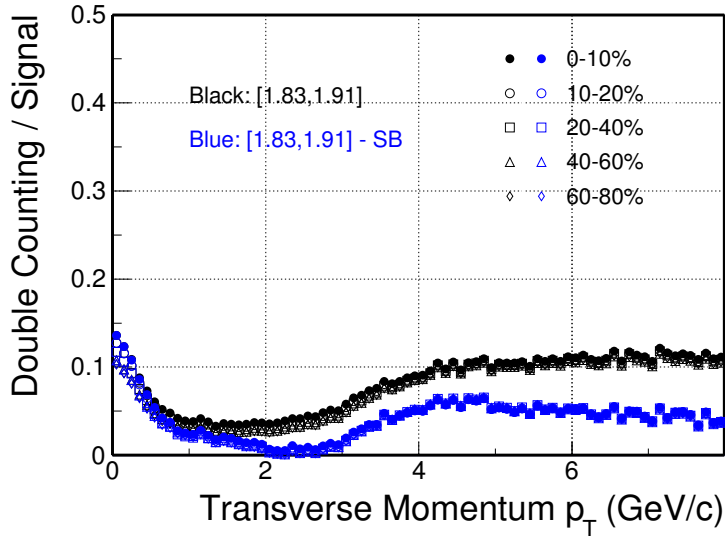


FIG. 35: Estimated doubly-counted D^0 fraction to the real signal with two calculation methods from different centrality bins in Au+Au 200 GeV collisions.

430 $3P_{SS}/2 - P_{SB}/2 + (1 - \Delta m_S/\Delta m_B)^2 P_{SB}/2 = \sqrt{S}(1 + 3P_{SS}/2 - 3P_{SB}/8)$. Comparing with the
 431 statistic error measured assuming all counts are independent $\sqrt{S}(1 + P_{SS}/2 - P_{SB}/4)$, the relative
 432 difference is $P_{SS} - P_{SB}/8$. In Fig. 35 we know at maximum, $P_{SS} = 0.1$ and $P_{SS} - P_{SB}/2 = 0.06$.
 433 So $P_{SS} - P_{SB}/8$ should be less than 9%.

434 The double mis-PID also exists in combinatorial background. It will not cause any trouble for
 435 the measured central value of D^0 raw yield or v_2 , since the combinatorial background can be well
 436 reproduced by like-sign and mixed events. However in terms of influence on statistic error, and it's
 437 even more complicated than the double mis-PID of D^0 signal. The P_{SS} and P_{SB} will be slightly
 438 different from the simulation of D^0 above, since the true invariant mass is not fixed at D^0 mass but
 439 is distributed in the whole signal region. Also there are new components with the true invariant
 440 mass in the side band region, so there are P_{BB} and P_{BS} terms. Additionally, the combinatorial
 441 background can be $\pi^+\pi^-$ or K^+K^- pairs, mis-identified as $K^+\pi^-$ or π^+K^- . So one pair can
 442 also be counted twice, as $K^+\pi^-$ and π^+K^- , each with one particle mis-identified. A detailed
 443 calculation like the double mis-PID for D^0 signal above will be complicated, requiring knowledge
 444 of true PID components of the combinatorial background. However, since the double mis-PID in
 445 combinatorial background also require 2 mis-PID, and the invariant mass spread due to swap of
 446 the mass of the 2 particles is the same (as in Fig. 33and 34), the relative difference of statistic error
 447 between measurement and reality should be also on or below the level of 10%.

448 In general, whether the D^0 measurement statistic error is dominated by the signal or back-

449 ground, the measured v_2 central value will not be influenced by double mis-PID, while the mea-
450 sured statistic error will be relatively 10% smaller at most. We thus neglect this effect on the v_2
451 measurement.

452

v₂ CALCULATION WITH EVENT PLANE METHOD

453 The event plane method basically follows the paper by A. M. Poskanzer and S. A. Voloshin,
 454 Phys. Rev. C 58, 1671 (1998).

455

Event plane reconstruction

456 The event plane is reconstructed by calculating a Q vector for each event, from selected charged
 457 tracks. $Q_x = \Sigma(q_x - \langle q_x \rangle)$, $Q_y = \Sigma(q_y - \langle q_y \rangle)$, where $q_x = p_T \cos(2\phi)$, $q_y = p_T \sin(2\phi)$.
 458 The p_T weight here is to increase the event plane resolution because hadron v_2 increases with p_T .
 459 The subtraction of $\langle q_x \rangle$ and $\langle q_y \rangle$ is called recentering (moving the (q_x, q_y) 2 dimensional dis-
 460 tribution so it is centered at $(0, 0)$), in order to correct for azimuthally non uniform TPC efficiency.
 461 Then event plane can be obtained by $\Psi = \text{atan}(Q_y/Q_x)/2$.

462 The tracks for event plane reconstruction are TPC global tracks with the following cuts

463 • nHitsFit ≥ 16

464 • $0.15 < p_T < 2 \text{ GeV}/c$

465 • $|\eta| < 1$

466 • global DCA $< 3 \text{ cm}$

467 Daughter tracks of D^0 are removed from reconstructing event plane, since they are azimuthally
 468 correlated automatically.

469 Recentering is done run by run for $\eta > 0$, $\eta < 0$ respectively. Fig. 36 and Fig. 37 show event
 470 plane distribution before and after recentering respectively.

471 Tracks with $|\Delta\eta| \lesssim 0.15$ from the D^0 candidate is also rejected from eventplane reconstruction,
 472 to suppress non-flow correlation like jet fragmentation and decay. This is done by dividing the η
 473 range of -1 to 1 into 20 equal bins, and 3 bins around the D^0 candidate is excluded from the event
 474 plane reconstruction. Event plane resolution is obtained using eta sub event method, in which the
 475 $\eta > 0$ sub event plane is correlated with the $\eta < 0$ sub event plane. Then an event plane with
 476 any eta coverage can be calculated (A. M. Poskanzer and S. A. Voloshin, Phys. Rev. C 58, 1671
 477 (1998)), assuming the track η distribution is flat. The result event plane resolution is shown in
 478 Fig. 38. The different color markers represent different number of rejected 0.1 η bins around the

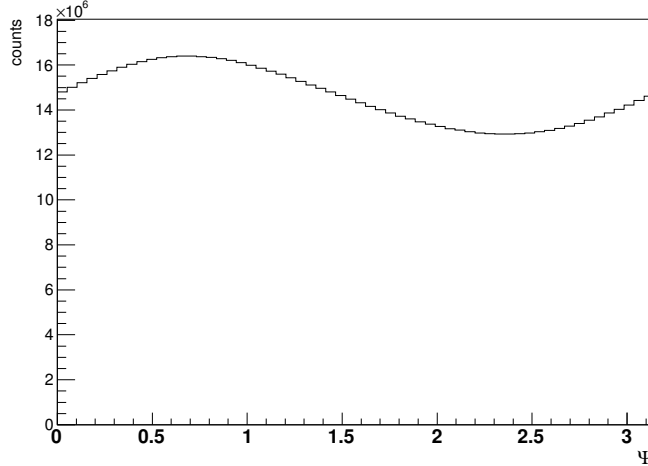


FIG. 36: Event plane distribution before recentering

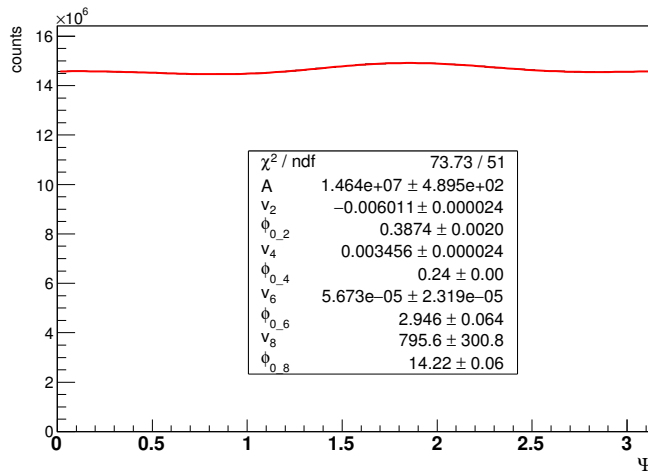


FIG. 37: Event plane distribution after recentering

479 D^0 candidate. The light green one with 3 0.1 η bins around the D^0 candidate rejected from event
 480 plane reconstruction is used for the final result.

481 To check the event plane and resolution, hadron v_2 is calculated and compared with published
 482 results in Phys. Rev. Lett. 93, 252301 (2004), shown in Fig. 39 as black profile and red markers
 483 respectively. No η gap is applied for this comparison.

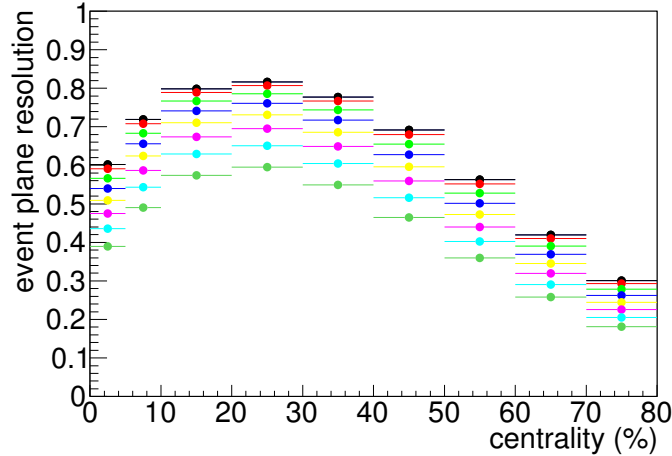


FIG. 38: Event plane resolution vs. centrality. The different color markers represent different number of rejected 0.1η bins around the D^0 candidate: black: 0; red: 1; light green: 3; blue: 5... dark green: 13

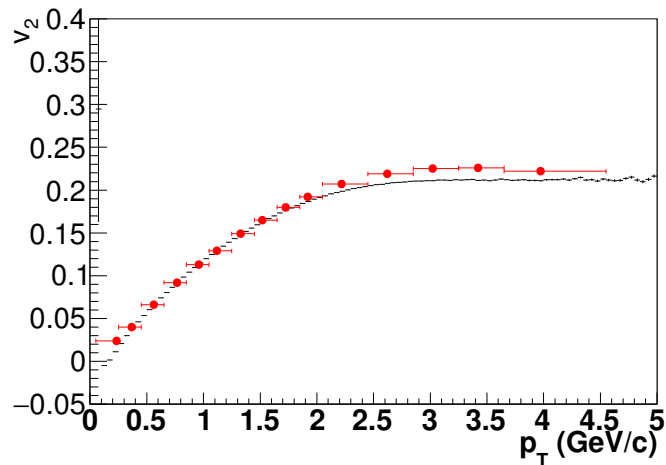


FIG. 39: hadron v_2 vs. p_T for 20-60% central events. The black histogram is calculated in this analysis, while the red markers are published results (Phys. Rev. Lett. 93, 252301 (2004))

484

Obtain D^0 yield in different $\Delta\phi$ bins and fit v_2

485 After the event plane is reconstructed, v_2 can be calculated. Take p_T 3.-4. GeV/c, centrality
 486 0-80 % for example. The $K\pi$ invariant mass distribution for the unlike sign foreground, like
 487 sign background and the scaled mixed event background are shown in Fig. 40. The mixed event
 488 background is scaled to the like sign in the plotted invariant mass range of $1.6-2.1 \text{ GeV}/c^2$. First
 489 the scaled mixed event background is subtracted from the unlike sign foreground. The result is
 490 shown in Fig. 41. Then the invariant mass distribution is fit with a 1st order polynomial + Gaussian
 491 function. The polynomial is taken as background and the Gaussian is taken as the signal.

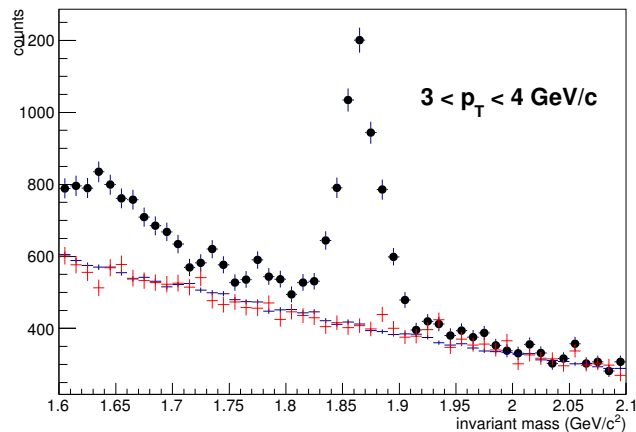


FIG. 40: $K\pi$ invariant mass distribution for the unlike sign foreground (black markers), like sign background (red) and the scaled mixed event background (blue), for p_T 3.-4. GeV/c, 0-80% centrality

492

Then the counts are divided into 10 $\phi - \Psi$ bins, and each 2 bins symmetrical to $\pi/2$ are combined
 493 into one. Fig. 42 shows the foreground and background invariant mass distributions for different
 494 combined $\Delta\phi$ bins, and Fig. 43 shows invariant mass distributions of foreground with mixed event
 495 background subtracted for different combined $\Delta\phi$ bins. To cope with variating VPD minibias
 496 trigger efficiency, D^0 reconstruction efficiency and event plane resolution in a large centrality bin,
 497 the histograms are weighted by inverse efficiency and event plane resolution in each centrality bin
 498 (arXiv:1212.3650). The D^0 reconstruction efficiency, shown in Fig. 44, is calculated by the D^0
 499 raw yield in this analysis divided by the expected yield from a fit to the published data (Phys. Rev.
 500 Lett. 113 (2014) 142301) and number of events used in this analysis.

501

In each $\phi - \Psi$ bin, the weighted D^0 yield can be obtained by 2 different methods:

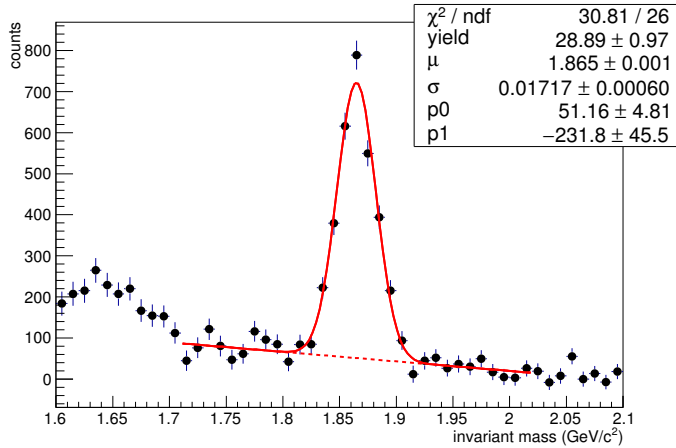


FIG. 41: $K\pi$ invariant mass distribution with mixed event background subtracted for p_T 3.-4. GeV/c, 0-80% centrality

502 the fit method: fix the μ and σ of the Gaussian by the fitting in Fig. 41 and fit D^0 yield
 503 and background with the foreground subtract mixed event background invariant mass distributions
 504 in Fig. 43; The fit range is 1.71-2.02 for central value v_2 calculation. And 1.73-2.00 is used for
 505 systematic error.

506 the side band method: count signal between invariant mass between $1.82 \text{ GeV}/c^2$ and 1.91
 507 GeV/c^2 , then subtract the scaled counts in two side band invariant mass ranges. The side bands
 508 are a) 1.71-1.80 and 1.93-2.02; b) 1.73-1.78 and 1.95-2.00. a) is used for default value and b) is
 509 used to estimate the systematic error.

510 The fit method is used for p_T bins 1-2, 2-3, 3-4, and 4-5 GeV/c , while the side band method is
 511 used for the last 5-10 GeV/c bin with not enough statistics to have a controllable fit. When both
 512 applicable, the fit method has slightly better statistic error because it consider the shape of the D^0
 513 signal rather than treat all counts in the signal range equally when calculating v_2 .

514 Then the D^0 yield vs. $\phi - \Psi$ is fit with $N(1 + 2v_2^\sim \cos(2(\phi - \Psi)))$ to get the observed v_2^\sim , as
 515 shown in Fig. 45.

516 At last the v_2^\sim is divided by average inverse event plane resolution, weighted by the D^0 yield,
 517 to get physics v_2 .

518 When the $\phi - \Psi$ bin width Δ is finite, the integral yield of a distribution with the form of
 519 $A(1 + 2v_2 \cos(2(\phi - \Psi)))$ in a $\phi - \Psi$ bin is a little different from $\Delta A(1 + 2v_2 \cos(2(\phi - \Psi)))$,
 520 where $\phi - \Psi$ is at the bin center. The deducing is below:

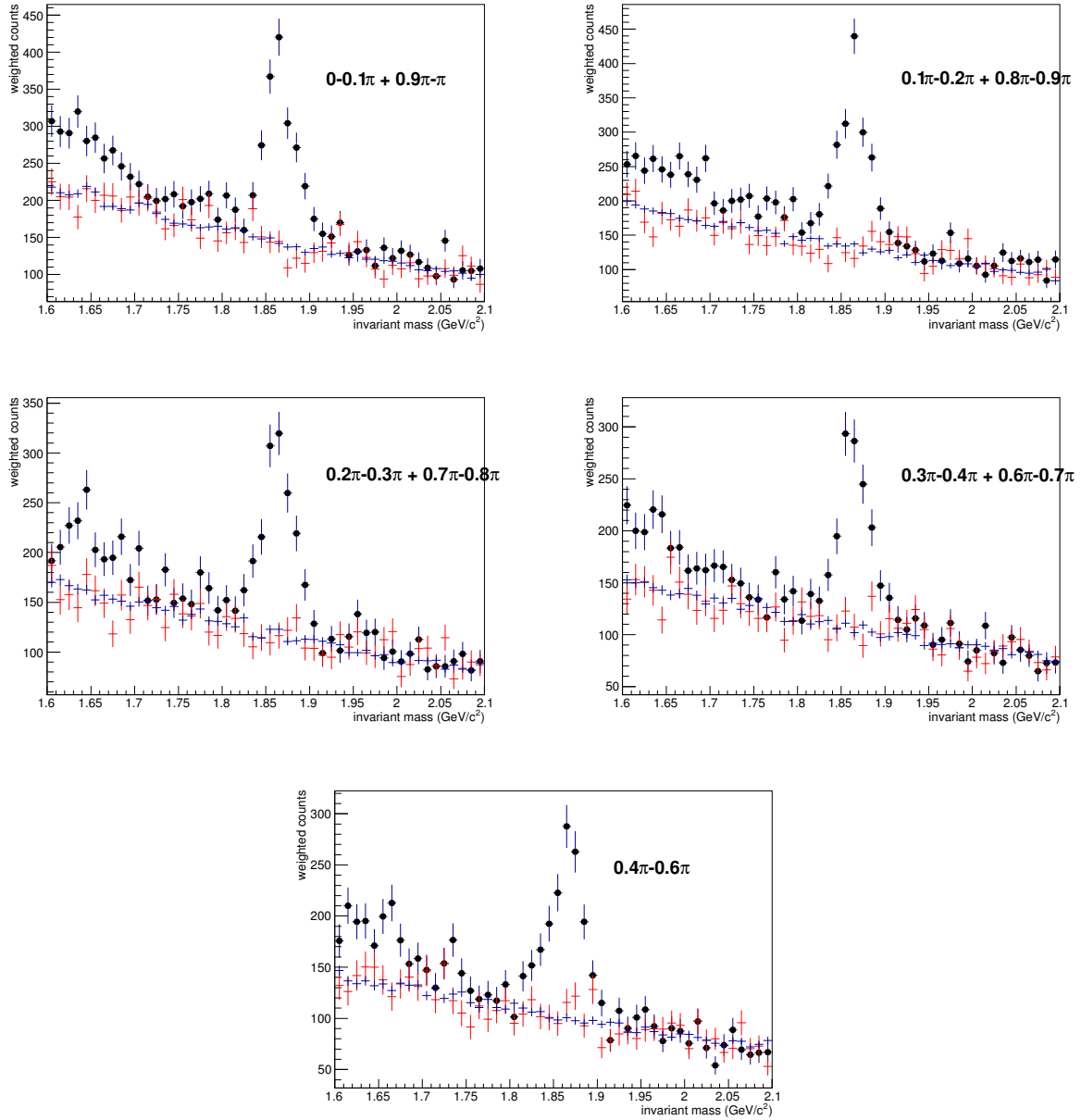


FIG. 42: $K\pi$ invariant mass with the D^0 signal in different combined $\phi - \Psi$ bins for p_T 3.-4. GeV/c , 0-80% centrality

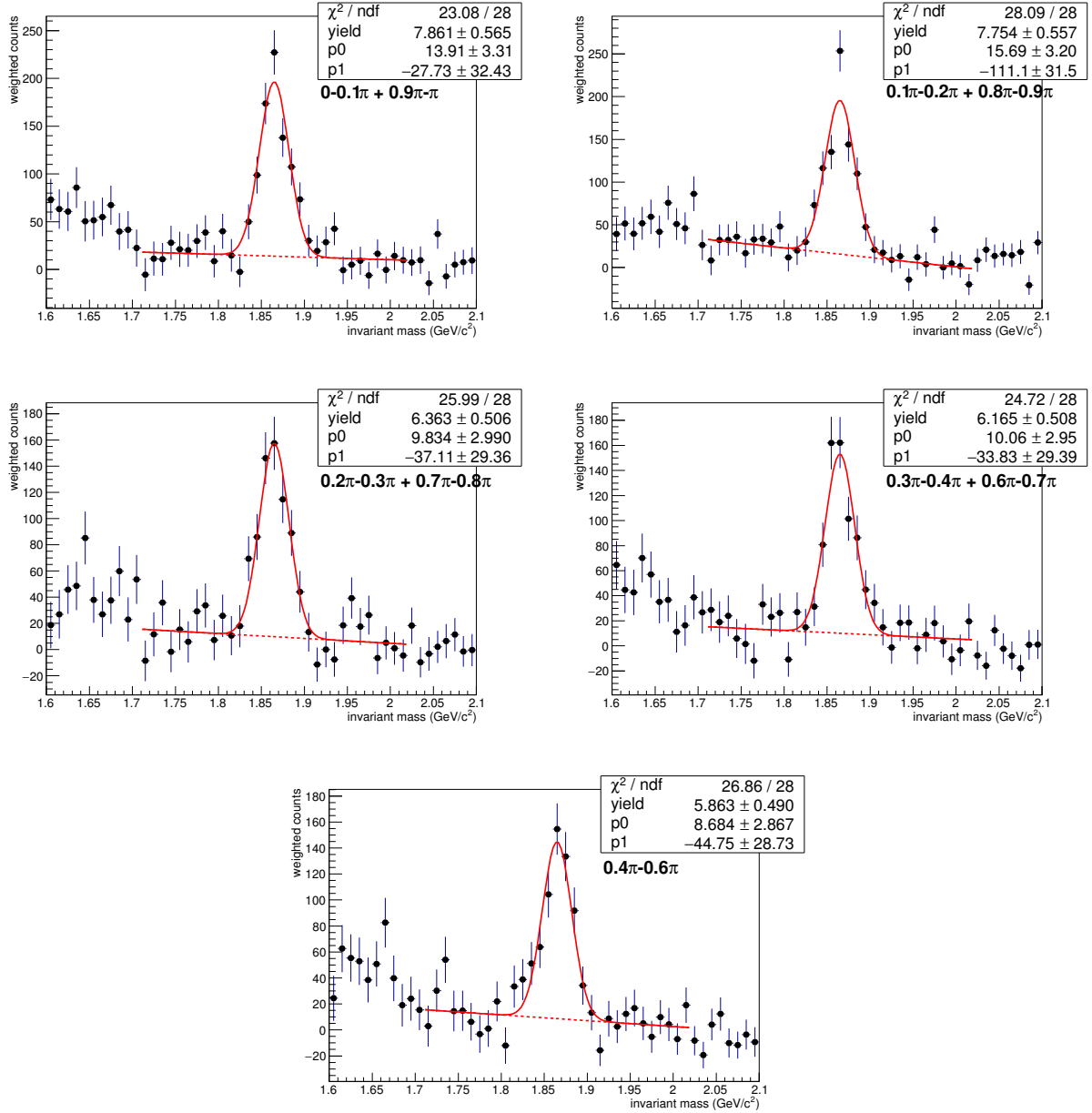
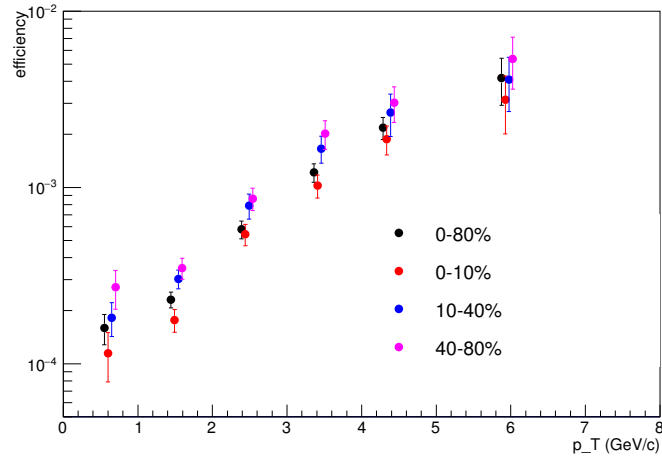
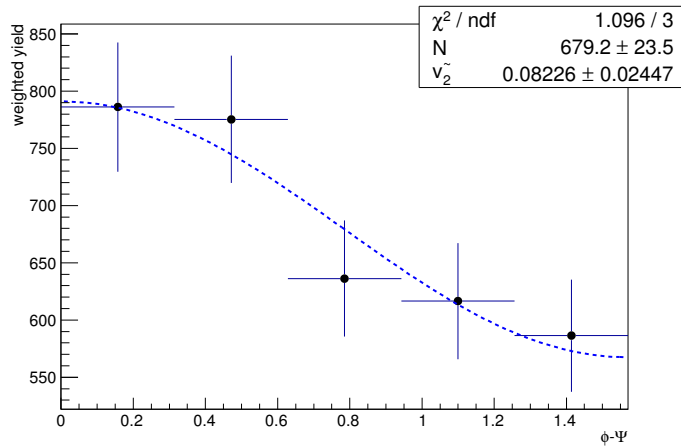


FIG. 43: $K\pi$ pairs invariant mass unlike sign - scaled mixed event background with Gaussian + pol1 fit for different combined $\phi - \Psi$ bins, for p_T 3.-4. GeV/c , 0-80% centrality

FIG. 44: D^0 reconstruction efficiency vs. p_T for different centralitiesFIG. 45: yield in different $\phi - \Psi$ bins from fit signal and background, for p_T 3.-4. GeV/c, 0-80% centrality

The integral yield in the $\phi - \Psi$ bin from $i\Delta$ to $(i+1)\Delta$ is

$$\begin{aligned}
 & \int_{i\Delta}^{(i+1)\Delta} A(1 + 2v_2 \cos(2(\phi - \Psi))) d(\phi - \Psi) \\
 &= A(\Delta + v_2 \int_{i\Delta}^{(i+1)\Delta} \cos(2(\phi - \Psi)) d(2(\phi - \Psi))) \\
 &= A(\Delta + v_2 \sin(2(\phi - \Psi))|_{i\Delta}^{(i+1)\Delta}) \quad (3) \\
 &= A(\Delta + v_2 (\sin(2(i+1)\Delta) - \sin(2i\Delta))) \\
 &= A(\Delta + v_2 2 \sin \Delta \cos((2i+1)\Delta)) \\
 &= A\Delta(1 + 2v_2 (\sin \Delta / \Delta) \cos(2(i+1/2)\Delta))
 \end{aligned}$$

521 $(i+1/2)\Delta$ is the bin center. Comparing with the original distribution $A(1 + 2v_2 \cos(2(\phi - \Psi)))$,
 522 we can see the v_2 obtained from fit to integrals in $\phi - \Psi$ bins is actually $v_2(\sin \Delta / \Delta)$. As a result,
 523 a further scale of $\Delta / \sin \Delta = 1.01664$ is done to correct for this effect, where $\Delta = 0.1\pi$ for this
 524 analysis.

525 Detailed plots of calculating v_2 with event plane method for all p_T bins are in appendix.

526

Systematic errors for the event plane method

527 The most important systematics on the measurement considered here is from the assumptions in
 528 background treatment. The inverse D^0 reconstruction efficiency weight also introduce systematics
 529 due to the uncertainty from the published D^0 p_T spectra and finite centrality bin width (0-10-40-
 530 80% from the published p_T spectra). These 2 systematics will be estimated in details below and
 531 added up quadratically. The non-flow and B feeddown contribution is common for the event plane
 532 and the correlation method, which will be described later in a separate section. The following
 533 small influences on the v_2 measurement are neglected:

534 a) Since v_2 changes with p_T , different D^0 reconstruction efficiency for different p_T can in-
 535 troduce bias on the measured v_2 . But the effect is small since the p_T bins for this analysis are
 536 small.

537 b) When v_2 changes with rapidity y , different D^0 reconstruction acceptance and efficiency in
 538 the quoted $|y| < 1$ range can bias the measured v_2 . But we know v_2 changes very little for $|y| < 1$
 539 for other particles. So this bias should also be small for D^0 .

540 c) There are some residue second order term (~ 0.006) in the event plane distribution after

541 recentering, as shown in Fig. 37. The $D^0 \phi$ distribution (Fig. 49) shows counts per bin within
 542 250 ± 50 , so the second Fourier term is less than $50/250/2 \sim 0.1$. The v_2 correlation between D^0
 543 and event plane due to non-flat event plane is then on or below the order $0.006 * 0.1 = 0.0006$,
 544 which can be neglected with the current measured v_2 error.

545 Both the fit and the side band method described above assume that the residual background
 546 yield after mixed event subtraction has a linear relationship with the invariant mass within the
 547 range for fit or side bands. This is not completely true. The double mis-PID will form a wider
 548 bump below the D^0 peak. And the D meson to other decay channels will form another bump
 549 below invariant mass $1.7 \text{ GeV}/c^2$. These have second order effects on the measured v_2 . We
 550 estimate the systematics from the different v_2 obtained with fit and side bands methods mentioned
 551 above, different invariant mass ranges for fit and for side bands, and different topology cut sets. As
 552 mentioned above, The fit range a (1.71-2.02) is used for central value v_2 calculation, and b (1.73-
 553 2.00) is used for systematic error; the side bands a (1.71-1.80 and 1.93-2.02) are used for central
 554 value and side bands b (1.73-1.78 and 1.95-2.00) are used for systematic error. The topology
 555 cut sets are varied to have 50% and 150% D^0 yield relative to the best cuts. They are also from
 556 the TMVA tuning, as the best significance (rejecting most background) cuts with that certain D^0
 557 signal efficiency, listed in Table IV and V. Fig. 46 shows the v_2 results with fit and side band
 558 methods with different fit / side band ranges and different topology cuts. Assuming the v_2 from all
 559 these combinations form a uniform distribution, the mean square root error can be obtained as the
 560 maximum differences among all combinations divided by $\sqrt{12}$, this is quoted as the systematic
 561 error of the measured v_2 . Detailed plots to obtain v_2 with all this different methods, invariant mass
 562 ranges and topology cuts are also in the appendix.

563 The inverse D^0 reconstruction efficiency weight has uncertainty from the uncertainty of the
 564 published $D^0 p_T$ spectra. Also the finite centrality bin width may not be fine enough. As a con-
 565 served estimation, the systematic uncertainty on v_2 is taken as the difference between the measured
 566 v_2 with and without inverse D^0 reconstruction efficiency weight. Fig. 47 shows the measured v_2
 567 with and without inverse D^0 reconstruction efficiency weight.

568 Table X summarizes $D^0 p_T$, v_2 , v_2 statistic error, 2 v_2 systematic error components and the total
 569 v_2 systematic error.

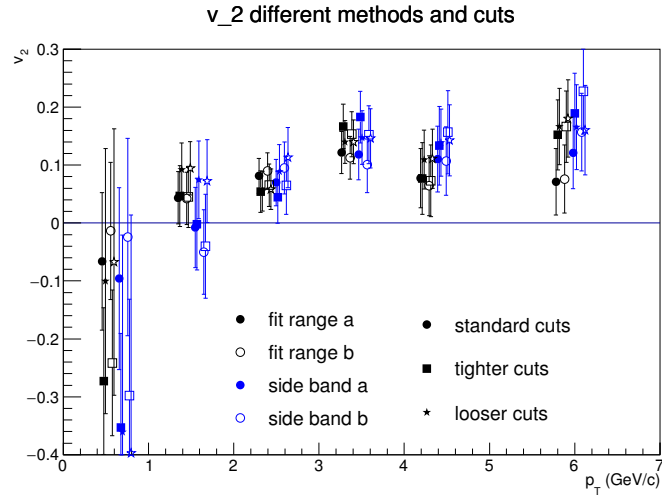


FIG. 46: v_2 vs. p_T with fit and side band methods with different fit / side band ranges

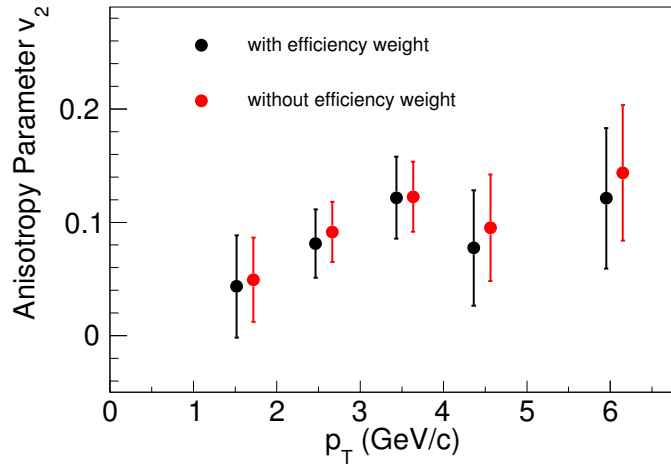


FIG. 47: v_2 vs. p_T with and without inverse D^0 reconstruction efficiency weight

570

Results from the event plane method

571 The result of $D^0 v_2$ from the event plane method is shown in Fig. 48. The first p_T bin 0-1 GeV/c
 572 is not included into final results due to large statistic error.

TABLE VII: $D^0 p_T$, v_2 , v_2 statistic error, v_2 systematic error from different methods, invariant mass ranges, cuts, v_2 systematic error from inverse D^0 reconstruction efficiency weight, and total v_2 systematic error

$D^0 p_T$ (GeV/c)	0.63	1.52	2.47	3.43	4.36	5.95
v_2	-0.066	0.043	0.081	0.122	0.077	0.121
v_2 statistic error	0.119	0.045	0.030	0.036	0.051	0.062
systematics (methods, invariant mass ranges, cuts)	0.111	0.042	0.020	0.024	0.027	0.045
systematics (inverse efficiency weight)	0.005	0.006	0.010	0.001	0.018	0.022
total v_2 systematic error	0.111	0.042	0.022	0.024	0.032	0.050

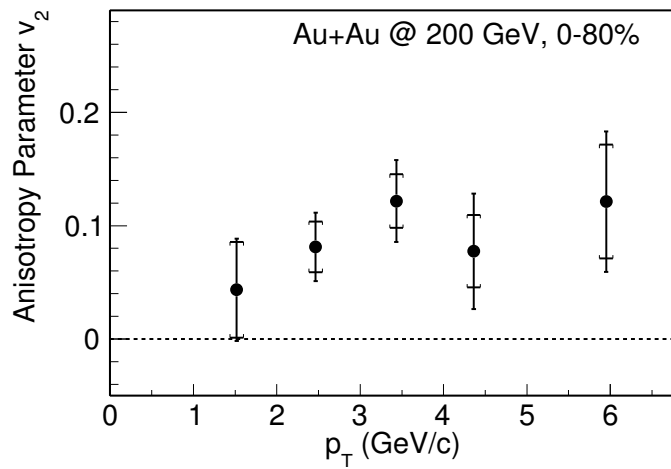


FIG. 48: v_2 vs. p_T from event plane method

573

CORRELATION v_2

574 In this note, the two-particle correlation method(<http://arxiv.org/pdf/1010.0233.pdf>) is used to
 575 calculate $D^0 v_2$. The methodology is based on Equation. 4 For each D^0 candidate, we sum up all
 576 the hadron correlated with this D^0 candidate in same event $\sum_i \cos(2\phi_{D^0} - 2\phi_{hadron_i})$. Then sum
 577 over all D^0 candidate in all events. Finally divide by the total number of $D^0 - hadron$ pairs in all
 578 events to get $\langle \cos(2\phi_D - 2\phi_h) \rangle$.

$$\begin{aligned} v_2^{D,h} &= \langle \cos(2\phi_D - 2\phi_h) \rangle \\ &= \langle \cos(2\phi_D - 2\psi_{EP}) \rangle \cdot \langle \cos(2\phi_h - 2\psi_{EP}) \rangle \\ &= v_2^D \cdot v_2^h \end{aligned} \quad (4)$$

579 Equation 4 is used to calculate the product of v_2^D and v_2^{hadron} . To use the same method but
 580 the correlation of charged hadrons, the v_2^{hadron} can be estimated. For different $D^0 p_T$ range, the
 581 unlike-sign $K\pi$ pairs in mass window are used as foreground; the sidebands (both like-sign and
 582 unlike-sign) and like-sign in D^0 mass window pairs are used as background.

$$cumulant = \frac{\cos(2\phi_D) \cdot \sum_{hadrons} \cos(2\phi) + \sin(2\phi_D) \cdot \sum_{hadrons} \sin(2\phi)}{hadron\#} \quad (5)$$

583 In the analysis, we are using cumulant method to get the correlation. The formula used is
 584 Equation. 5. The cumulant value is calculated D^0 -by- D^0 (not event-by-event). For each D^0 ,
 585 calculate the cumulant requiring an η gap 0.15 between hadron and D^0 . The final correlation $v_2^{D,h}$
 586 is the average value of cumulant with weight as number of correlated hadron of each D^0 .

$$\begin{aligned} V_2^{D,h} &= \langle \cos(2\phi_D - 2\phi_h) \rangle \\ &= \frac{\sum_{D^0} w_i \cdot cumulant}{\sum_{D^0} w_i} \end{aligned} \quad (6)$$

587 The $\langle \rangle$ denote average over all D^0 s in all events. And $w_i = (N_{correlatedHadron}) \cdot reweight / \epsilon_{D^0}$.
 588 Where $N_{correlatedHadron}$ is the number of hadrons correlated to the D^0 ; $reweight$ is the reweight
 589 factor of vpd trigger; ϵ_{D^0} is the D^0 reconstruction efficiency.

590

Acceptance correction

591 The azimuthal angle ϕ distribution should be flat for a perfect detector. However, in the experiments,
 592 the detectors may have a finite or non-uniform acceptance which may lead to anisotropy
 593 distributions in the lab frame. In Figure. 49, the non-flat phi distribution is because of the detector.
 594 It introduces bias to the v_2 calculation. In the two-particle correlation analysis, the re-centering
 595 method is used to correct the non-uniform effect. Equation. 7 is used to fix the non-uniformed
 596 acceptance by subtracting the averaged two terms in the calculation of two-particle correlation
 597 equation 4. In this formula, the $\langle \cos(2\phi_D - 2\phi_h) \rangle$ term is calculated using D^0 cumulant with
 598 number of correlated hadron as weight. The correction, for example the $\langle \sin(2\phi_h) \rangle$ term, is
 599 the averaged value of hadrons used in the correlation.

$$v_2^{D \cdot h} = \langle \cos(2\phi_D - 2\phi_h) \rangle - \langle \cos(2\phi_D) \rangle \cdot \langle \cos(2\phi_h) \rangle - \langle \sin(2\phi_D) \rangle \cdot \langle \sin(2\phi_h) \rangle \quad (7)$$

600 Figure. 50 shows the $D^0 v_2$ before and after the fixing.

601

 $\Delta\eta$ between D^0 (hadron) to hadron

602 In order to reduce the anisotropy from now-flow effect, $\Delta\eta$ between the correlated two particles
 603 are added. In this analysis, the $\Delta\eta = 0.15$ is used on D^0 -hadron pairs. Since in the calculation of
 604 V_2 , the number of hadrons correlated to D^0 is treated as the weight of that D^0 . We choose same
 605 number of hadrons for each D^0 . An assumption is that the number of hadrons is independent with
 606 eta. We fix the eta range of the correlated hadrons to make sure there is no bias for different D^0 s.
 607 For maximum statistics, the widest eta range should be $2 - 2 * \Delta\eta$ (the eta range of TPC is -1
 608 to 1). For the hadron v_2 , the cumulants are calculated by groups of hadrons from $\eta < -0.075$
 609 and $\eta > 0.075$ ranges. So the η gap between the two groups is 0.15, which is consistent with
 610 D^0 -hadron pairs.

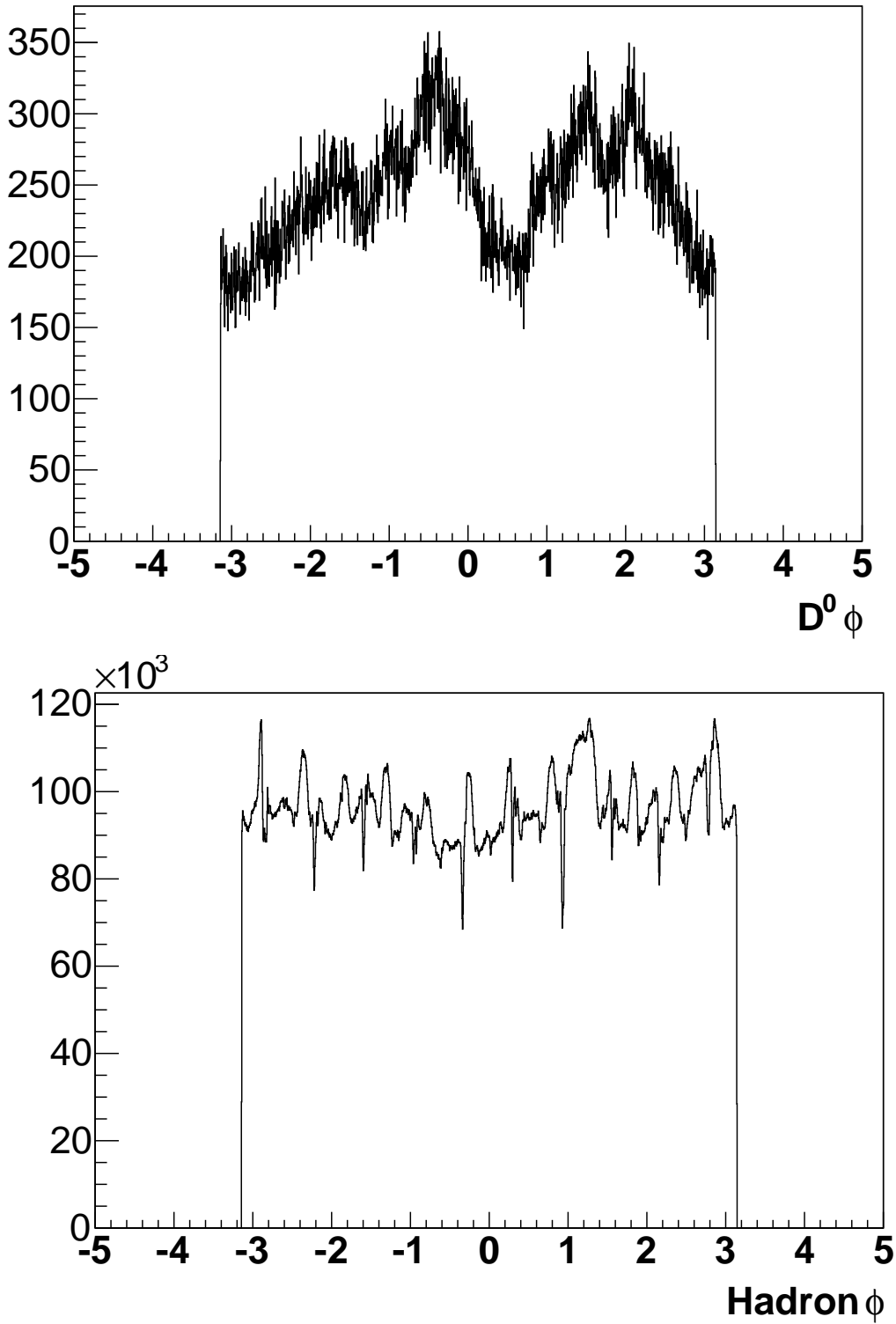


FIG. 49: The ϕ distribution of D^0 candidates and hadrons. The top panel is ϕ distribution of D^0 candidates. The bottom panel is ϕ distribution of primary tracks in $|\eta| < 1$.

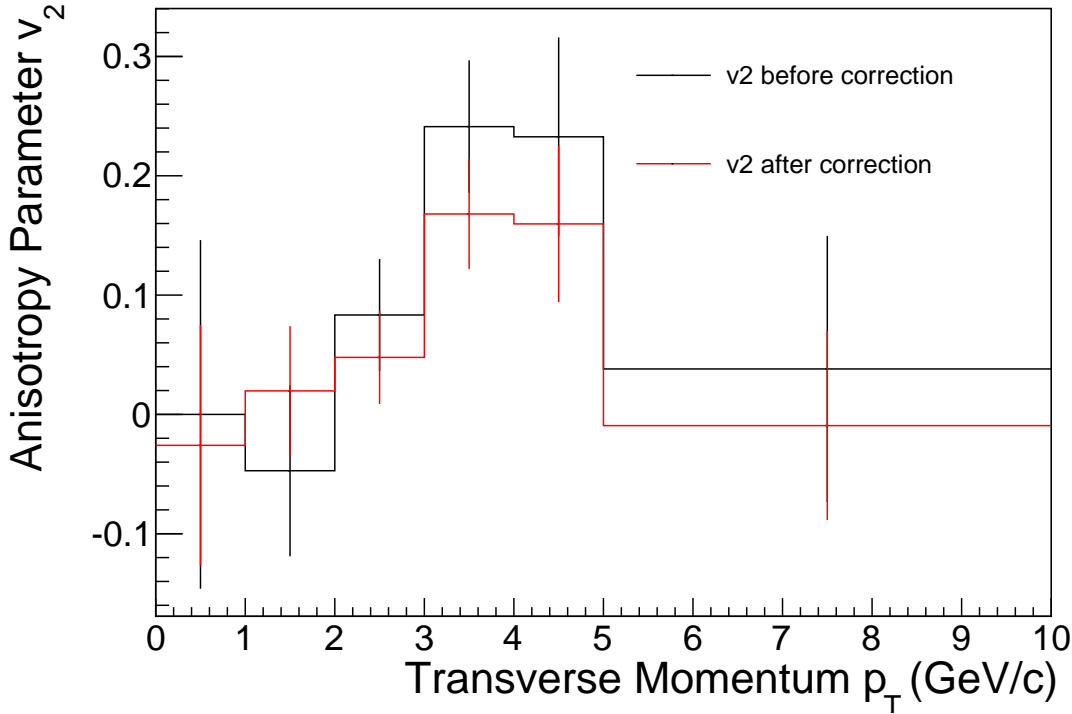


FIG. 50: $D^0 v_2$ before and after the fixing of the non-uniformed acceptance of detector

611

Reference hadron v_2

612 The reference hadron v_2 is calculated in Equation. 8. For each event, we split all hadrons to
 613 group#1 from $\eta < -0.075$ and hadron#2 comes from group $\eta > 0.075$. And calculate the
 614 cumulant for each group. Then calculate the average value of the product of two cumulant value
 615 in each event with the product of number in two samples as weight. And use formula. 9 to calculate
 616 hadron v_2 .

617 $\Delta\eta \geq 0.15$ between two groups is required in hadron v_2 calculation for two reasons: the first
 618 reason is to suppress the non-flow effect between hadrons; and the second reason is about track
 619 merging. We will discuss more about track merging later.

$$(v_2^h)^2 = \langle \cos(2\phi_{h1} - 2\phi_{h2}) \rangle \quad (8)$$

centrality	hadron $v_2 (\Delta\eta > 0)$ %	error of hadron v_2 %	hadron $v_2 (\Delta\eta > 0.15)$ %	error of hadron v_2 %
0 – 5%	2.5513	0.0008	2.5525	0.0008
5 – 10%	3.6103	0.0007	3.6077	0.0008
10 – 20%	5.0629	0.0005	5.0554	0.0006
20 – 30%	6.5791	0.0006	6.5654	0.0007
30 – 40%	7.4333	0.0008	7.4101	0.0008
40 – 50%	7.6808	0.0010	7.6407	0.0011
50 – 60%	7.4187	0.0015	7.3495	0.0016
60 – 70%	6.8690	0.0029	6.7478	0.0032
70 – 80%	6.4067	0.0072	6.2187	0.0080

TABLE VIII: Reference hadron v_2 in different centrality bins.

$$v_2^{hadron} = \frac{\sum_{events} \left(\sum_{group\#1} \cos(2\phi) \cdot \sum_{group\#2} \cos(2\phi) + \sum_{group\#1} \sin(2\phi) \cdot \sum_{group\#2} \sin(2\phi) \right)}{\sum_{event} (hadron\#(group1) \cdot hadron\#(group2))} \quad (9)$$

620 The hadron v_2 is a good test of the two-particle correlation method, a comparison with Run 10
 621 result (<https://drupal.star.bnl.gov/STAR/starnotes/private/psn0577>) is
 622 shown in figure. 51. The method used in Run 10 analysis is to loop all particles twice. So it
 623 introduced non-flow effect makes the v_2 larger than the method in this note. But in very central
 624 events, the Run 10 v_2 is smaller, this might be due to track merging. When 2 very near tracks are
 625 reconstructed as one, the very strong correlation between them are not counted, this will decrease
 626 the measured v_2 . This decrease will not happen when η gap is applied.

627 Background subtraction

628 Equation. 4 is used to get the v_2 of D^0 candidates. Then equation. 10 is used to subtract the
 629 background. The N_{cand} is the yield of unlike-sign $K\pi$ pair in 3σ within the mass window. Where
 630 σ is the square root of variance from the fitting Gaussian function. And the N_{sig} is the fitting
 631 result. Then $N_{bkg} = N_{cand} - N_{sig}$. The v_2^{cand} also comes from the correlation of unlike-sign pair
 632 in 3σ mass window to the hadrons. In two-particle correlation method, the η gap between D^0 and
 633 hadrons can be required. In this way the effect of non-flow can be suppressed effectively. Figure
 634 52 is the correlation ($\cos(2\phi_D - 2\phi_{hadron})$) as a function of p_T .

The v_2^{bkg} comes from 1)like-sign pair in $\pm 3\sigma$; 2) like-sign pair in $(\pm 4\sigma, \pm 9\sigma)$ side-band and 3)

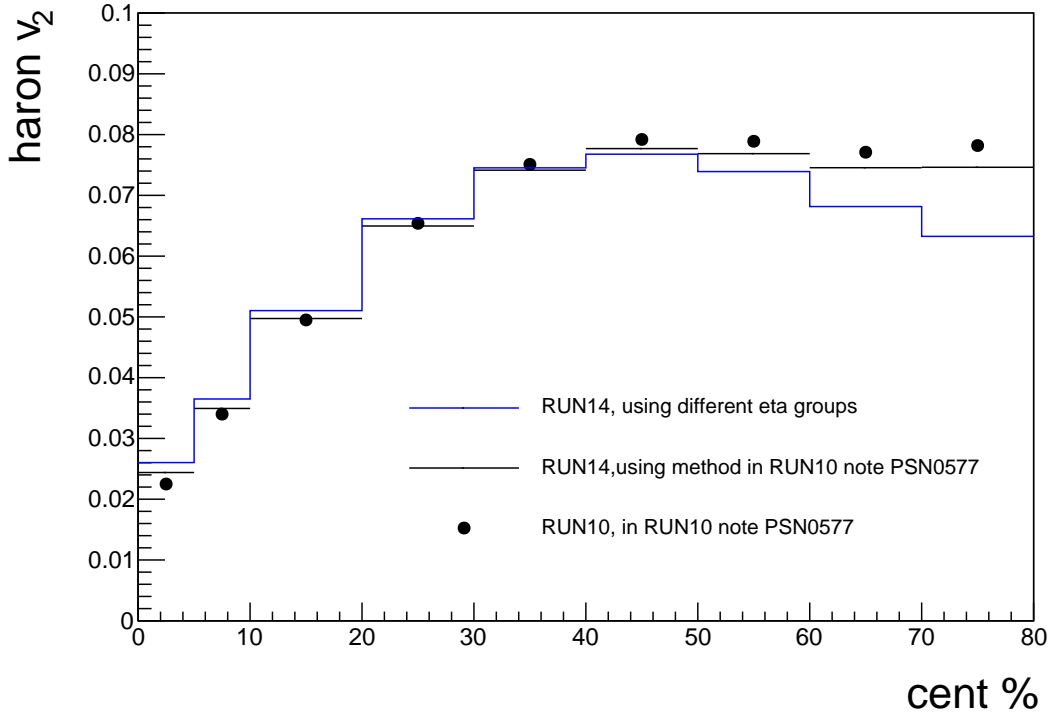


FIG. 51: Comparison between Run 14 and Run 10 hadron v_2 measurements. The black dots comes from Run 10 notes. The black line is using exact same method in Run 10 note but with Run 14 data. The blue line is using two-group method with Run 14 data.

unlike-sign pair in $(\pm 4\sigma, \pm 9\sigma)$ side-band. These three samples are almost all statistic we can use as background. But both the unlike-sign and side-band background are biased. The like-sign pairs cannot describe background in unlike-sign pairs due to different combinatorial background components; while the double-counting ratio in D^0 mass window and side-band region are different.

$$\begin{aligned}
 N_{cand} &= N_{signal} + N_{bkg} \\
 \frac{N_{cand}}{d\phi} &= \frac{N_{signal}}{d\phi} + \frac{N_{bkg}}{d\phi} \\
 N_{cand}[1 + 2v_2^{cand}\cos(2\phi)] &= N_{signal}[1 + 2v_2^{signal}\cos(2\phi)] + N_{bkg}[1 + 2v_2^{bkg}\cos(2\phi)] \\
 v_2^{sig} &= \frac{N_{cand} \cdot v_2^{cand} - N_{bkg} \cdot v_2^{bkg}}{N_{signal}}
 \end{aligned} \tag{10}$$

635 Figure. 53 is correlation of different background source. The black dot is the weighted average
 636 value of the three background samples. It is the default value used in v_2 calculation. The maximum
 637 difference between the three sample v_2 to the default background v_2 is considered as systematic

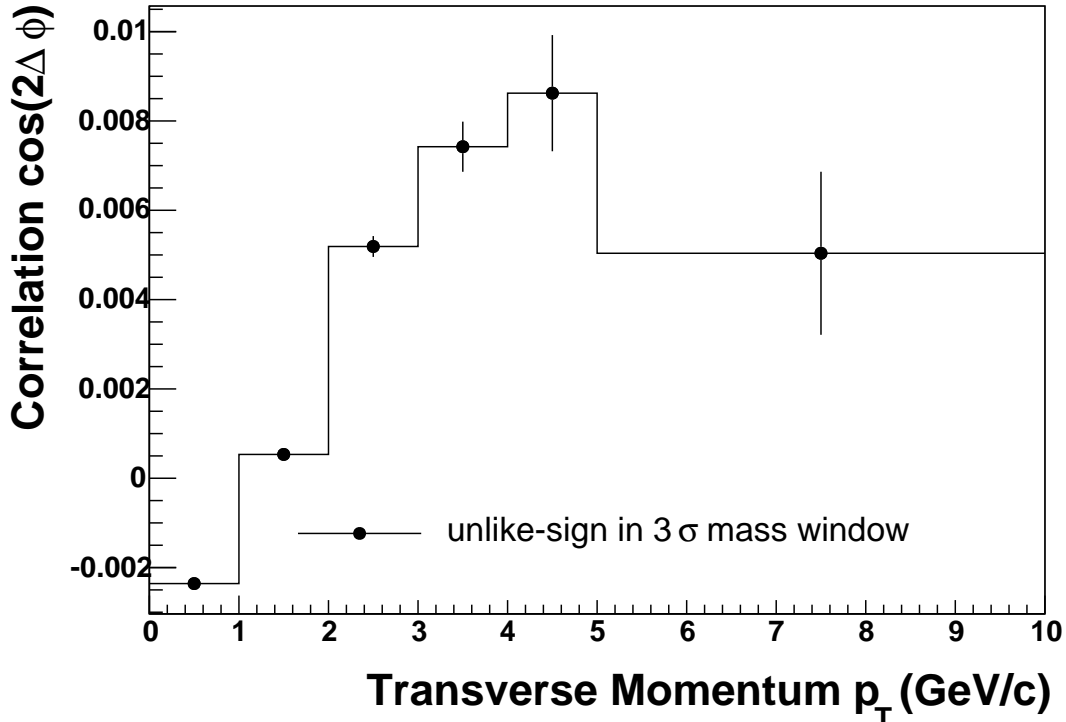


FIG. 52: Candidate v_2 vs. p_T . The candidate sample is unlike-sign $K\pi$ pairs within 3σ , where σ is the square root of variance from fitted Gaussian.

uncertainty. In the higher p_T bin (4-5GeV/c and 5-10GeV/c), the systematic uncertainty is big.
 This is because of the statistical fluctuation. Figure. 55 shows v_2 as function of invariance mass of both unlike-sign pair and like-sign pair.

641

Statistic error

We have v_2^{cand} , v_2^{bkg} , N_{cand} , N_{bkg} and N_{sig} in the formula to calculate $D^0 v_2$. The v_2 of candidates and backgrounds, which is the mean value of $\cos(2\phi)$, is calculated by TProfile in ROOT. The TProfile also offers the error of the mean. And this error takes into account the statistical error of $K\pi$ pair and correlated hadrons. For this reason, the number of N_{cand} is a value with no error in the calculation. Or not the error will be duplicated. The N_{sig} comes from fitting, so the fitting error is included in the number N_{sig} . Finally, to avoid overestimation the statistical error, we re-write the formula as in Equation. 11. In this formula, we substitute N_{sig} with $N_{cand} - N_{bkg}$.

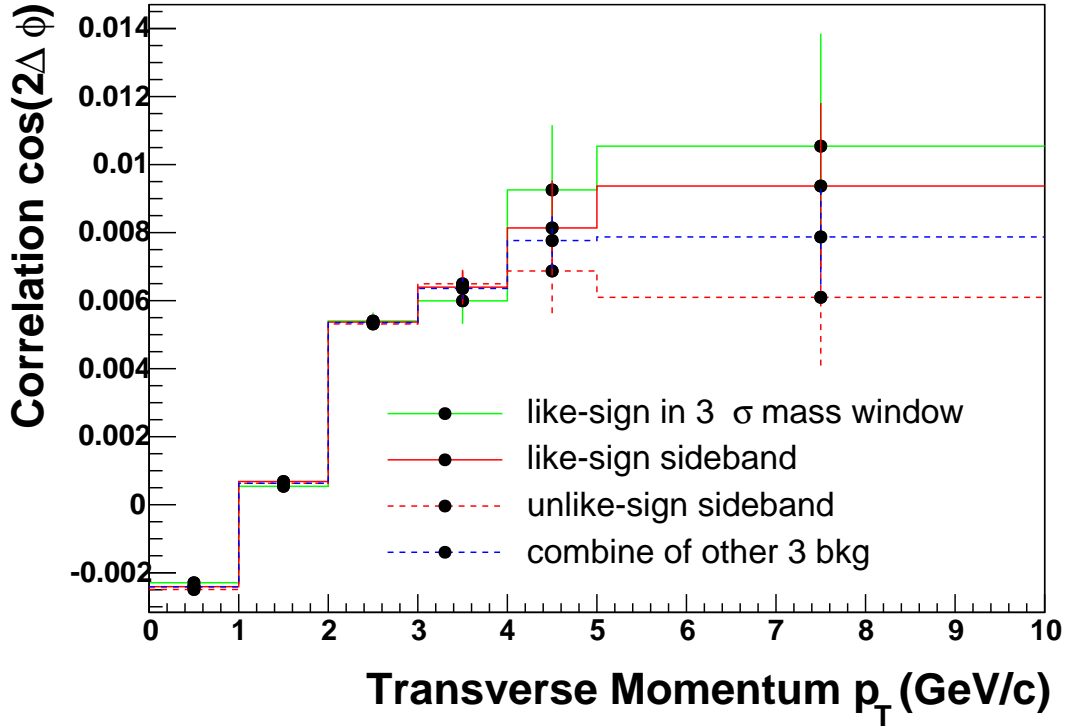


FIG. 53: Background v_2 vs. p_T from different samples and the average value. The colored three lines are from different samples. And the blue line is weighted average value of the three colored samples.

$$\begin{aligned}
 v_2^{sig} &= \frac{N_{cand} \cdot v_2^{cand} - N_{bkg} \cdot v_2^{bkg}}{N_{signal}} \\
 &= \frac{N_{cand}}{N_{signal}} \cdot (v_2^{cand} - v_2^{bkg}) + v_2^{bkg}
 \end{aligned} \tag{11}$$

$D^0 p_T$	#Candidate	#Signal	$V_2^{candidate}$	$V_2^{background}$	v_2^{D*0}
0-1 GeV/c	859030 ± 861.70	8936.6 ± 1046.54	$-0.00286399 \pm 0.0000306$	$-0.00289401 \pm 0.0000306$	0.0043 ± 0.1794
1-2 GeV/c	317965 ± 527.17	13062.4 ± 622.88	$0.000519041 \pm 0.0000483$	$0.000611292 \pm 0.0000483$	-0.0475 ± 0.0745
2-3 GeV/c	51610.4 ± 213.80	7112.81 ± 254.71	$0.00504505 \pm 0.000112372$	$0.0049624 \pm 0.000112372$	0.1253 ± 0.0473
3-4 GeV/c	9311.33 ± 92.27	2609.28 ± 106.53	$0.00718012 \pm 0.000300545$	$0.00617099 \pm 0.000300545$	0.2174 ± 0.0560
4-5 GeV/c	2227.26 ± 45.83	977.97 ± 53.50	$0.00704185 \pm 0.00079957$	$0.00724018 \pm 0.00079957$	0.1400 ± 0.0845
5-10 GeV/c	1509.08 ± 38.56	734.82 ± 44.88	$0.00449162 \pm 0.00134489$	$0.00694821 \pm 0.00134489$	0.0241 ± 0.1112

TABLE IX: Candidate and background yield and V_2 in different p_T bin

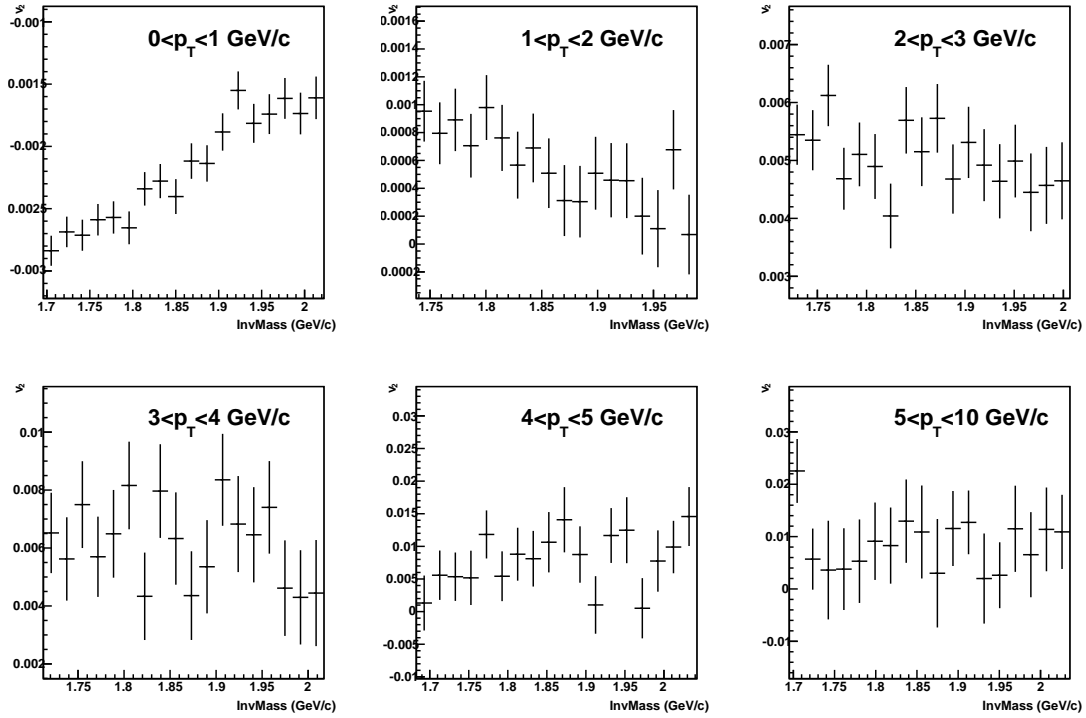


FIG. 54: v_2 vs. invariant mass of like-sign pair in different p_T bins for 0-80% central events

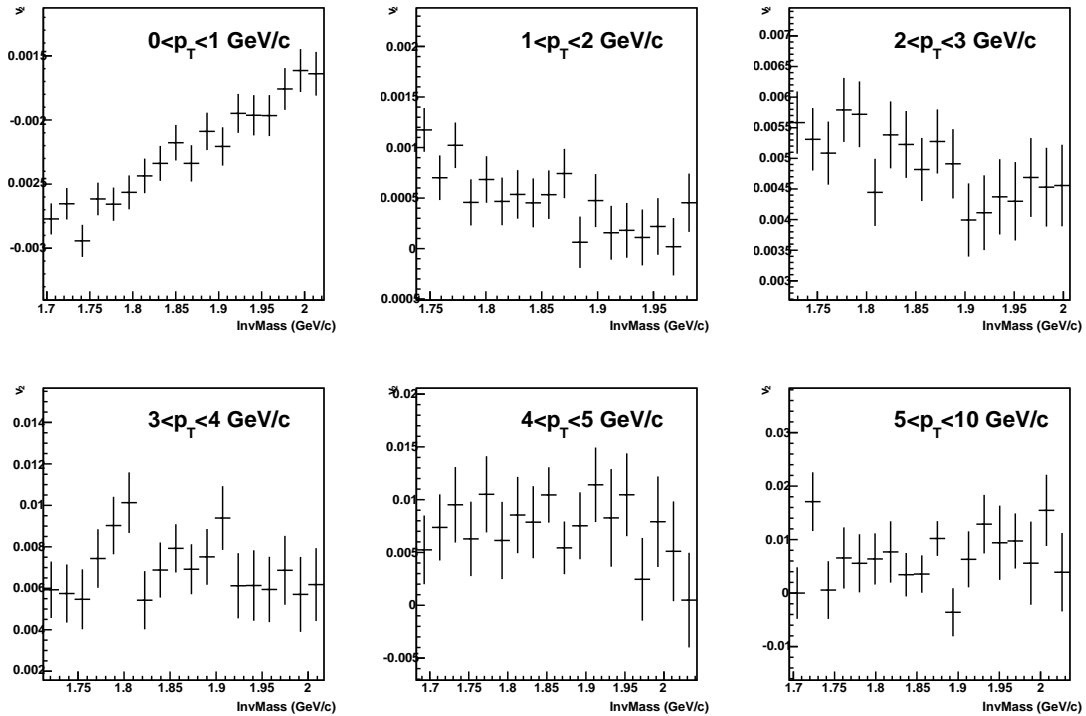


FIG. 55: v_2 vs. invariant mass of unlike-sign pair in different p_T bins for 0-80% central events

649

Systematic uncertainties for correlation method

650 In this analysis, three different systematic uncertainties are introduced. The first one is the un-
 651 certainty of D^0 yield. The function of second order polynomial is used to describe the background
 652 invariance mass distribution. To calculate the uncertainty, the exponential function is used as ref-
 653 erence to compare with the default value. And the difference translated to $D^0 v_2$ is considered as
 654 systematic uncertainty.

655 The second source of systematic uncertainty comes from background v_2 estimation. As men-
 656 tioned before, we choose side-band of like-sign, unlike-sign pairs, also like-sign pairs in D^0 mass
 657 window as different background estimation and the average value as the default value used for the
 658 $D^0 v_2$ calculation. Also the topological cuts with 50% and 150% D^0 yields are used for estimated
 659 the systematic background. Fig. 56 shows the v_2 results with different backgrounds and different
 660 topological cuts. Assuming the v_2 from all these combinations form a uniform distribution, the
 661 mean square root error can be obtained as the maximum differences among all combinations di-
 662 vided by $\sqrt{12}$, this is quoted as the systematic error of the measured v_2 , as described in event plane
 663 result.

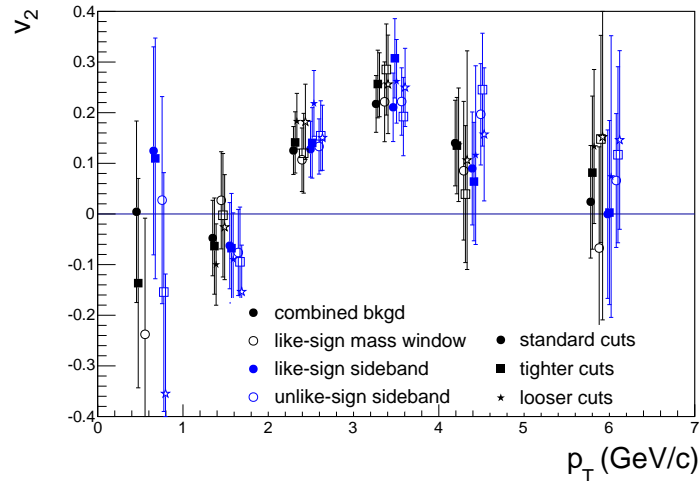


FIG. 56: v_2 vs. p_T with different backgrounds and topological cuts

664 Same as in event plane method, the inversed D^0 reconstruction efficiency weight uncertainty
 665 is the third systematic uncertainty. Fig. 57 shows $D^0 v_2$ with and without inversed D^0 reconstruc-
 666 tion efficiency weight. The difference between them is a conserved estimation of this systematic
 667 uncertainty.

668 Table X summarizes $D^0 p_T, v_2, v_2$ statistic error, 2 v_2 systematic error components and the total

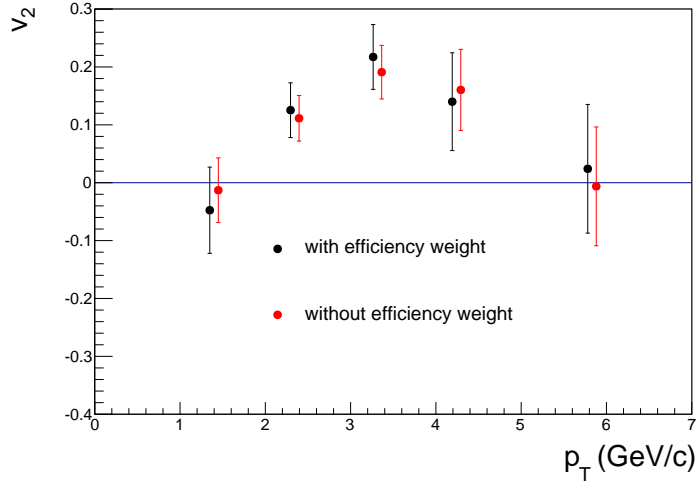


FIG. 57: v_2 vs. p_T with and without inverse D^0 reconstruction efficiency weight

669 v_2 systematic error.

670

Results from the correlation method

Figure. 58 is $D^0 v_2\{2\}$ result. In the two particle correlation method

$$\langle \cos(2(\phi_1 - \phi_2)) \rangle = \langle v_2^2 \rangle + \delta_2$$

671 . The δ_2 represents the non-flow contribution, which comes from correlations not related to the
 672 initial system geometry. To suppress non-flow contribution, η gap between D^0 and hadron can be
 673 added. In figure. 58, the $v_2\{2\}$ with η gap 0.15 is shown.

TABLE X: $D^0 p_T, v_2, v_2$ statistic error, v_2 systematic error from different fitting functions, different backgrounds, topological cuts, v_2 systematic error from inverse D^0 reconstruction efficiency weight, and total v_2 systematic error

$D^0 p_T$ (GeV/c)	0.63	1.52	2.47	3.43	4.36	5.95
v_2	0.0043	-0.0475	0.1253	0.2174	0.1400	0.0241
v_2 statistic error	0.1794	0.0745	0.0473	0.0560	0.0845	0.1112
systematics (fitting yields)	N/A	0.0024	0.0000	0.0016	0.0011	0.0099
systematics (backgrounds, cuts)	0.2207	0.0306	0.0362	0.0627	0.0404	0.0369
systematics (inverse efficiency weight)	N/A	0.0346	0.0140	0.0263	0.0204	0.0304
total v_2 systematic error	0.2207	0.0462	0.0388	0.0680	0.0453	0.0486

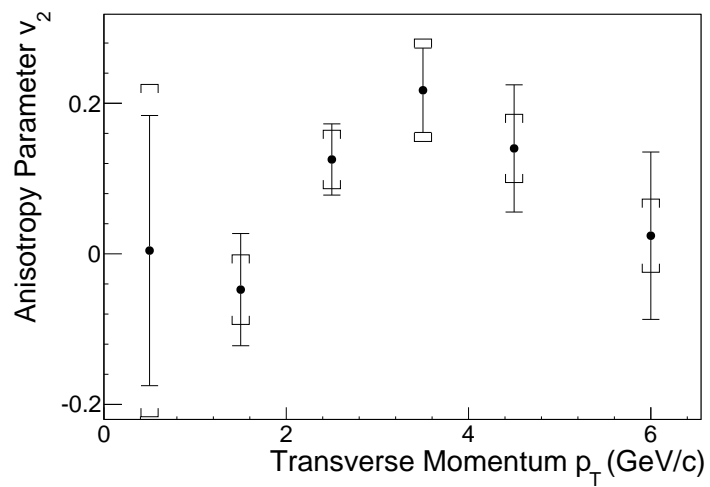


FIG. 58: v_2 vs. p_T from two-particle correlation method

674

COMMON SYSTEMATIC UNCERTAINTIES

675 There are two common possible systematic uncertainties for both the event plane method and
 676 the 2 particle correlation method: the non-flow effect, and the B feed down to D contribution.

677

Non-flow

678 Although an η gap is applied between tracks to reconstruct the event plane and the D^0 can-
 679 didate, there is still non-flow effect that can influence the v_2 measurement. The non-flow effect
 680 can be estimated from D^0 -hadron correlation in p+p 200 GeV collisions. However, the D^0 signal
 681 in p+p 200 GeV collisions with current obtained data by STAR is not strong enough to make a
 682 good D^0 -hadron correlation measurement. Thus the $D^{*\pm}$ hadron is used as an substitute of D^0 .
 683 Fig. 59 shows the $D^{*\pm}$ signal in p+p 200 GeV collisions from Run 12 VPDMB-nobsmd (370011)
 684 and BHT2 (370531) triggered events. The following cuts are applied: $VertexRanking > 0$;
 685 $numberOfFitPoints \geq 15$; $nFitPoints/nMax > 0.52$; $p_T > 0.16$ GeV/c; $gDca < 2.0$
 686 cm; $|eta| < 1$; $|VertexZ| < 60$ cm. Dmeson Daughter PID cuts: $|nSigmaPion| < 2.0$;
 687 $|nSigmaKaon| < 2.0$.

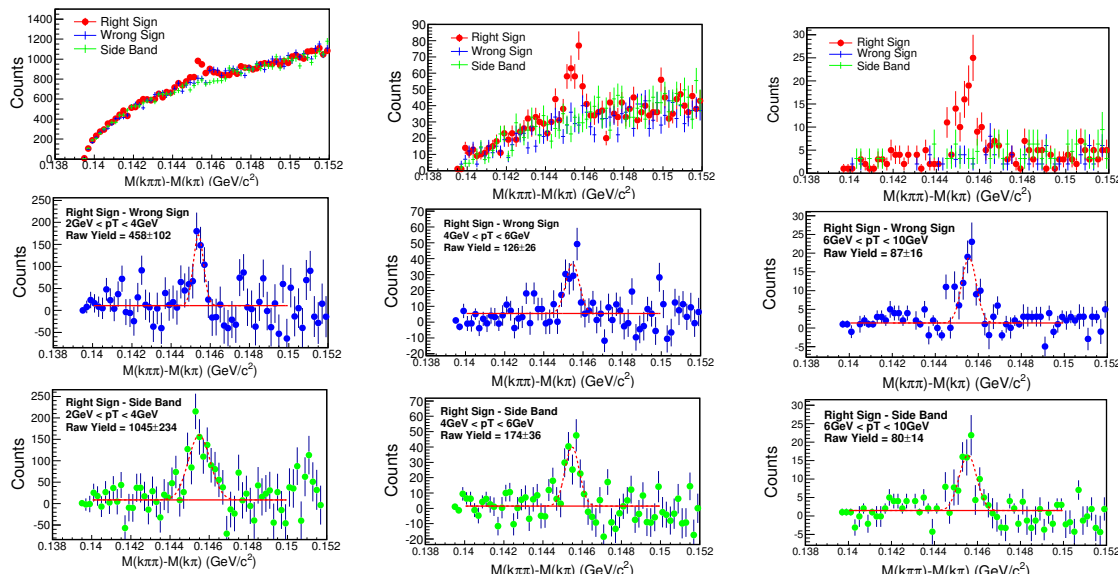


FIG. 59: $m(KK\pi) - m(K\pi)$ with the $D^{*\pm}$ signal for p_T 2-4 (left), 4-6 (middle), and 6-10 (right) GeV/c, in p+p 200 GeV collisions.

688

Fig. 60 shows $D^{*\pm}$ -hadron azimuthal correlation in Run 12 p+p 200 GeV collisions. And

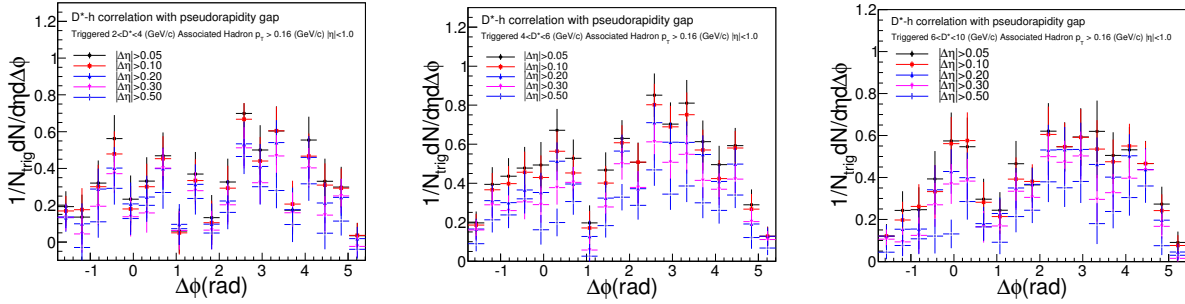


FIG. 60: $D^{*\pm}$ -hadron azimuthal correlation in pp 200 GeV collisions, with different trigger D^* p_T and η gaps.

Fig. 61 shows $\langle \sum_i \cos 2(\phi(p_T) - \phi_i) \rangle$ vs. p_T for $D^{*\pm}$ -hadron correlation with different η gaps. Because charm fragmentation to D^0 is very similar to charm fragmentation to $D^{*\pm}$, $D^{*\pm}$ -hadron correlation is a very good substitute for D^0 -hadron correlation. However, the decay feed-down to $D^{*\pm}$ is very different from D^0 . For example, D^0 can come from the decay of $D^{*\pm}$, generating correlation with the other daughter particle of $D^{*\pm}$. The different correlation from feed-down is simulated with Hijing. Fig. 62 shows $\langle \sum_i \cos 2(\phi(p_T) - \phi_i) \rangle$ vs. p_T for $D^{*\pm}$ -hadron, $D^{*\pm}$ -hadron from decay feed-down only, D^0 -hadron from feed-down only, and the deduced D^0 -hadron correlation.

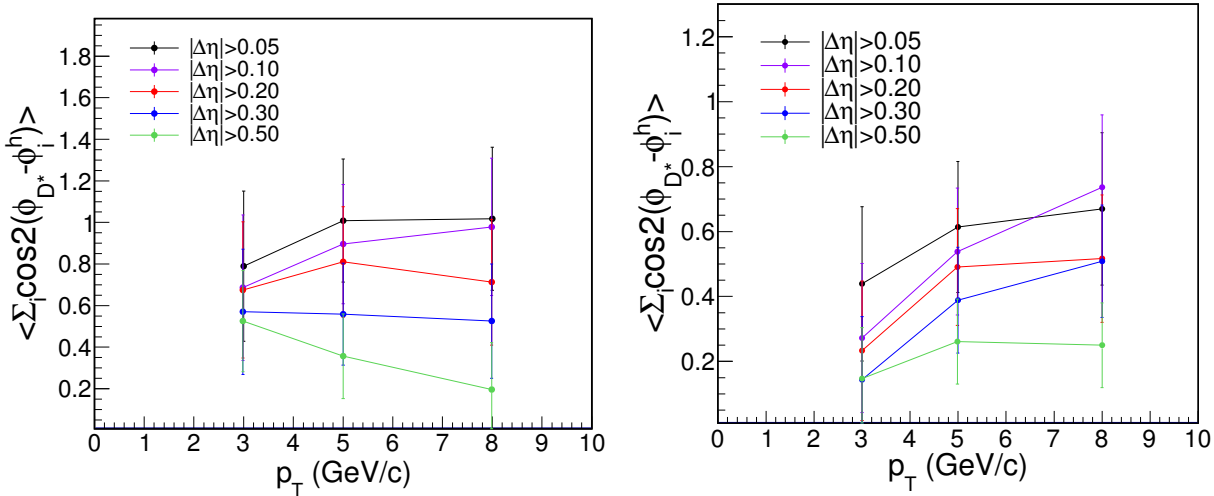


FIG. 61: $D^{*\pm}$ -hadron correlation $\langle \cos(2(\Delta\phi)) \rangle$ vs. p_T in pp 200 GeV collisions, with different η gaps. The left and right panel sum up correlations for and whole 2π range and for the near side only, respectively.

As in Phys. Rev. Lett. 93, 252301 (2004), the accumulative correlation of a particle from a given p_T bin with all other particles in the region $0.15 < p_T < 2.0$ GeV/c and $|\eta| < 1.0$ can be

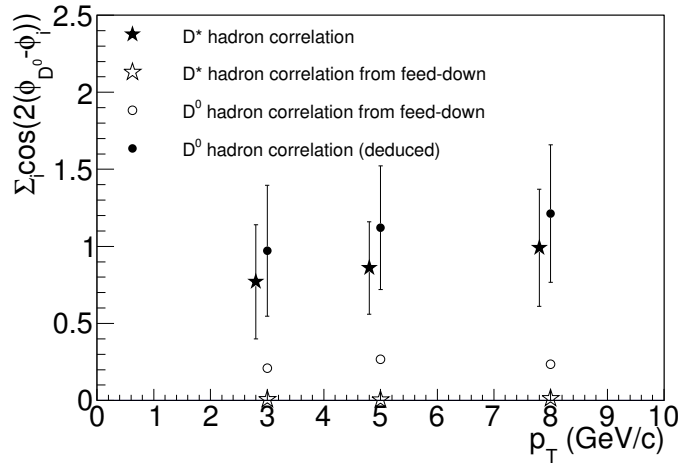


FIG. 62: $D^{*\pm}$ -hadron correlation $<\Sigma_i \cos(2(\phi(p_T) - \phi_i))>$ vs. p_T for $D^{*\pm}$ -hadron, $D^{*\pm}$ -hadron from decay feed-down only, D^0 -hadron from feed-down only, and the deduced D^0 -hadron correlation.

699 written as $<\Sigma_i \cos(2(\phi(p_T) - \phi_i))> = M v_2(p_T) \bar{v}_2 + \text{non-flow}$, where $\phi(p_T)$ is the azimuthal
 700 angle of the particle from a given p_T bin. The first term in the r.h.s. represents the elliptic flow
 701 contribution, where $v_2(p_T)$ is the elliptic flow of particles with a given p_T , and \bar{v}_2 is the average
 702 flow of particles used in the sum; M is the multiplicity of particles contributing to the sum, as
 703 shown in Fig. 63.

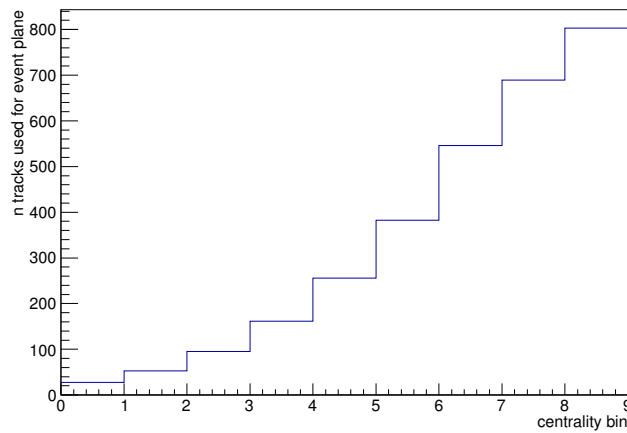


FIG. 63: multiplicity used in event plane reconstruction

704 Assuming the non-flow correlation in Au+Au collisions are the same as the correlation in p+p
 705 collisions, the non-flow effect on calculated $D^0 v_2$ should be $<\Sigma_i \cos(2(\phi(p_T) - \phi_i))> / M \bar{v}_2$. The
 706 D^0 -hadron correlation and the estimated non-flow effect on $D^0 v_2$ are shown in Fig. 64. Since

707 the away side correlation may be modified in the medium in Au+Au collisions, only the near side
 708 correlation is taken into the calculation.

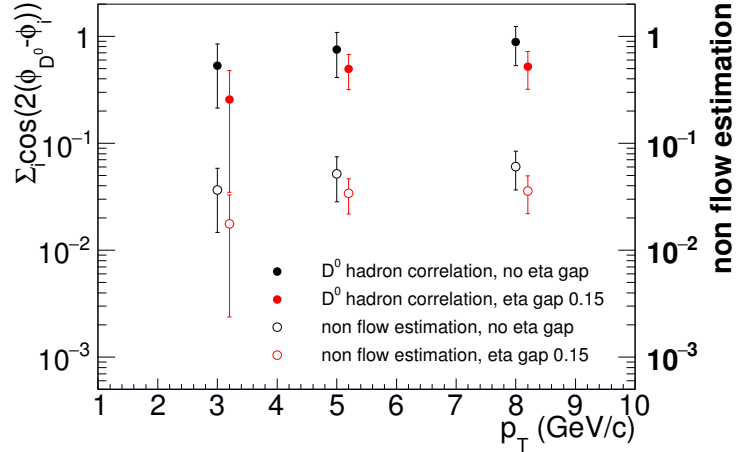


FIG. 64: D^0 -hadron correlation and the estimated non-flow effect on $D^0 v_2$

709 Another method commonly used to estimate non-flow effect is by looking at the difference
 710 between $v_2\{2\}$ and $v_2\{4\}$. Using the same statistics, $v_2\{4\}$ has a much larger error than $v_2\{2\}$ (5
 711 times larger for STAR). So this method won't give results with acceptable error for this analysis,
 712 due to the limited D^0 significance.

713

B feed-down contribution to D^0

714 Originally from PYTHIA simulation, the B feed-down contribution for inclusive D^0 is negligible.
 715 Because B mesons have longer life than D^0 mesons, the D^0 from B-decay has larger DCA
 716 than prompt D^0 . So is the daughter pion and kaon. Basically, lower D^0 DCA cut will decrease the
 717 B feed-down contribution for inclusive D^0 . When apply larger pion and kaon DCA cuts, however,
 718 the B feed-down contribution should get enhanced. This simulation is to check how much larger
 719 or lower the B feed-down contribution will get after apply topology cuts from data analysis.

720 We use a fast simulator based on TPythia6Decayer. Firstly, we input D^0 and B^+ mesons
 721 respectively to decay. Then we smear the daughter pions' and kaons' transverse momentum and
 722 DCA. At last, we use the smeared position and momentum to reconstruct D^0 .

We use p_T spectra in pp 200GeV and R_{AA} in AuAu 200GeV to get the input p_T spectra in
 AuAu 200GeV by:

$$\frac{d^2N_{AA}^i}{dydp_T} = R_{AA} \cdot N_{coll} \cdot \frac{d^2N_{pp}^i}{dydp_T} \quad (12)$$

723 The i represents the observed hadron species.

724 The B and D^0 mesons' p_T spectra in pp 200GeV is calculated from FONLL (<http://www.lpthe.jussieu.fr/~cacciari/fonll/fonllform.html>), which is showed in
 725 Fig. 65(a). Fig. 65(b) is B and D^0 mesons' R_{AA} as a function of p_T (Figure 5.8, Cao S. Heavy
 726 Flavor Dynamics in Relativistic Heavy-ion Collisions[D]. Duke University, 2014.).

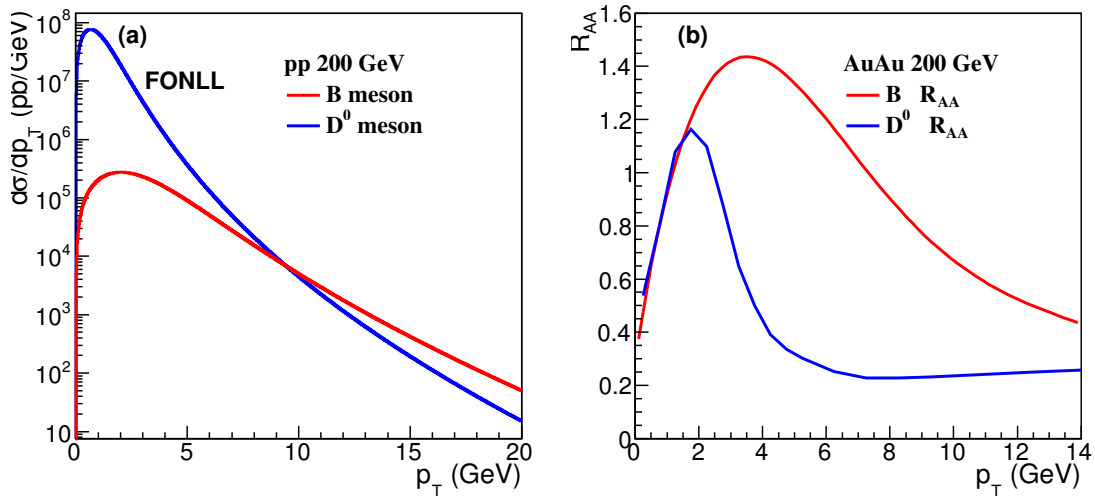


FIG. 65: (a) B and D^0 meson p_T spectra in pp 200GeV, (b) B and D^0 meson R_{AA} in AuAu 200GeV

Fig. 66(a) is B and D^0 mesons' p_T spectra in AuAu 200GeV. With the $b \rightarrow B^+$ fragmentation ratio (FR) and $B^+ \rightarrow D^0$ branch ratio (BR) in Table. XI, the input B^+/D^0 ratio can be calculated, which is showed in Fig. 66(b).

Particle	$c\tau(\mu m)$	Mass(GeV/ c^2)	$b \rightarrow B^+ X(FR)$	$B^+ \rightarrow \bar{D}^0 X(BR)$
B^+	491	5.279	0.4	0.79

TABLE XI: PDG values of B^+ mesons.

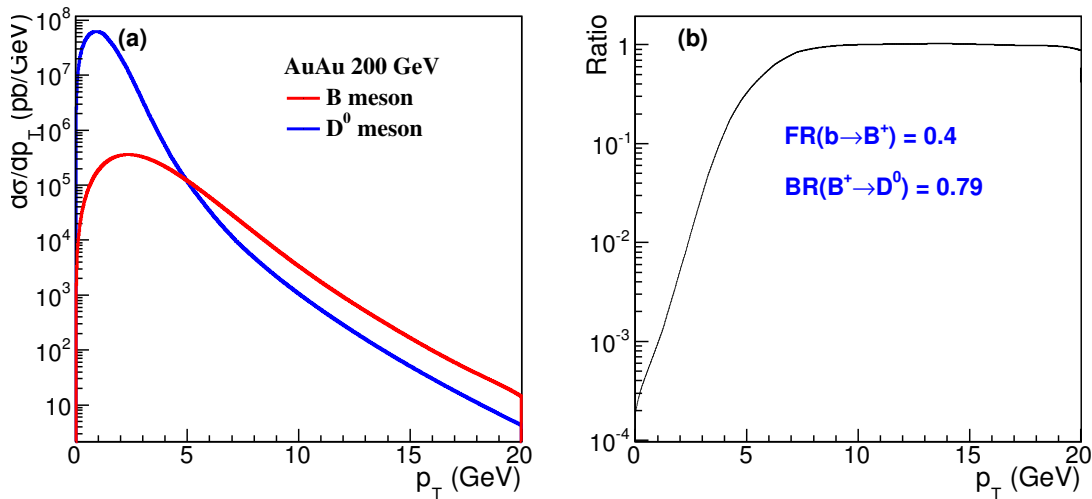


FIG. 66: (a) B and D^0 meson p_T spectra in AuAu 200GeV, (b) the input B^+/D^0 ratio as a function of p_T

In this simulation, we input 10 million B^+ and D^0 mesons respectively with a flat p_T distribution (0-20GeV). The B^+ and D^0 mesons are generated with uniform distribution in the rapidity interval $-1 < y < 1$ and uniform in azimuth. The B^+ are forced to decay to D^0 ($B^+ \rightarrow \bar{D}^0 \nu_e e^+$) with 100% branch ratio and D^0 (\bar{D}^0) are forced to decay to kaon and pion ($D^0 \rightarrow k^- \pi^+$, $\bar{D}^0 \rightarrow k^+ \pi^-$) with 100% branch ratio. Then we use the p_T spectra in Figure 2(a) as a weight to push the B^+ and D^0 p_T distribution into the real situation in AuAu 200GeV collisions. The input ratio of B^+/D^0 is showed in Fig. 66(b).

The daughter track position resolution is considered in 2 methods. In Method 1, the hit positions in inner PXL layer and outer PXL layer are calculated from the daughter track (using a straight line model since the distance is small) position and momentum direction. Then these 2 hit positions are smeared with the PXL point resolution ($16\mu m$). At last the daughter track is reconstructed with

741 the smeared points and the multiple scattering effect at the inner layer, described by the following
 742 equation.

$$\theta_{plane}^{rms} = \frac{13.6 MeV}{\beta cp} z \sqrt{\frac{x}{X_0}} \left[1 + 0.038 \ln \frac{x}{X_0} \right] \quad (13)$$

743 Here p , βc , and z are the momentum, velocity, and charge number of the incident particle, and
 744 $\frac{x}{X_0}$ is the thickness of the scattering medium in radiation lengths.

745 In Method 2, the daughter track position is smeared with (DCA_{xy} , DCA_z) distributions (for
 746 different p_T , η , ϕ) from real data.

747 The transverse momentum is smeared with a resolution function fit to embedding data, shown
 748 in Fig. 67 for pion and kaon.

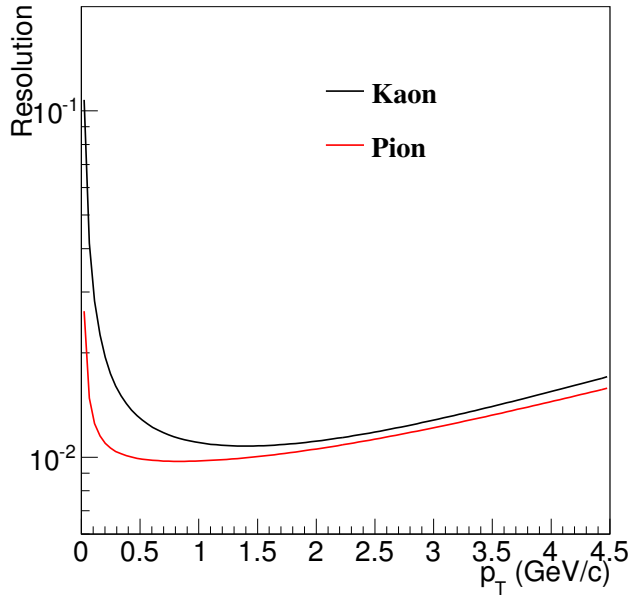


FIG. 67: pion and kaon transverse momentum resolution from data

749 Fig. 68 shows some distributions from our simulation at the range $5 < p_T < 8$ GeV and -0.5
 750 $< y < 0.5$. The black dotted line is from inclusive D^0 , the red line is from D^0 of B decay, the blue
 751 line is from prompt D^0 .

752 Fig. 69 is $D_{B-decay}^0/D_{total}^0$ ratio varies when apply a single topology cut. The cut value is the
 753 same as data analysis (Table. XII). As we can see, with different topology cuts, the ratio (B feed-
 754 down contribution) is small (Max ratio 13%). Individually, B feed-down contribution gets less
 755 when apply lower D^0 DCA cut and get enhanced when apply other cuts (except dcaDaughter cut).

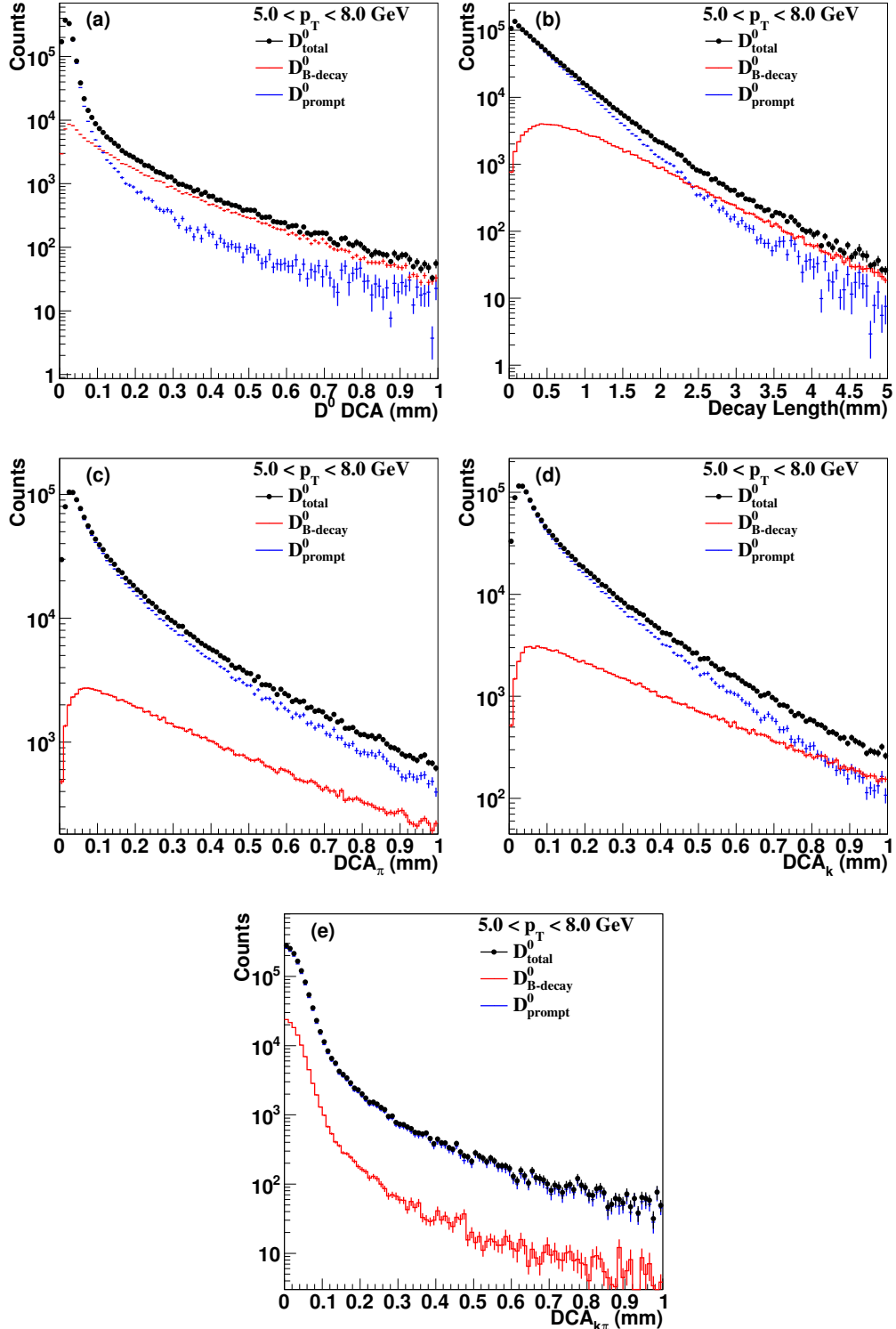


FIG. 68: some distributions at $5 < p_T < 8$ GeV and $|y| < 0.5$. The black dotted line is from inclusive D^0 , the red line is from D^0 of B^+ decay, the blue line is from prompt D^0 . (a) D^0 DCA distribution. (b) Decay length distribution. (c) Daughter pion DCA distribution. (d) Daughter kaon DCA distribution. (e) DCA between daughter pion and kaon distribution.

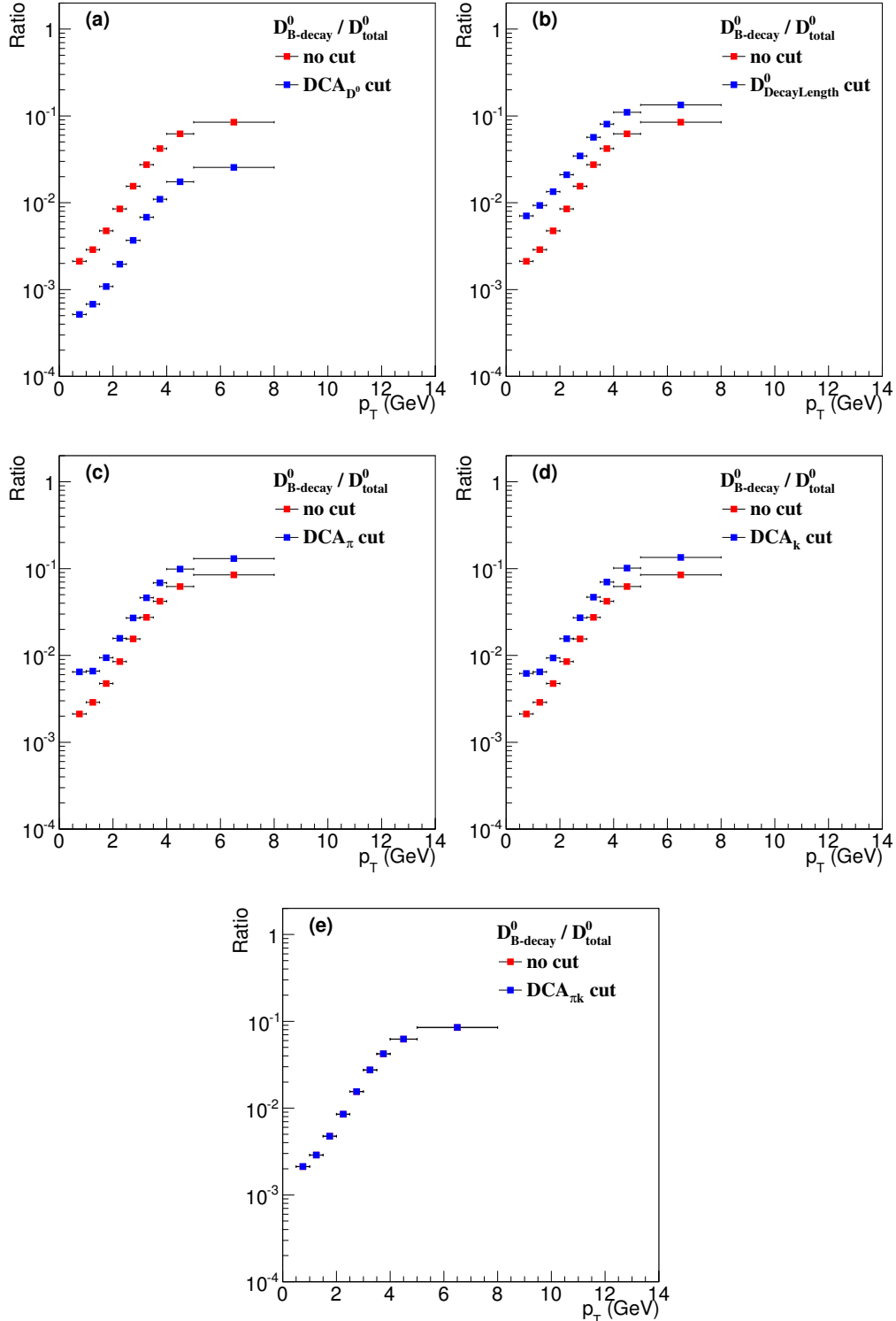


FIG. 69: D^0 from B decay over inclusive D^0 ratio as a function of p_T . The red square represents ratio without any cuts, the blue square is ratio with the cut: (a) D^0 DCA, (b)decayLength, (c) pion DCA, (d) kaon DCA, (e) dcaDaughters. The cut range is the same as that from data analysis.

Cut variable	DCA_{D^0}	DecayLength	DCA_π	DCA_k	$DCA_{k\pi}$
Cut range	$< 40\mu m$	$> 259\mu m$	$> 62\mu m$	$> 58\mu m$	$< 60\mu m$

TABLE XII: The topology cuts for D^0 from B decay simulation

Fig. 70 is the result when apply all topology cuts in Table. XII, which is the cuts for 5-10 GeV/c for the v_2 analysis. We can see, B feed-down contribution gets less (<4%) when applied all topology cuts, which is due to D^0 DCA cut.

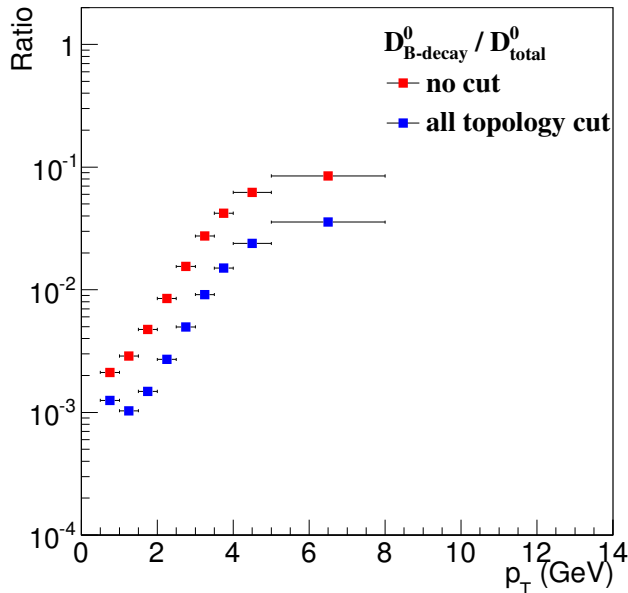


FIG. 70: D^0 from B decay over inclusive D^0 ratio as a function of p_T . The red square represents ratio without any cuts, the blue square is ratio with all topology cuts.

And we also compare the result with the two smear methods above. Fig. 71 shows that the two methods agree with each other very well.

With a single topology cut (pion DCA, kaon DCA, DecayLength), the B feed-down contribution ($D_{B-decay}^0/D_{total}^0$) maybe get enhanced to about 13% at p_T range from 5GeV to 8GeV. But the D^0 DCA cut ($< 40\mu m$) can decrease the B feed-down contribution to less than 2.6%, and it seems that the D^0 DCA cut plays a dominant role. When applying all topology cuts, B feed-down contribution gets less than 4%.

In the extreme case that B v_2 is 0, the measured $D^0 v_2$ will be less than 4% lower than v_2 of direct charm produced D^0 . The $D^0 v_2$ is on the level of 0.1 at maximum. Thus the absolute influence is $0.1*4\% = 0.004$, which is neglectable.

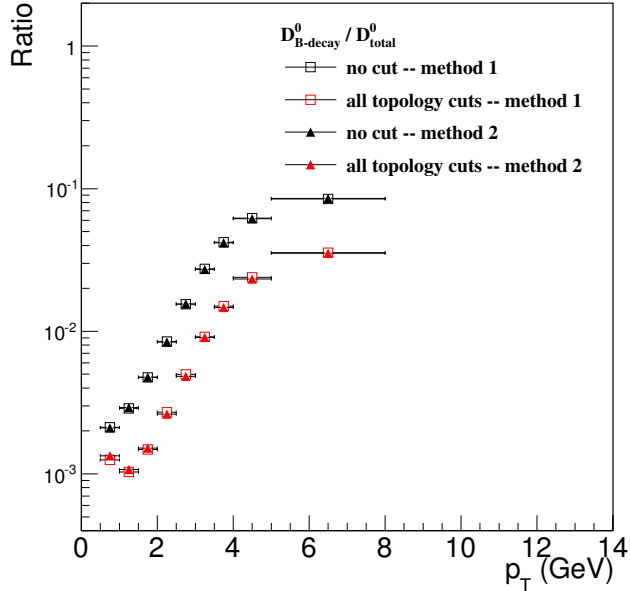


FIG. 71: D^0 from B decay over inclusive D^0 ratio as a function of p_T . The red square and triangle represents ratio without any cuts from method 1 and method 2 respectively, the blue square and triangle is ratio with all topology cuts from method 1 and method 2 respectively. In method 1, we smear daughter track start point by calculating. In method 2, we smear daughter track start point by data driven DCA 2D-projection distribution.

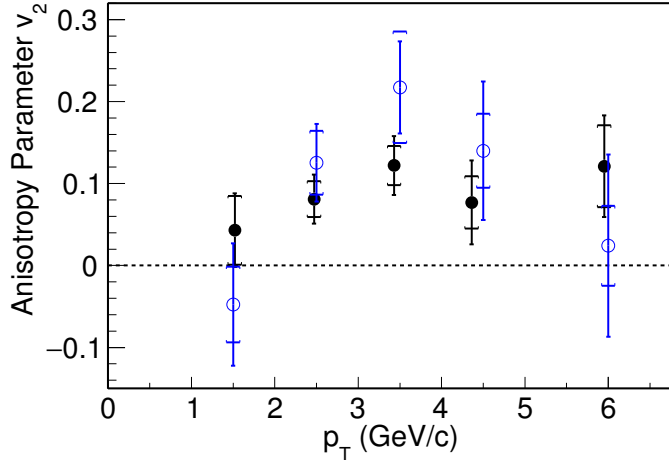


FIG. 72: v_2 vs. p_T from the event plane (black points) and the correlation method (open blue circles)

769

RESULT AND DISCUSSION

770 Figure 72 compares v_2 from the event plane and the correlation method. We can see the 2
 771 results are consistent within their errors. The event plane method treat each D^0 equally, regardless
 772 of the different final particle momentum eccentricity and multiplicity of different events. The
 773 correlation method, since it is measuring the correlation pair wise, is equivalent to treat D^0 with
 774 weight on event final particle eccentricity and multiplicity. So mathematically results from these
 775 two method are by definition different. But our result are far from sensitive enough to tell this
 776 difference. Neither is this difference important to the main physics question (the charm flow) we
 777 want to address in this paper. Thus in the following discussions, we use the event plane method
 778 result only, which has slightly smaller errors.

779 Figure 73 compares the measured $D^0 v_2$ from the event plane method in 0 – 80% central events
 780 with v_2 of K_s^0 (B. I. Abelev et al. (STAR), Phys. Rev. C77, 054901(2008)), ϕ and Ω (L. Adamczyk
 781 et al. (STAR), arXiv:1507.05247). Panel a) shows v_2 vs. p_T . The $D^0 v_2$ is finite for $p_T > 2$ GeV/c,
 782 but slightly lower than light flavor hadrons between 2 and 5 GeV/c. To account for the effects of
 783 different particle mass and Number of Constituent Quarks (NCQ), v_2/NCQ vs. $(m_T - m_0)/NCQ$
 784 is plotted in Fig. 73 b). Here m_0 is the mass of the particle, and $m_T = \sqrt{p_T^2 + m_0^2}$. The ϕ , K_s^0 and
 785 Ω fall into the same trend in the v_2/NCQ vs. $(m_T - m_0)/NCQ$ plot, but there is an indication that
 786 the $D^0 v_2$ is still systematically lower than the light flavor particles. This may suggest that charm
 787 quark is not fully thermalized and doesn't flow completely with the medium. The comparisons

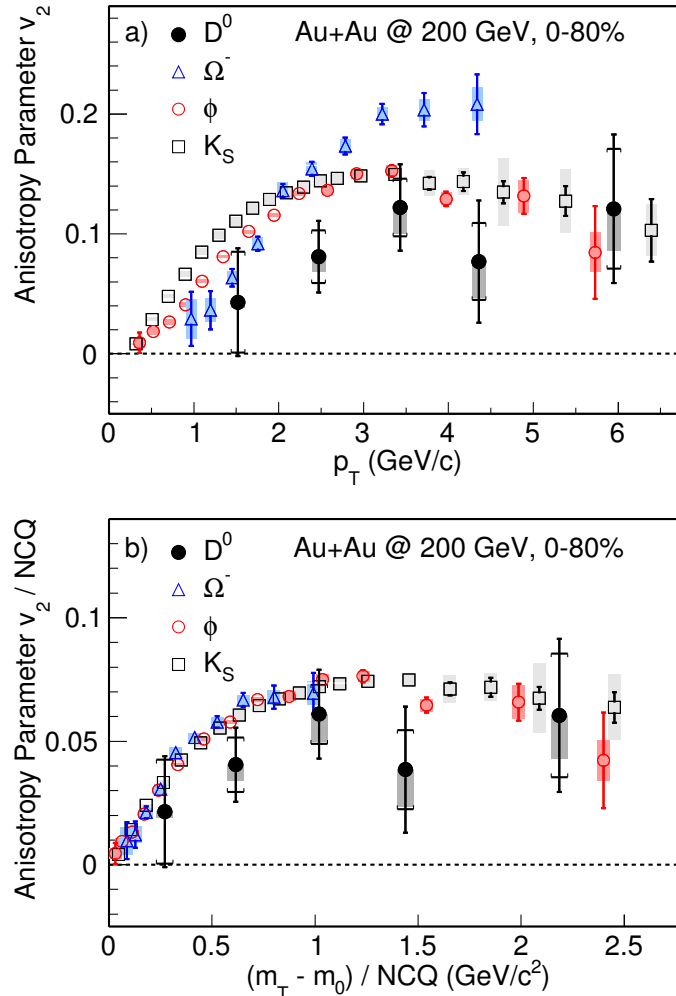


FIG. 73: a) v_2 vs. p_T and b) v_2/NCQ vs. $(m_T - m_0)/NCQ$ for D^0 from the event plane method in 0 – 80% central events compared with K_S^0 , ϕ and Ω . m_0 is the mass of the particle, and $m_T = \sqrt{p_T^2 + m_0^2}$.

788 between the measured D^0 v_2 and $0, K_S$ v_2 are quantified in terms of χ^2/NDF in Table XIII.

789 The main goal of measuring heavy flavor v_2 is to quantify medium properties of the sQGP.
 790 In the low p_T region that our measurement covers, the heavy quark-medium interaction is often
 791 characterized by a spacial diffusion coefficient D_s , or a dimensionless coefficient $2\pi TD_s$, where
 792 T is the medium temperature (G. D. Moore and D. Teaney, Phys. Rev. C71, 064904 (2005)). In
 793 Fig. 74 and 75, the measured D^0 v_2 and published $D^0 R_{AA}$ result (L. Adamczyk et al. (STAR),
 794 Phys. Rev. Lett. 113, 142301 (2014)) are compared with model calculations with different treat-
 795 ments of charm medium interaction and diffusion coefficient $2\pi TD_s$. The calculation from the
 796 SUBATECH group (reference below) employs pQCD calculation plus the Hard Thermal Loop
 797 (HTL) approximation for soft collisions, and describes our v_2 measurement of well over the en-

tire p_T range. This model also provides a good description of the published $D^0 R_{AA}$ result. The model from the TAMU group uses a non-perturbative T-matrix approach, assuming that the two-body interaction can be described by a potential as a function of the 4-momentum transfer. There are 2 curves in Fig. 74 from the TAMU model. The default solid curve (blue) with charm quark diffusion agrees with the data, while the dotted curve (pink) without charm quark diffusion is systematically lower than the measured data points. This supports finite charm quark flow. The default TAMU model also predicts the major trend of the R_{AA} vs. p_T . The Duke group developed a model with a free constant charm diffusion coefficient $2\pi TD_s$. To describe the LHC high $p_T R_{AA}$ data (B. Abelev et al. (ALICE), JHEP 09, 112 (2012)), $2\pi TD_s \approx 7$. The calculated R_{AA} at RHIC using this value shows a qualitative agreement with data. However, the predicted v_2 shows a trend lower than our measurements as shown in Fig. 74. In the Parton-Hadron-String Dynamics (PHSD) transport approach charm quarks scatter in the QGP with the off-shell partons. The PHSD model matches the measured $D^0 v_2$ well. It can also reproduce the major structure of the R_{AA} vs. p_T . The hydrodynamic model, which assumes local thermal equilibrium, can be tuned to describe v_2 for light hadrons. It predicts a $D^0 v_2$ trend that is consistent but slightly higher than the data, which also indicates that charm quark doesn't flow completely with the medium. However the errors of our measurement are too large to make a conclusion. Table XIII summarized the predicted $2\pi TD_s$ of the above models and their comparisons with the measured $D^0 v_2$ and R_{AA} in terms of χ^2/NDF and the p value. In general, several models with charm diffusion coefficient $2\pi TD_s$ ranging from 2 to 12 are consistent with our measurement, while the predicted v_2 is different from our measurement if charm quark diffusion is turned off. This supports finite charm medium interaction and charm quark flow at the top RHIC energy. It should also be mentioned that besides the different treatments of the charm medium interaction briefly stated above, there are also various differences among these models for the initial state, the space-time description of the QGP evolution, the hadronization, and the interactions in the hadronic matter. Besides precise experimental measurements, more solid model treatments of these aspects are needed in order to better interpret the information about charm medium interaction from the $D^0 v_2$ measurement.

The references to the models mentioned above are the following:

[SUBATECH] P. B. Gossiaux, J. Aichelin, T. Gousset, and V. Guiho, Strangeness in quark matter. Proceedings, 14th International Conference, SQM 2009, Buzios, Rio de Janeiro, Brazil, September 27-October 2, 2009, J. Phys. G37, 094019 (2010); M. Nahrgang, J. Aichelin, S. Bass, P. B. Gossiaux, and K. Werner, Phys. Rev. C91, 014904 (2015); and private communication.

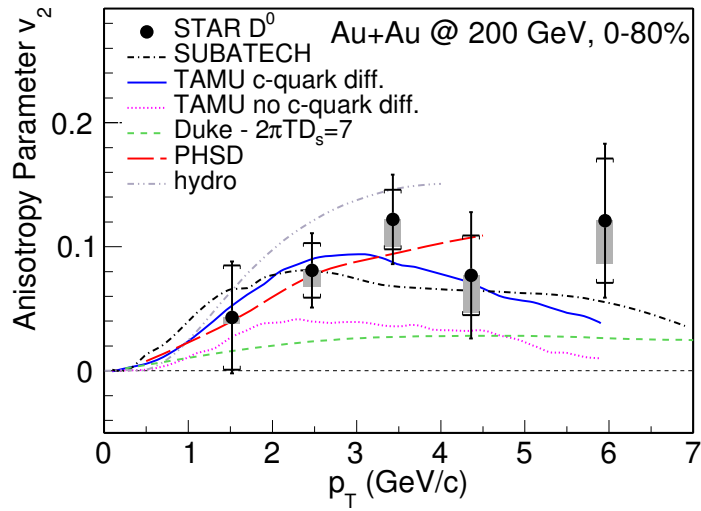


FIG. 74: v_2 vs. p_T for D^0 from the event plane method in 0 – 80% central events compared with different model calculations.

[TAMU] M. He, R. J. Fries, and R. Rapp, Phys. Rev. C86, 014903 (2012); Phys. Rev. Lett. 110, 112301 (2013); and private communication.

[DUKE] S. Cao, G.-Y. Qin, and S. A. Bass, Phys. Rev. C88, 044907 (2013); C92, 024907 (2015); and private communication.

[PHSD] H. Berrehrah, P. B. Gossiaux, J. Aichelin, W. Cassing, J. M. Torres-Rincon, and E. Bratkovskaya, Phys. Rev. C90, 051901 (2014); H. Berrehrah, E. Bratkovskaya, W. Cassing, P. B. Gossiaux, and J. Aichelin, C91, 054902 (2015).

[hydro] L.-G. Pang, Y. Hatta, X.-N. Wang, and B.-W. Xiao, Phys. Rev. D91, 074027 (2015).

Table XIII summarized the predicted $2\pi TD_s$ of the above models and their comparisons with the measured $D^0 v_2$ in terms of χ^2/NDF and the p value. In general, several models with charm diffusion coefficient $2\pi TD_s$ ranging from 2 to 12 are consistent with our measurement, while the predicted v_2 is different from our measurement if charm quark diffusion is turned off. This supports finite charm medium interaction and charm quark flow at the top RHIC energy. It should also be mentioned that besides the different treatments of the charm medium interaction briefly stated above, there are also various differences among these models for the initial state, the space-time description of the QGP evolution, the hadronization, and the interactions in the hadronic matter. Besides precise experimental measurements, more solid model treatments of these aspects are needed in order to better interpret the information about charm medium interaction from the $D^0 v_2$ measurement.

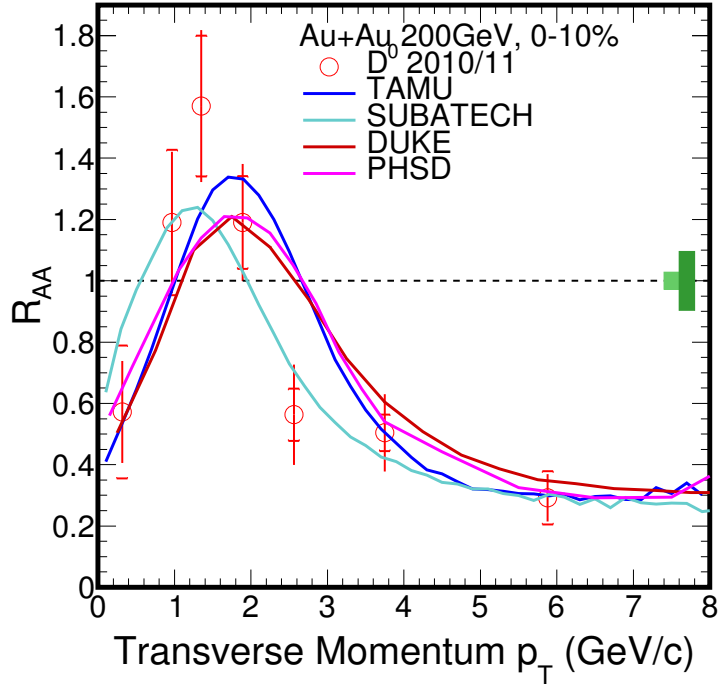


FIG. 75: R_{AA} vs. p_T for D^0 in 0 – 10% central events compared with different model calculations.

TABLE XIII: $D^0 v_2$ and R_{AA} compared with 0, $K_s v_2$ and model calculations (with the quoted $2\pi TD_s$) quantified by χ^2/NDF and the p value (the probability of observing a χ^2 that exceeds the current measured χ^2 by chance). The comparison with K_s is done with v_2/NCQ vs. $(m_T - m_0)/NCQ$.

compare with	$2\pi TD_s$	$v_2 \chi^2/NDF$	$v_2 p$ value	$R_{AA} \chi^2/NDF$	$R_{AA} p$ value
0	-	14.3 / 5	1.4×10^{-2}	-	-
K_s	-	5.6 / 5	0.35	-	-
SUBATECH	2-4	2.0 / 5	0.85	3.5 / 7	0.84
TAMU c quark diff.	2-7	1.5 / 5	0.91	9.0 / 7	0.25
TAMU no c quark diff.	-	6.4 / 5	0.26	-	-
DUKE	7	7.9 / 5	0.16	8.9 / 7	0.26
PHSD	5-12	0.6 / 4	0.96	9.0 / 7	0.25
hydro	-	1.3 / 3	0.73	-	-

849

APPENDIX

850

Event plane method plots for different p_T bins

standard geometry cuts, p_T 0-1 GeV/c

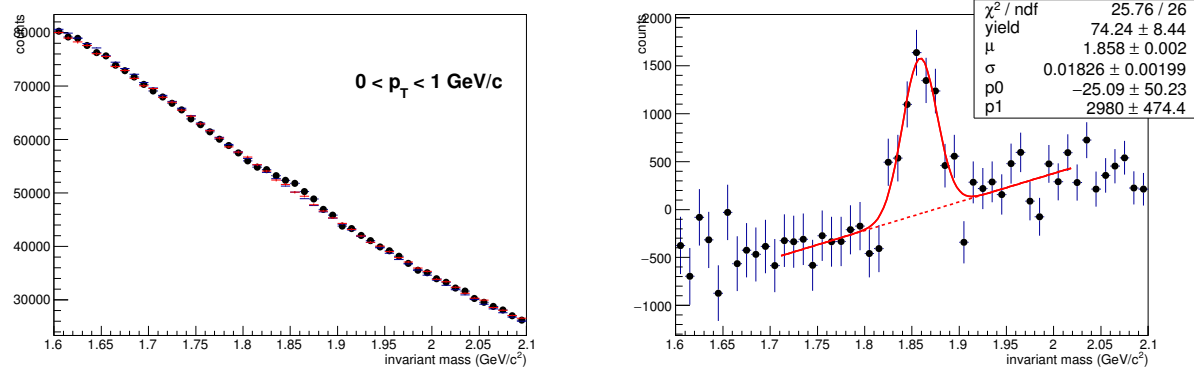


FIG. 76: $K\pi$ invariant mass distribution, left: unlike sign, like sign and scaled mixed event; right: unlike sign - mixed event

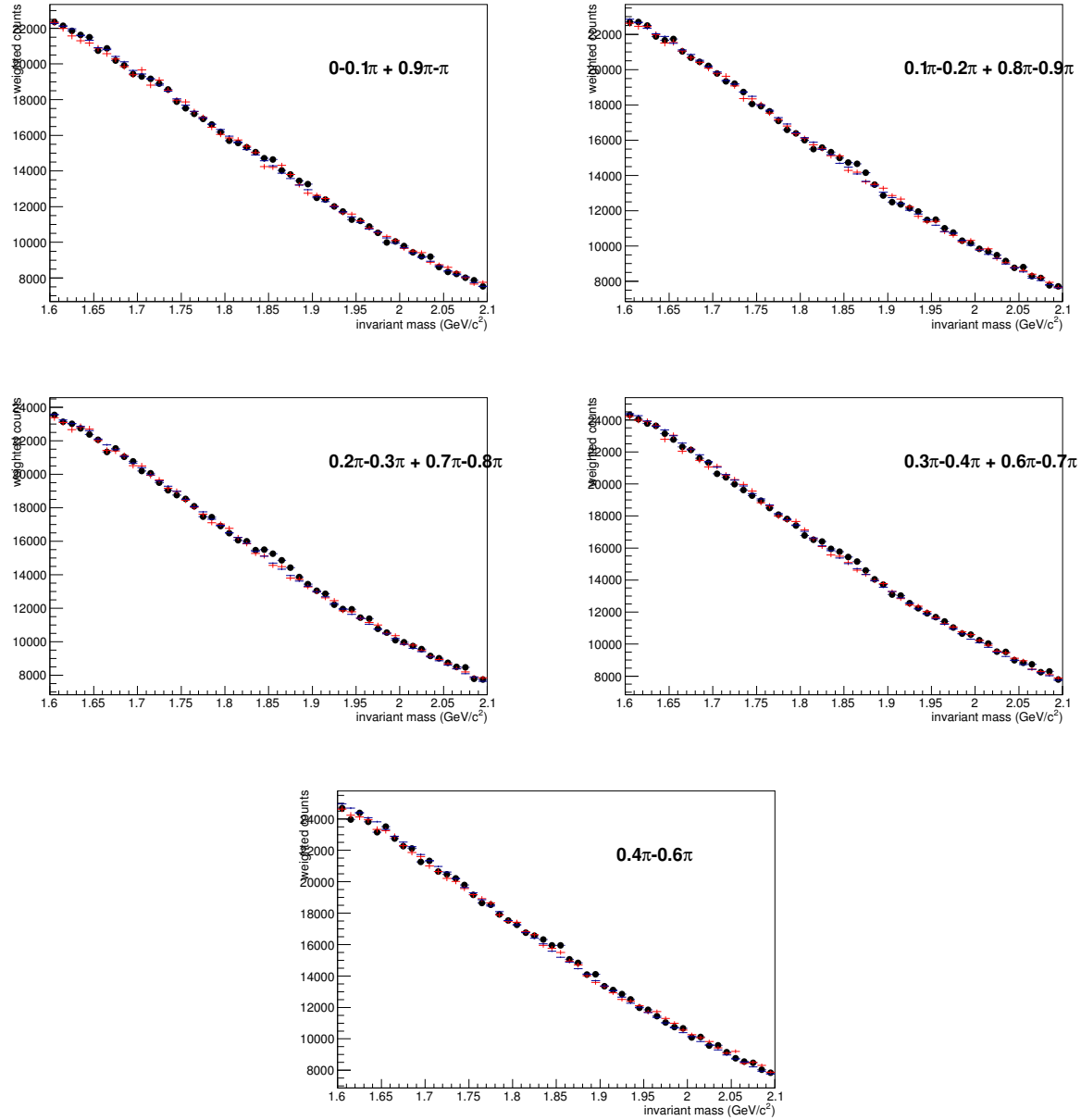


FIG. 77: $K\pi$ invariant mass in different $\phi - \Psi$ bins

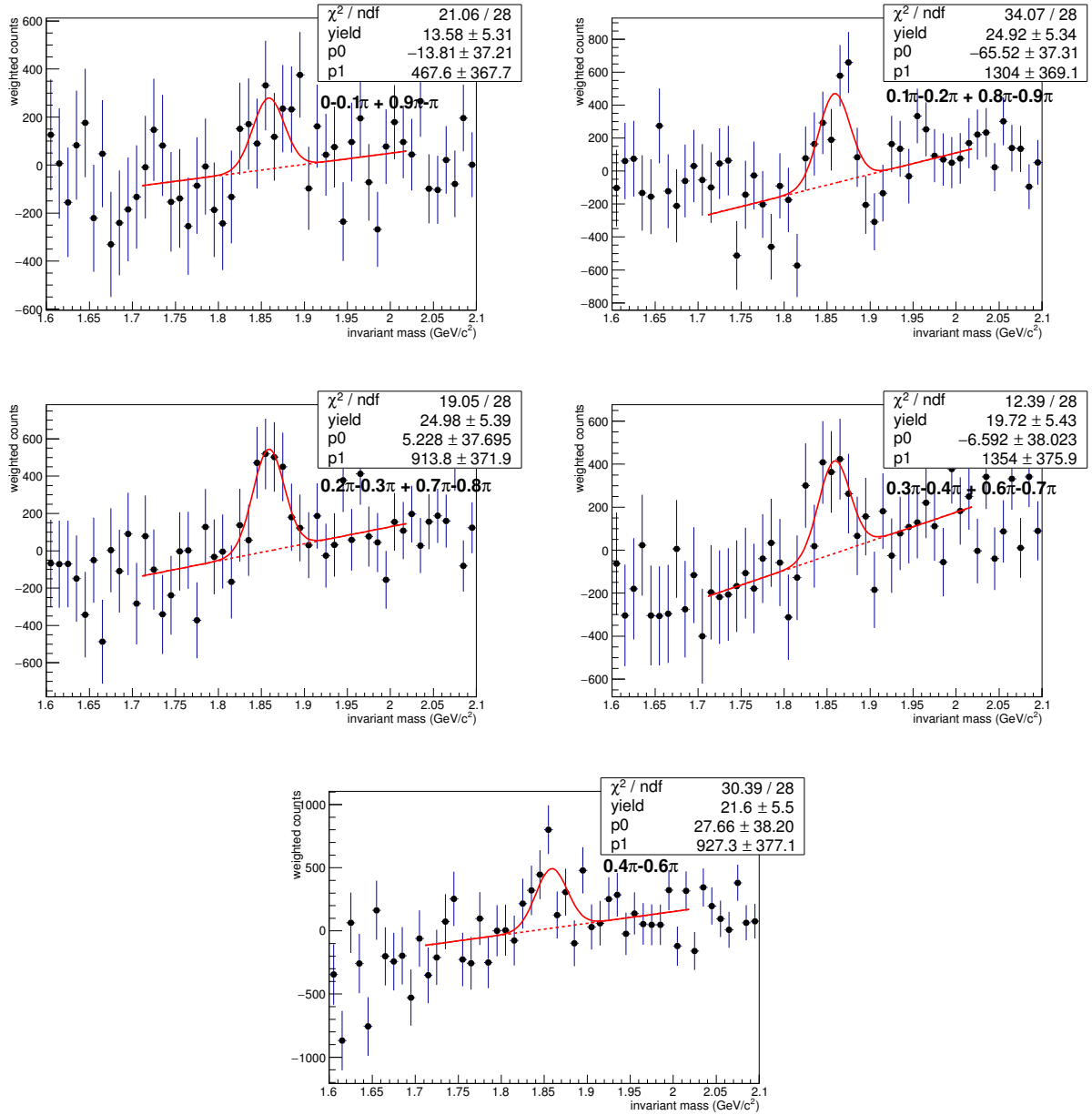


FIG. 78: $K\pi$ pairs invariant mass unlike sign - mixed event in different $\phi - \Psi$ bins, default fit range

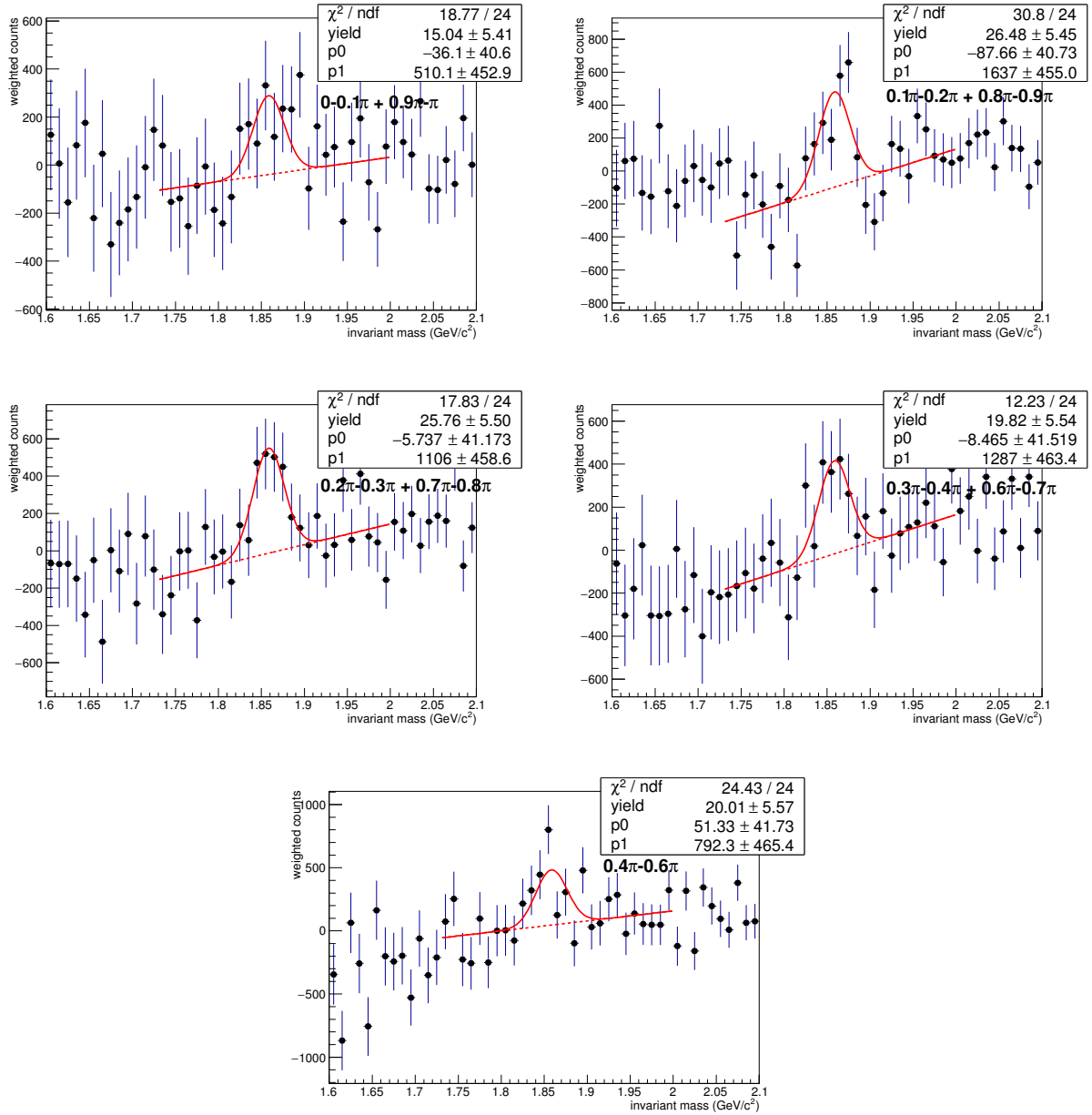


FIG. 79: $K\pi$ pairs invariant mass unlike sign - mixed event in different $\phi - \Psi$ bins, narrower fit range

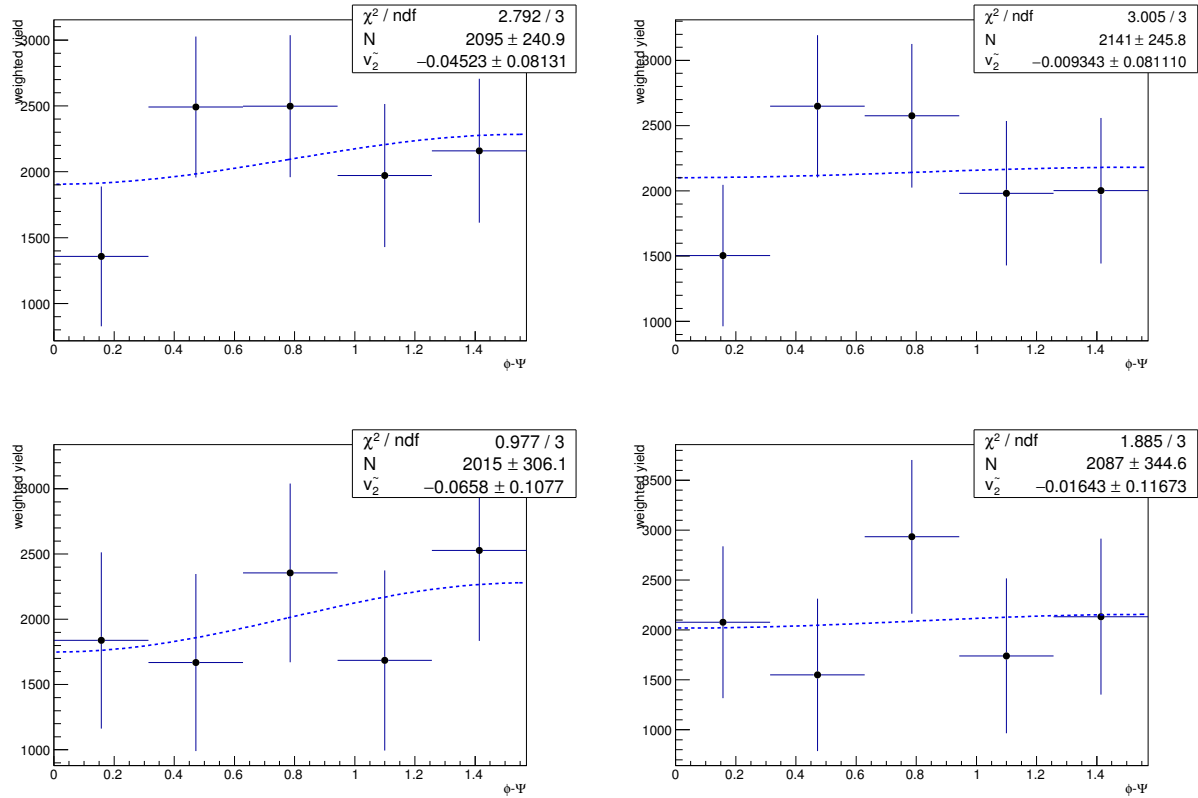


FIG. 80: yield vs. dPhi and $v_{2\text{observe}}$ fit, with yield from fit with standard range (top left), fit from narrower range (top right), side band with standard range (bottom left) and side band with narrower range (bottom right)

standard geometry cuts, p_T 1-2 GeV/c

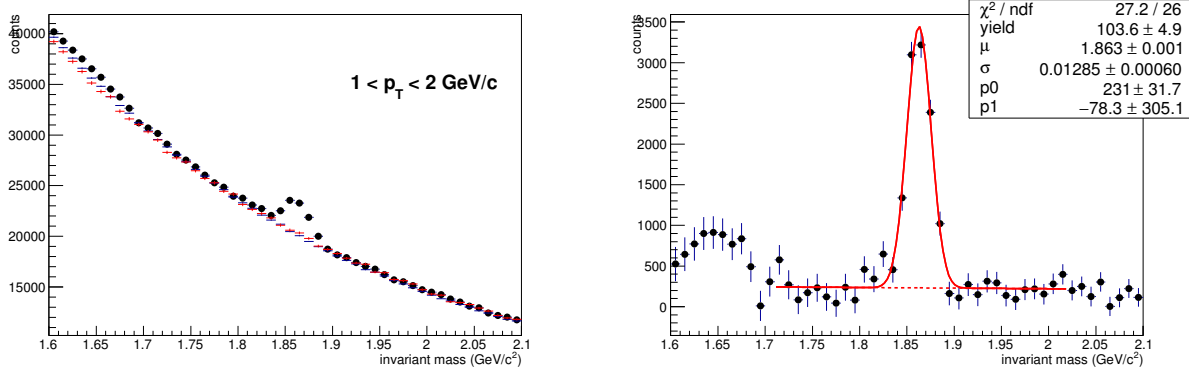


FIG. 81: $K\pi$ invariant mass distribution, left: unlike sign, like sign and scaled mixed event; right: unlike sign - mixed event

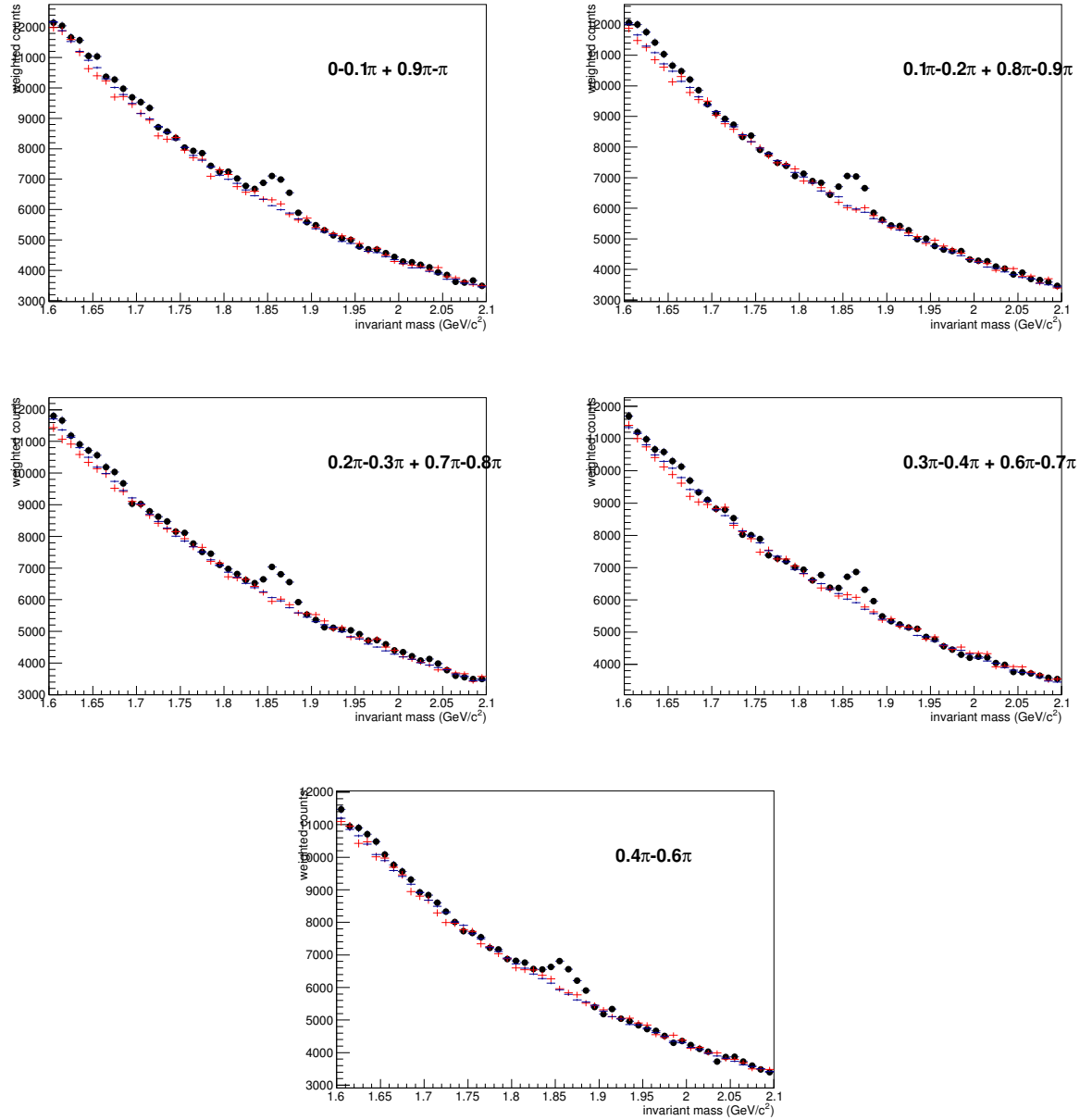


FIG. 82: $K\pi$ invariant mass in different $\phi - \Psi$ bins

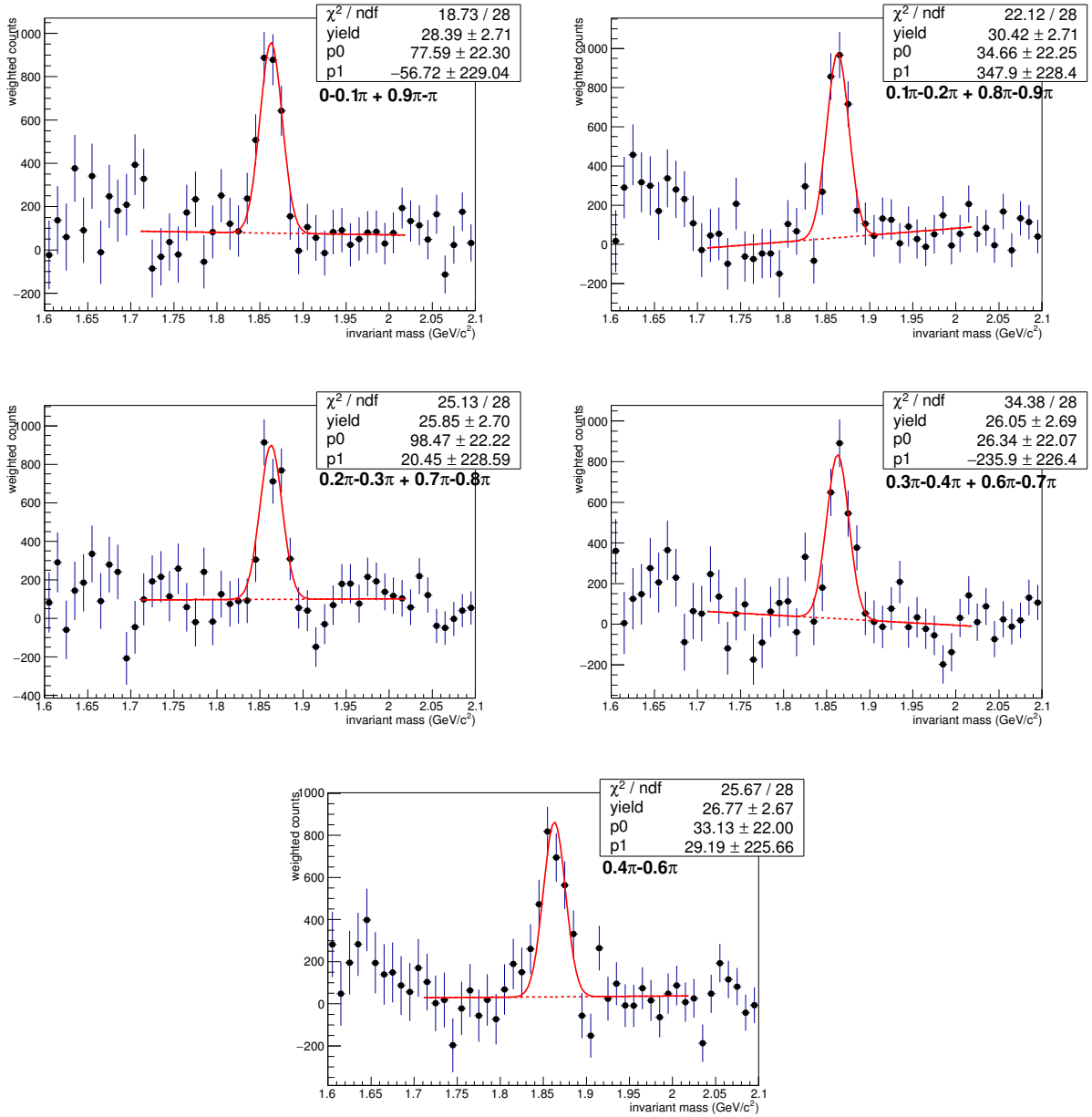


FIG. 83: $K\pi$ pairs invariant mass unlike sign - mixed event in different $\phi - \Psi$ bins, default fit range

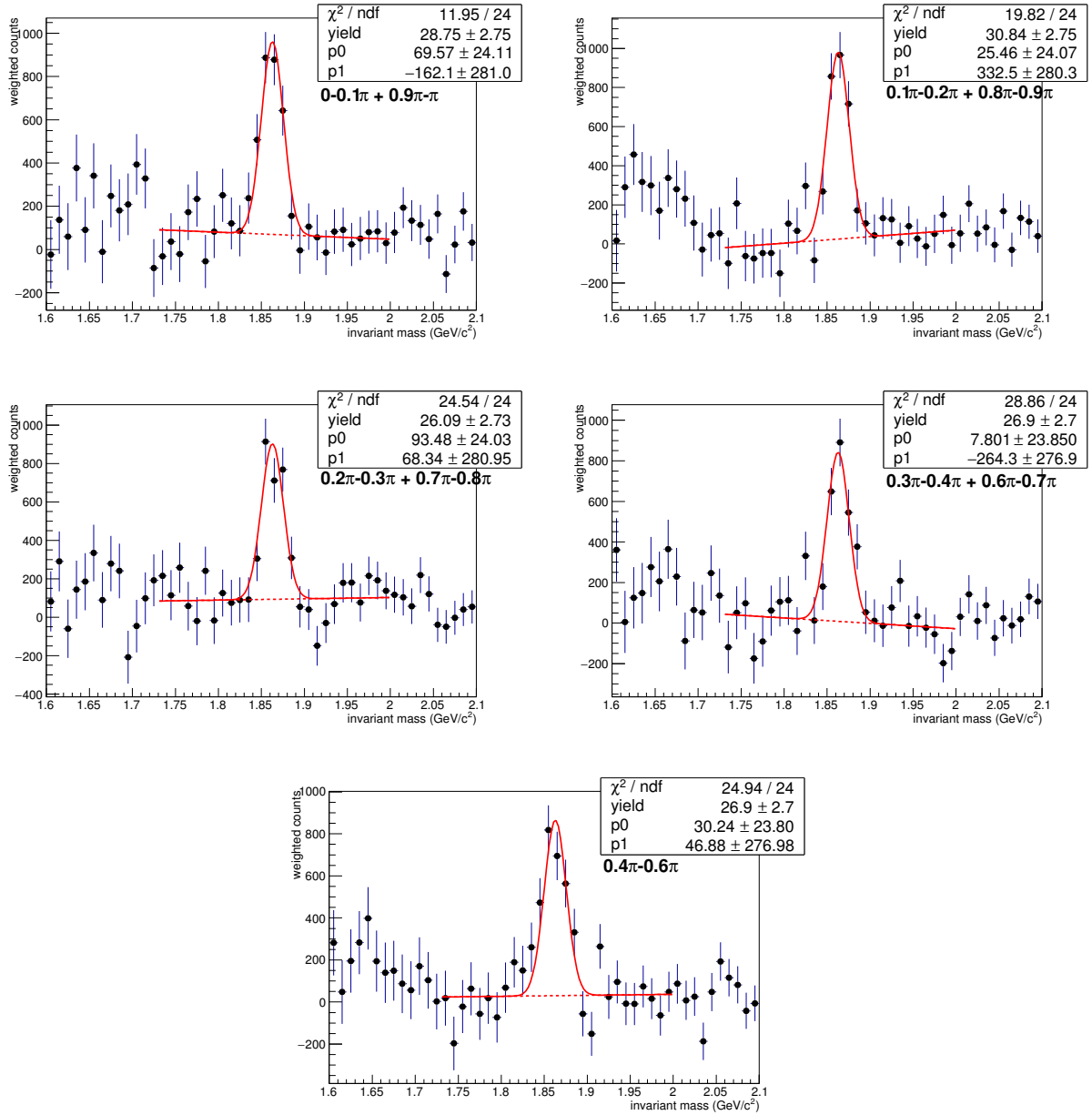


FIG. 84: $K\pi$ pairs invariant mass unlike sign - mixed event in different $\phi - \Psi$ bins, narrower fit range

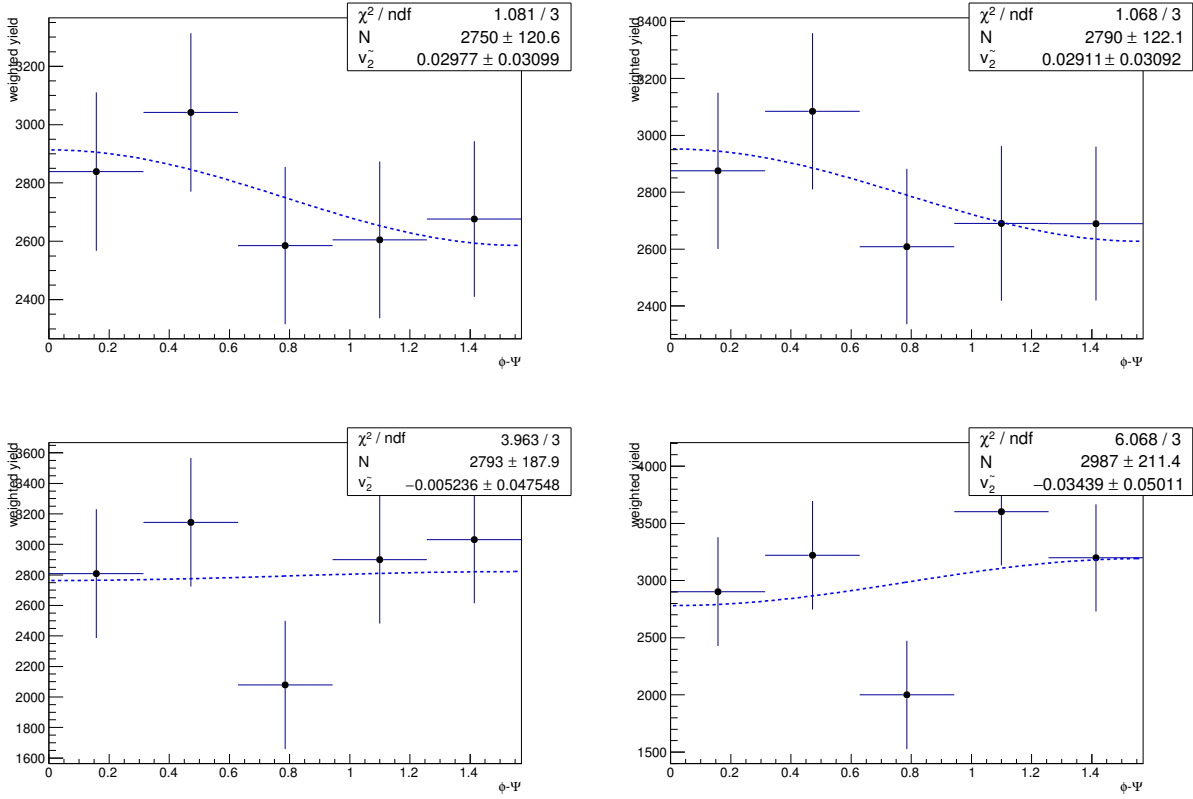


FIG. 85: yield vs. dPhi and $v_{2\text{observe}}$ fit, with yield from fit with standard range (top left), fit from narrower range (top right), side band with standard range (bottom left) and side band with narrower range (bottom right)

standard geometry cuts, p_T 2-3 GeV/c

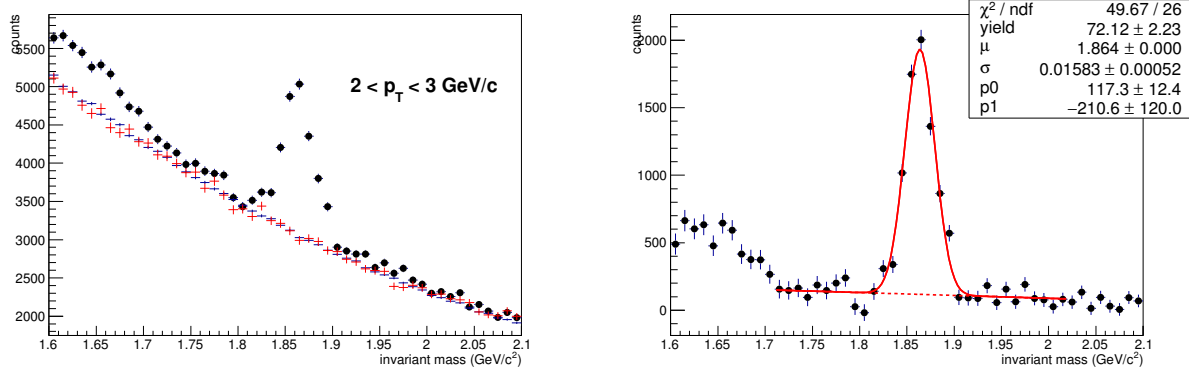


FIG. 86: $K\pi$ invariant mass distribution, left: unlike sign, like sign and scaled mixed event; right: unlike sign - mixed event

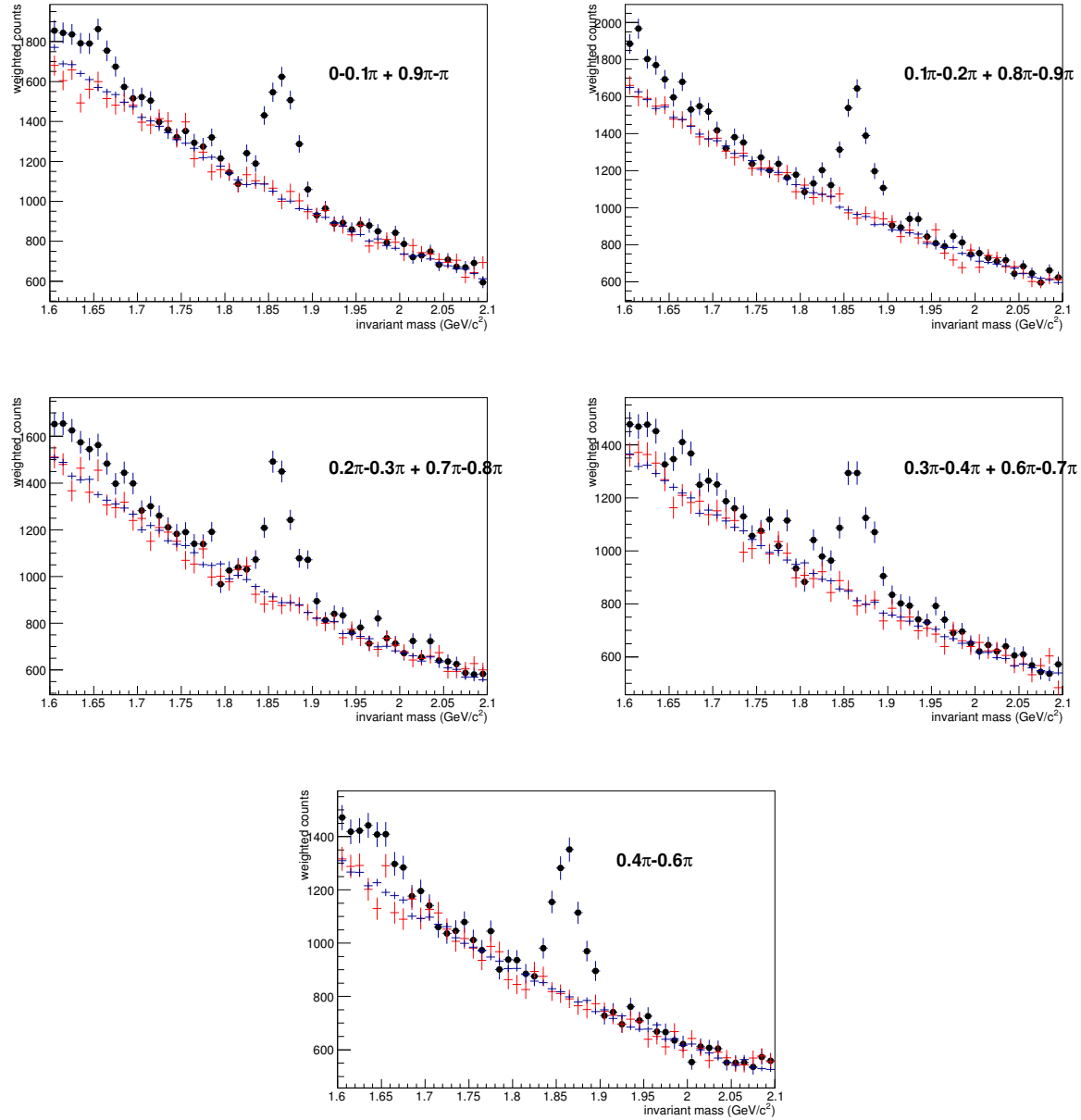


FIG. 87: $K\pi$ invariant mass in different $\phi - \Psi$ bins

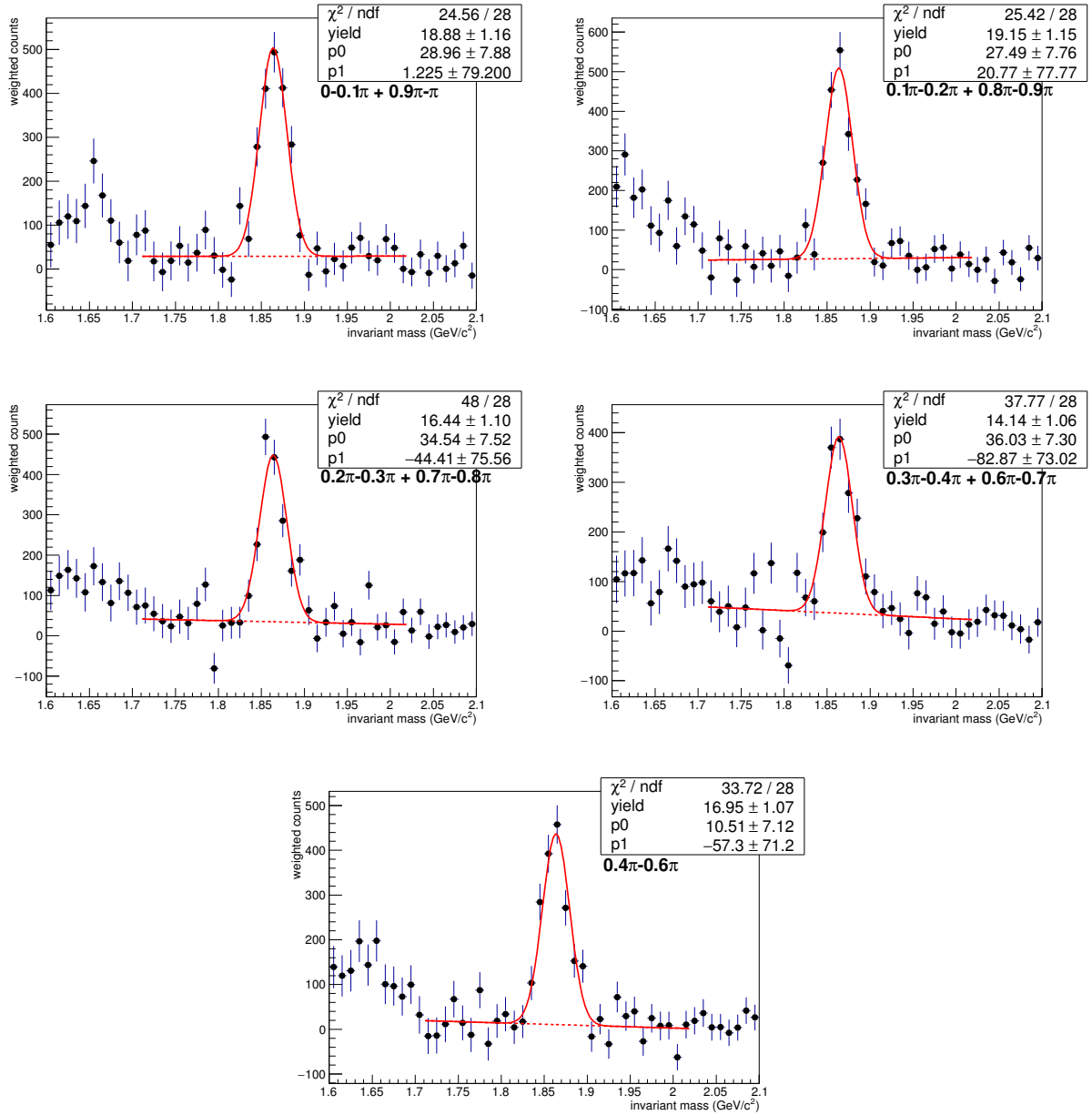


FIG. 88: $K\pi$ pairs invariant mass unlike sign - mixed event in different $\phi - \Psi$ bins, default fit range

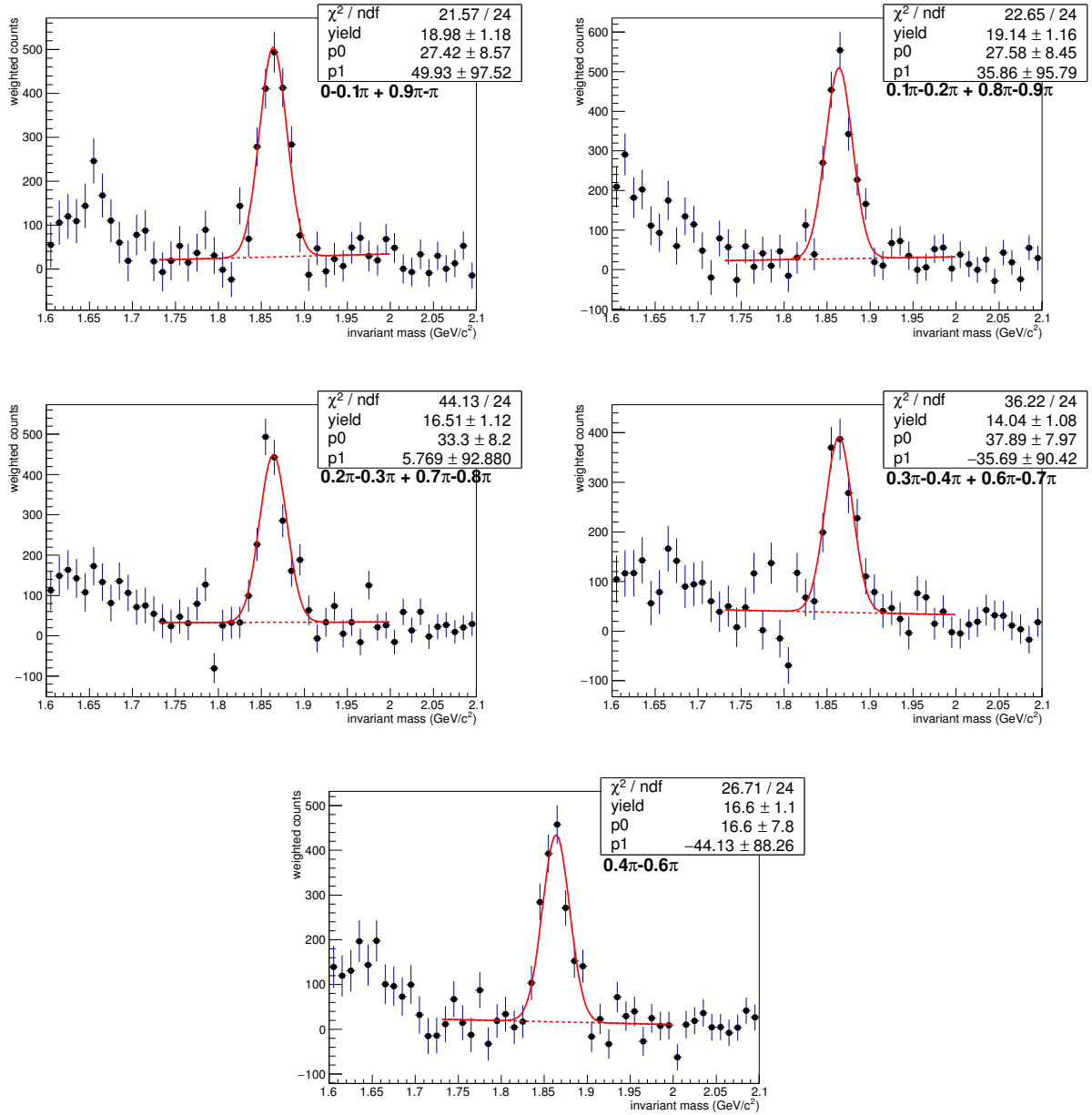


FIG. 89: $K\pi$ pairs invariant mass unlike sign - mixed event in different $\phi - \Psi$ bins, narrower fit range

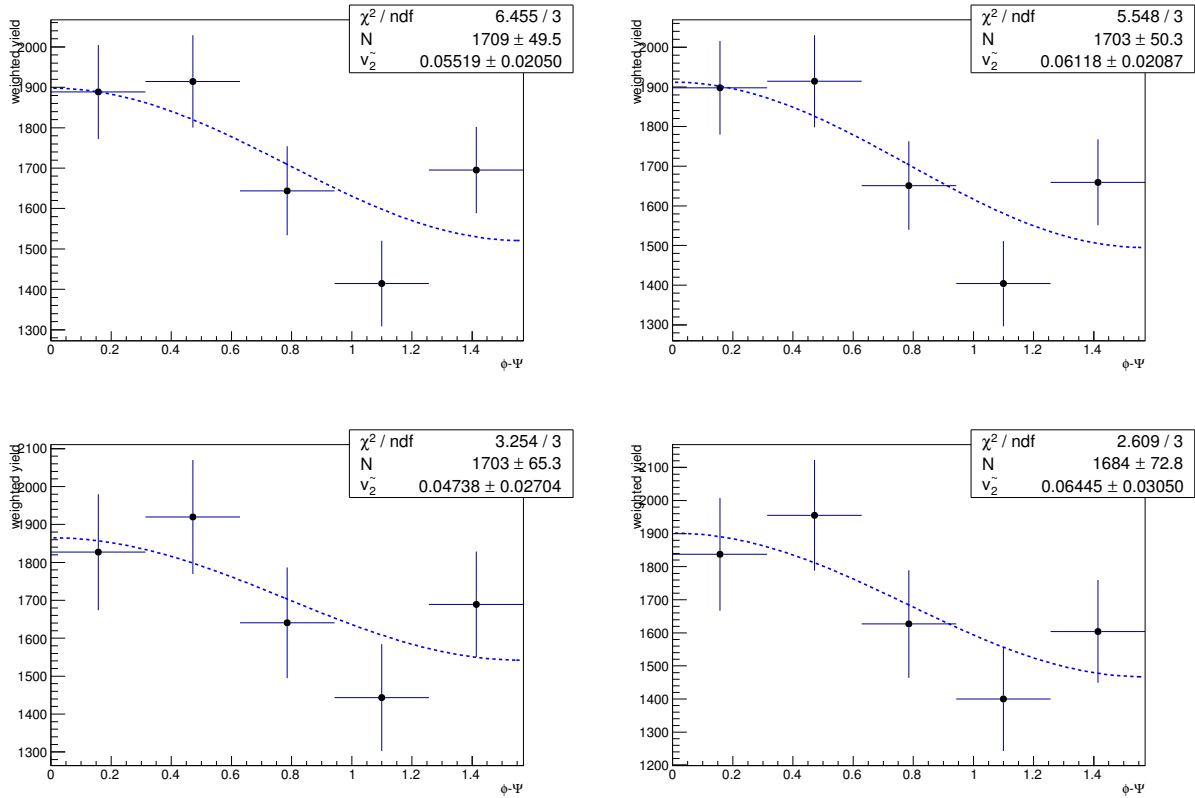


FIG. 90: yield vs. dPhi and $v_{2\text{observe}}$ fit, with yield from fit with standard range (top left), fit from narrower range (top right), side band with standard range (bottom left) and side band with narrower range (bottom right)

standard geometry cuts, p_T 3-4 GeV/c

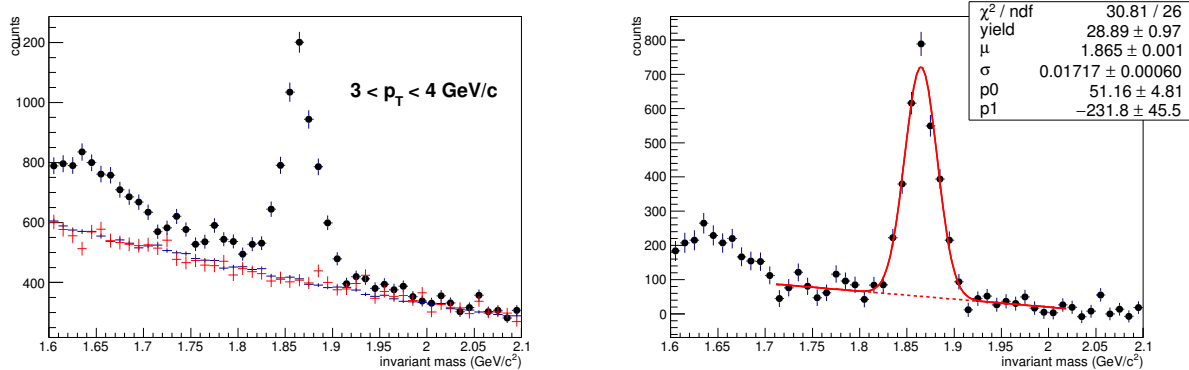


FIG. 91: $K\pi$ invariant mass distribution, left: unlike sign, like sign and scaled mixed event; right: unlike sign - mixed event

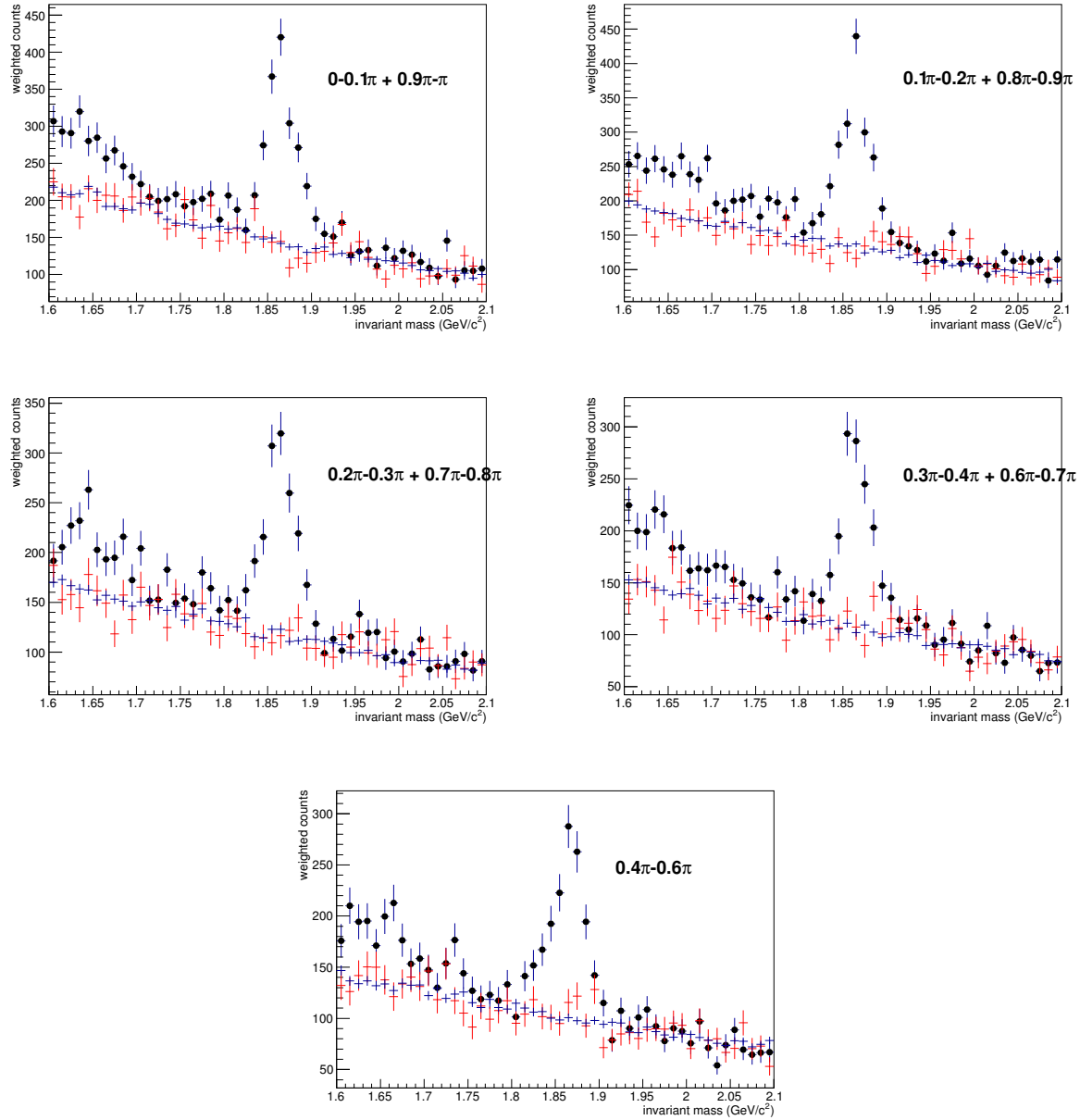


FIG. 92: $K\pi$ invariant mass in different $\phi - \Psi$ bins

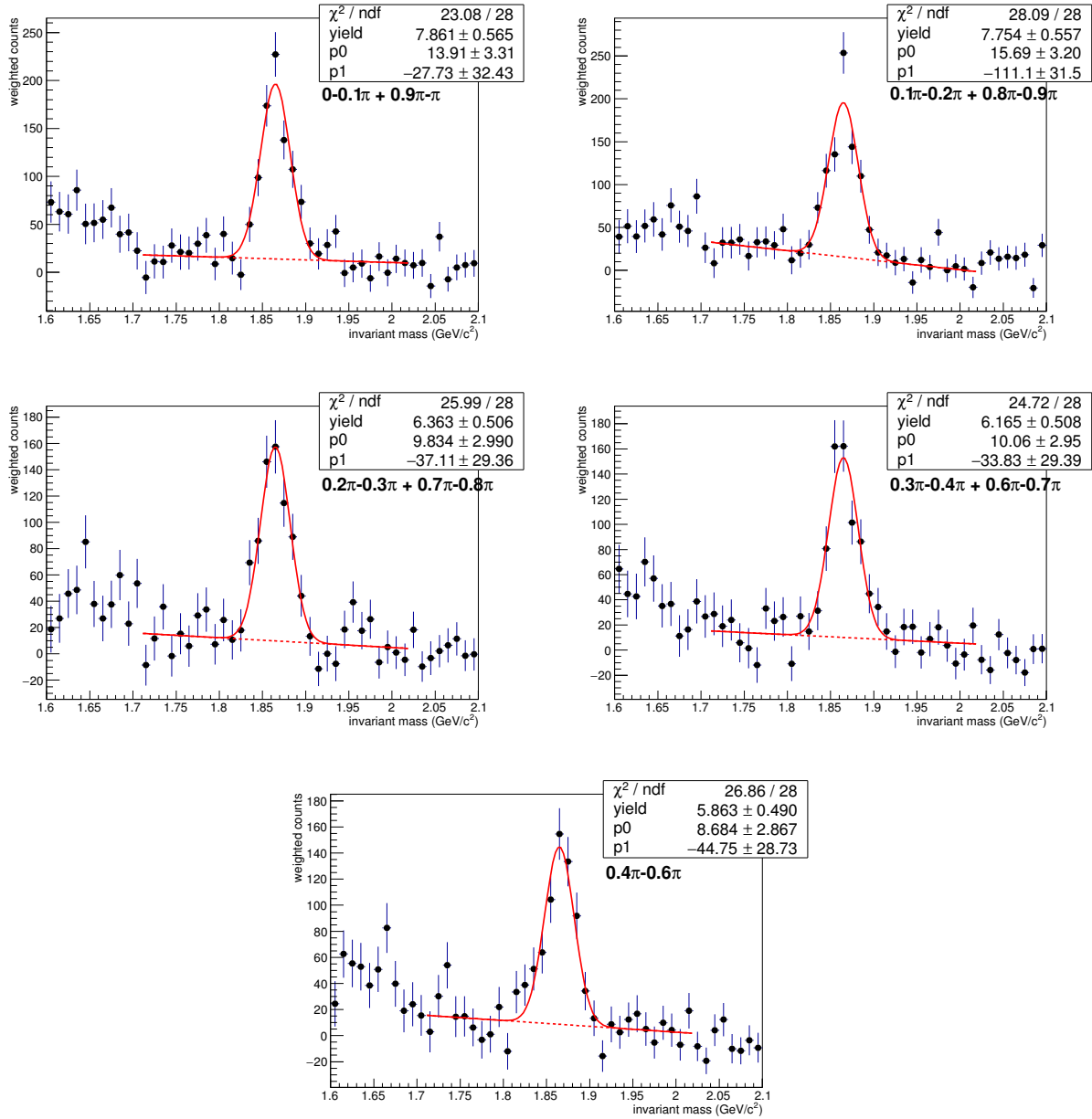


FIG. 93: $K\pi$ pairs invariant mass unlike sign - mixed event in different $\phi - \Psi$ bins, default fit range

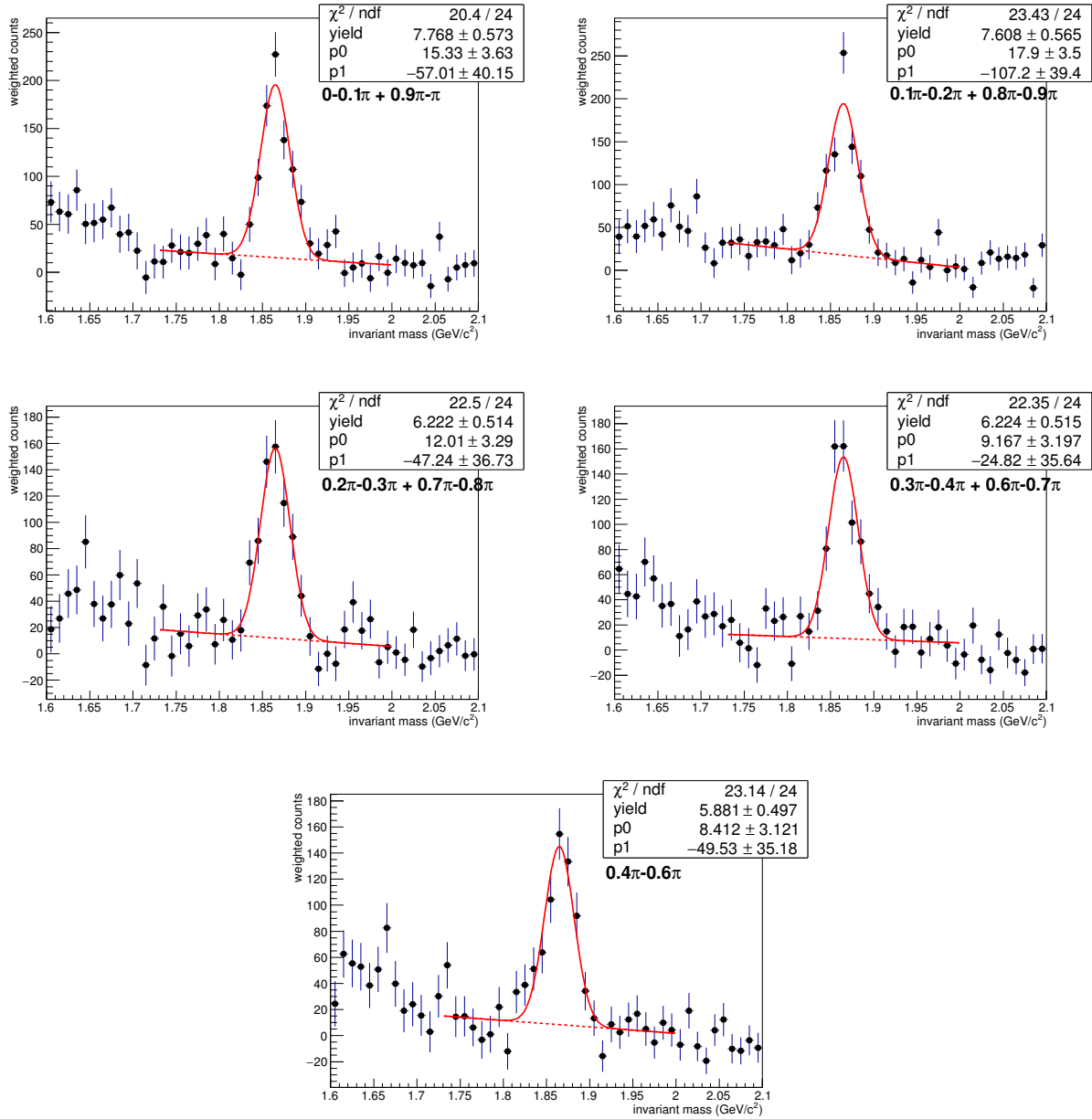


FIG. 94: $K\pi$ pairs invariant mass unlike sign - mixed event in different $\phi - \Psi$ bins, narrower fit range

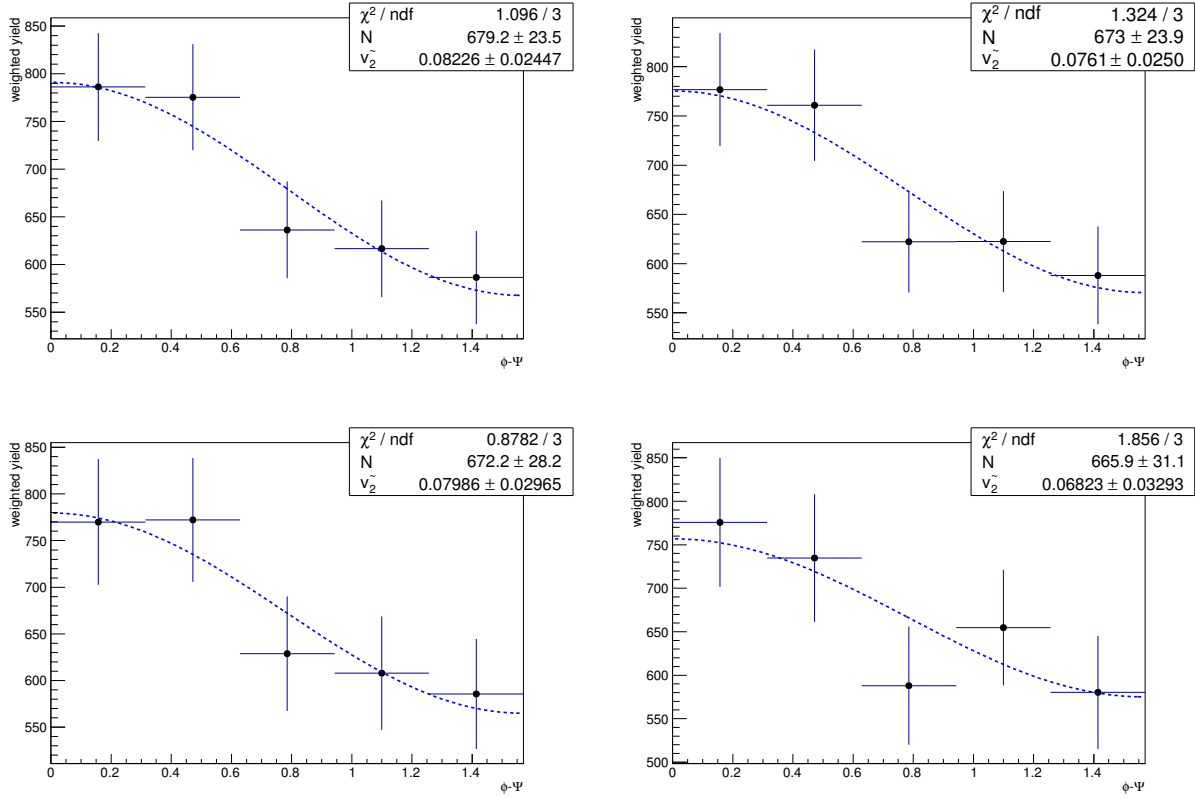


FIG. 95: yield vs. dPhi and $v_{2\text{observe}}$ fit, with yield from fit with standard range (top left), fit from narrower range (top right), side band with standard range (bottom left) and side band with narrower range (bottom right)

standard geometry cuts, p_T 4-5 GeV/c

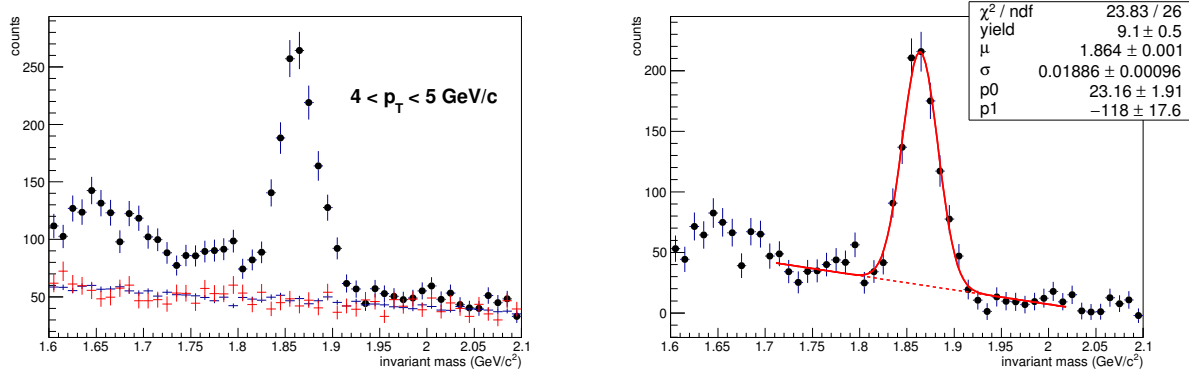


FIG. 96: $K\pi$ invariant mass distribution, left: unlike sign, like sign and scaled mixed event; right: unlike sign - mixed event

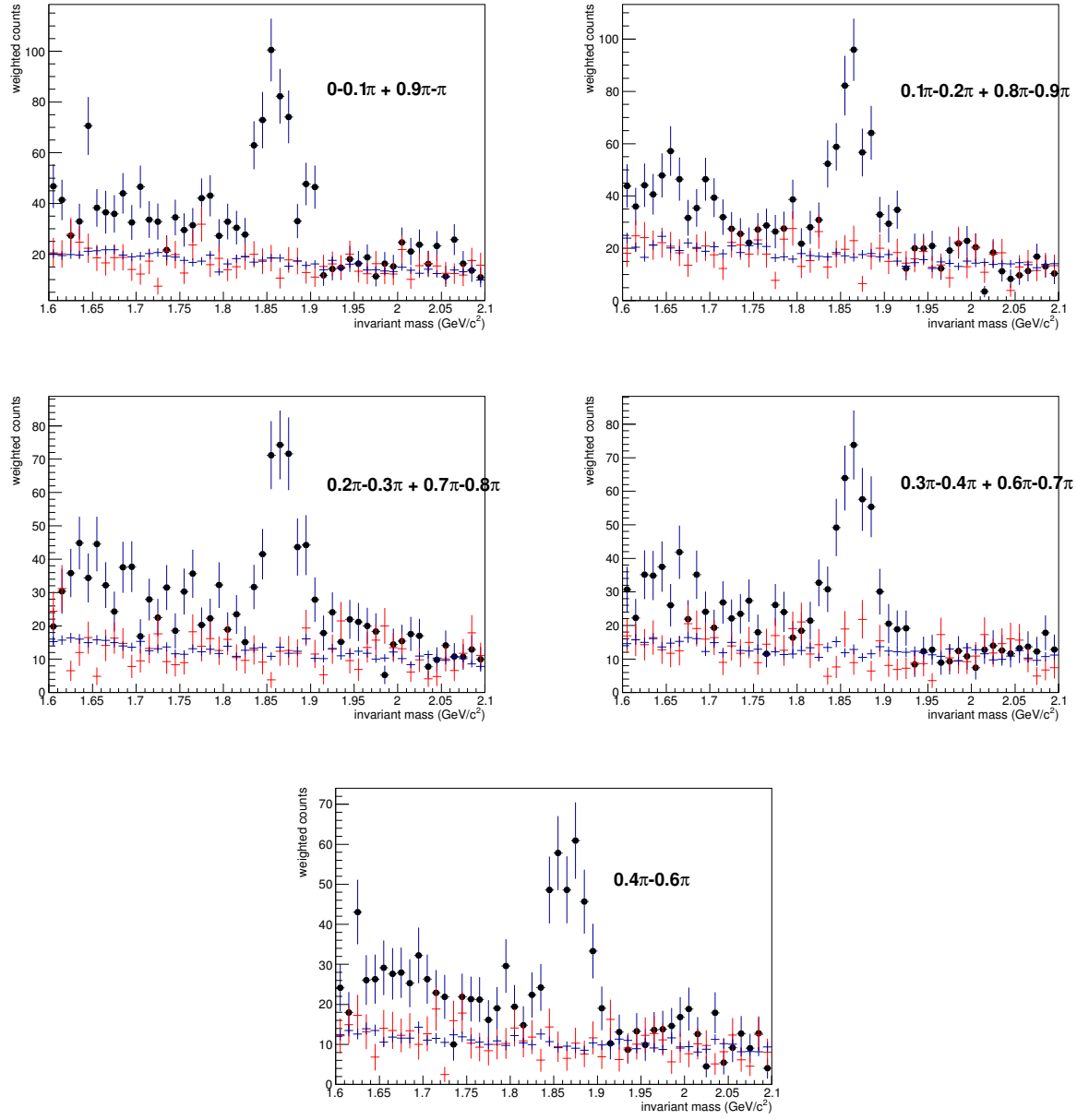


FIG. 97: $K\pi$ invariant mass in different $\phi - \Psi$ bins

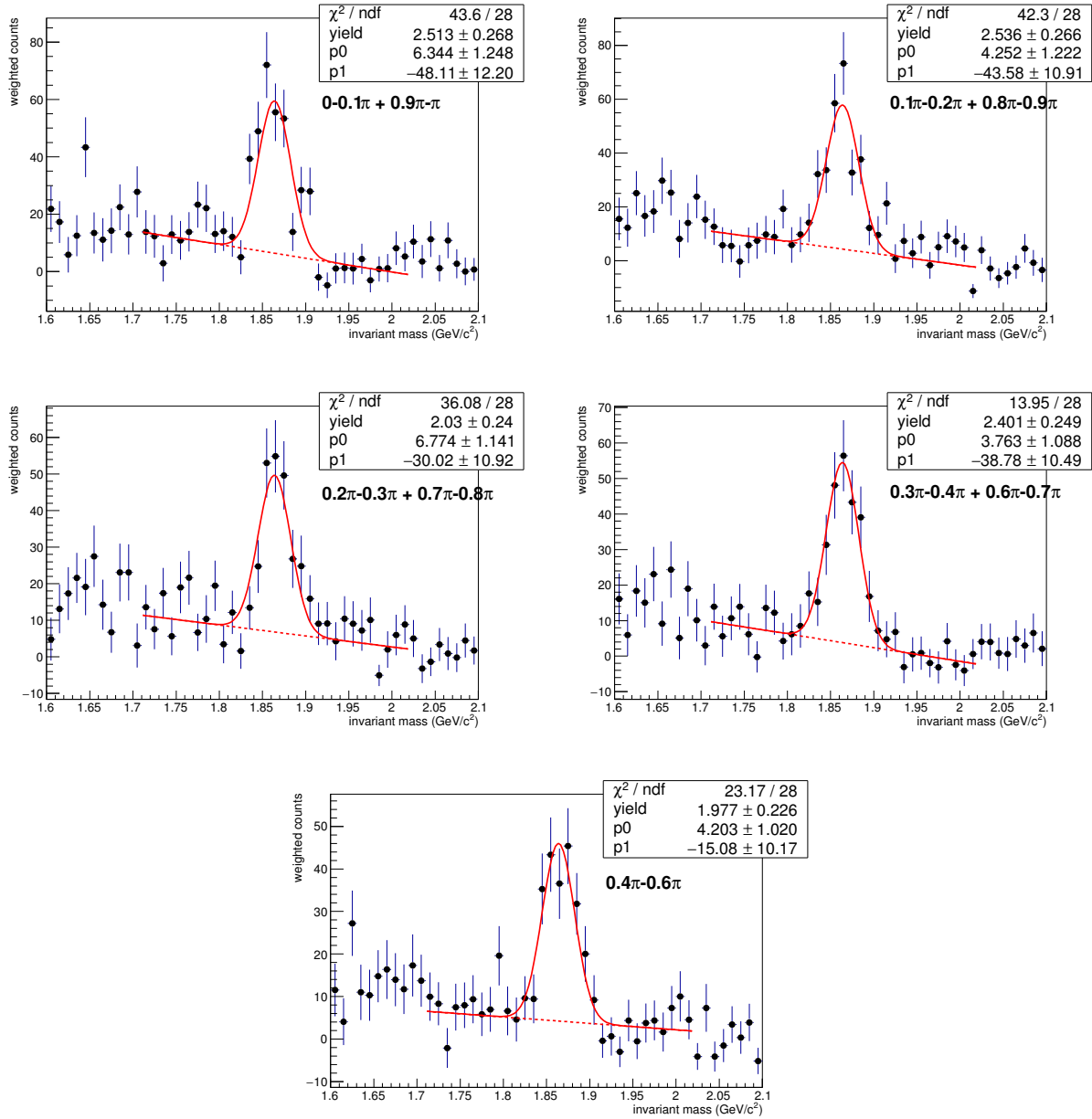


FIG. 98: $K\pi$ pairs invariant mass unlike sign - mixed event in different $\phi - \Psi$ bins, default fit range

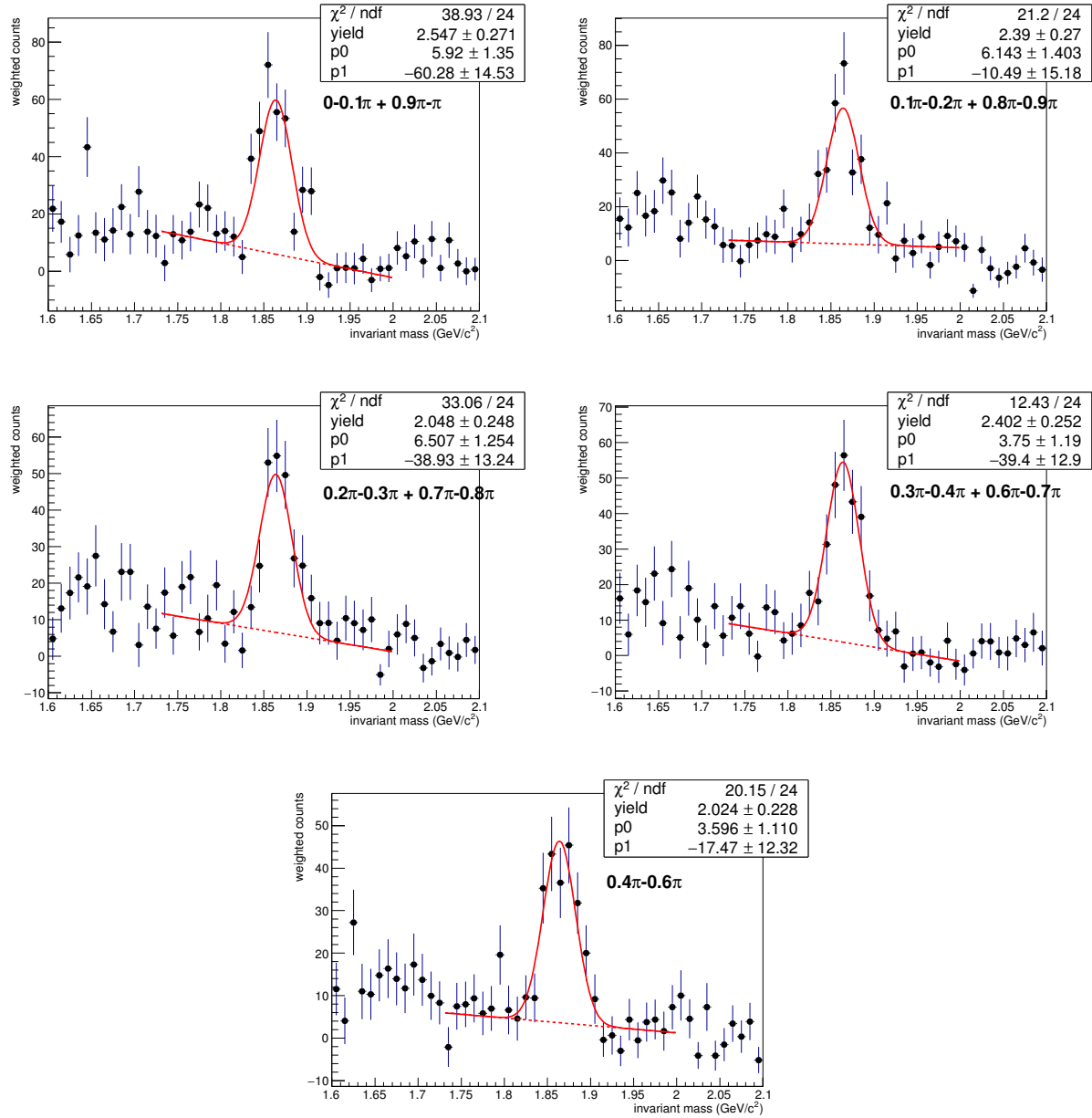


FIG. 99: $K\pi$ pairs invariant mass unlike sign - mixed event in different $\phi - \Psi$ bins, narrower fit range

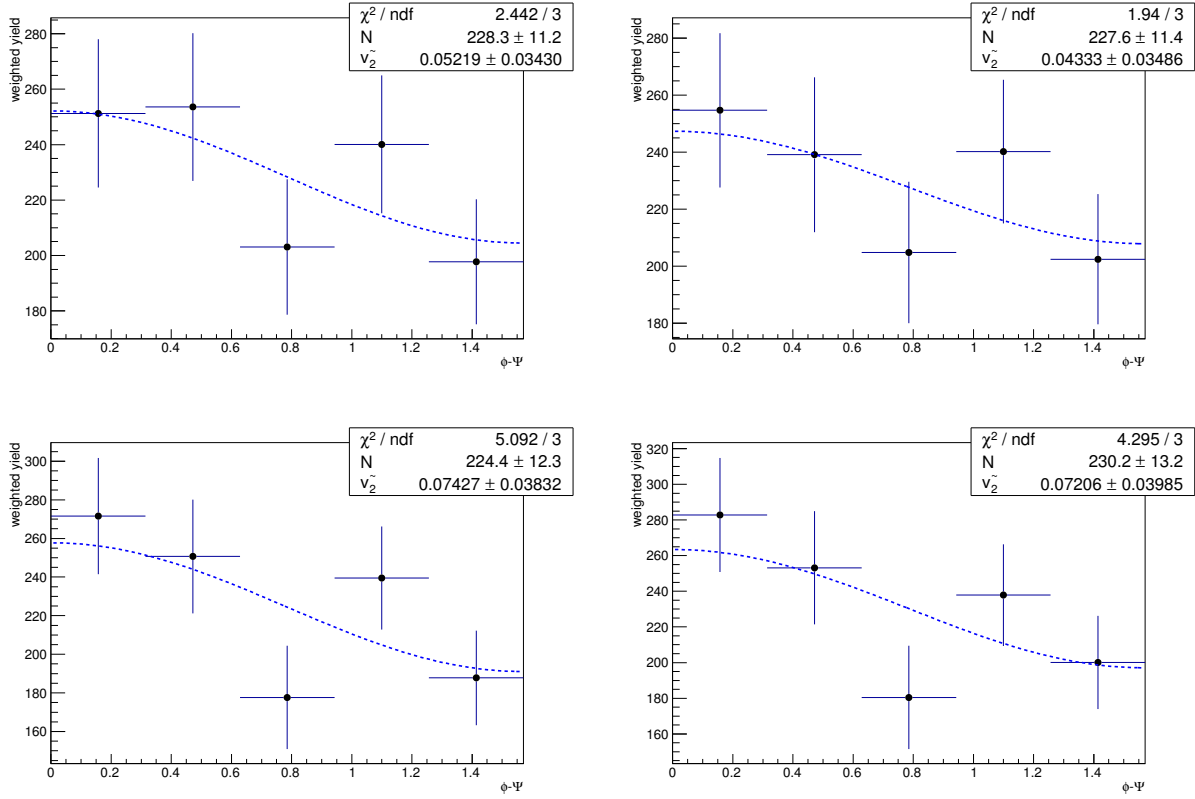


FIG. 100: yield vs. dPhi and $v_{2\text{observe}}$ fit, with yield from fit with standard range (top left), fit from narrower range (top right), side band with standard range (bottom left) and side band with narrower range (bottom right)

standard geometry cuts, p_T 5-10 GeV/c

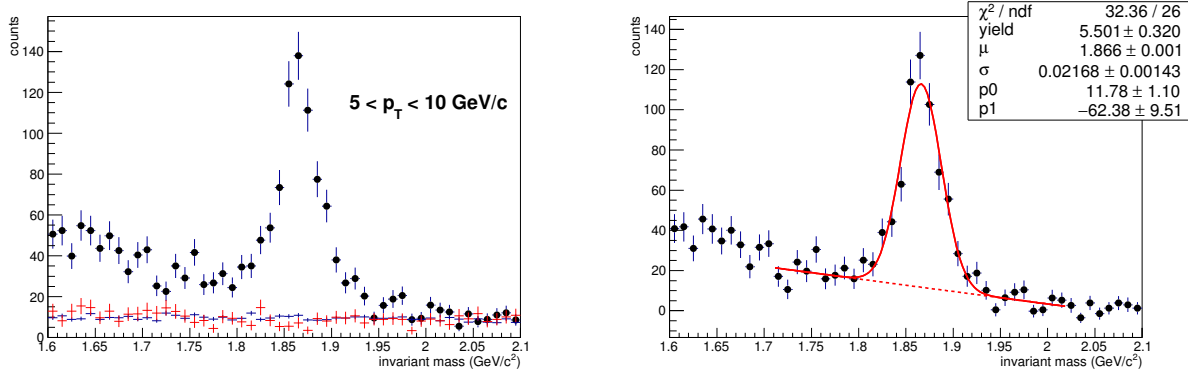


FIG. 101: $K\pi$ invariant mass distribution, left: unlike sign, like sign and scaled mixed event;
right: unlike sign - mixed event

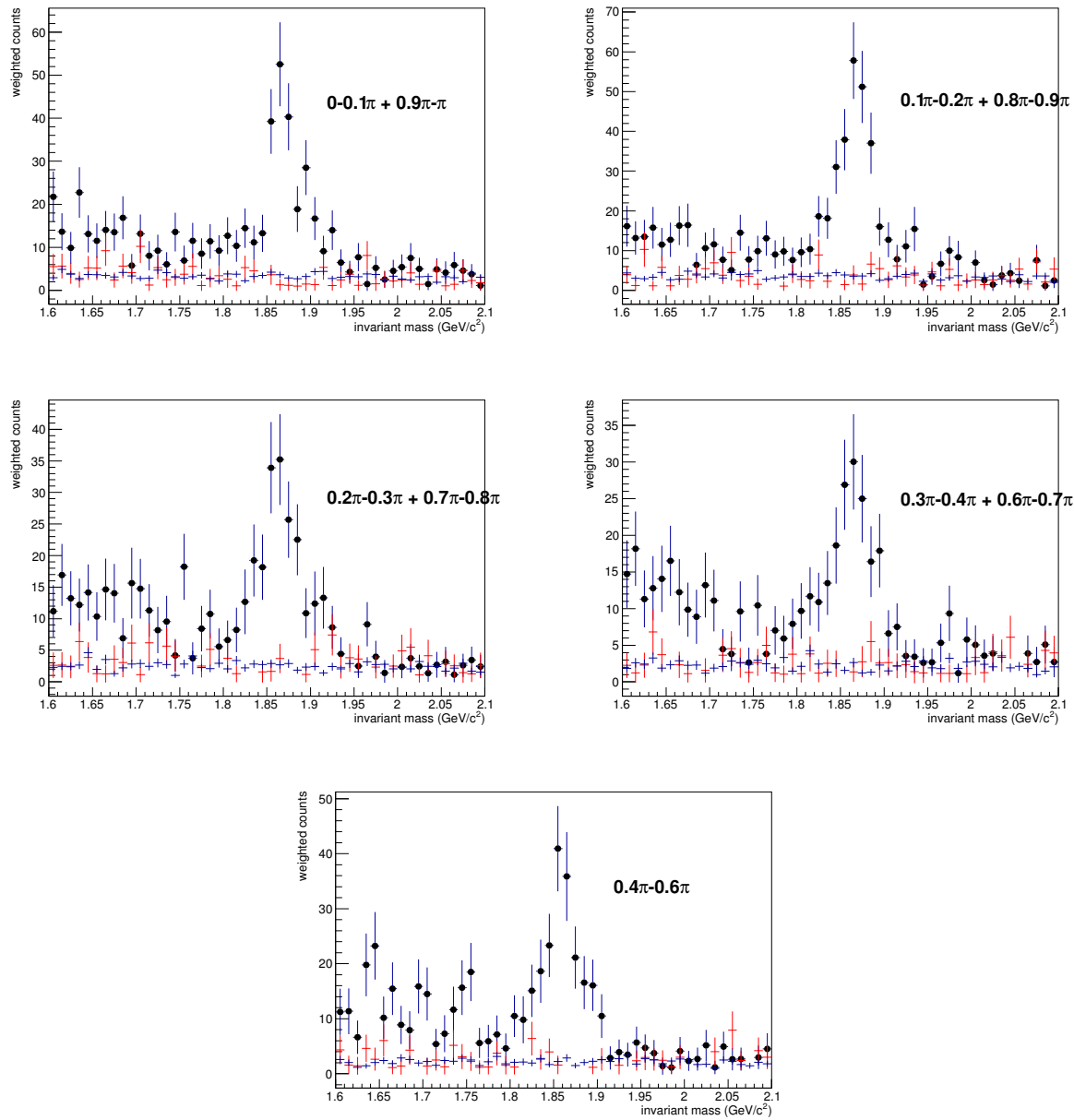


FIG. 102: $K\pi$ invariant mass in different $\phi - \Psi$ bins

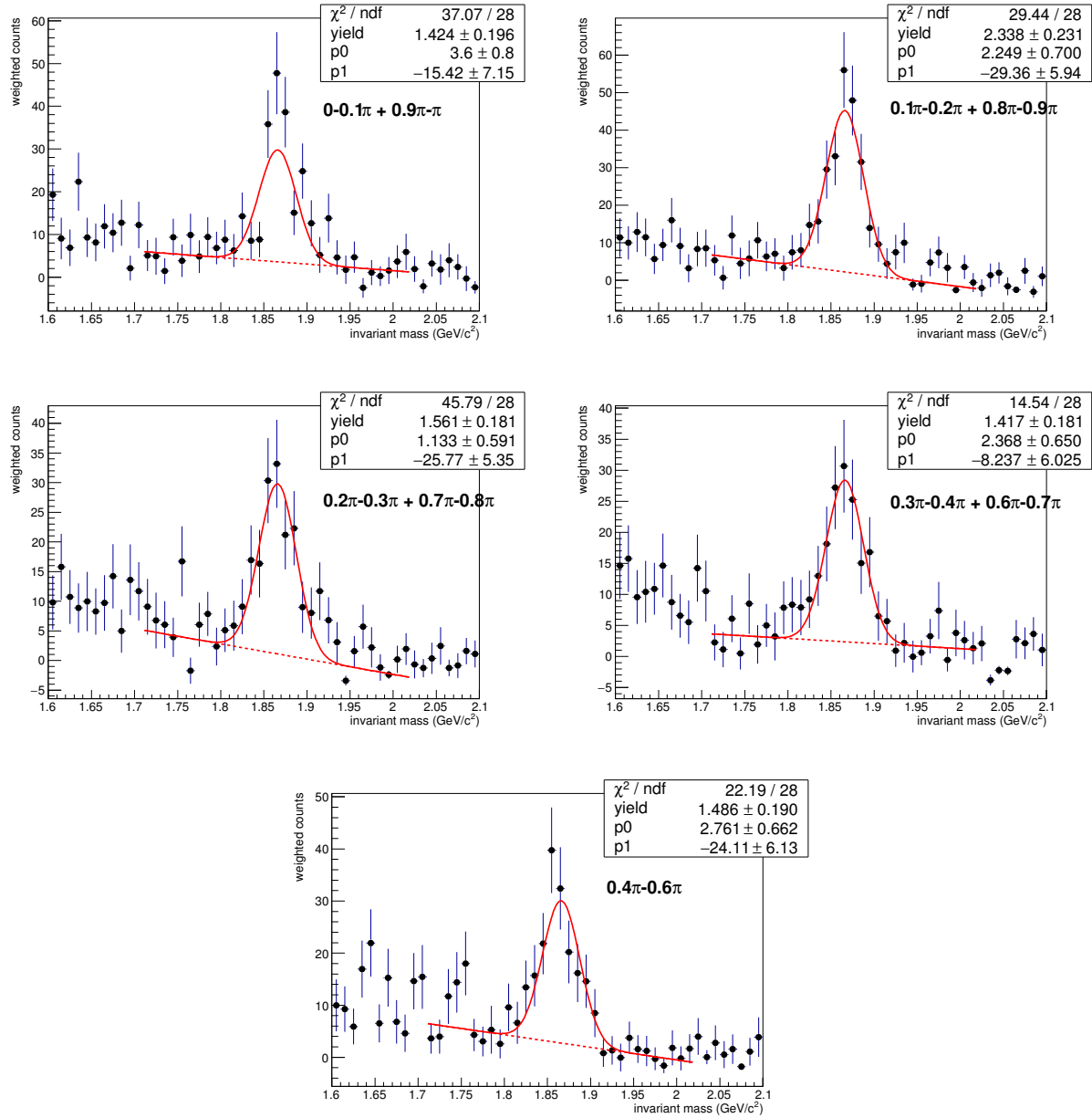


FIG. 103: $K\pi$ pairs invariant mass unlike sign - mixed event in different $\phi - \Psi$ bins, default fit range

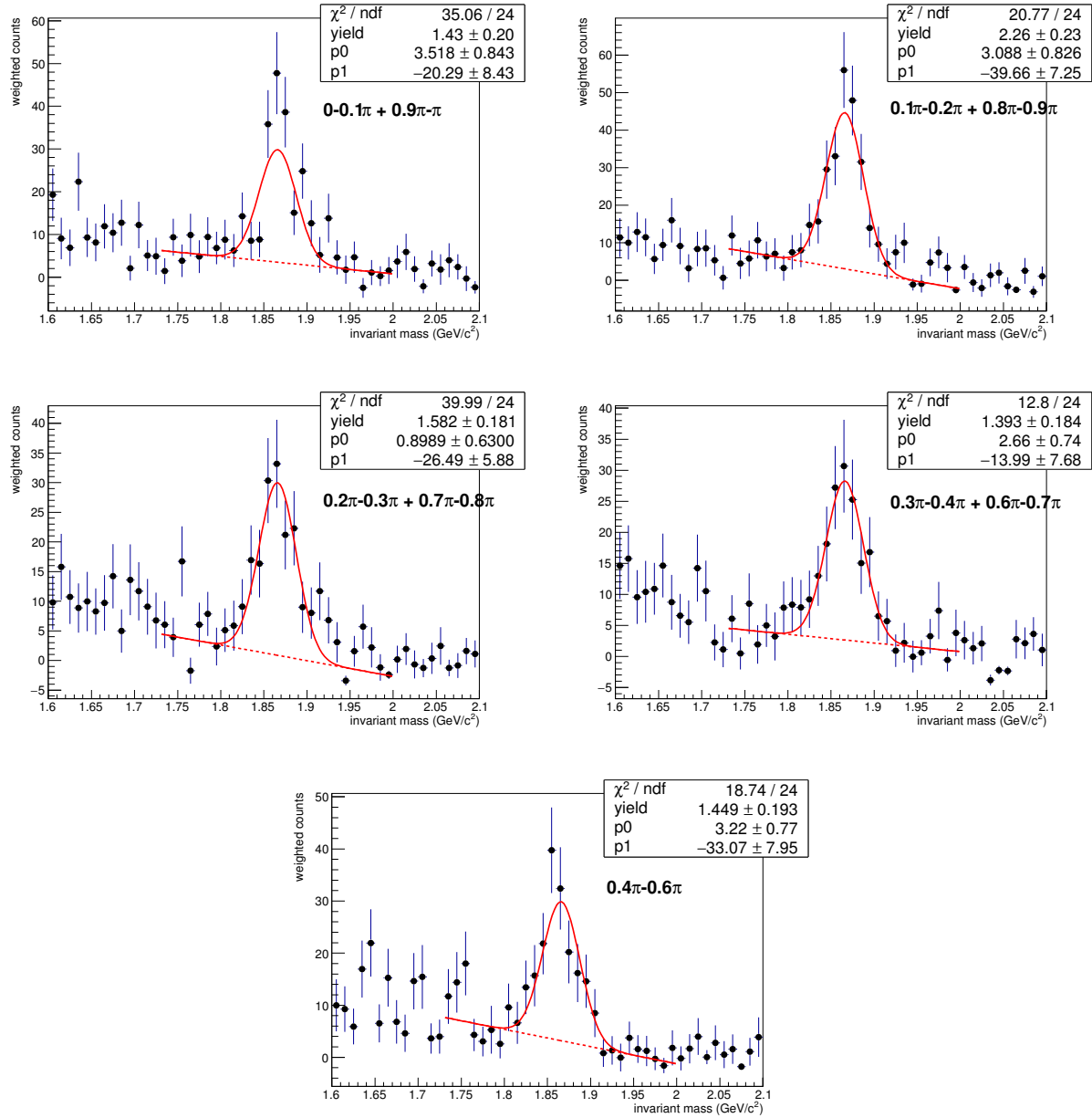


FIG. 104: $K\pi$ pairs invariant mass unlike sign - mixed event in different $\phi - \Psi$ bins, narrower fit range

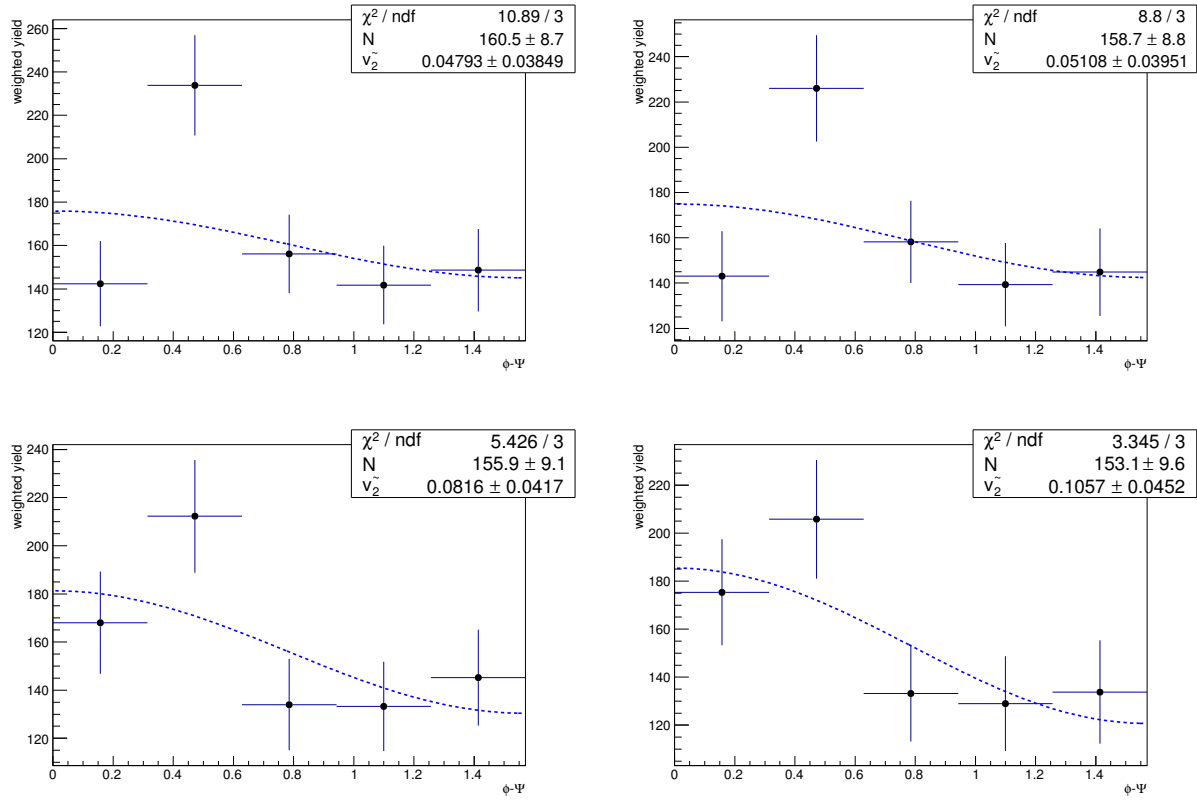


FIG. 105: yield vs. dPhi and $v_{2\text{observe}}$ fit, with yield from fit with standard range (top left), fit from narrower range (top right), side band with standard range (bottom left) and side band with narrower range (bottom right)

tight geometry cuts, p_T 0-1 GeV/c

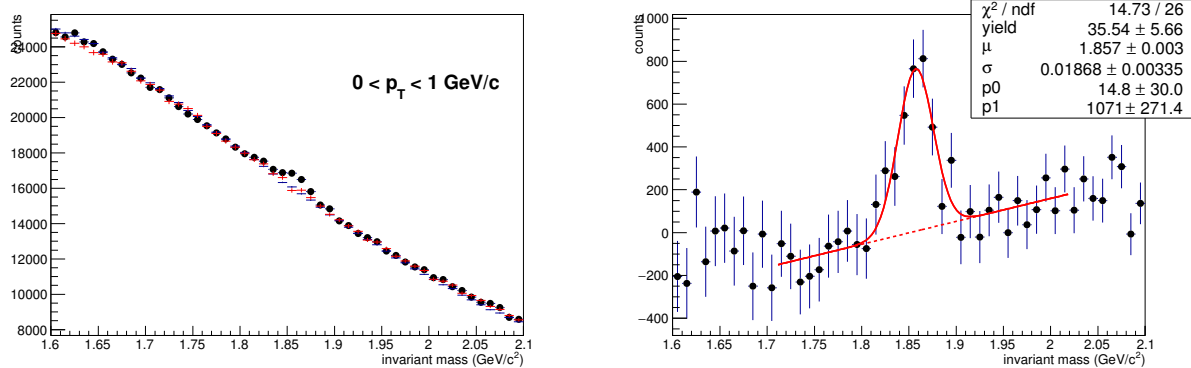
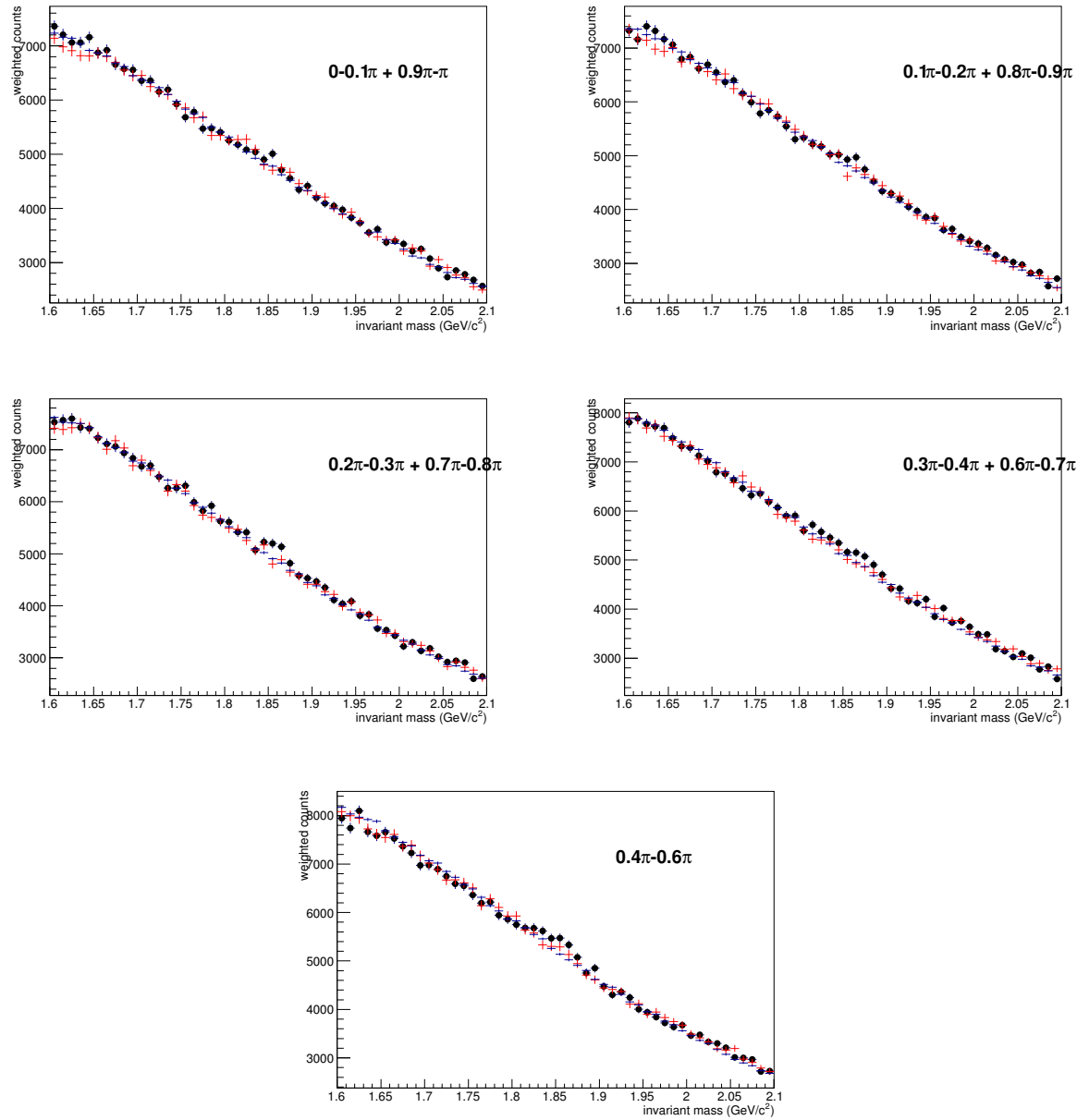


FIG. 106: $K\pi$ invariant mass distribution, left: unlike sign, like sign and scaled mixed event;
right: unlike sign - mixed event

FIG. 107: $K\pi$ invariant mass in different $\phi - \Psi$ bins

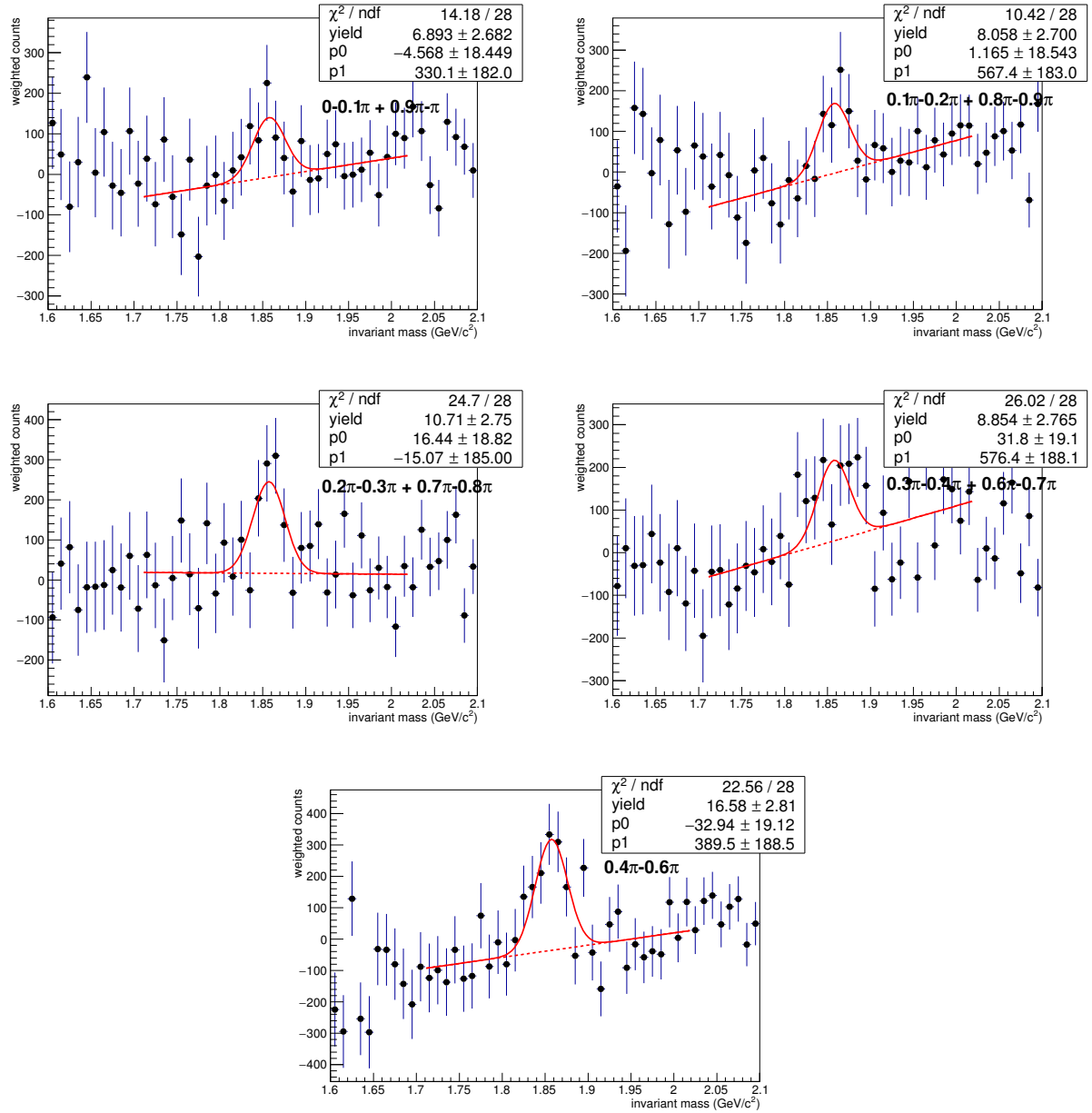


FIG. 108: $K\pi$ pairs invariant mass unlike sign - mixed event in different $\phi - \Psi$ bins, default fit range

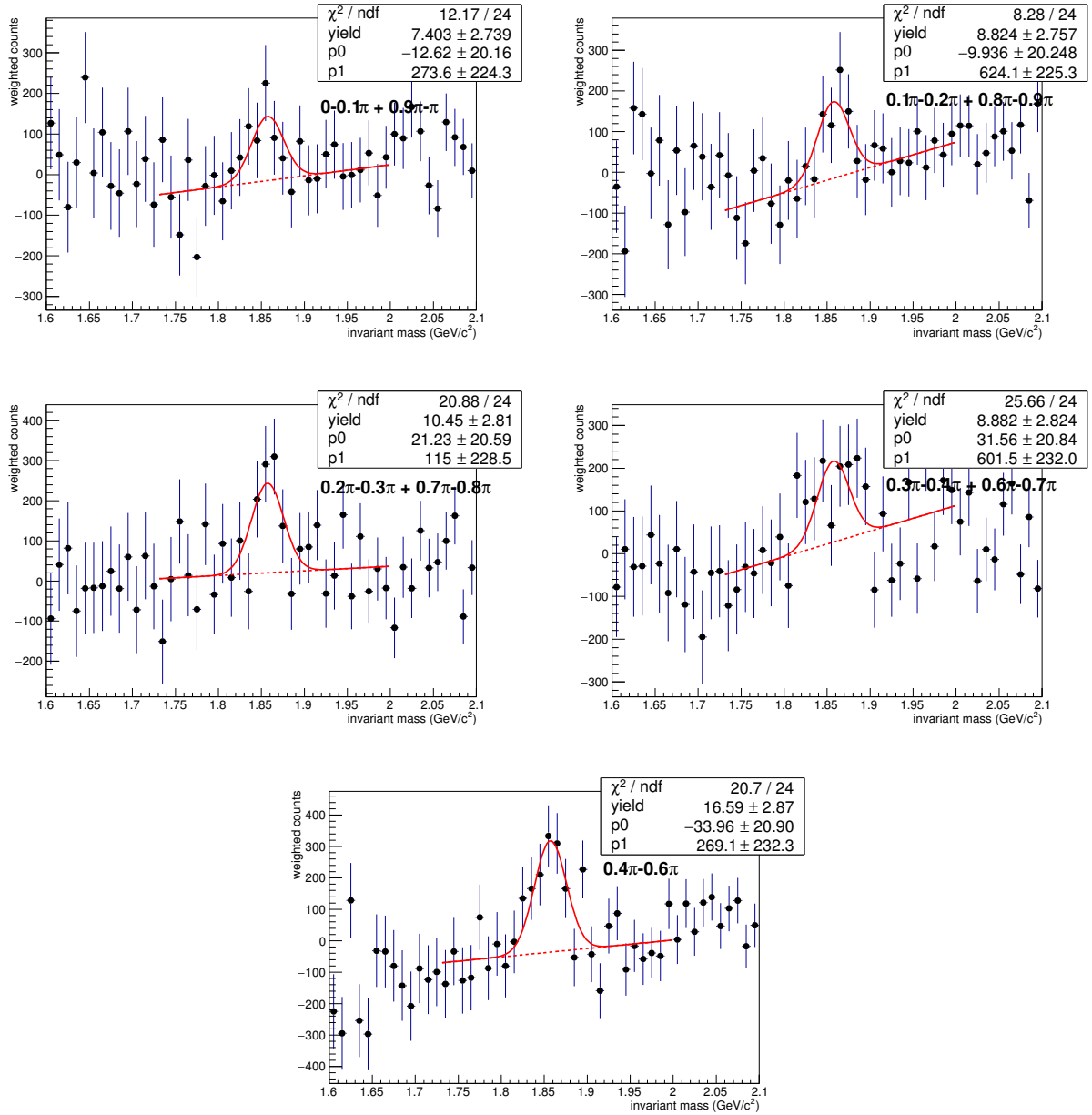


FIG. 109: $K\pi$ pairs invariant mass unlike sign - mixed event in different $\phi - \Psi$ bins, narrower fit range

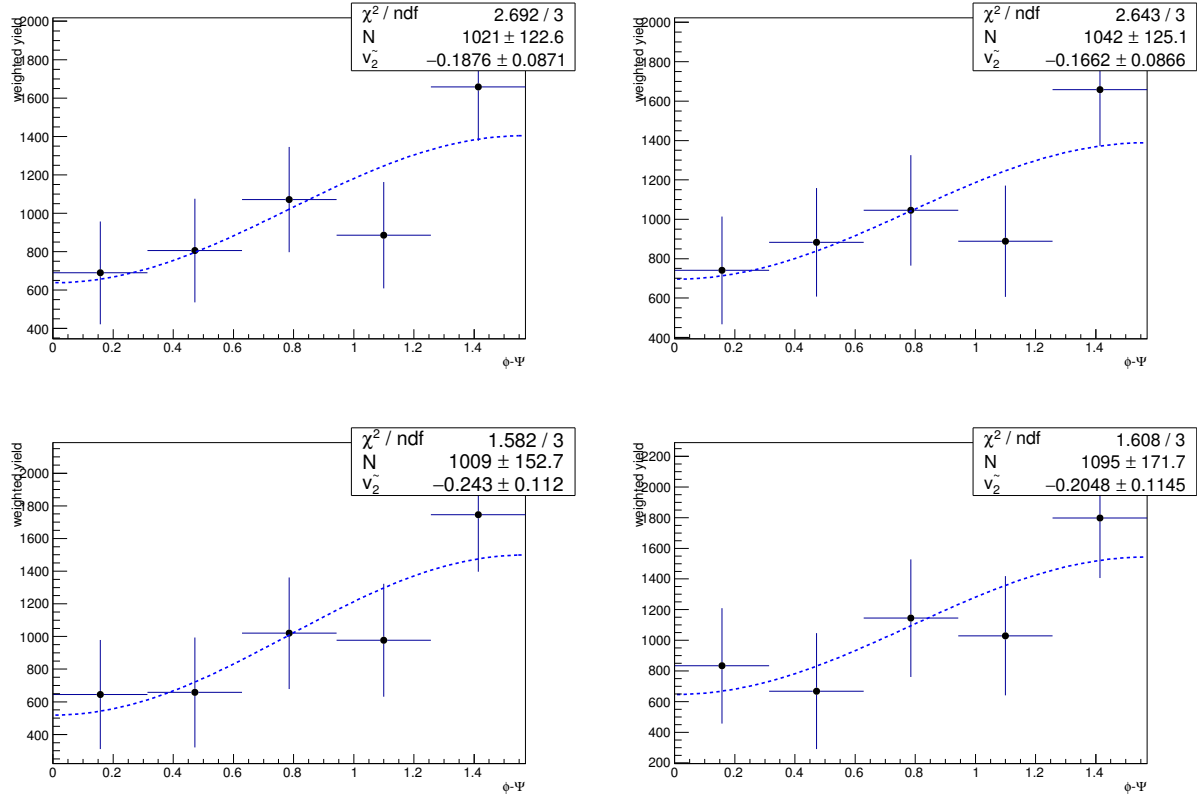


FIG. 110: yield vs. dPhi and $v_{2\text{observe}}$ fit, with yield from fit with standard range (top left), fit from narrower range (top right), side band with standard range (bottom left) and side band with narrower range (bottom right)

tight geometry cuts, p_T 1-2 GeV/c

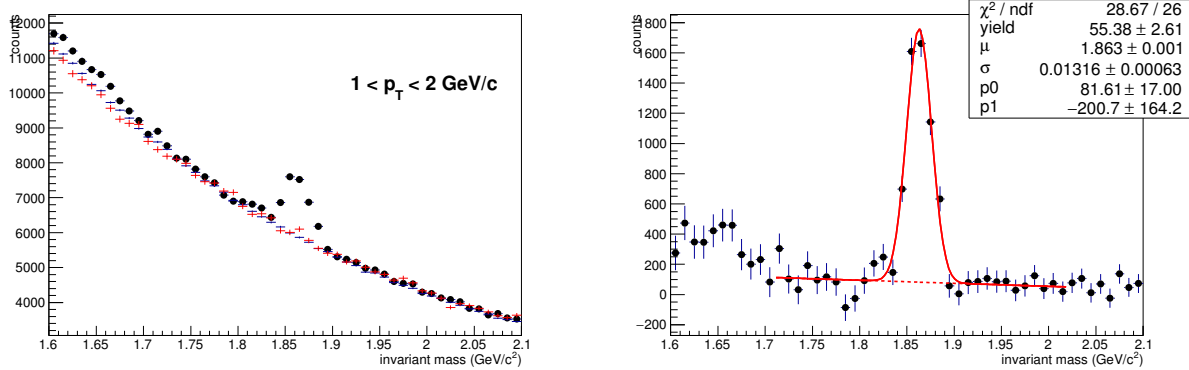
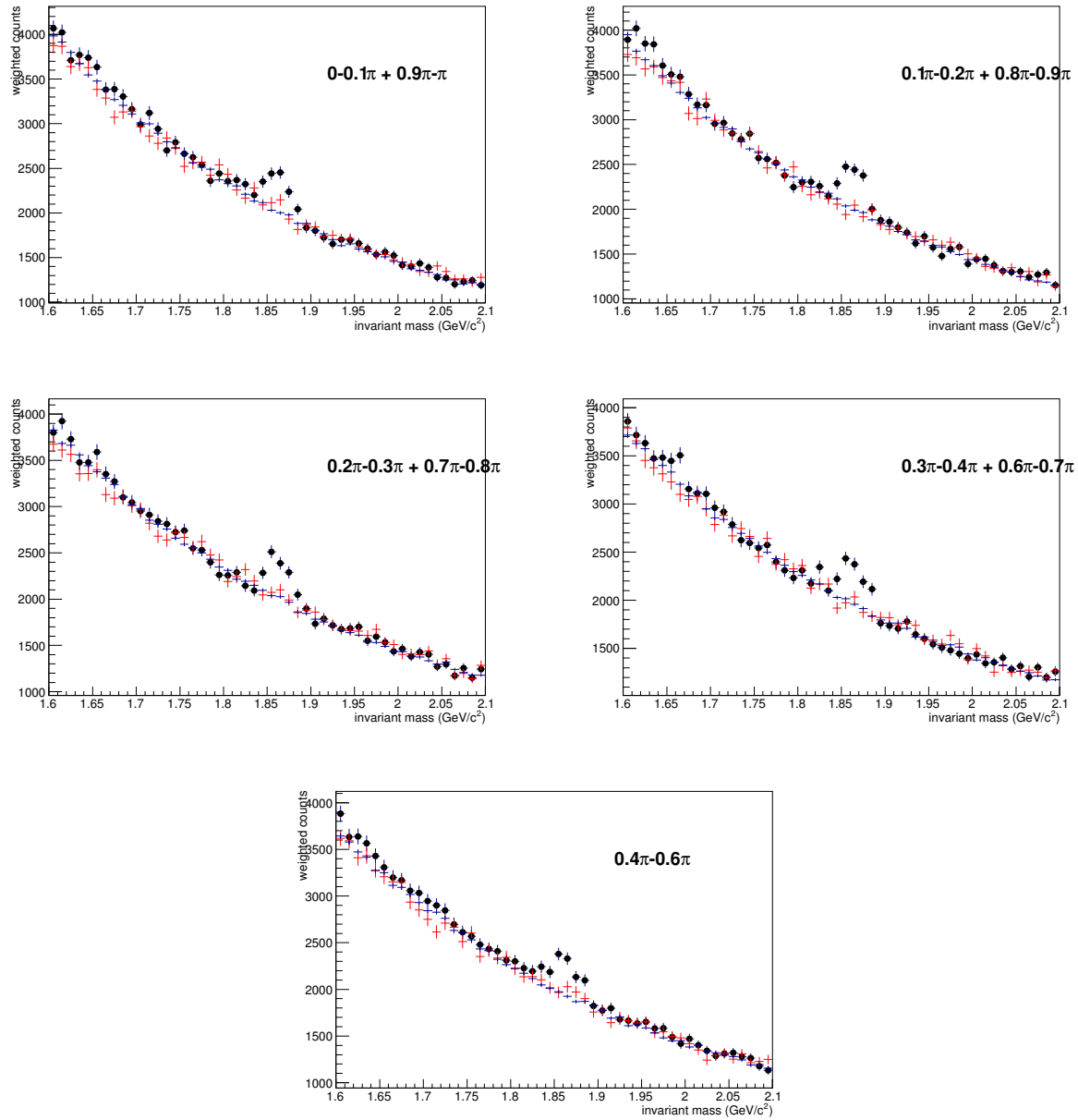


FIG. 111: $K\pi$ invariant mass distribution, left: unlike sign, like sign and scaled mixed event;
right: unlike sign - mixed event

FIG. 112: $K\pi$ invariant mass in different $\phi - \Psi$ bins

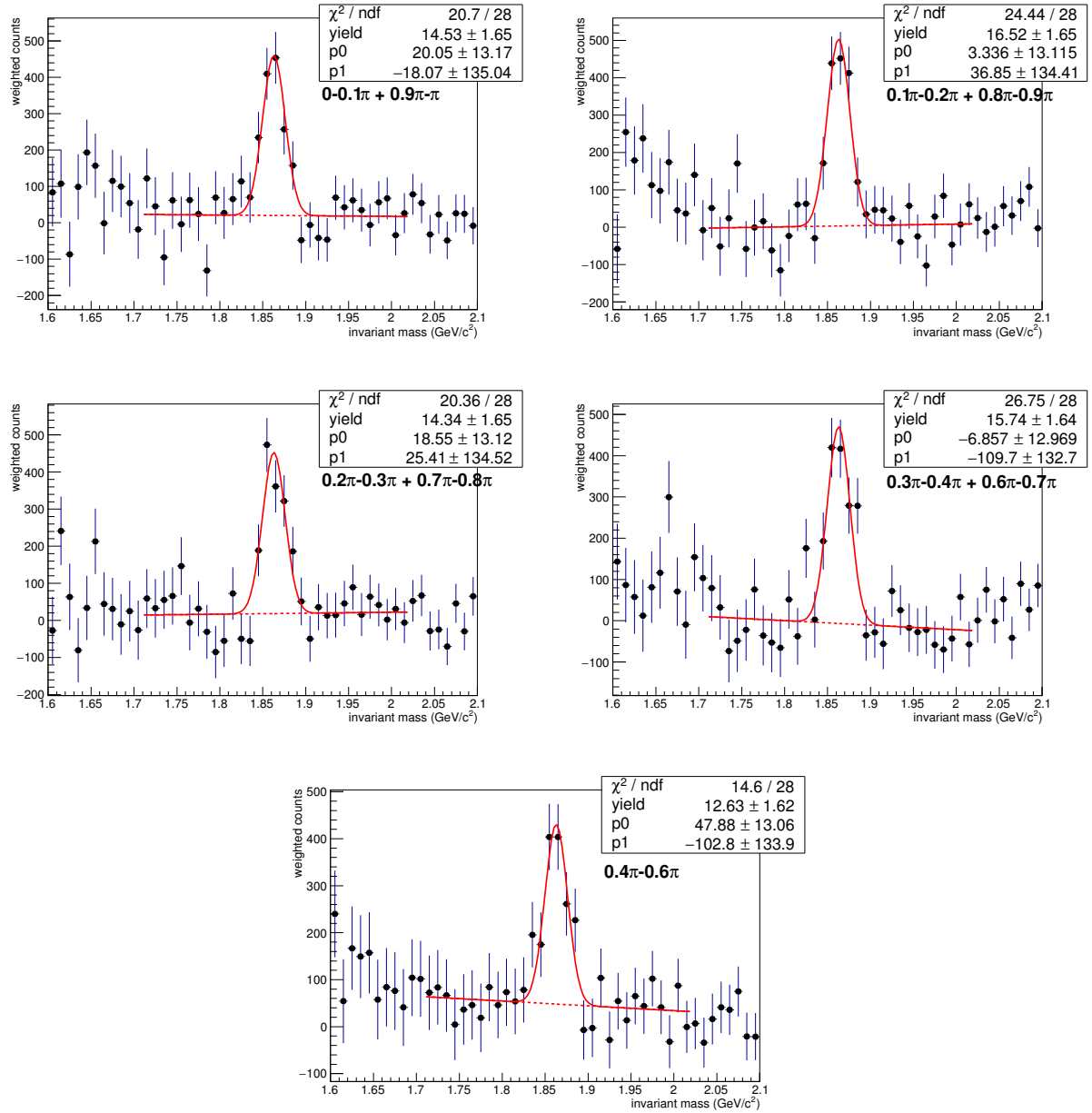


FIG. 113: $K\pi$ pairs invariant mass unlike sign - mixed event in different $\phi - \Psi$ bins, default fit range

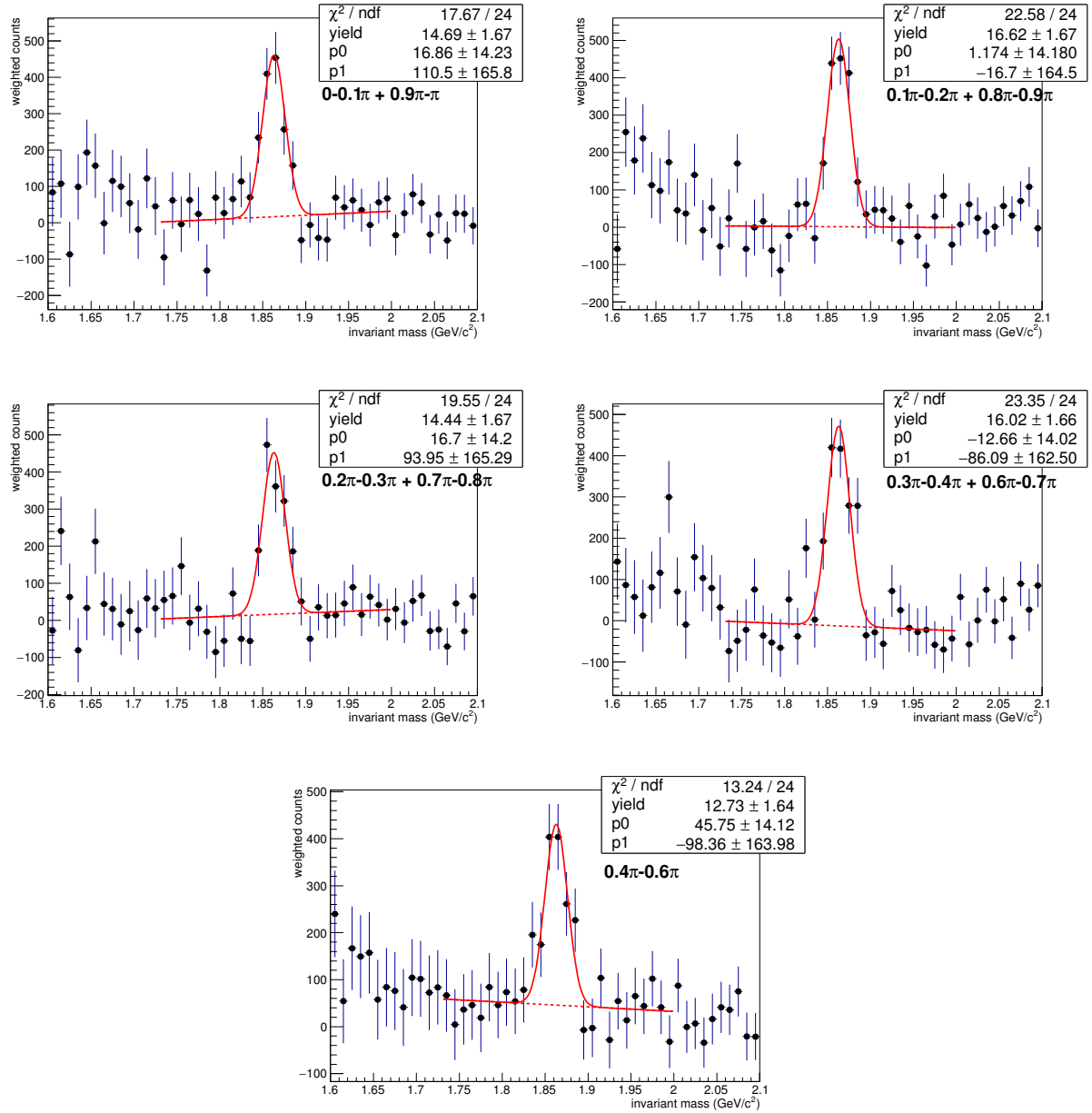


FIG. 114: $K\pi$ pairs invariant mass unlike sign - mixed event in different $\phi - \Psi$ bins, narrower fit range

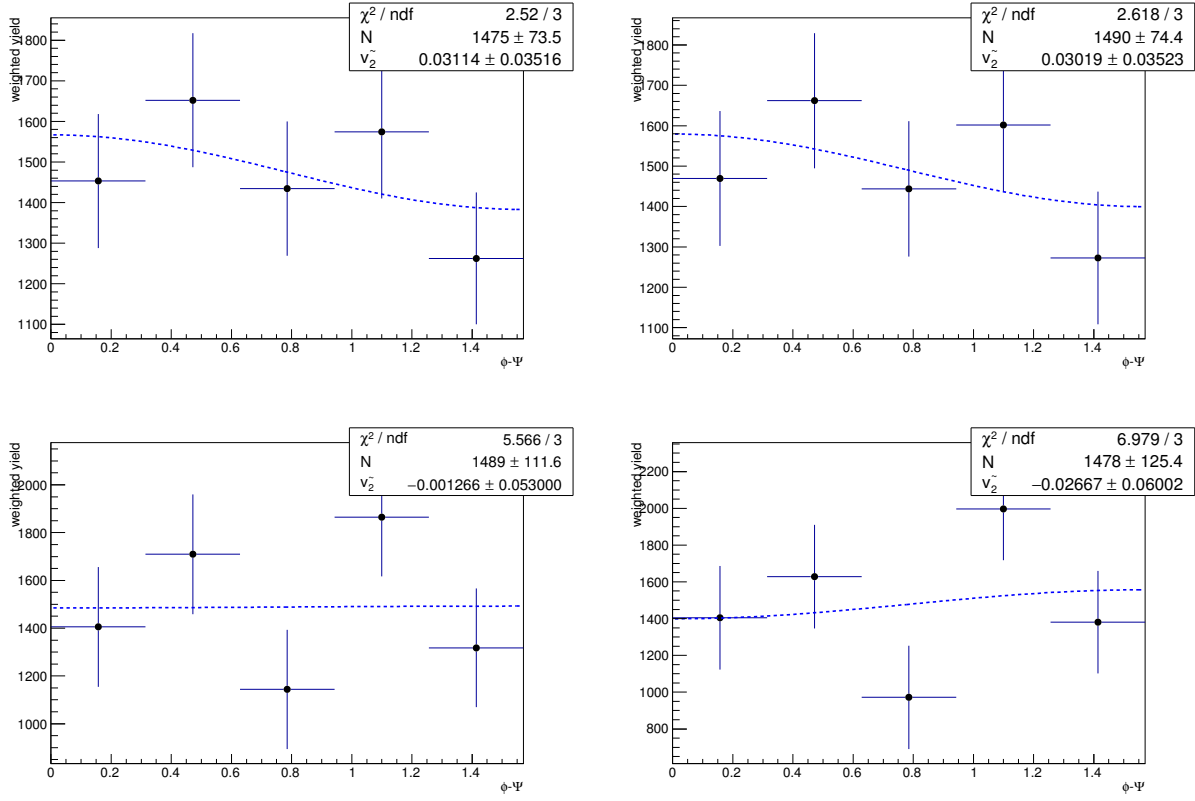


FIG. 115: yield vs. dPhi and $v_{2\text{observe}}$ fit, with yield from fit with standard range (top left), fit from narrower range (top right), side band with standard range (bottom left) and side band with narrower range (bottom right)

tight geometry cuts, p_T 2-3 GeV/c

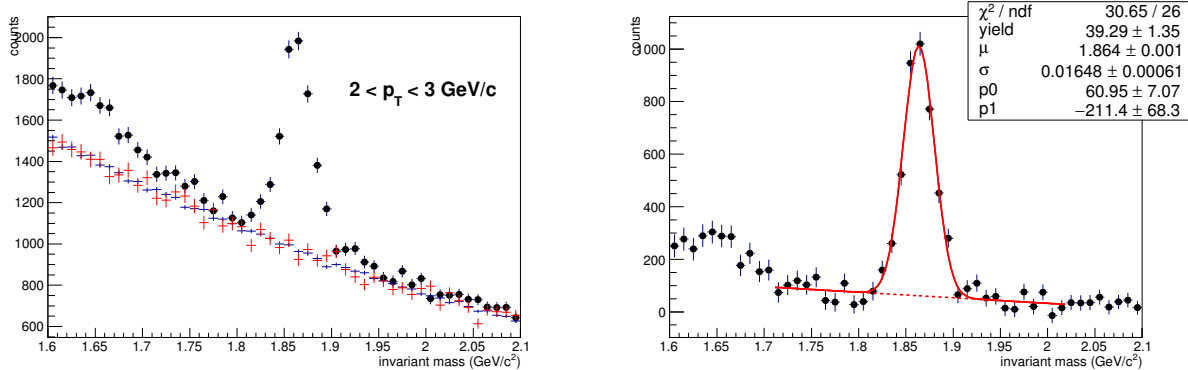


FIG. 116: $K\pi$ invariant mass distribution, left: unlike sign, like sign and scaled mixed event;
right: unlike sign - mixed event

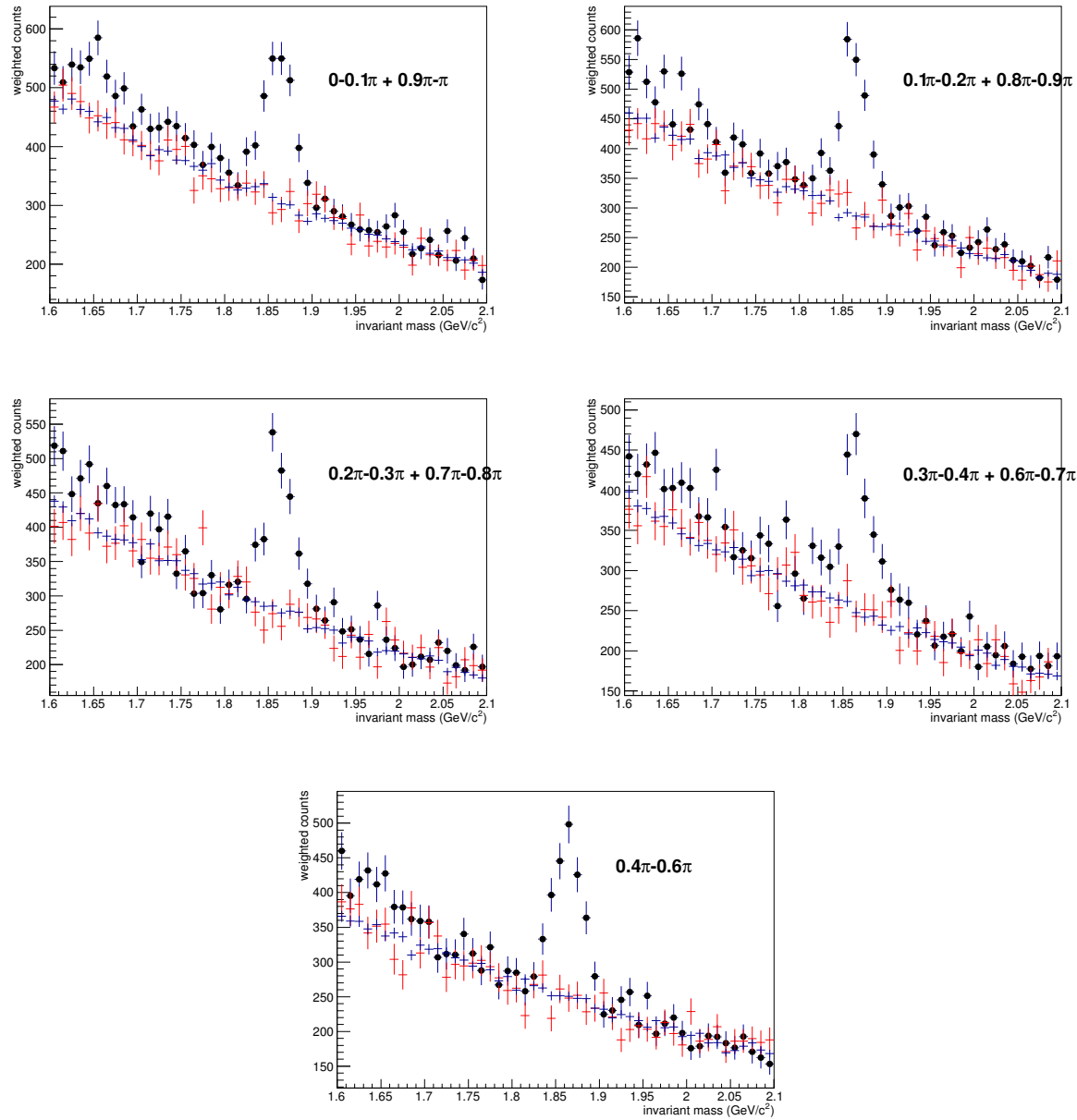


FIG. 117: $K\pi$ invariant mass in different $\phi - \Psi$ bins

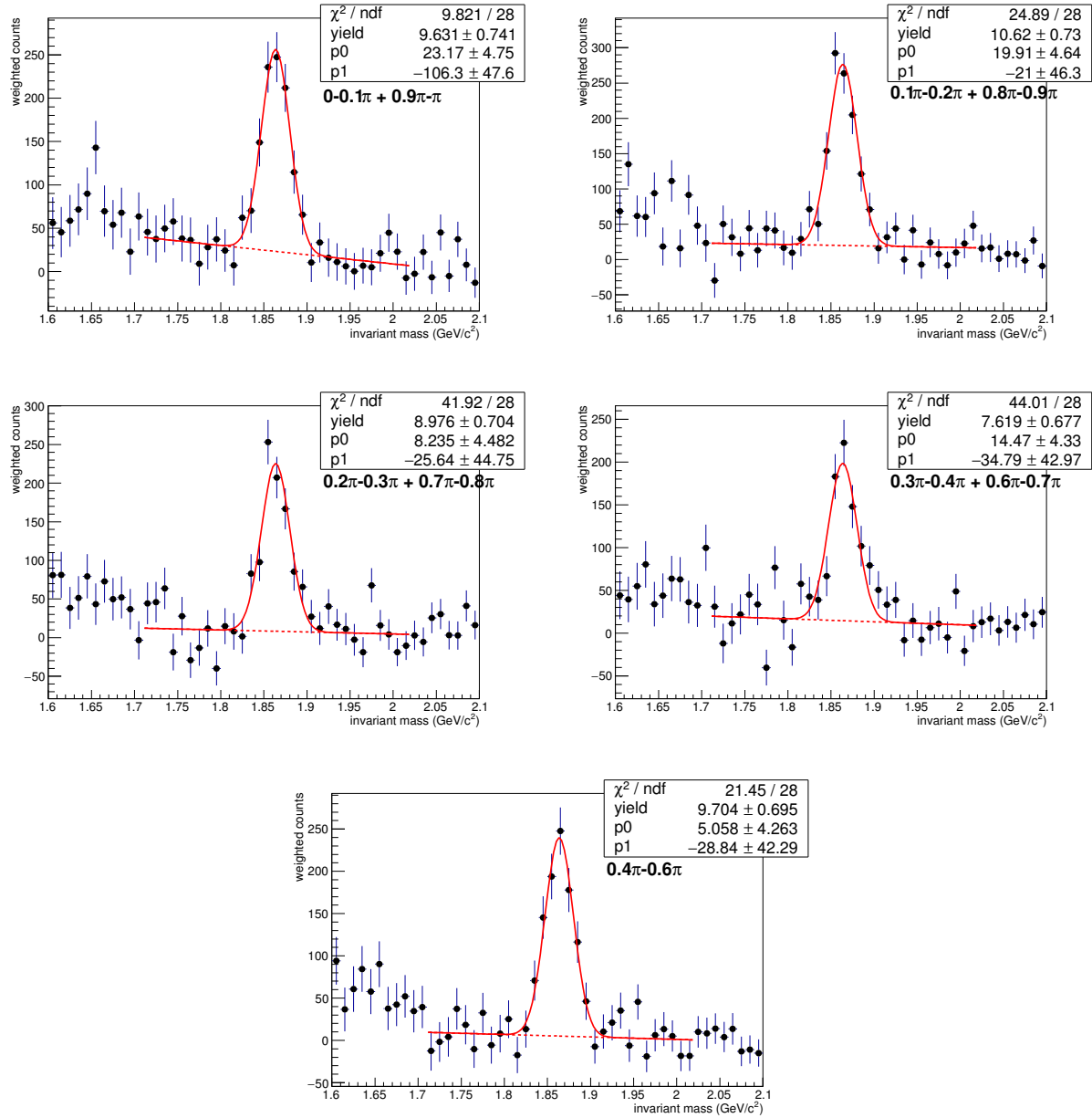


FIG. 118: $K\pi$ pairs invariant mass unlike sign - mixed event in different $\phi - \Psi$ bins, default fit range

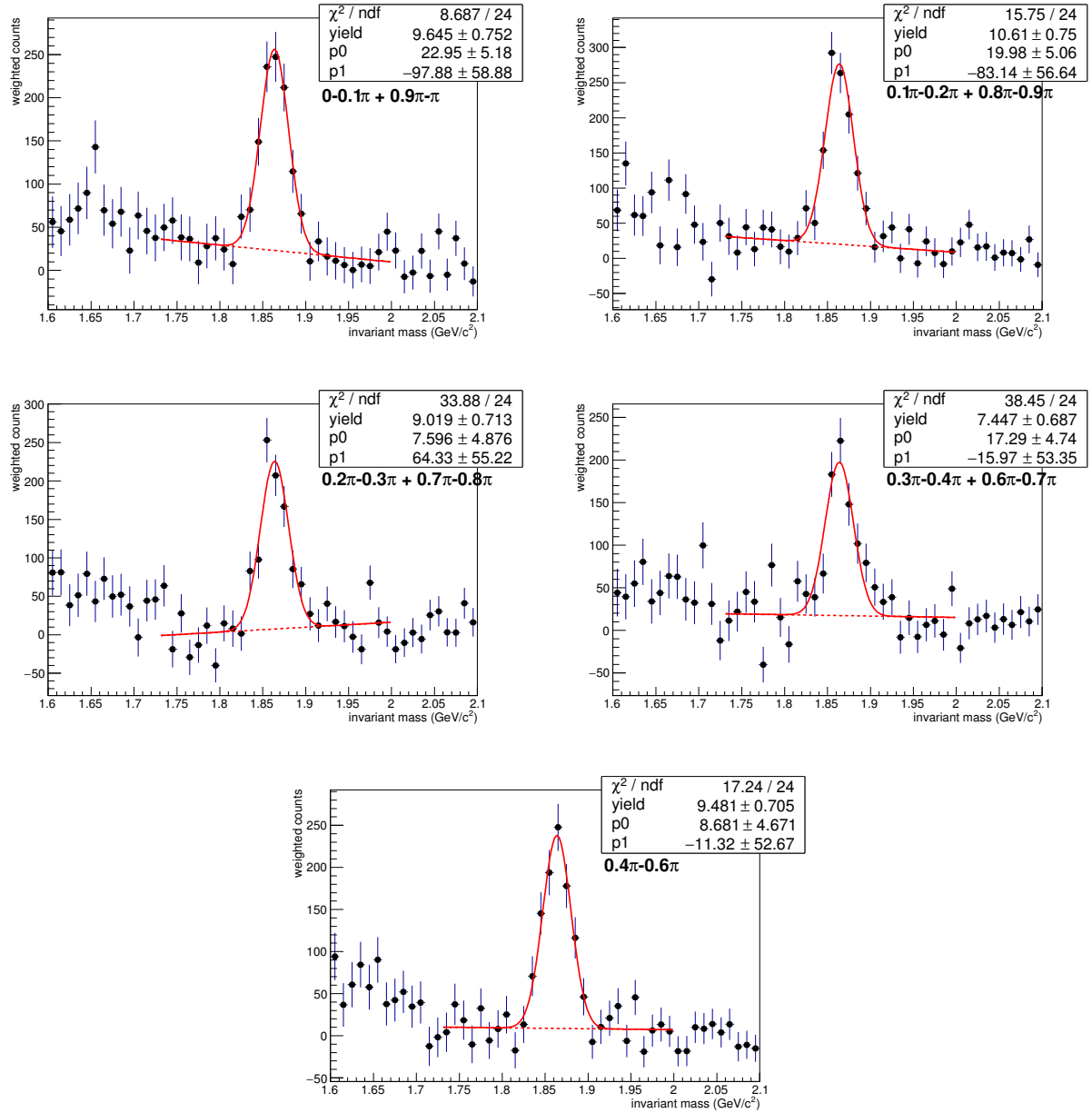


FIG. 119: $K\pi$ pairs invariant mass unlike sign - mixed event in different $\phi - \Psi$ bins, narrower fit range

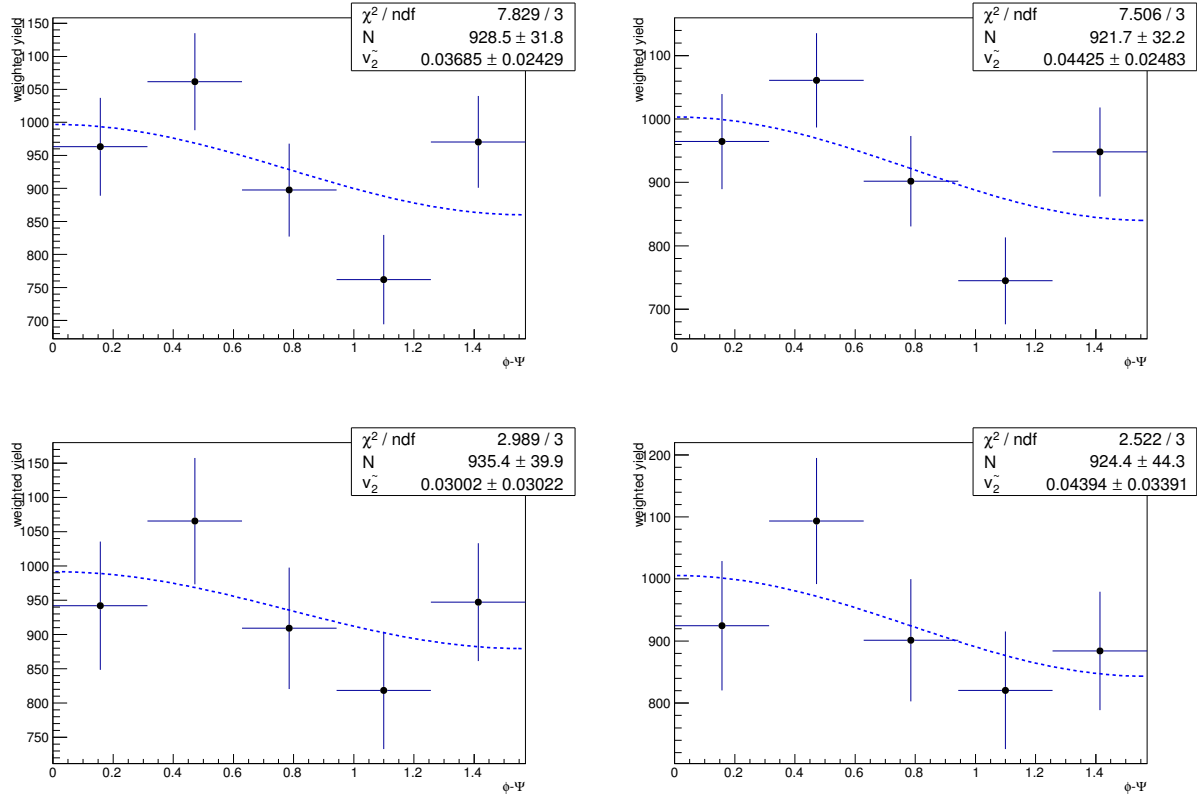


FIG. 120: yield vs. dPhi and $v_{2\text{observe}}$ fit, with yield from fit with standard range (top left), fit from narrower range (top right), side band with standard range (bottom left) and side band with narrower range (bottom right)

tight geometry cuts, p_T 3-4 GeV/c

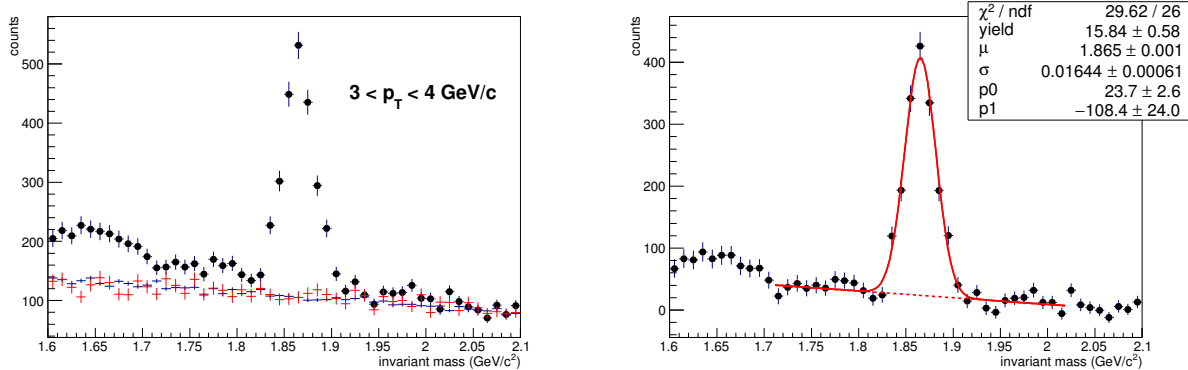


FIG. 121: $K\pi$ invariant mass distribution, left: unlike sign, like sign and scaled mixed event;
right: unlike sign - mixed event

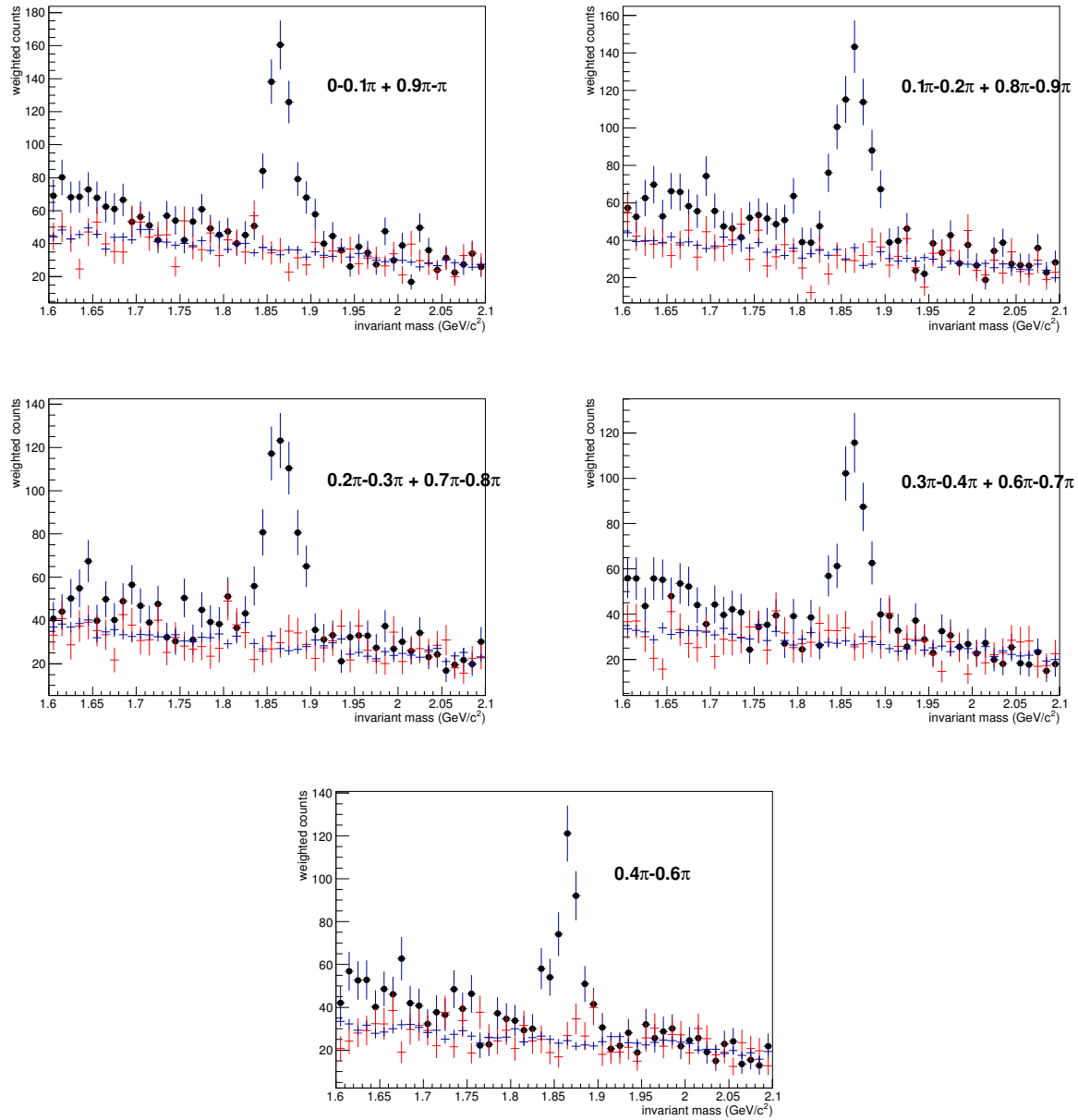


FIG. 122: $K\pi$ invariant mass in different $\phi - \Psi$ bins

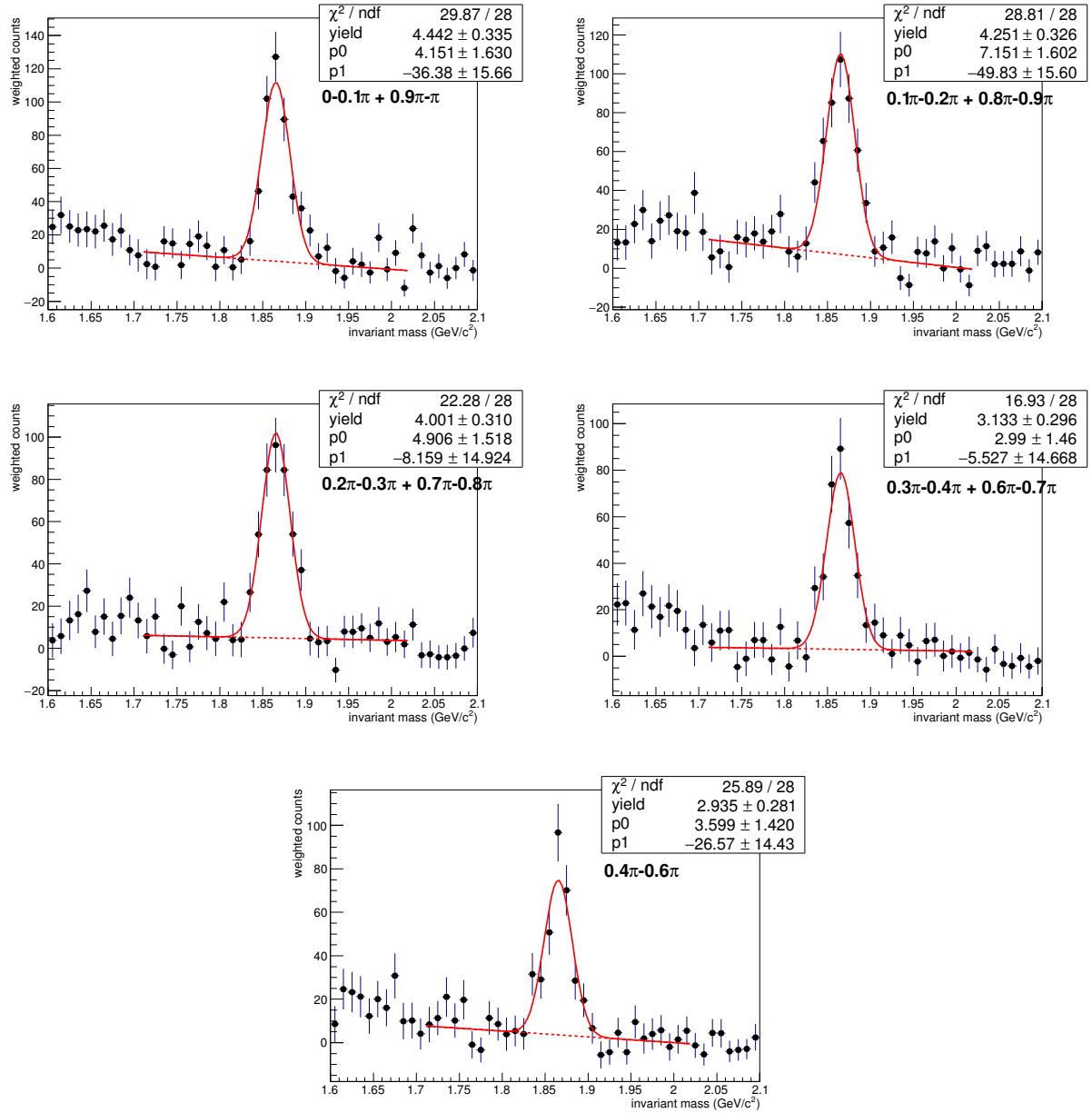


FIG. 123: $K\pi$ pairs invariant mass unlike sign - mixed event in different $\phi - \Psi$ bins, default fit range

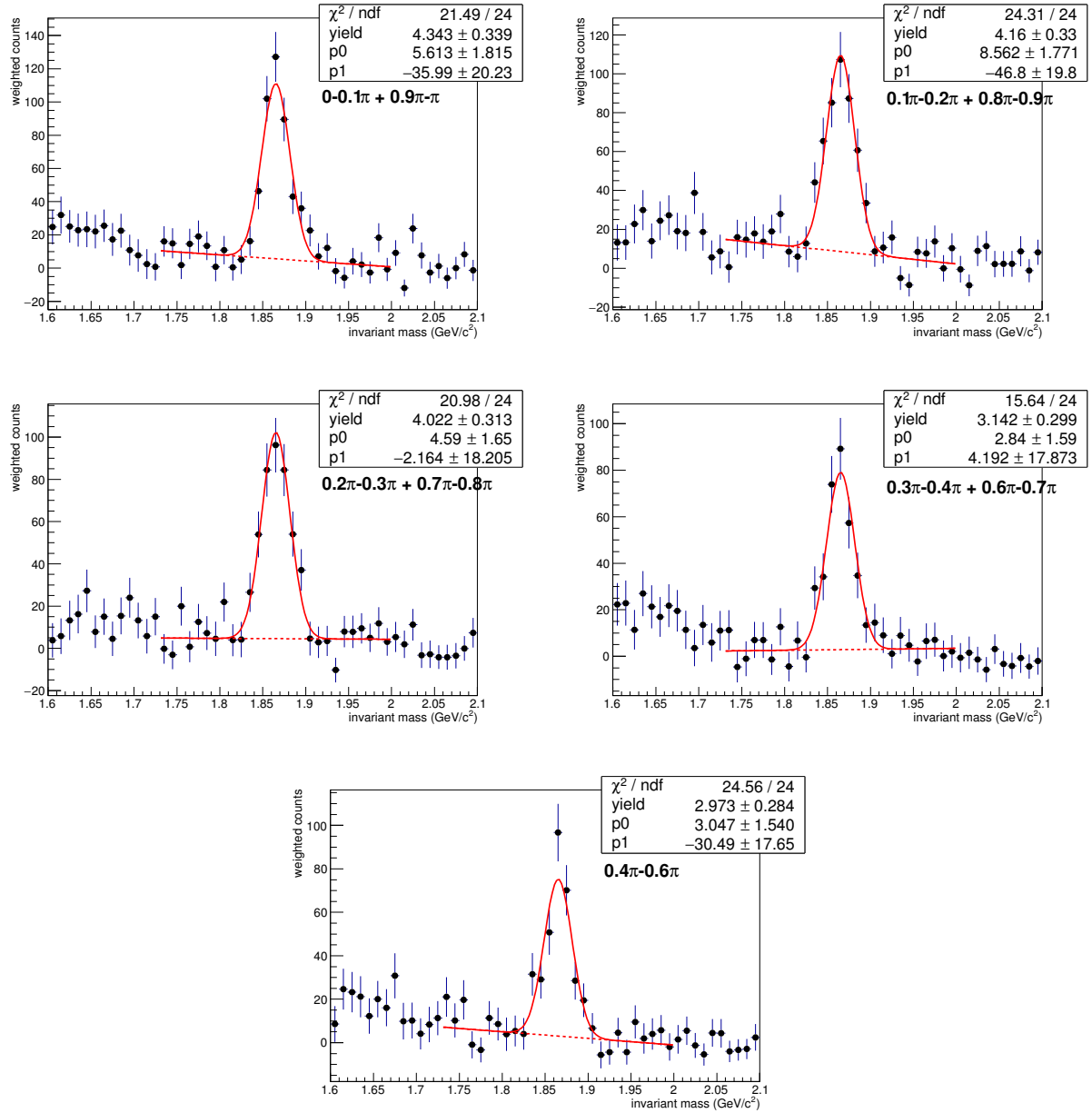


FIG. 124: $K\pi$ pairs invariant mass unlike sign - mixed event in different $\phi - \Psi$ bins, narrower fit range

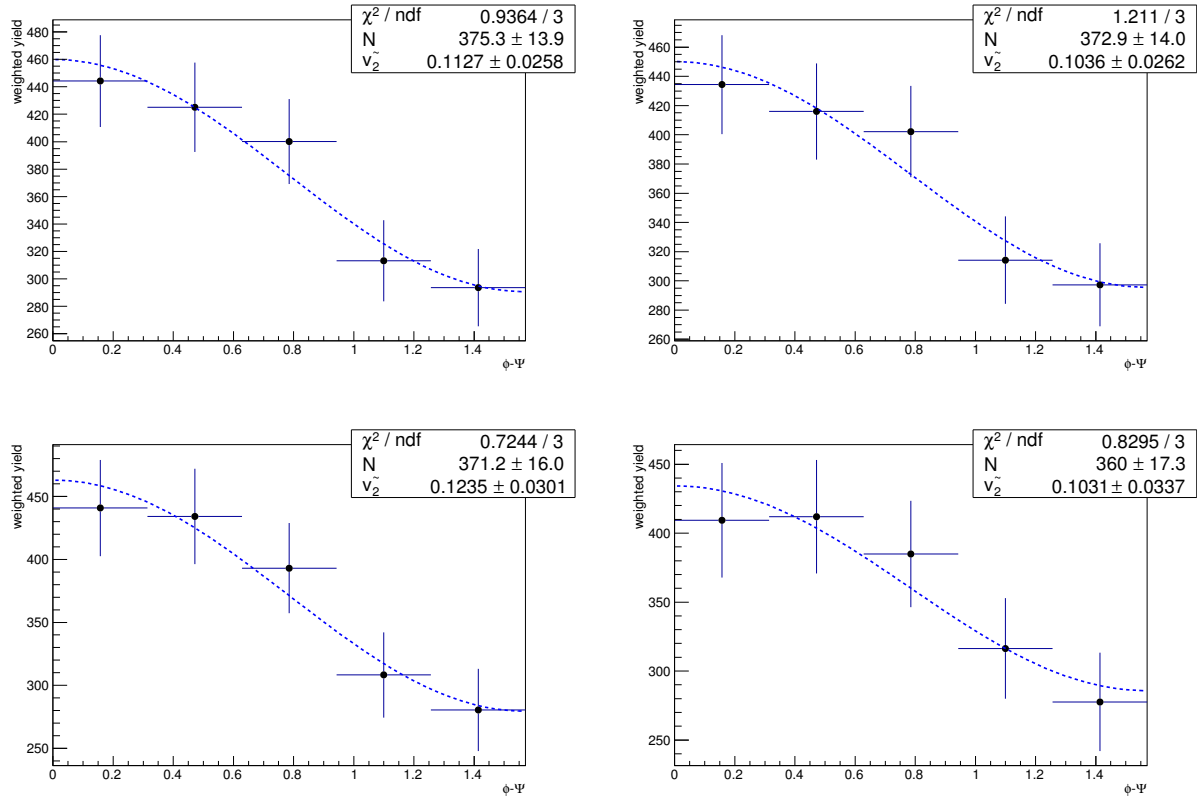


FIG. 125: yield vs. dPhi and $v_{2\text{observe}}$ fit, with yield from fit with standard range (top left), fit from narrower range (top right), side band with standard range (bottom left) and side band with narrower range (bottom right)

tight geometry cuts, p_T 4-5 GeV/c

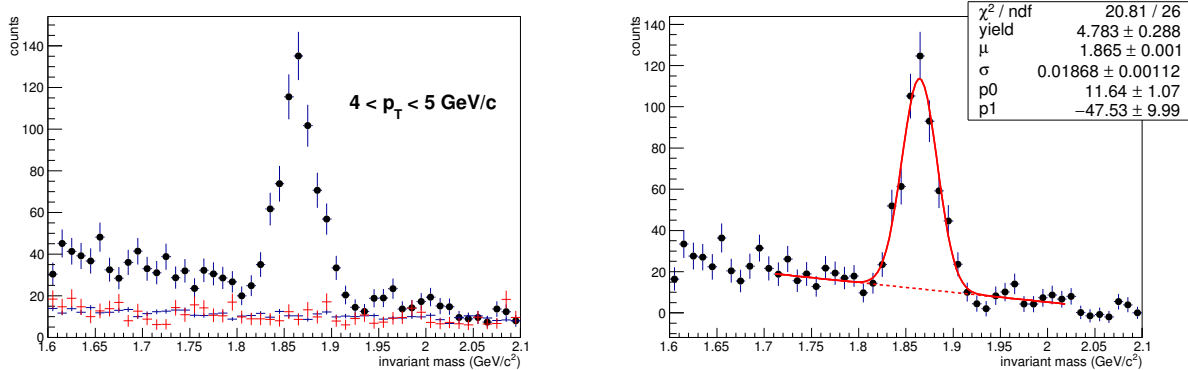
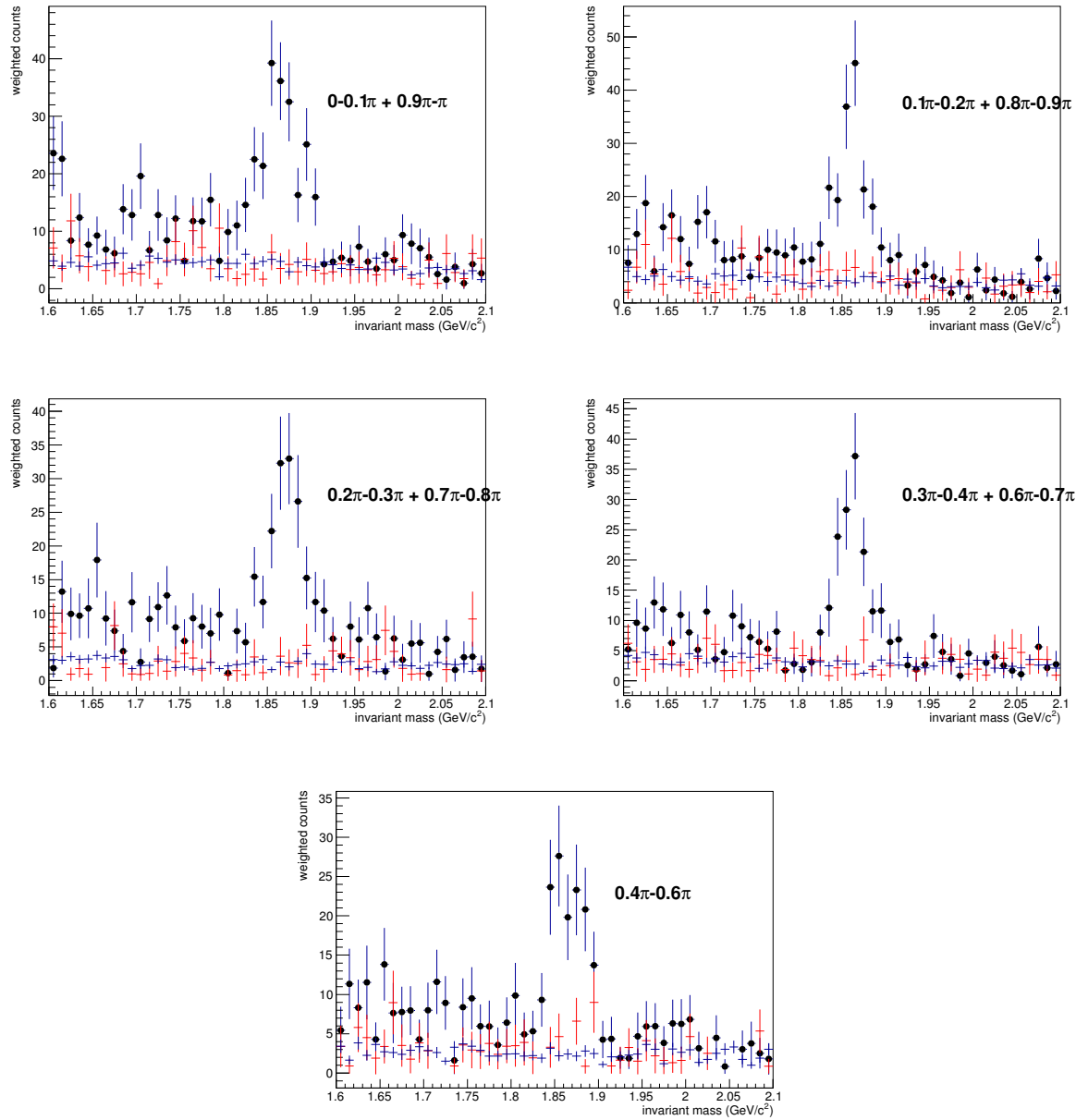


FIG. 126: $K\pi$ invariant mass distribution, left: unlike sign, like sign and scaled mixed event;
right: unlike sign - mixed event

FIG. 127: $K\pi$ invariant mass in different $\phi - \Psi$ bins

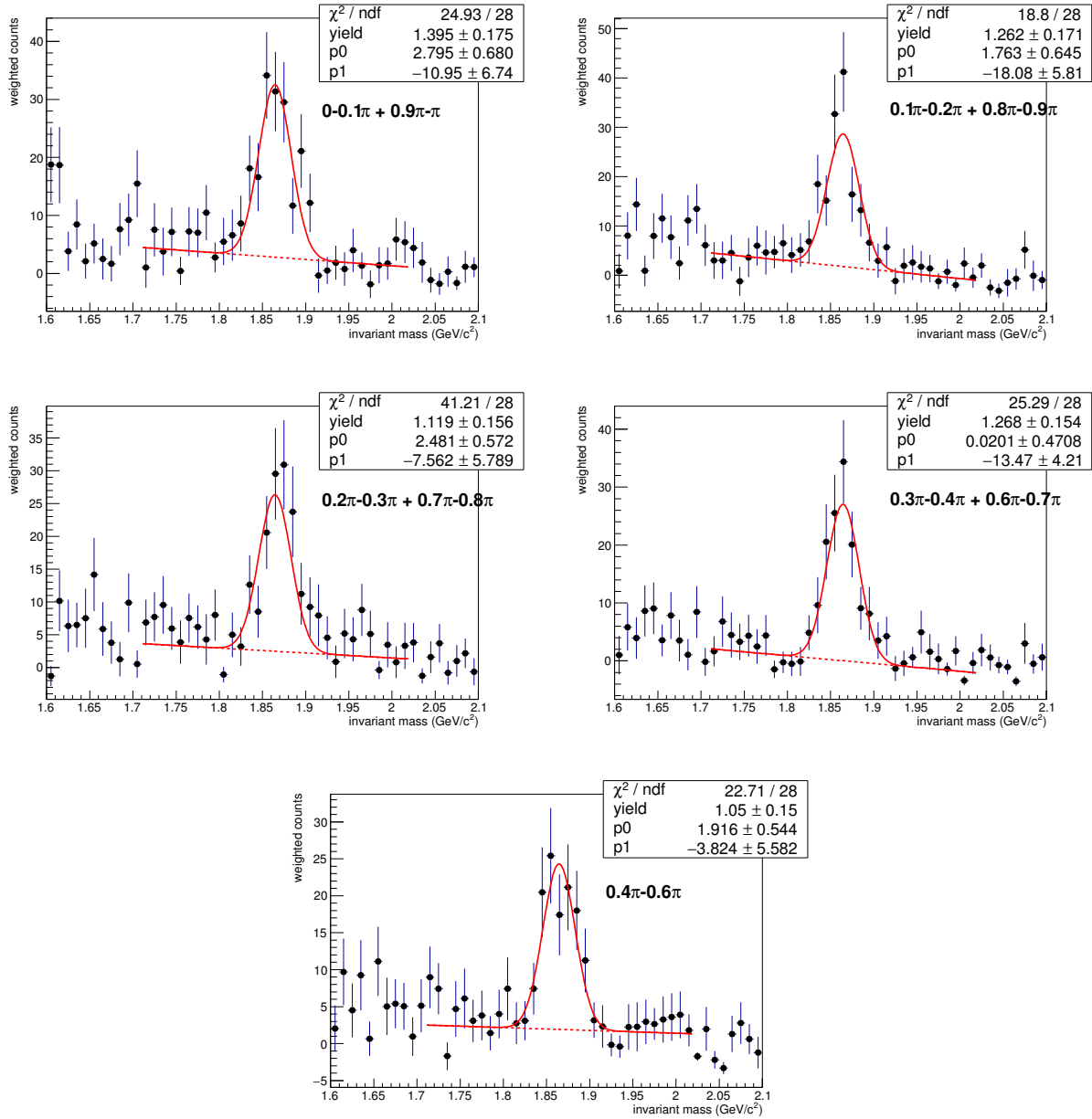


FIG. 128: $K\pi$ pairs invariant mass unlike sign - mixed event in different $\phi - \Psi$ bins, default fit range

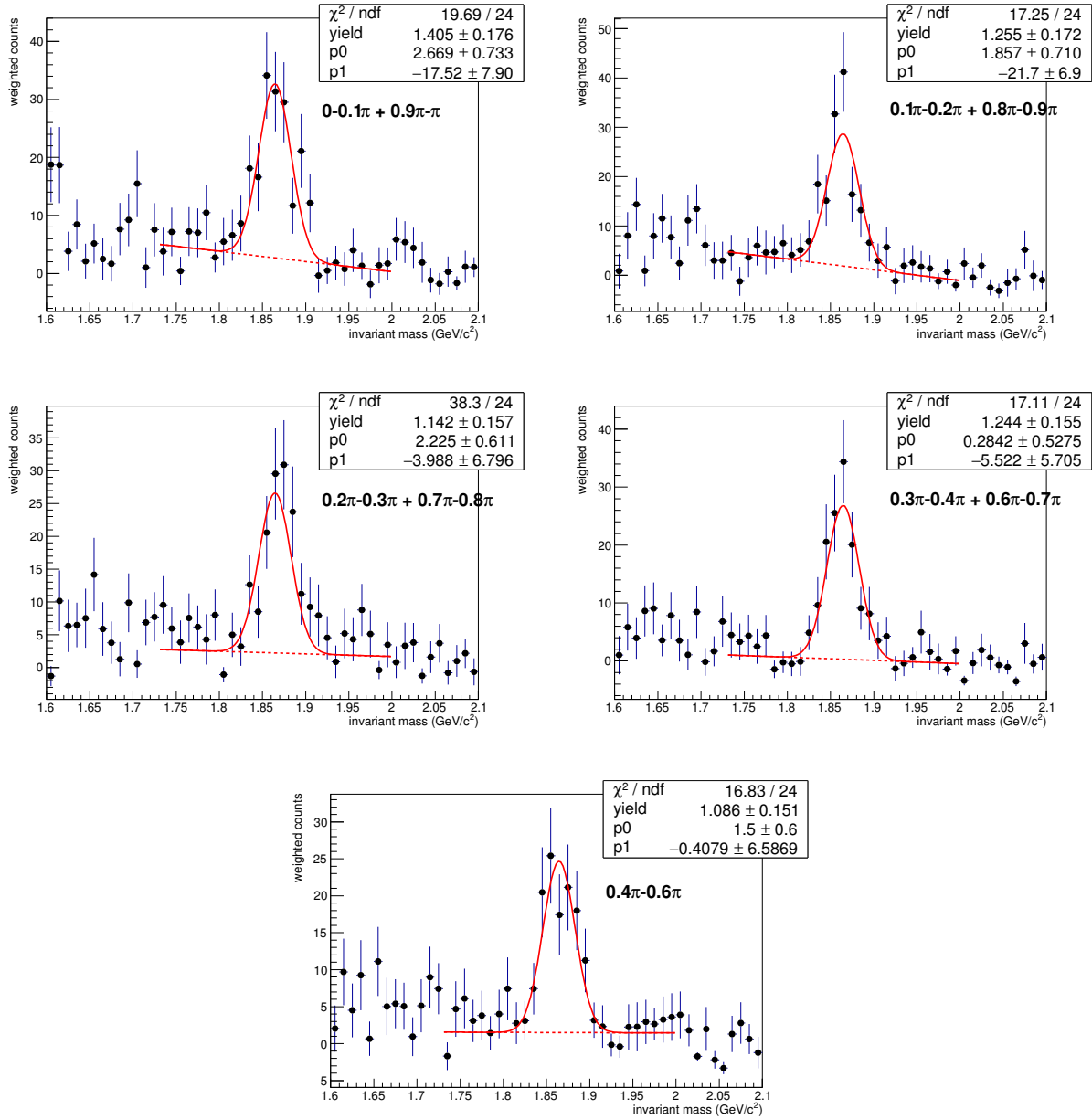


FIG. 129: $K\pi$ pairs invariant mass unlike sign - mixed event in different $\phi - \Psi$ bins, narrower fit range

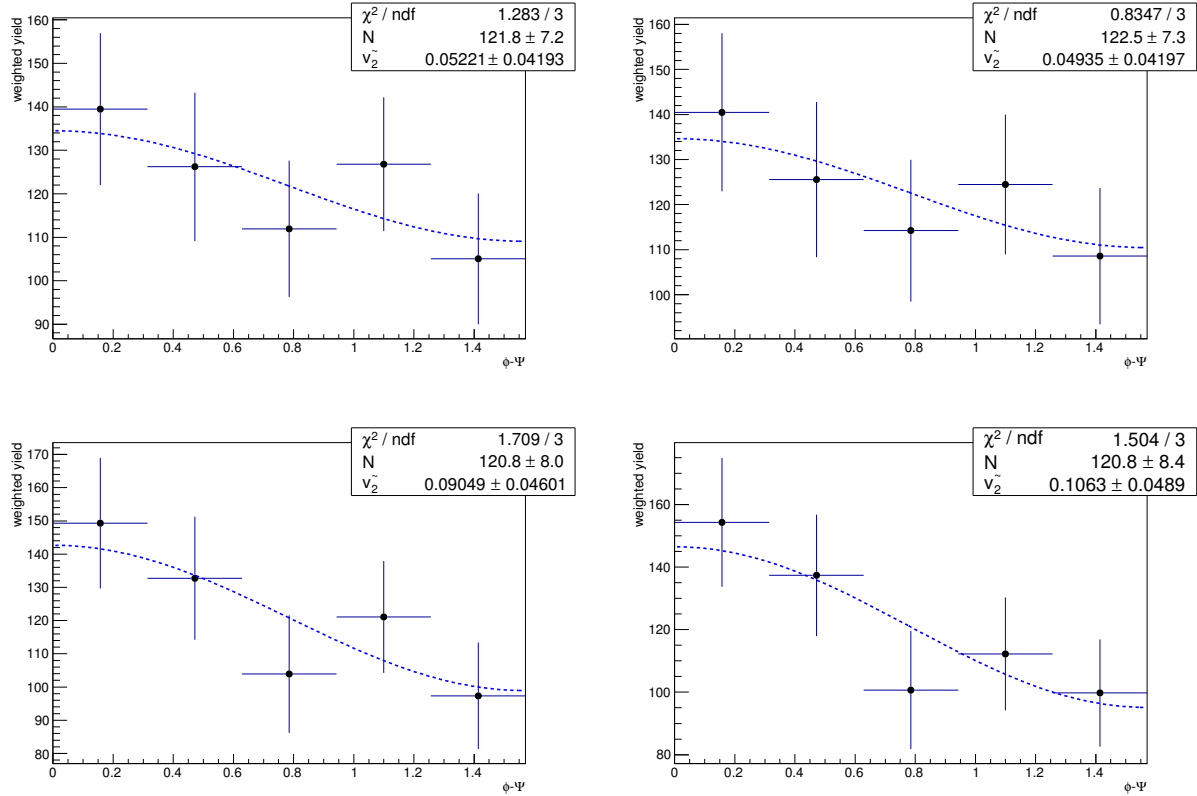


FIG. 130: yield vs. dPhi and $v_{2\text{observe}}$ fit, with yield from fit with standard range (top left), fit from narrower range (top right), side band with standard range (bottom left) and side band with narrower range (bottom right)

tight geometry cuts, p_T 5-10 GeV/c

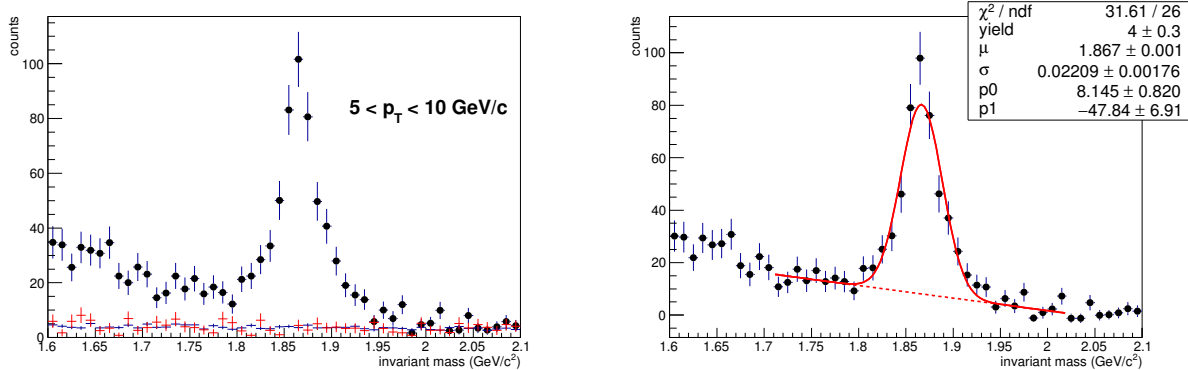


FIG. 131: $K\pi$ invariant mass distribution, left: unlike sign, like sign and scaled mixed event;
right: unlike sign - mixed event

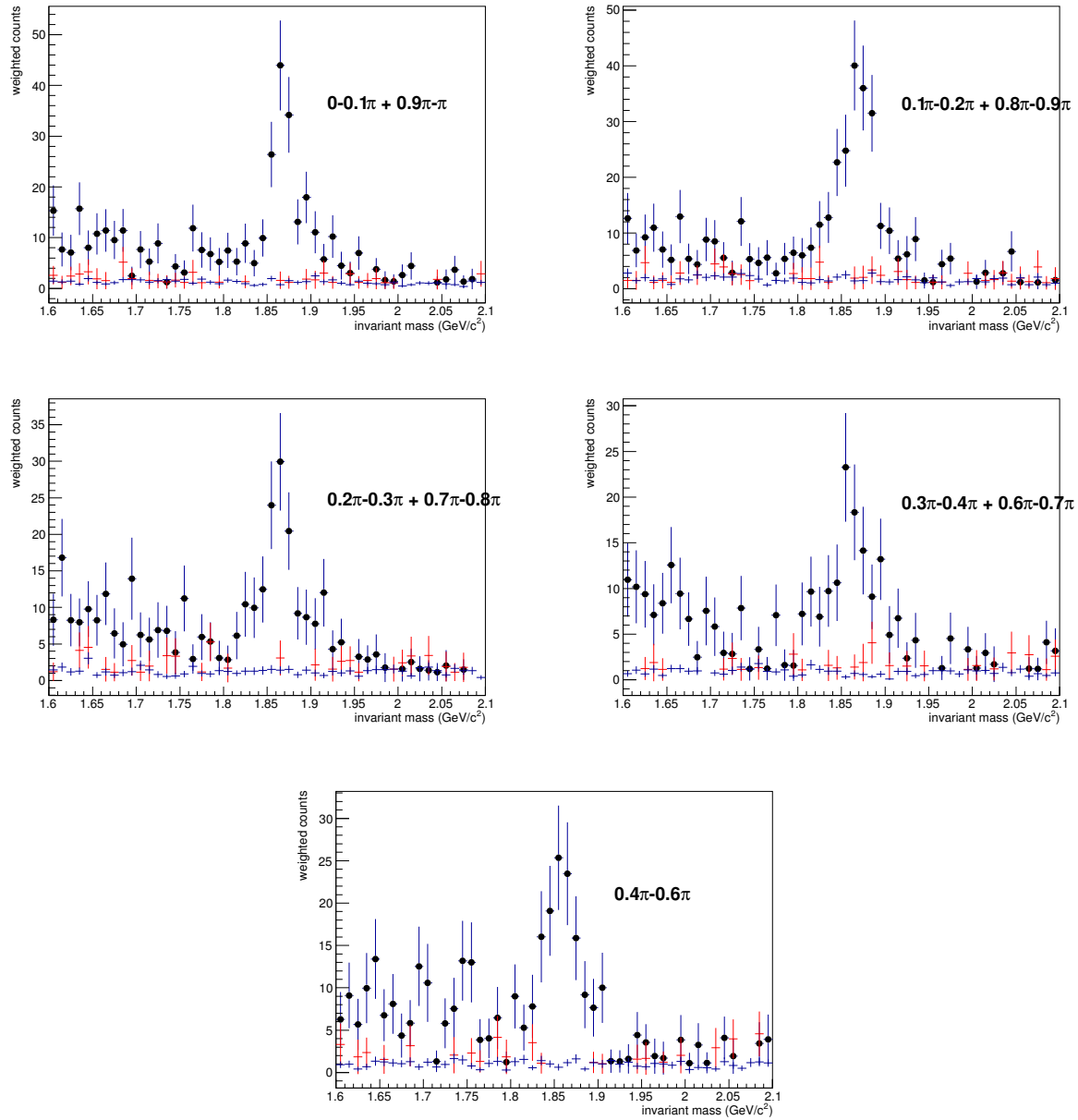


FIG. 132: $K\pi$ invariant mass in different $\phi - \Psi$ bins

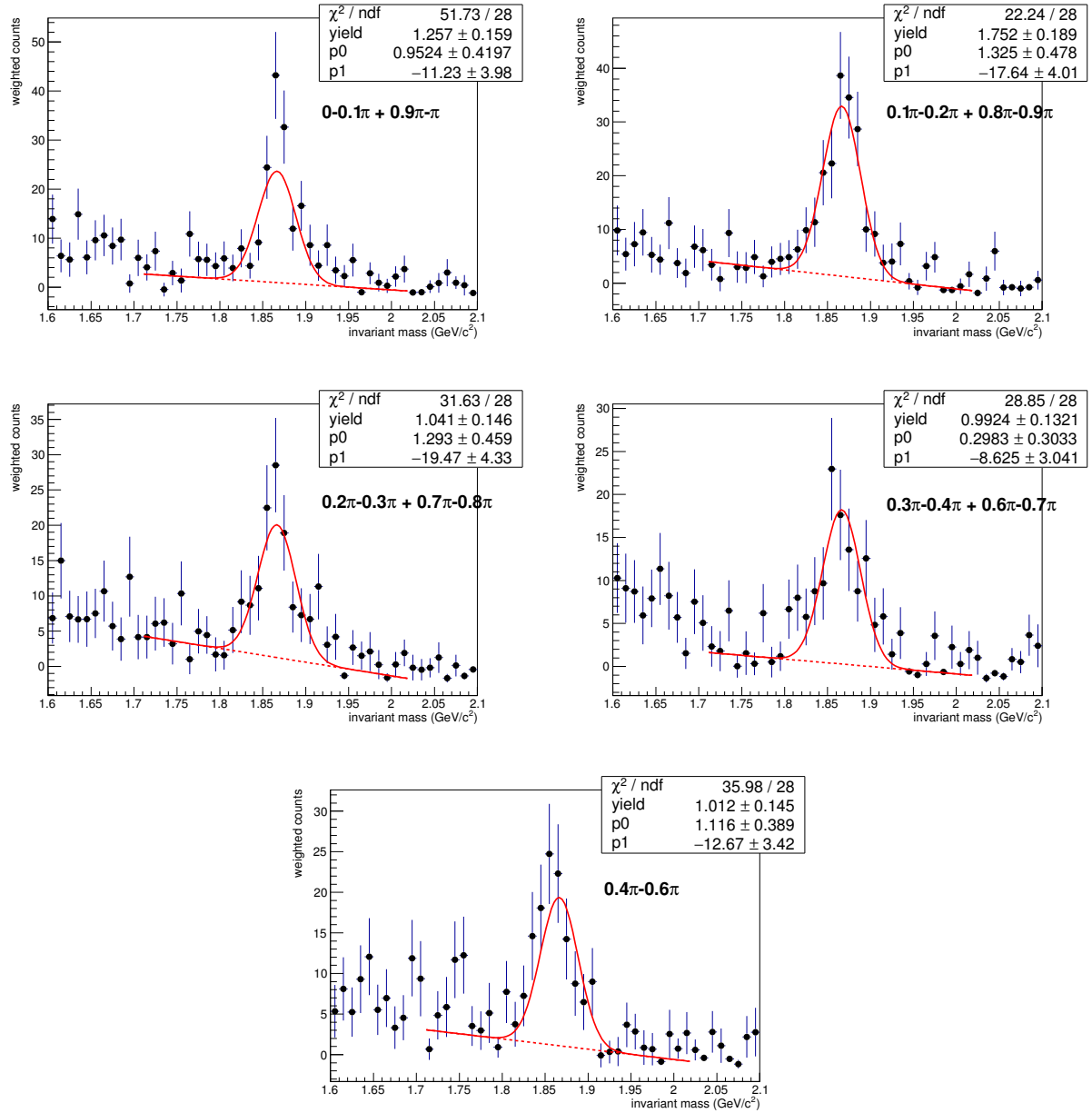


FIG. 133: $K\pi$ pairs invariant mass unlike sign - mixed event in different $\phi - \Psi$ bins, default fit range

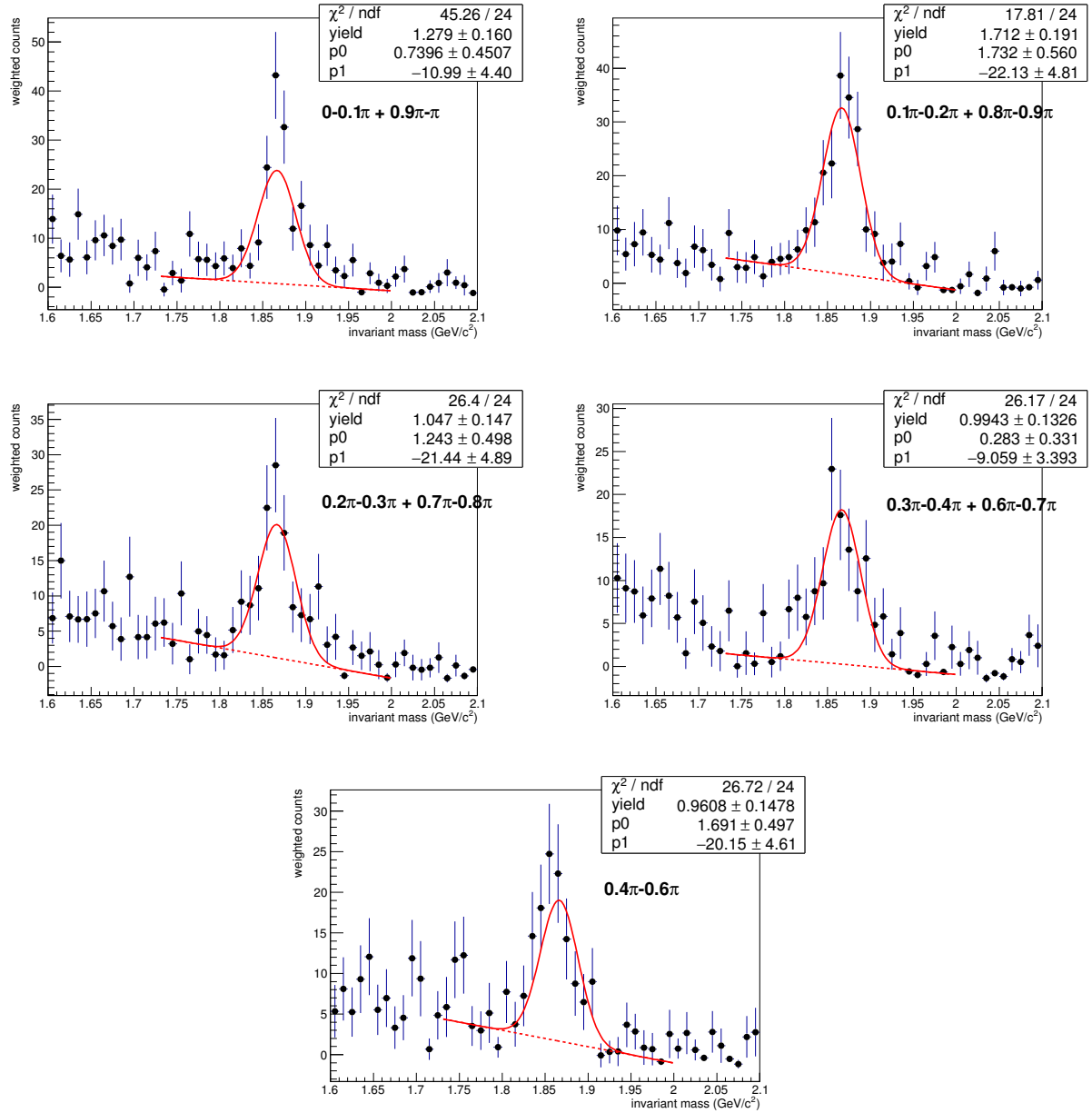


FIG. 134: $K\pi$ pairs invariant mass unlike sign - mixed event in different $\phi - \Psi$ bins, narrower fit range

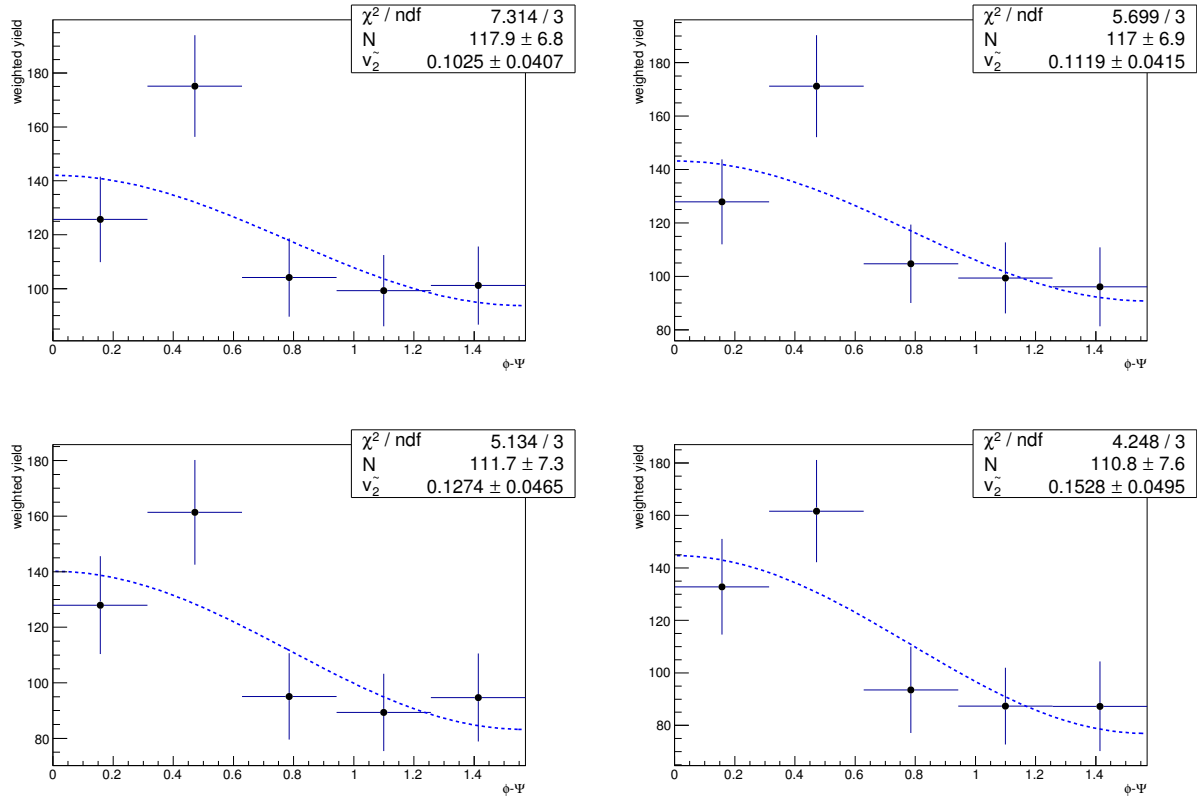


FIG. 135: yield vs. dPhi and $v_{2\text{observe}}$ fit, with yield from fit with standard range (top left), fit from narrower range (top right), side band with standard range (bottom left) and side band with narrower range (bottom right)

loose geometry cuts, p_T 0-1 GeV/c

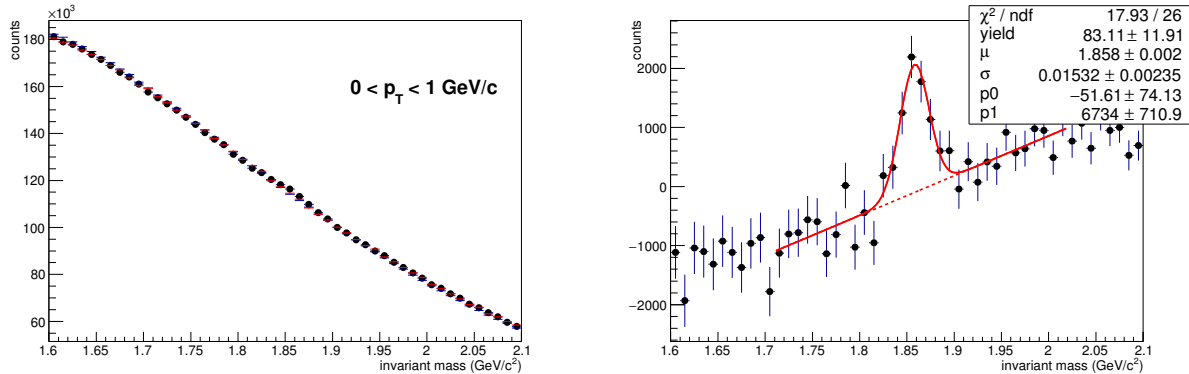
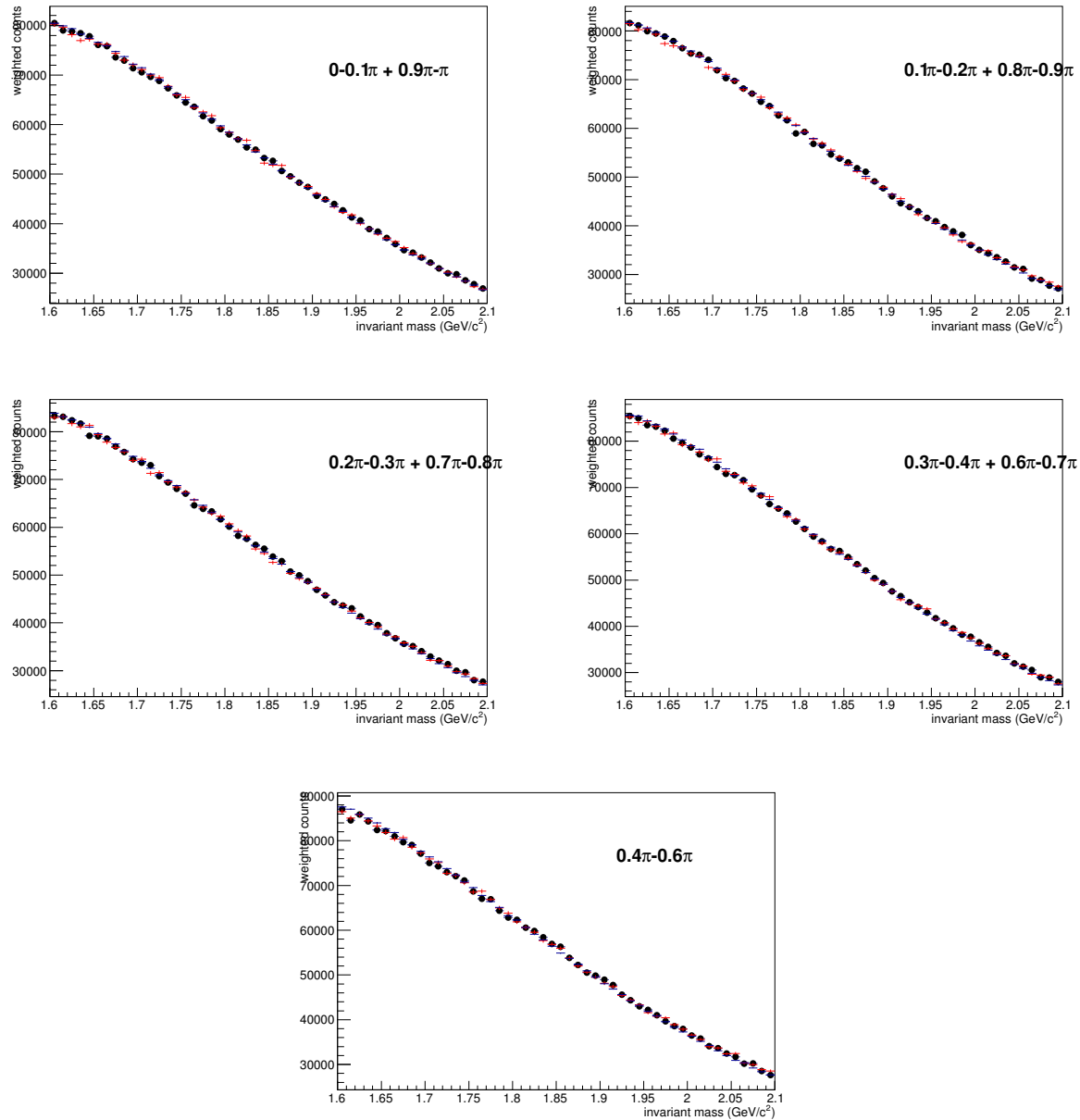


FIG. 136: $K\pi$ invariant mass distribution, left: unlike sign, like sign and scaled mixed event;
right: unlike sign - mixed event

FIG. 137: $K\pi$ invariant mass in different $\phi - \Psi$ bins

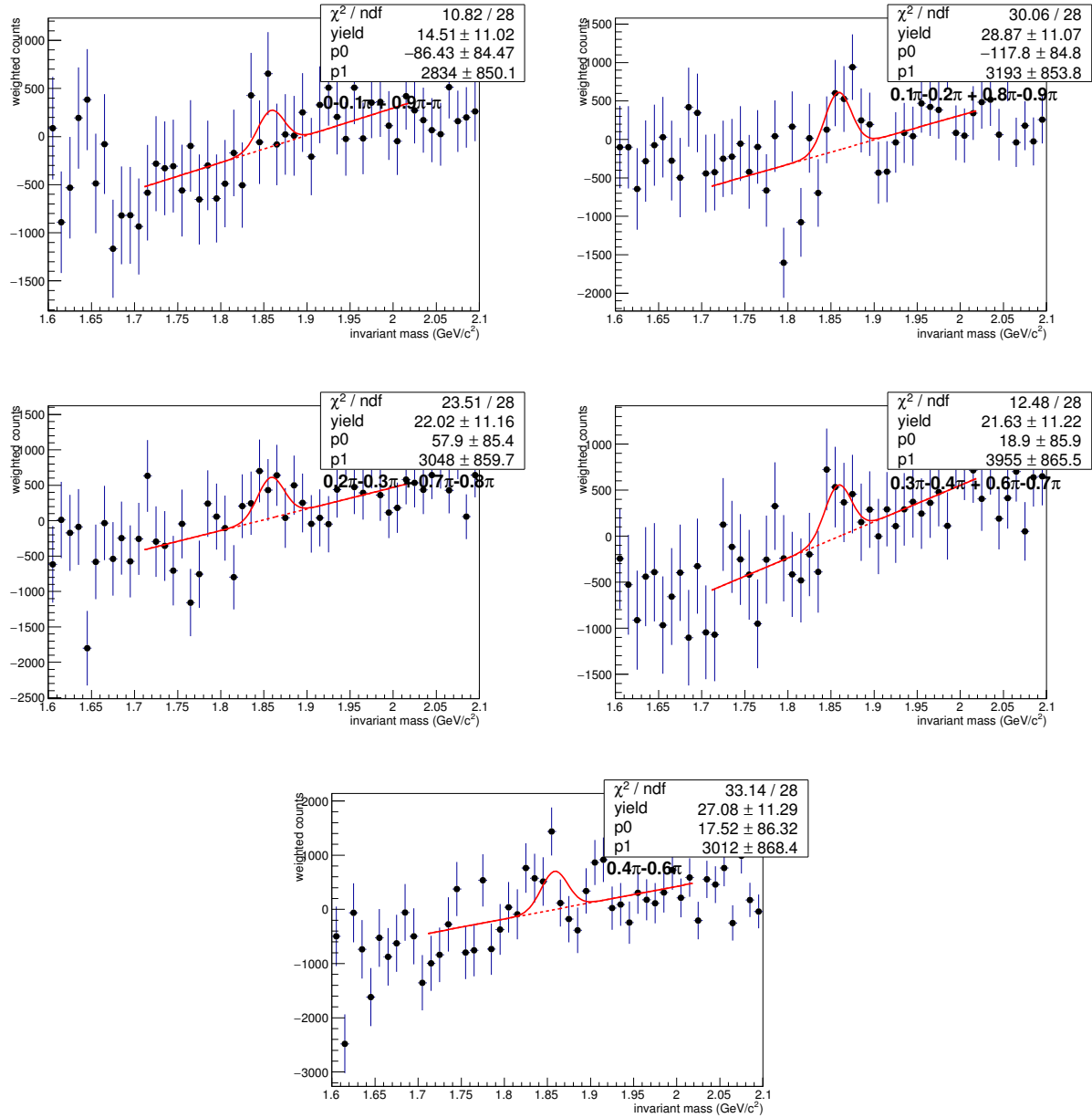


FIG. 138: $K\pi$ pairs invariant mass unlike sign - mixed event in different $\phi - \Psi$ bins, default fit range

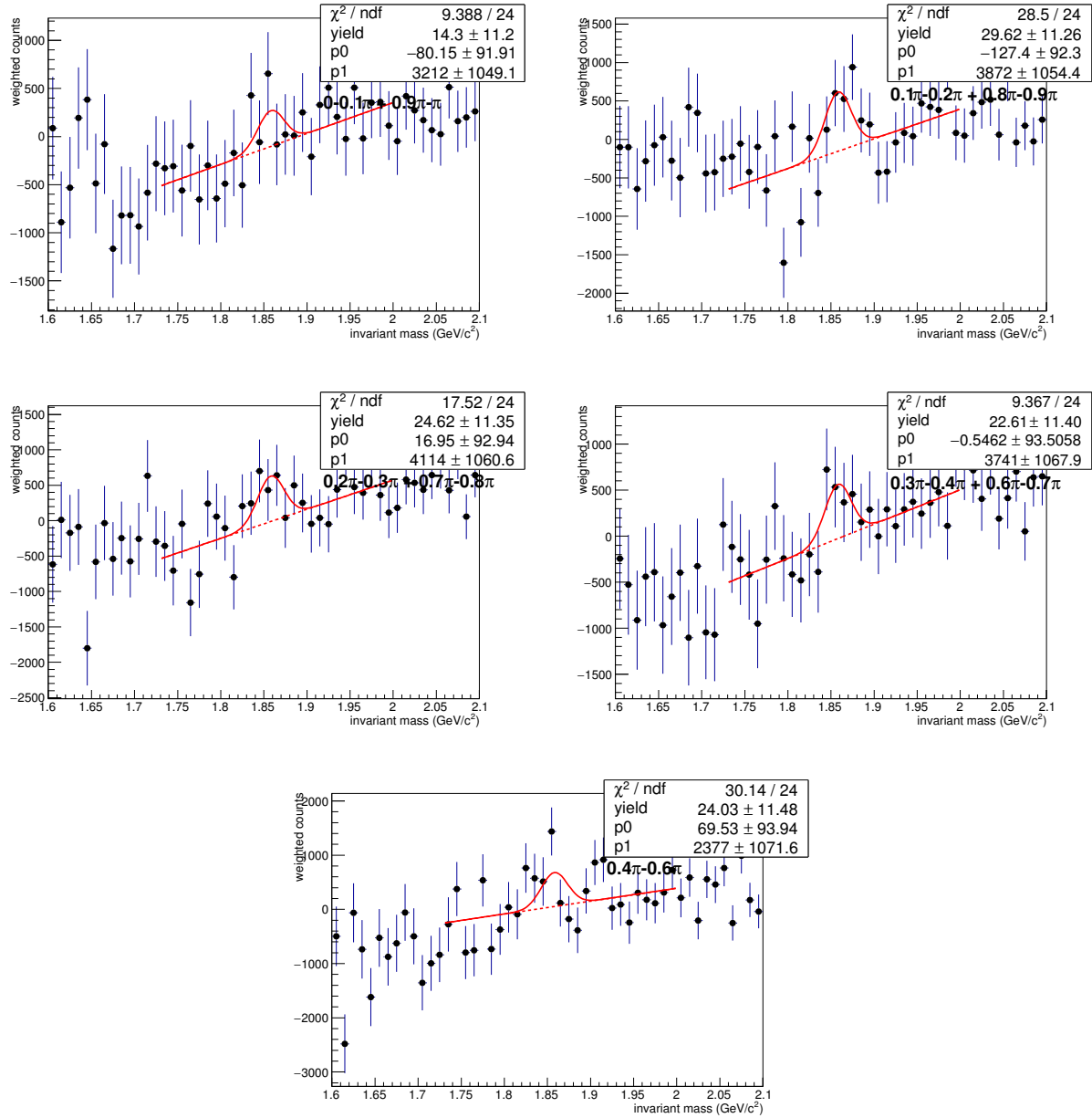


FIG. 139: $K\pi$ pairs invariant mass unlike sign - mixed event in different $\phi - \Psi$ bins, narrower fit range

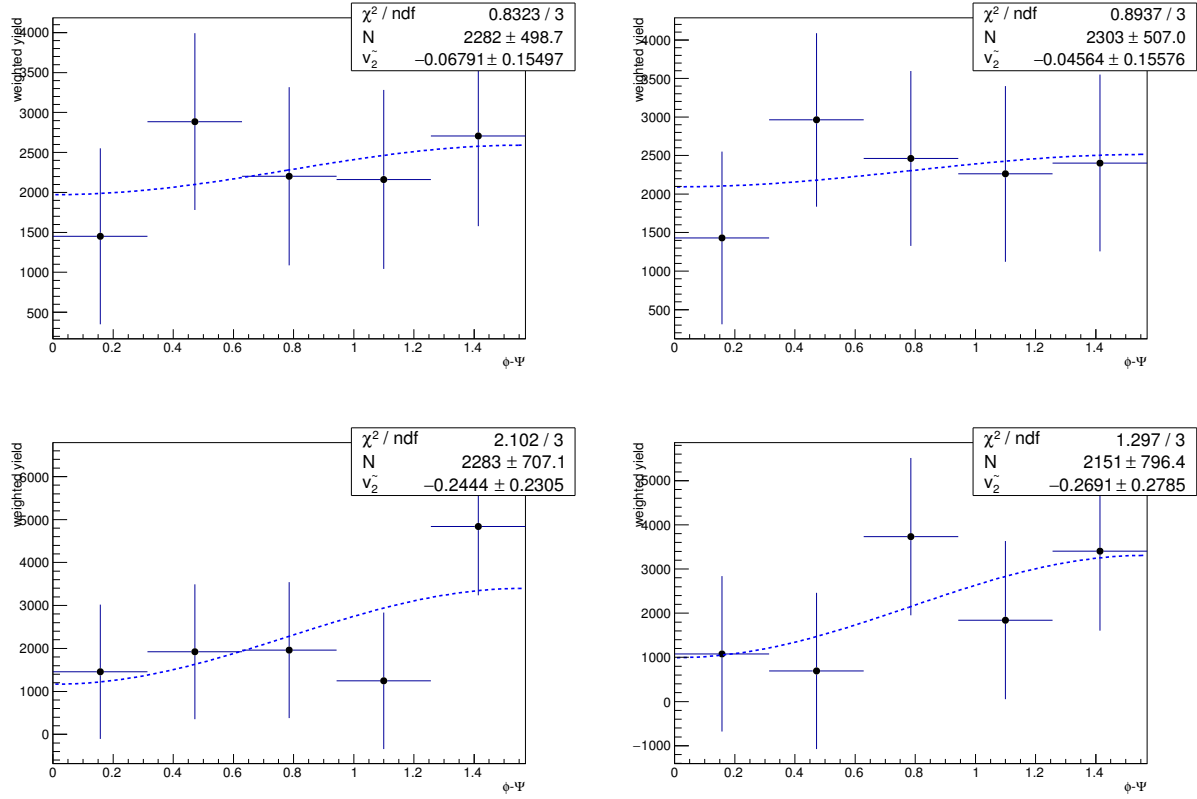


FIG. 140: yield vs. dPhi and $v_{2\text{observe}}$ fit, with yield from fit with standard range (top left), fit from narrower range (top right), side band with standard range (bottom left) and side band with narrower range (bottom right)

loose geometry cuts, p_T 1-2 GeV/c

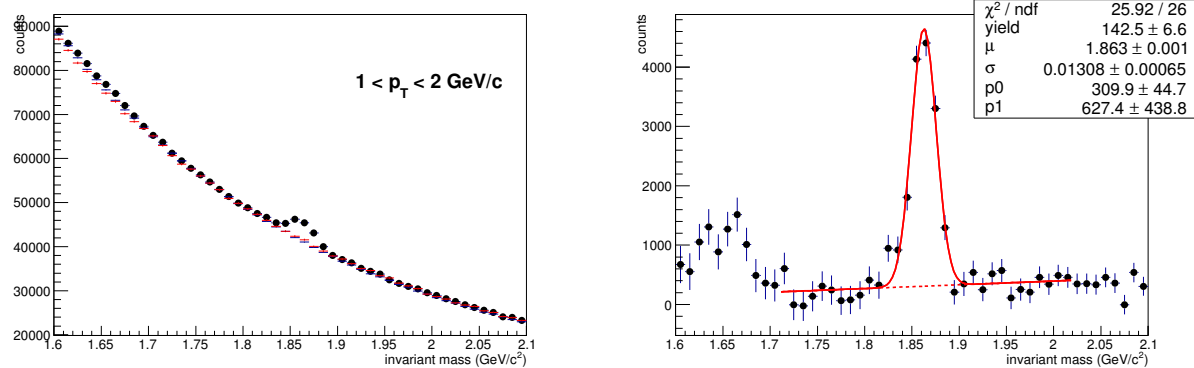


FIG. 141: $K\pi$ invariant mass distribution, left: unlike sign, like sign and scaled mixed event;
right: unlike sign - mixed event

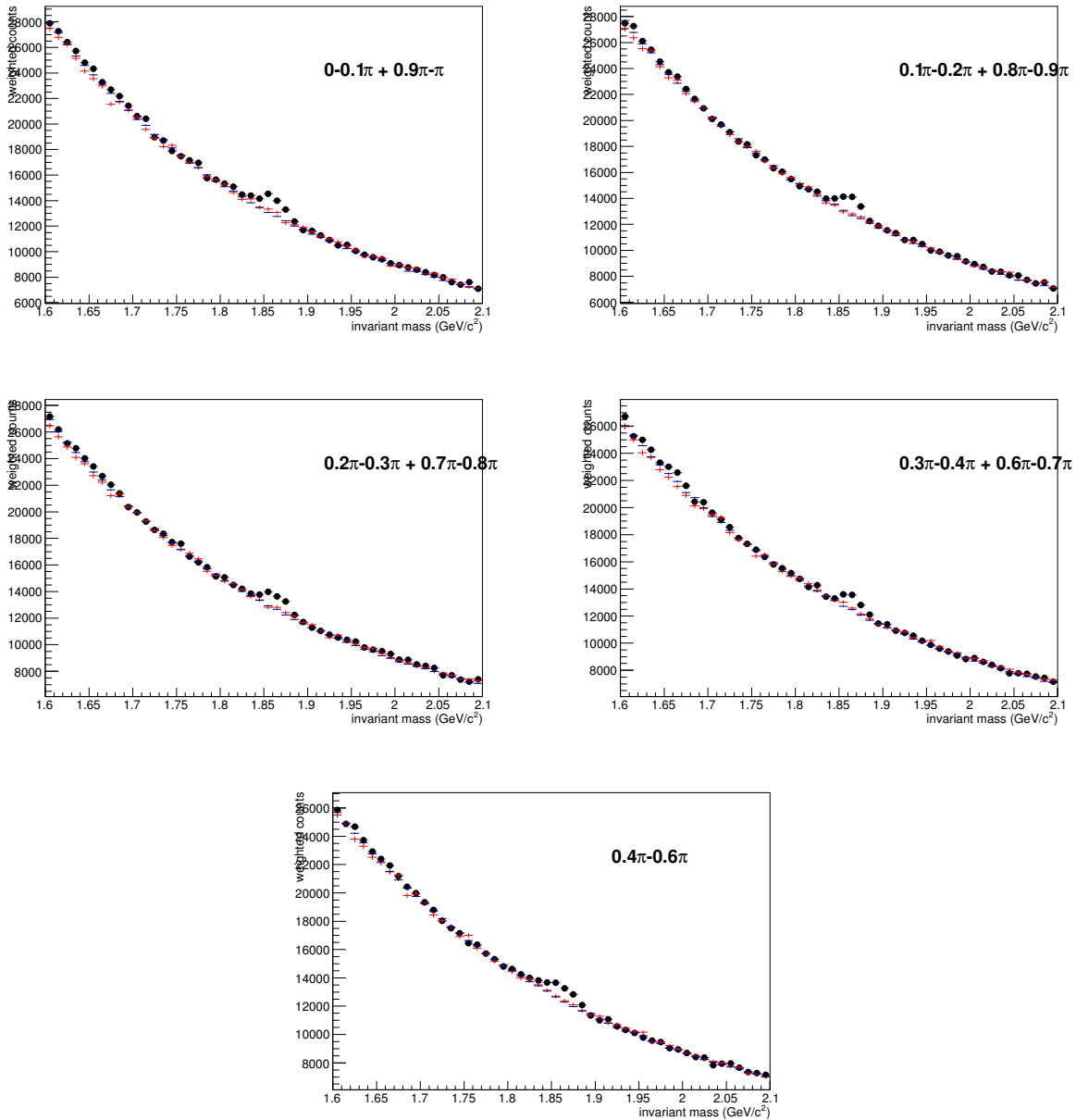


FIG. 142: $K\pi$ invariant mass in different $\phi - \Psi$ bins

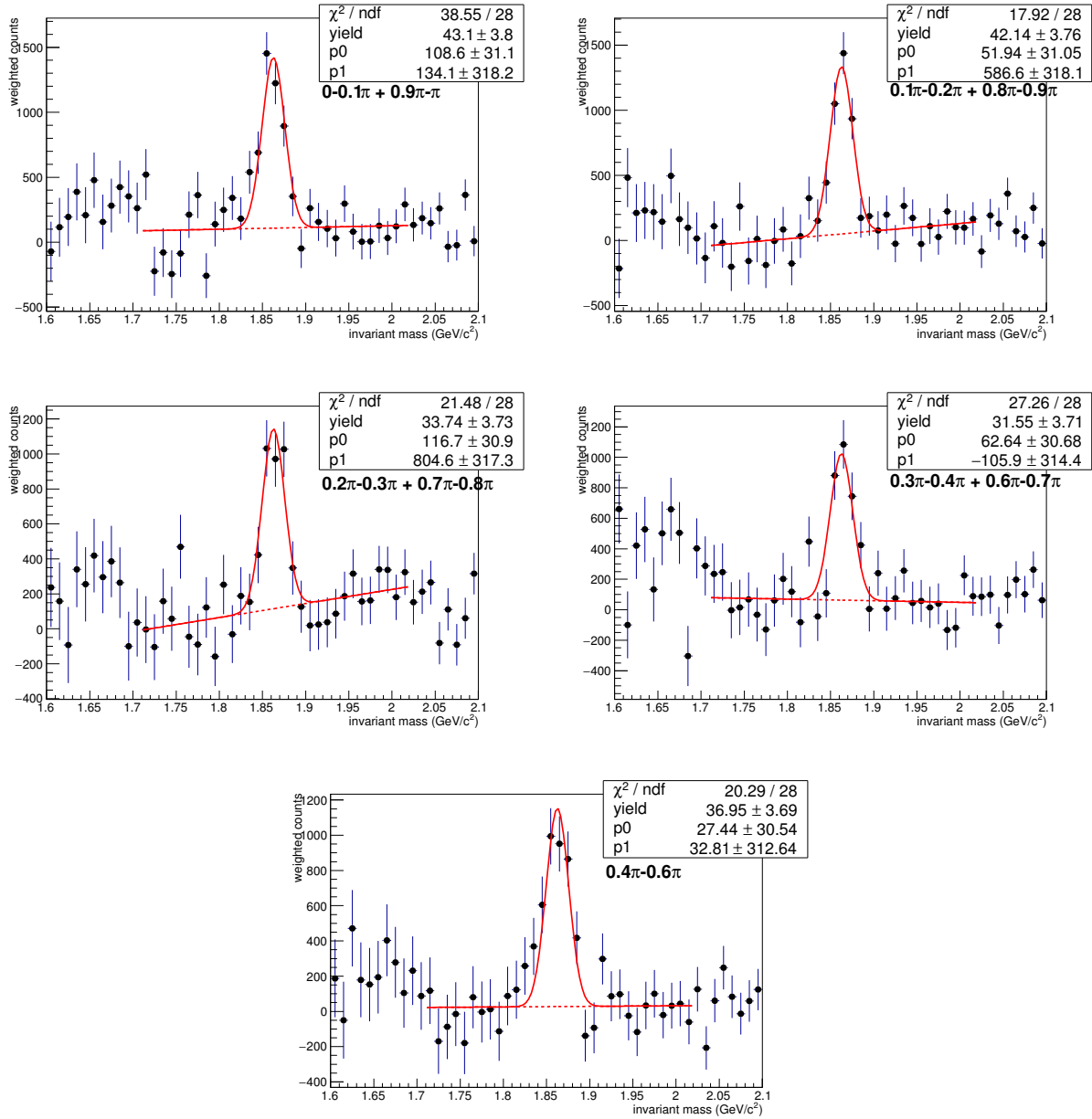


FIG. 143: $K\pi$ pairs invariant mass unlike sign - mixed event in different $\phi - \Psi$ bins, default fit range

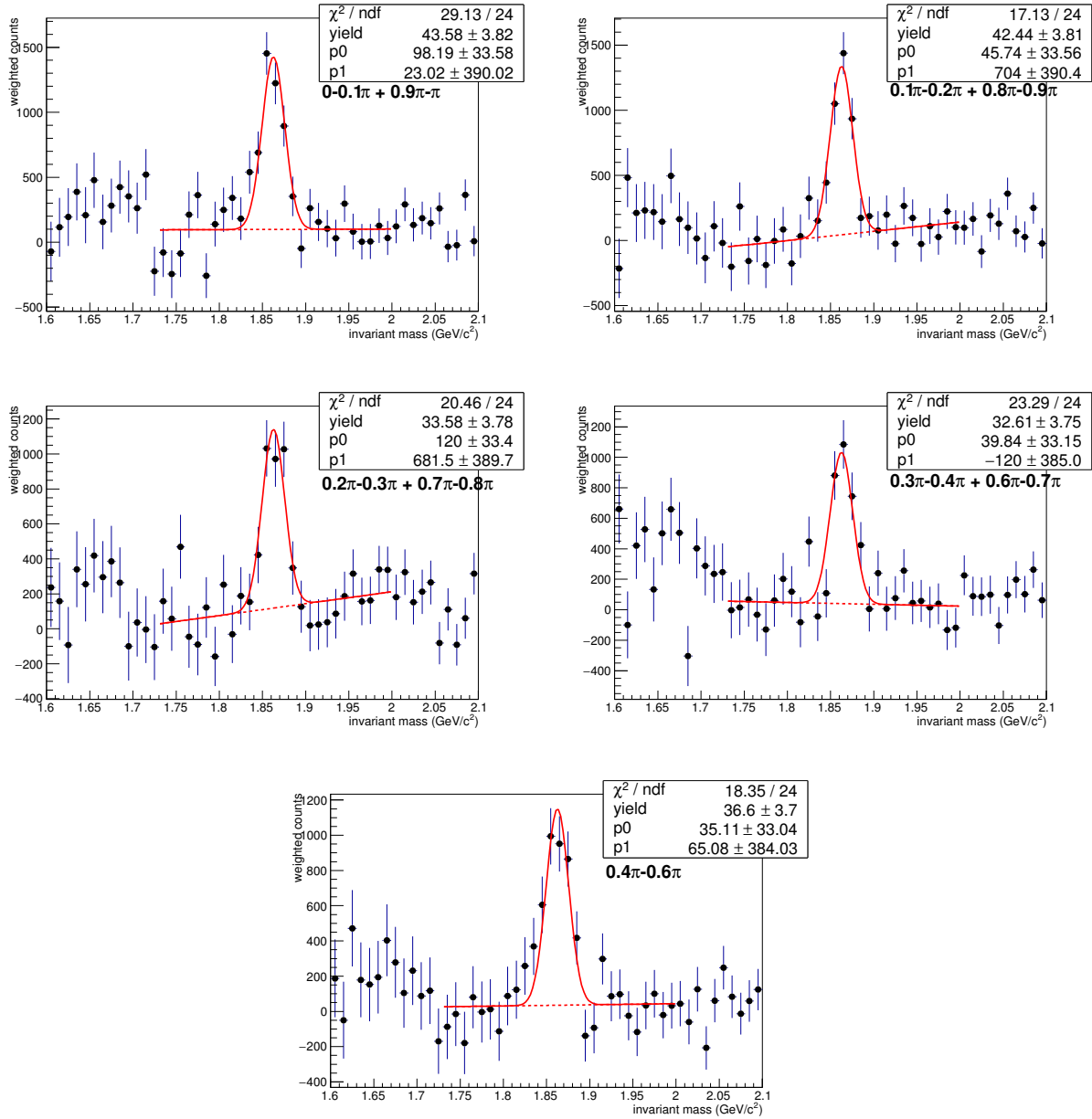


FIG. 144: $K\pi$ pairs invariant mass unlike sign - mixed event in different $\phi - \Psi$ bins, narrower fit range

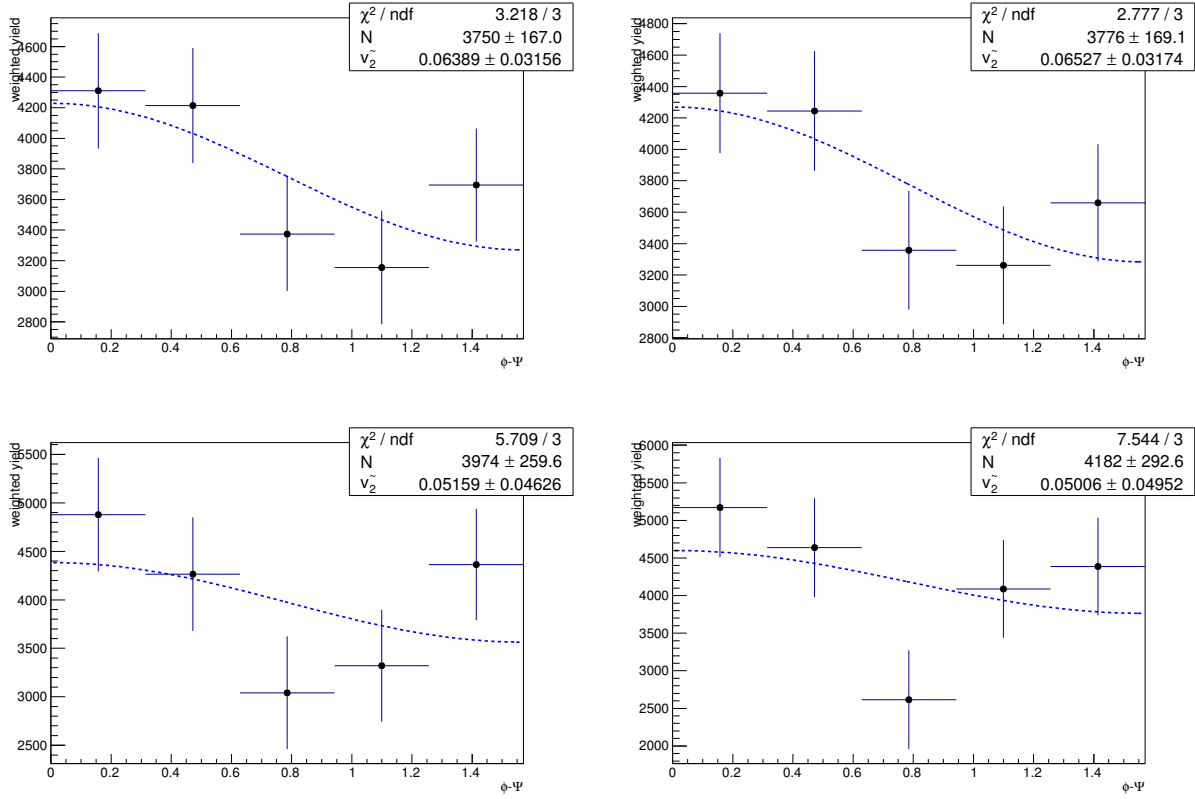


FIG. 145: yield vs. dPhi and $v_{2\text{observe}}$ fit, with yield from fit with standard range (top left), fit from narrower range (top right), side band with standard range (bottom left) and side band with narrower range (bottom right)

loose geometry cuts, p_T 2-3 GeV/c

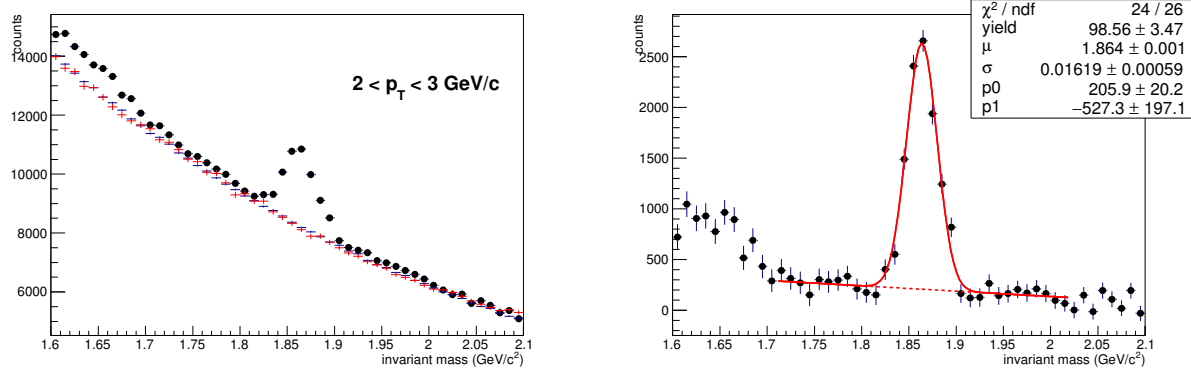
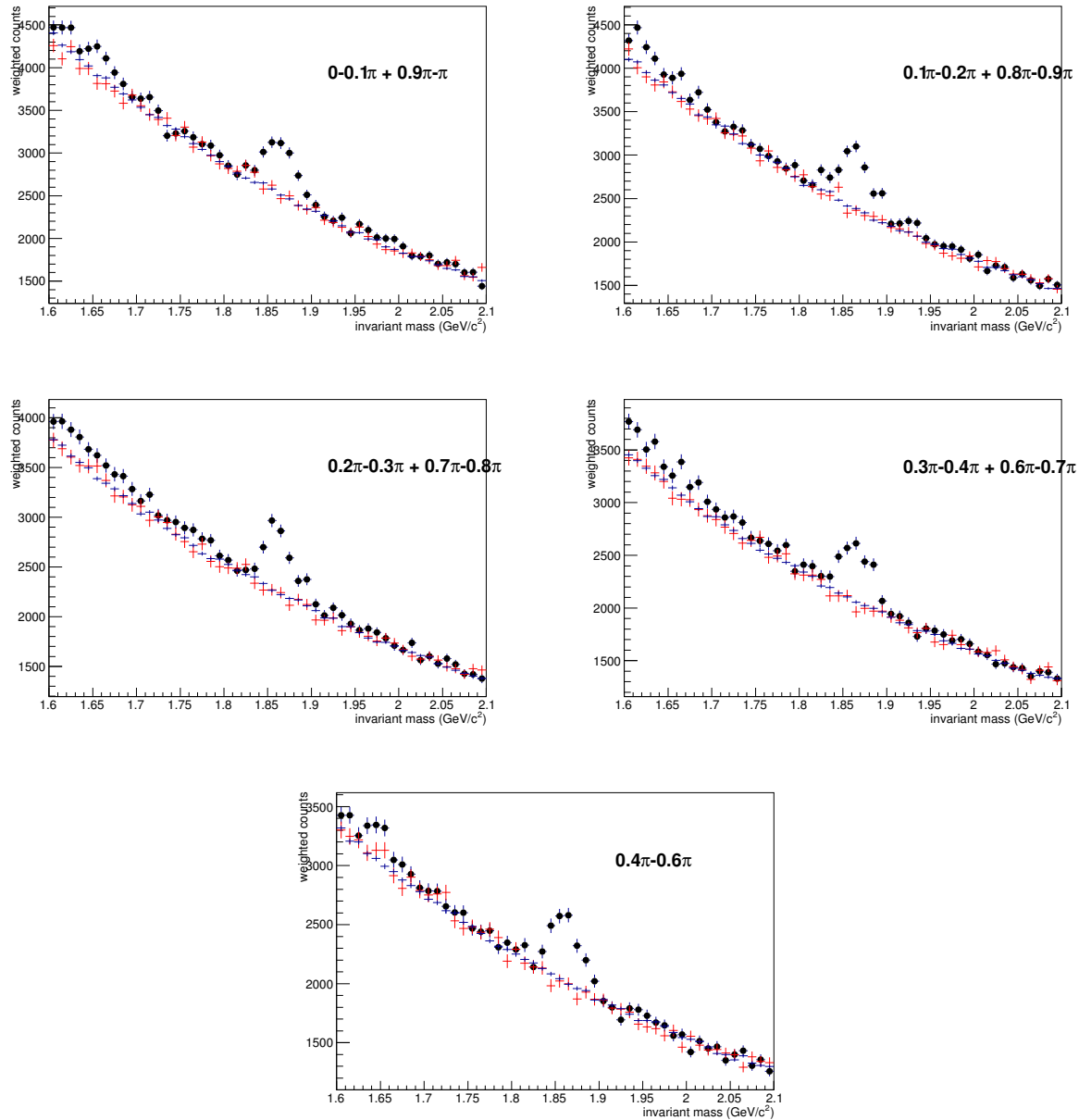


FIG. 146: $K\pi$ invariant mass distribution, left: unlike sign, like sign and scaled mixed event;
right: unlike sign - mixed event

FIG. 147: $K\pi$ invariant mass in different $\phi - \Psi$ bins

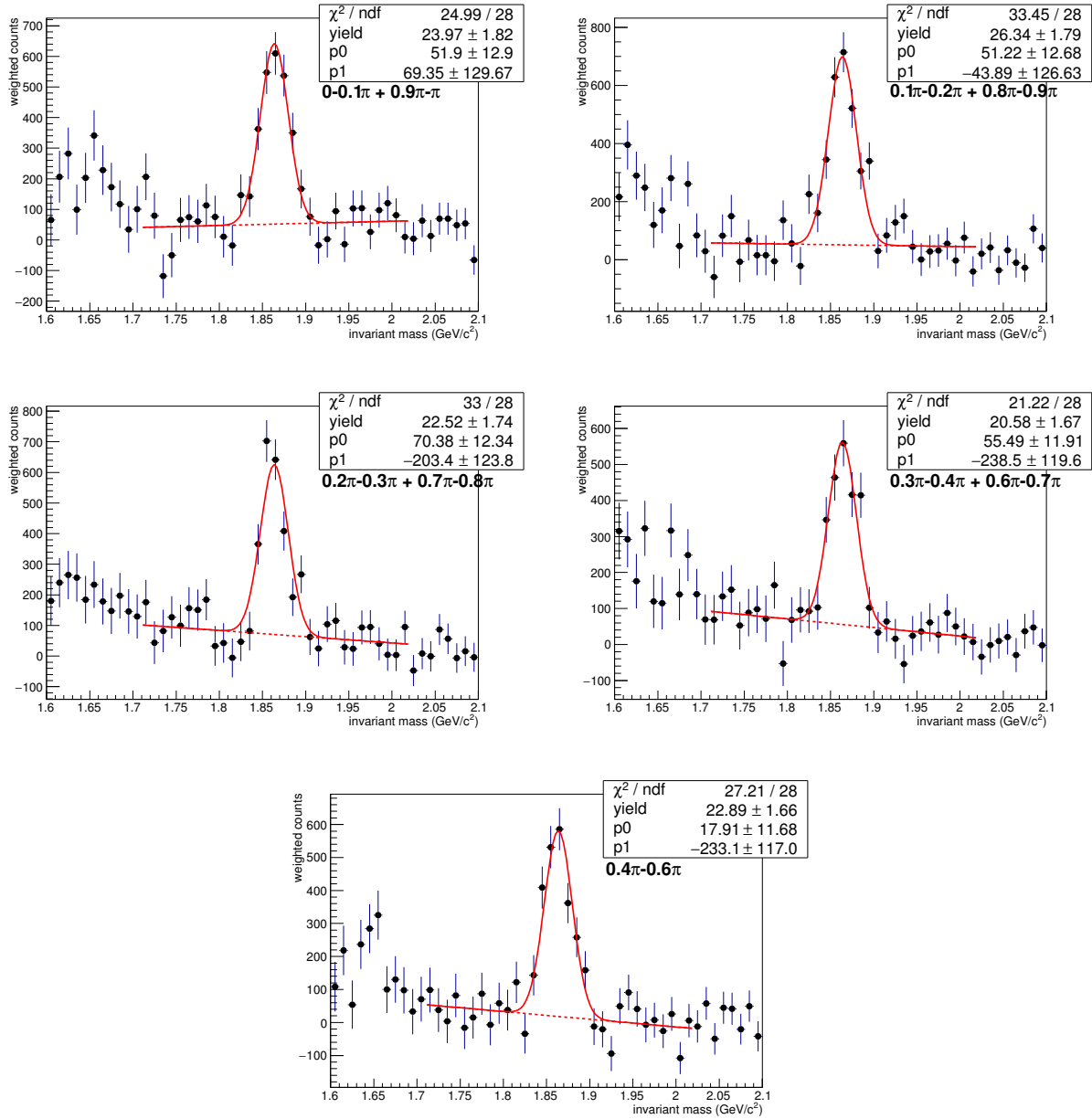


FIG. 148: $K\pi$ pairs invariant mass unlike sign - mixed event in different $\phi - \Psi$ bins, default fit range

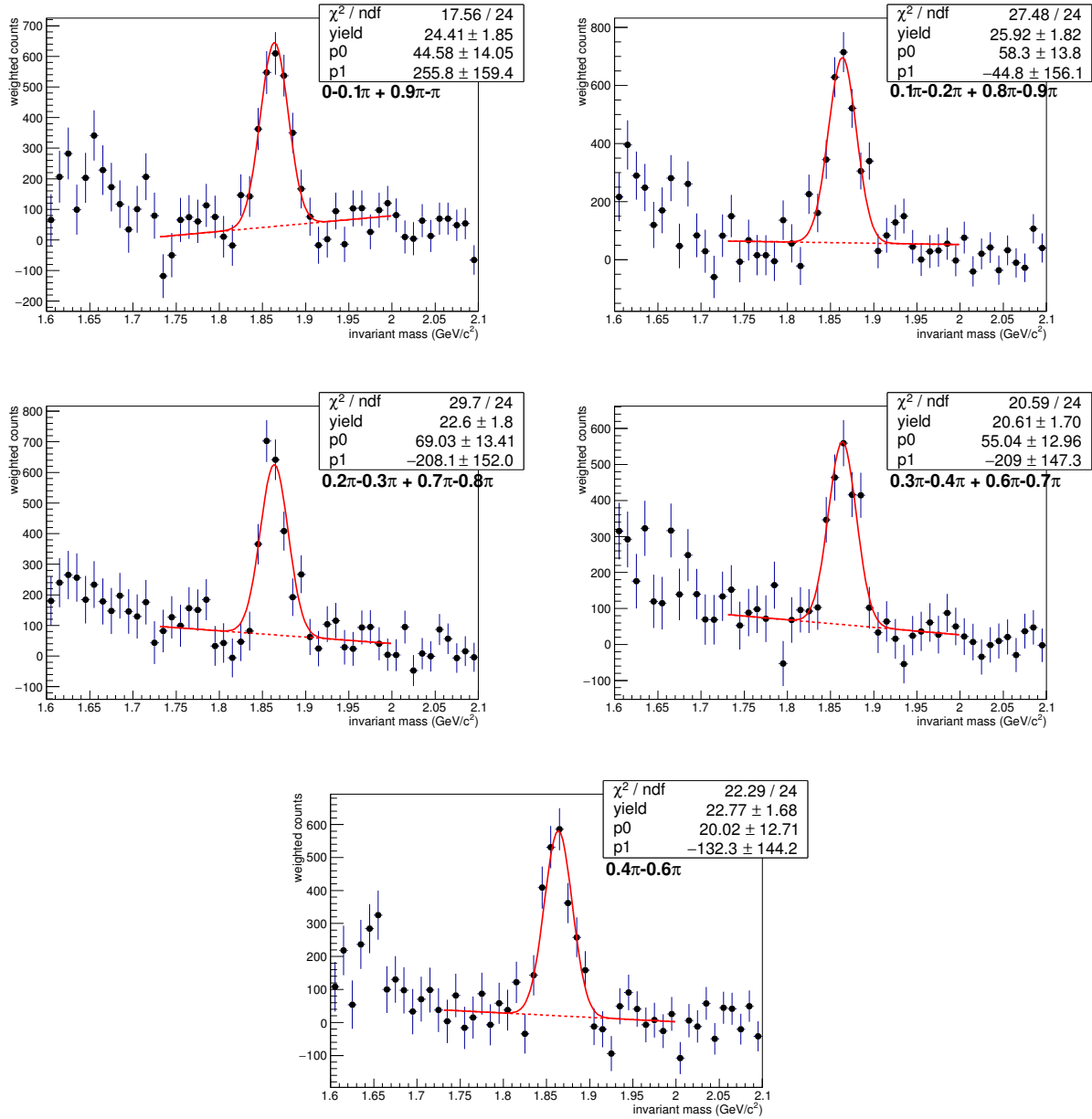


FIG. 149: $K\pi$ pairs invariant mass unlike sign - mixed event in different $\phi - \Psi$ bins, narrower fit range

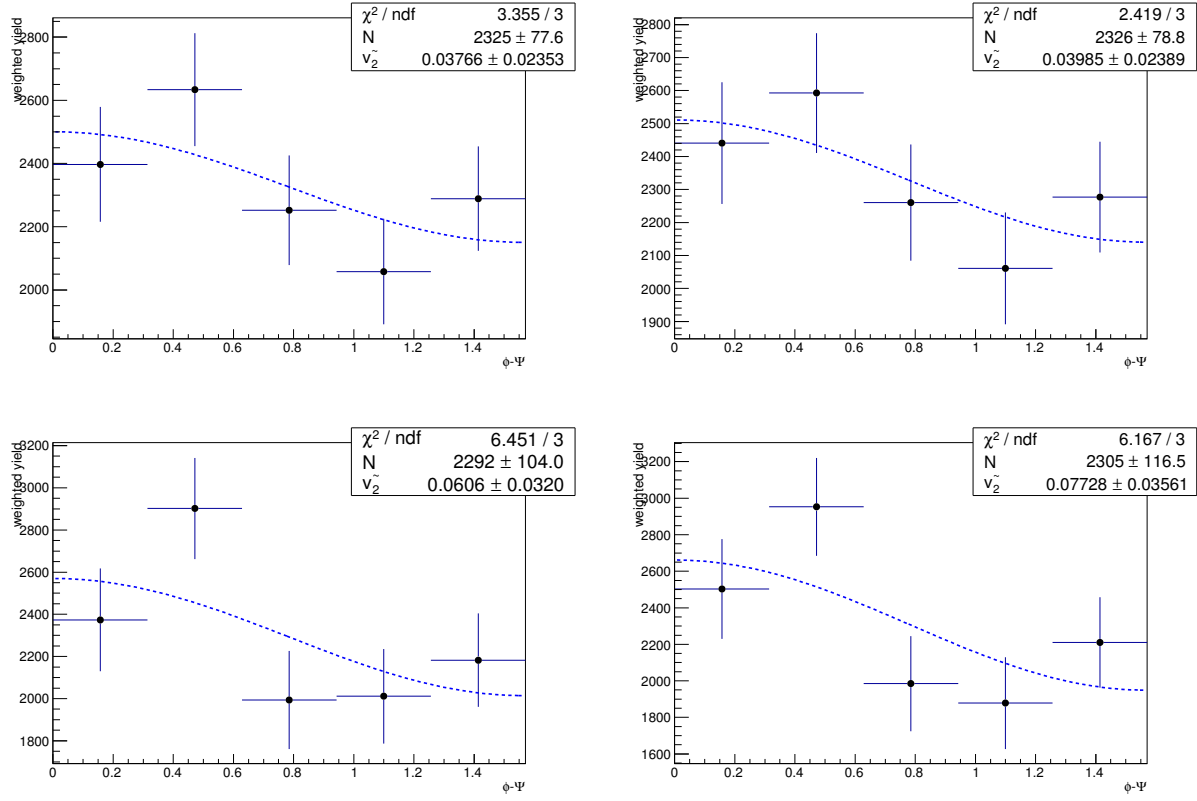


FIG. 150: yield vs. dPhi and $v_{2\text{observe}}$ fit, with yield from fit with standard range (top left), fit from narrower range (top right), side band with standard range (bottom left) and side band with narrower range (bottom right)

loose geometry cuts, p_T 3-4 GeV/c

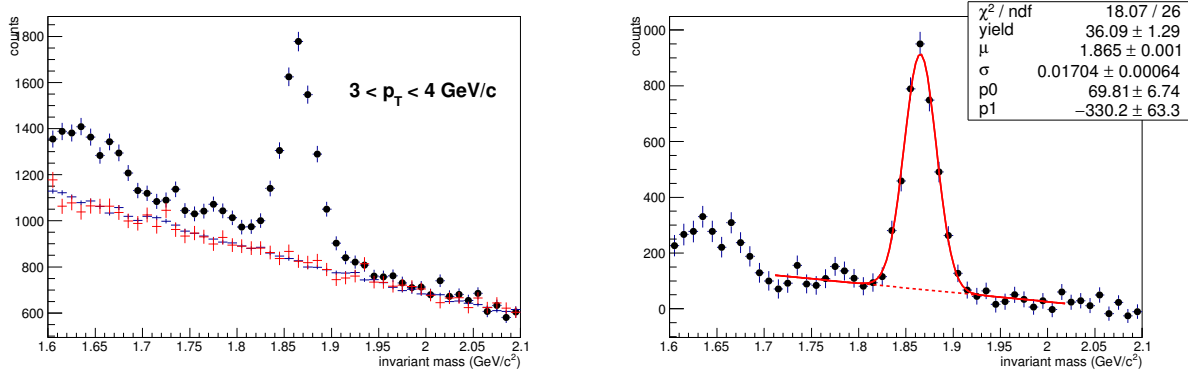


FIG. 151: $K\pi$ invariant mass distribution, left: unlike sign, like sign and scaled mixed event;
right: unlike sign - mixed event

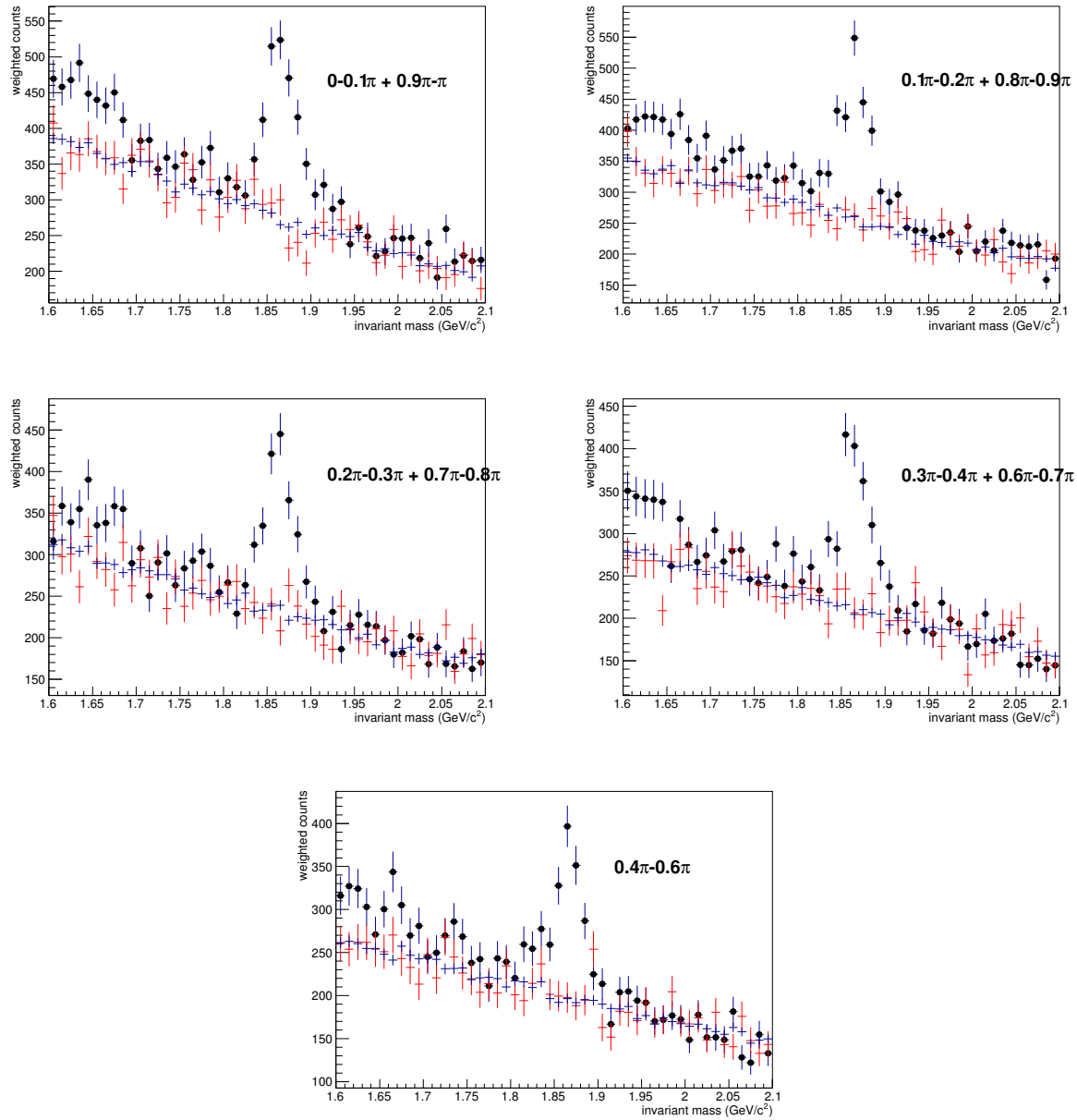


FIG. 152: $K\pi$ invariant mass in different $\phi - \Psi$ bins

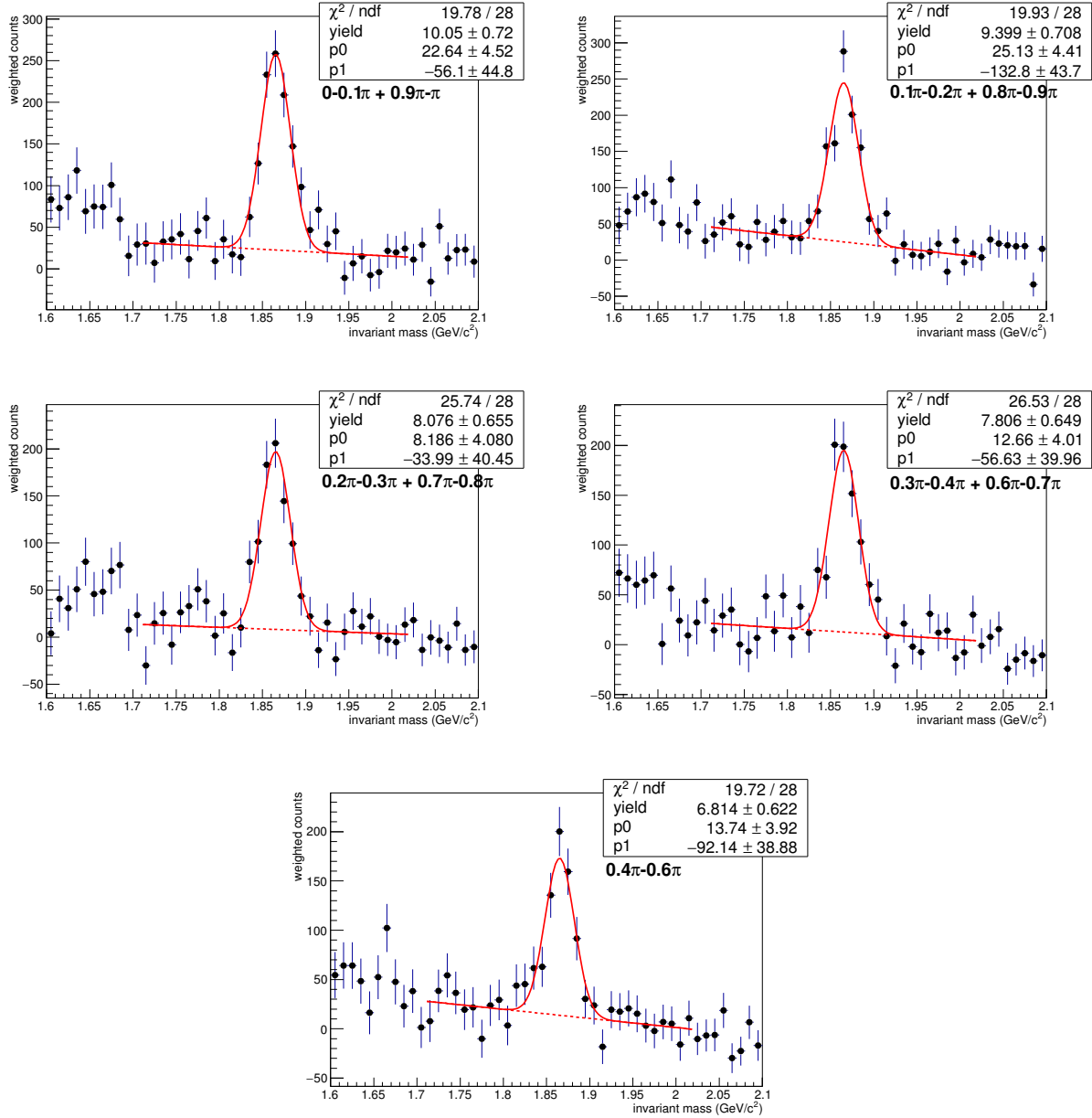


FIG. 153: $K\pi$ pairs invariant mass unlike sign - mixed event in different $\phi - \Psi$ bins, default fit range

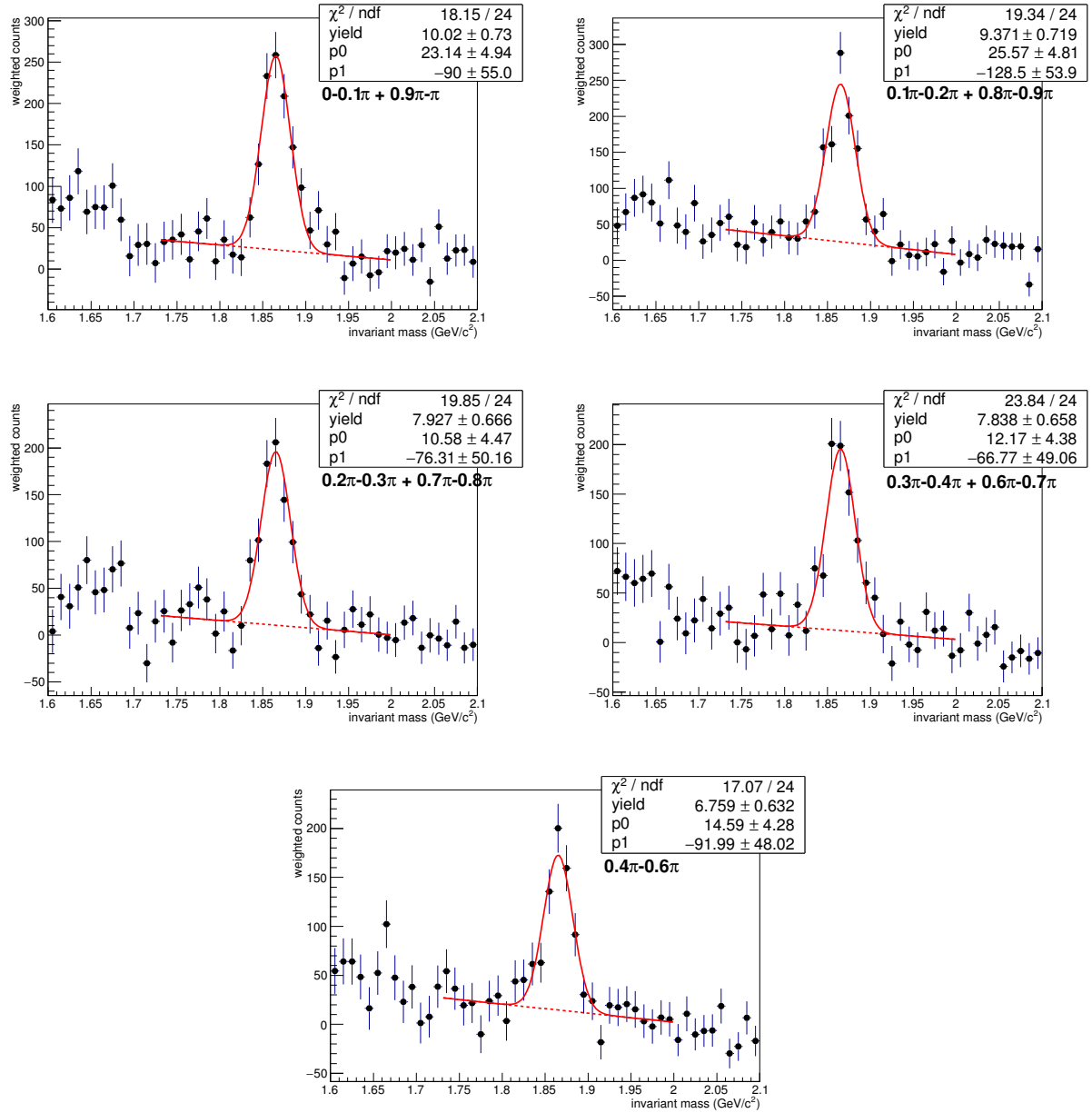


FIG. 154: $K\pi$ pairs invariant mass unlike sign - mixed event in different $\phi - \Psi$ bins, narrower fit range

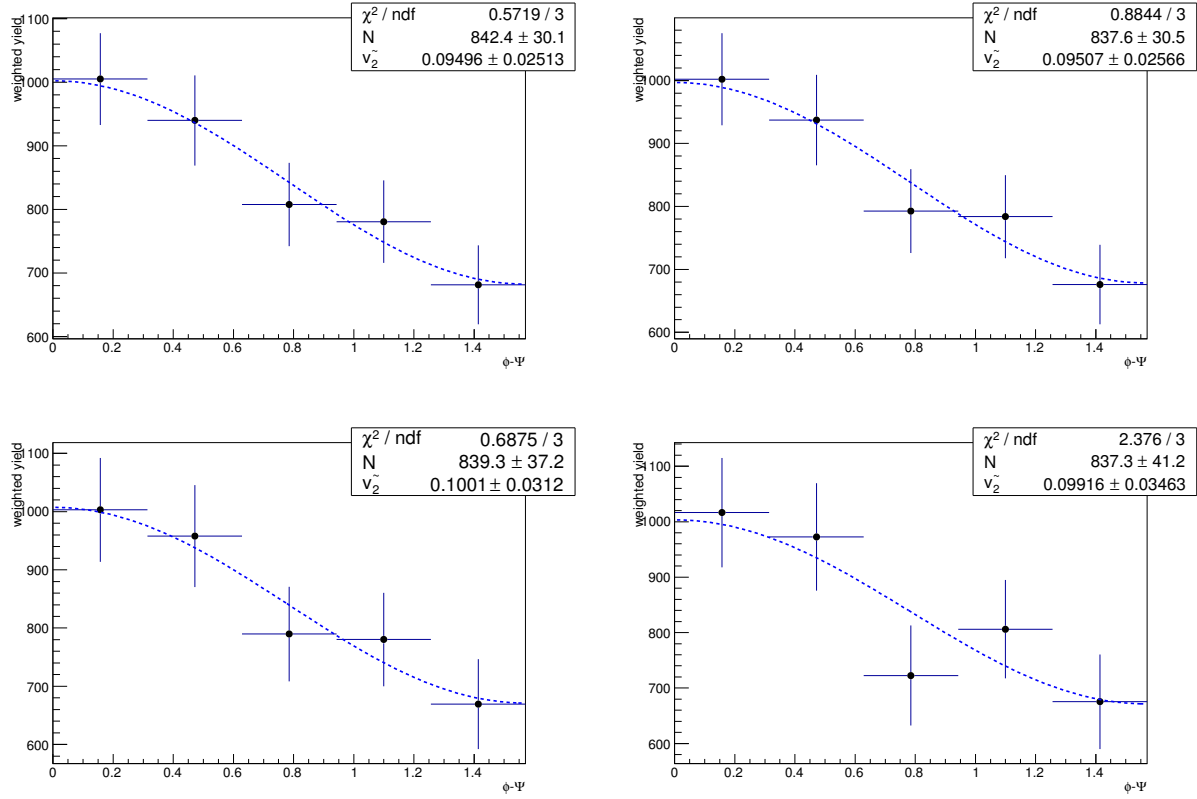


FIG. 155: yield vs. dPhi and $v_{2\text{observe}}$ fit, with yield from fit with standard range (top left), fit from narrower range (top right), side band with standard range (bottom left) and side band with narrower range (bottom right)

loose geometry cuts, p_T 4-5 GeV/c

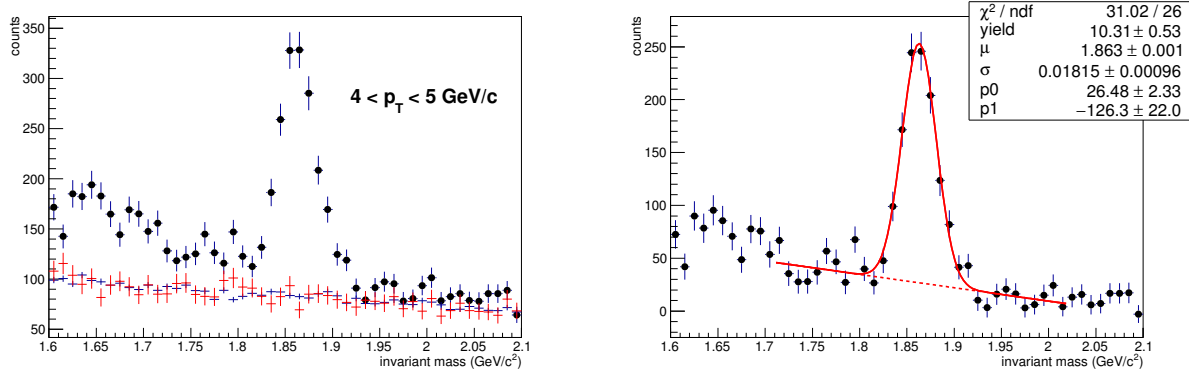


FIG. 156: $K\pi$ invariant mass distribution, left: unlike sign, like sign and scaled mixed event;
right: unlike sign - mixed event

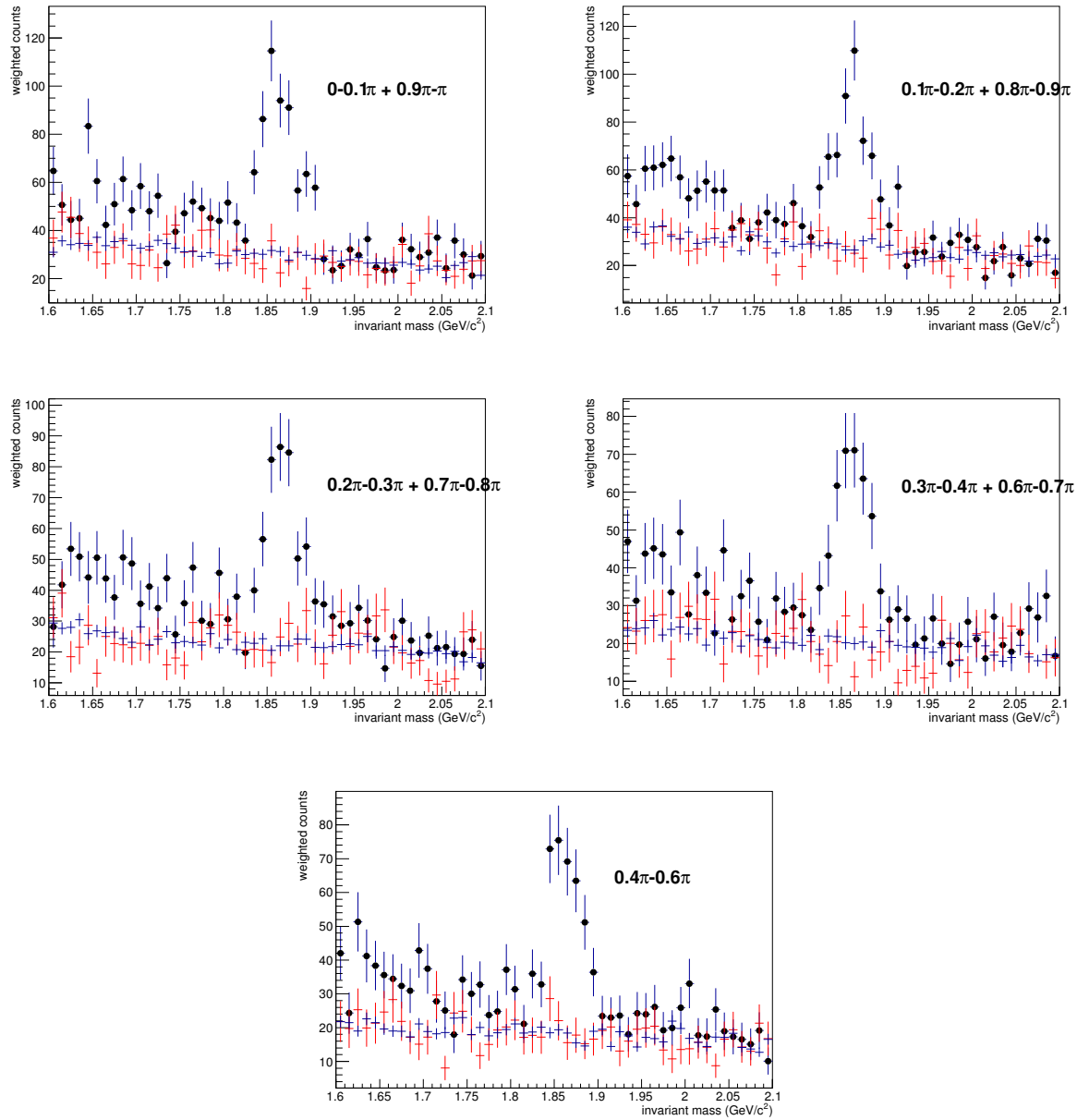


FIG. 157: $K\pi$ invariant mass in different $\phi - \Psi$ bins

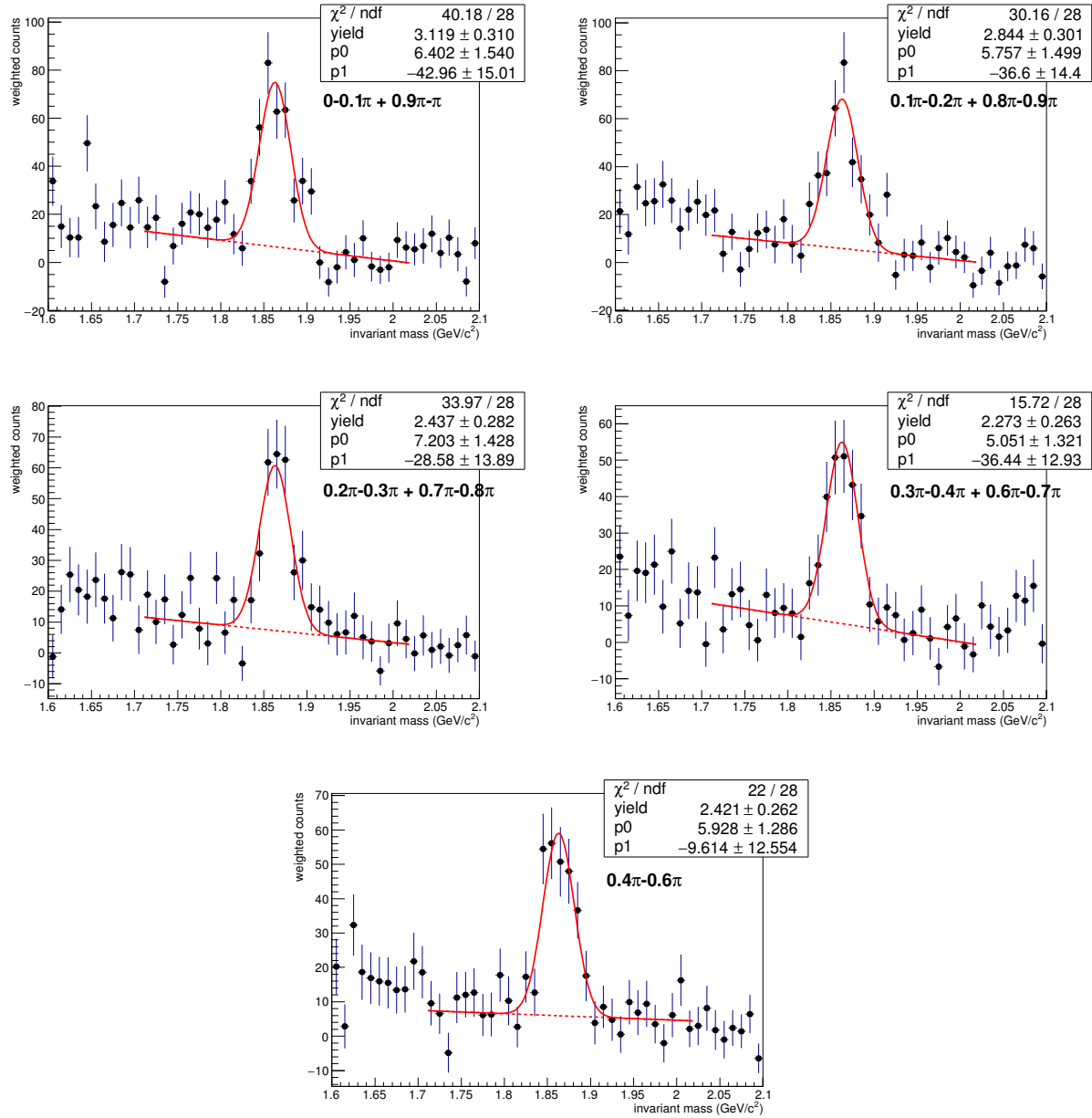


FIG. 158: $K\pi$ pairs invariant mass unlike sign - mixed event in different $\phi - \Psi$ bins, default fit range

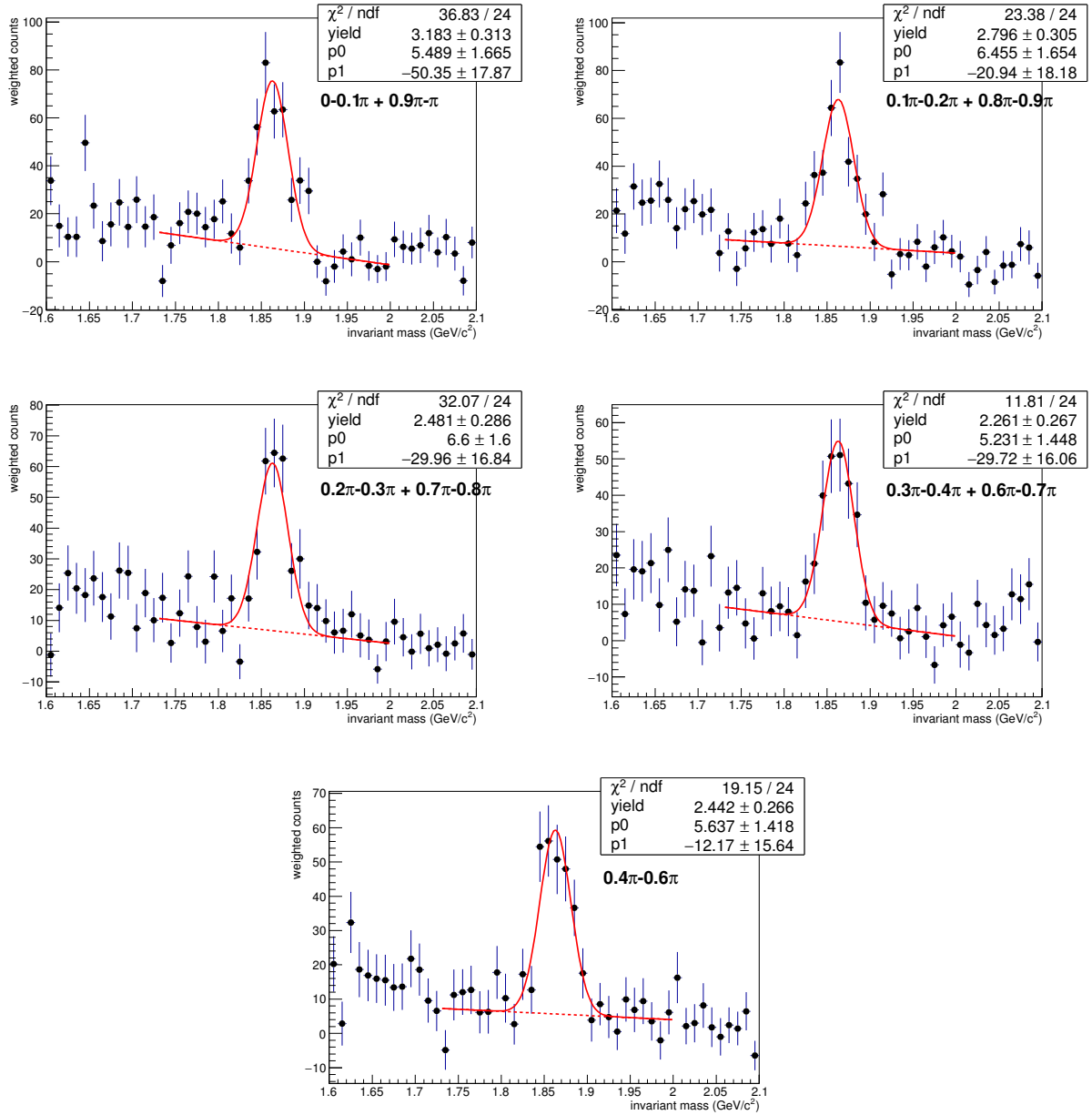


FIG. 159: $K\pi$ pairs invariant mass unlike sign - mixed event in different $\phi - \Psi$ bins, narrower fit range

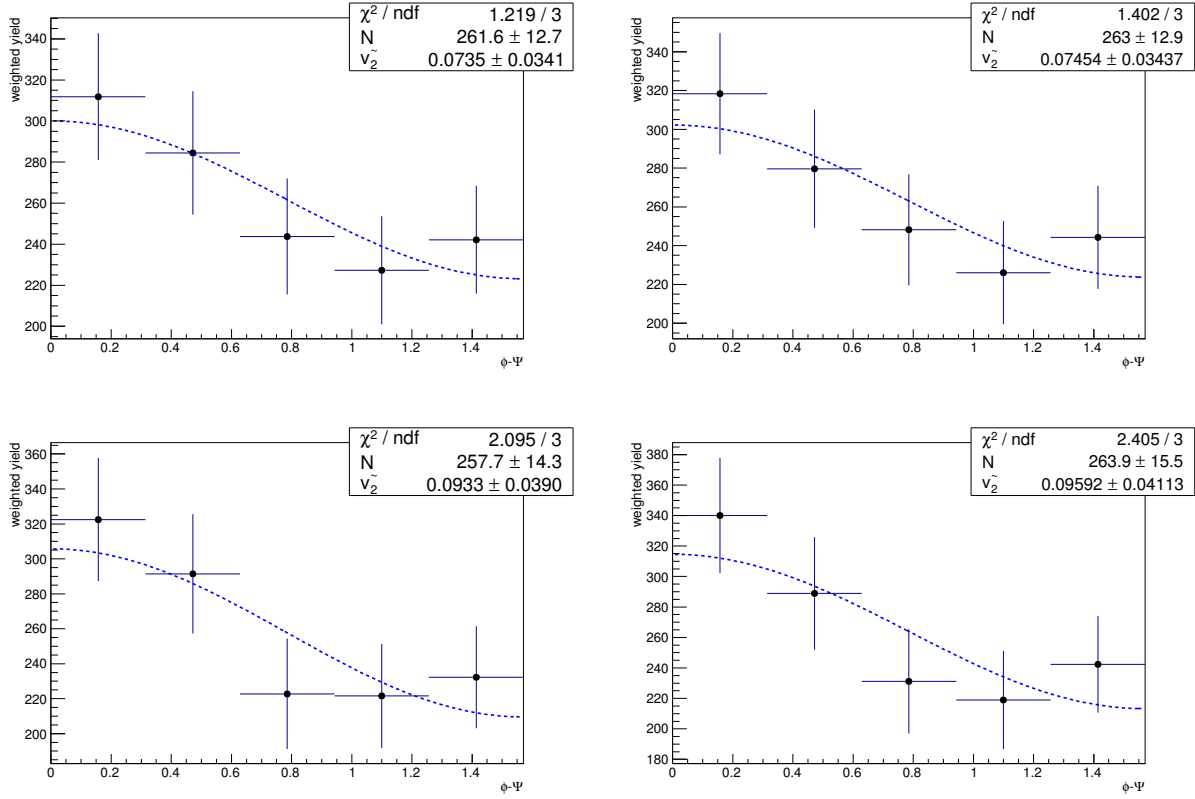


FIG. 160: yield vs. dPhi and $v_{2\text{observe}}$ fit, with yield from fit with standard range (top left), fit from narrower range (top right), side band with standard range (bottom left) and side band with narrower range (bottom right)

loose geometry cuts, p_T 5-10 GeV/c

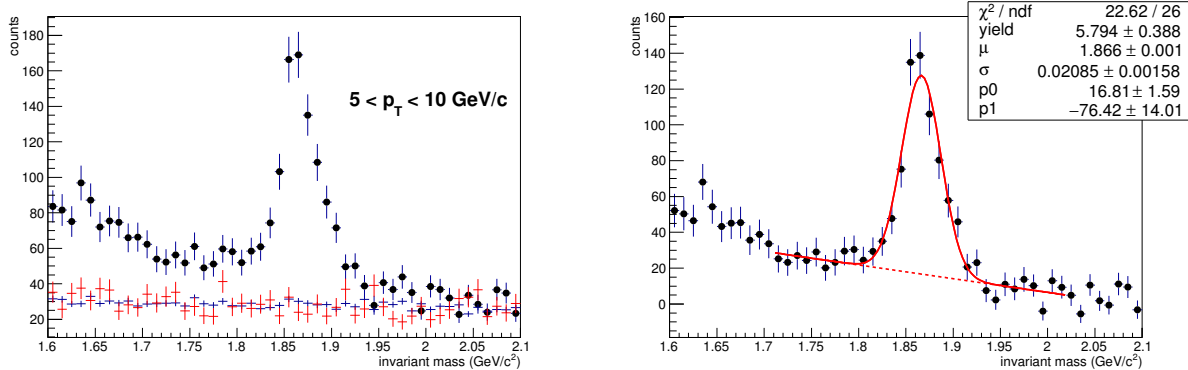
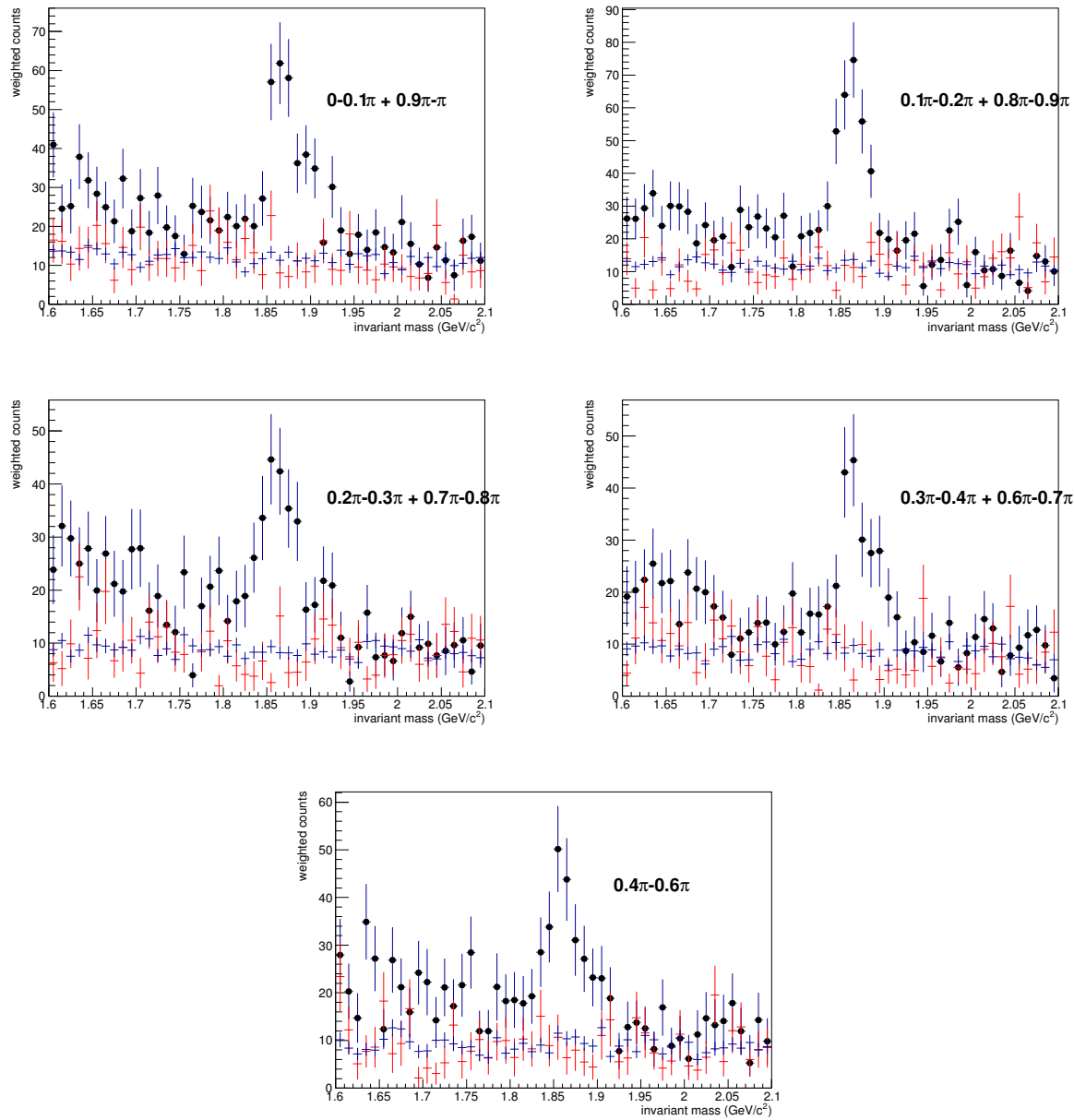


FIG. 161: $K\pi$ invariant mass distribution, left: unlike sign, like sign and scaled mixed event;
right: unlike sign - mixed event

FIG. 162: $K\pi$ invariant mass in different $\phi - \Psi$ bins

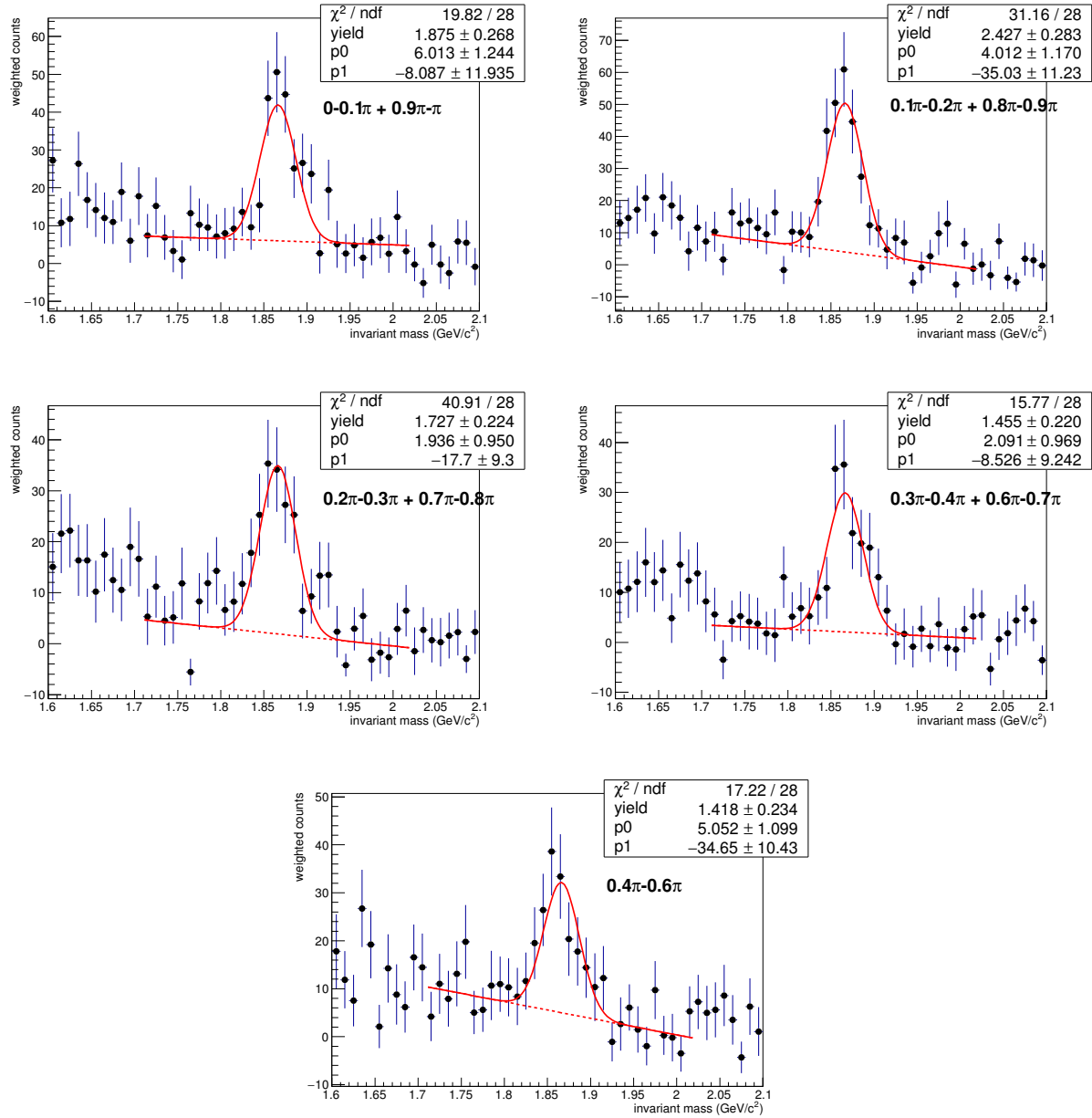


FIG. 163: $K\pi$ pairs invariant mass unlike sign - mixed event in different $\phi - \Psi$ bins, default fit range

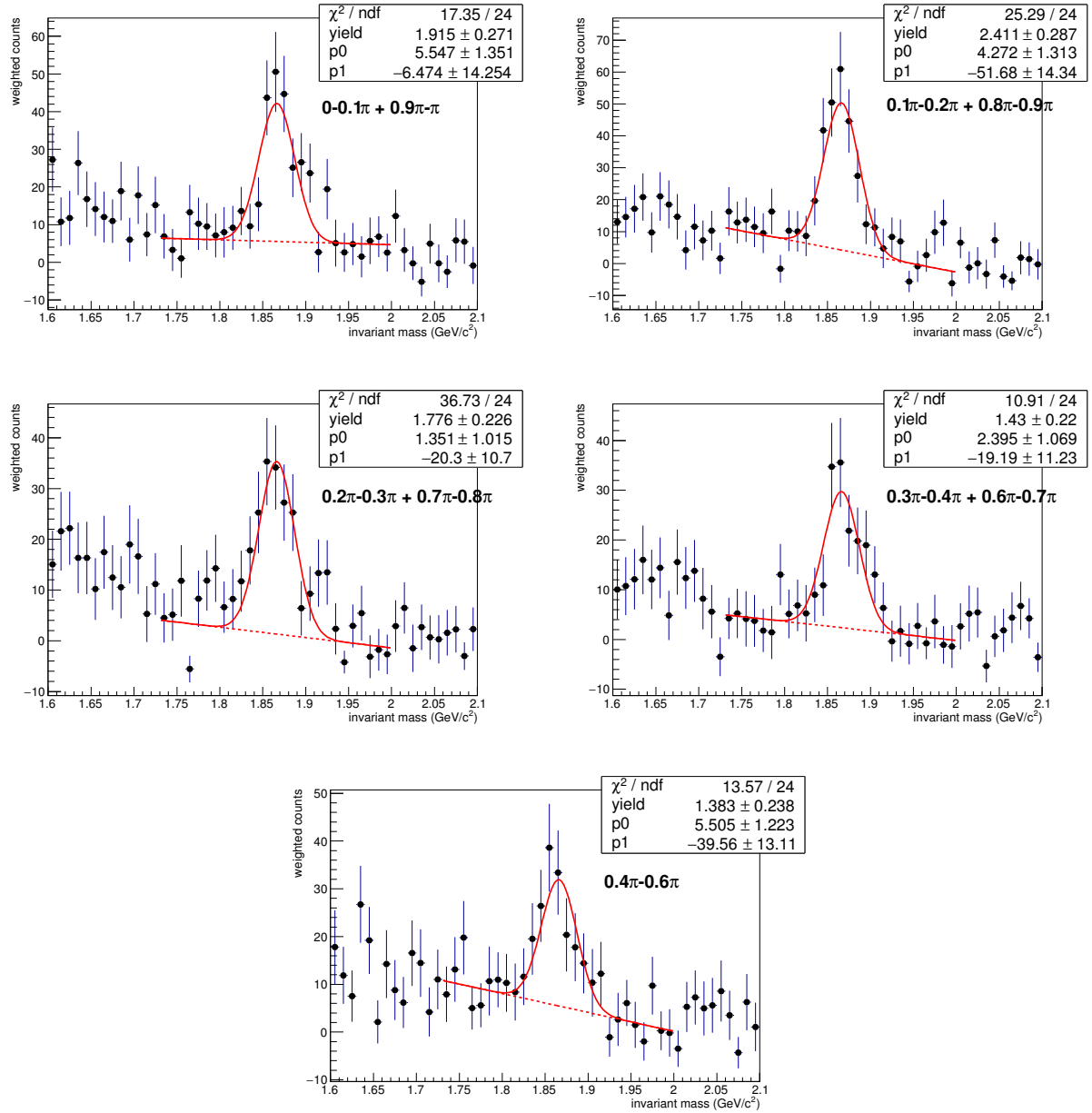


FIG. 164: $K\pi$ pairs invariant mass unlike sign - mixed event in different $\phi - \Psi$ bins, narrower fit range

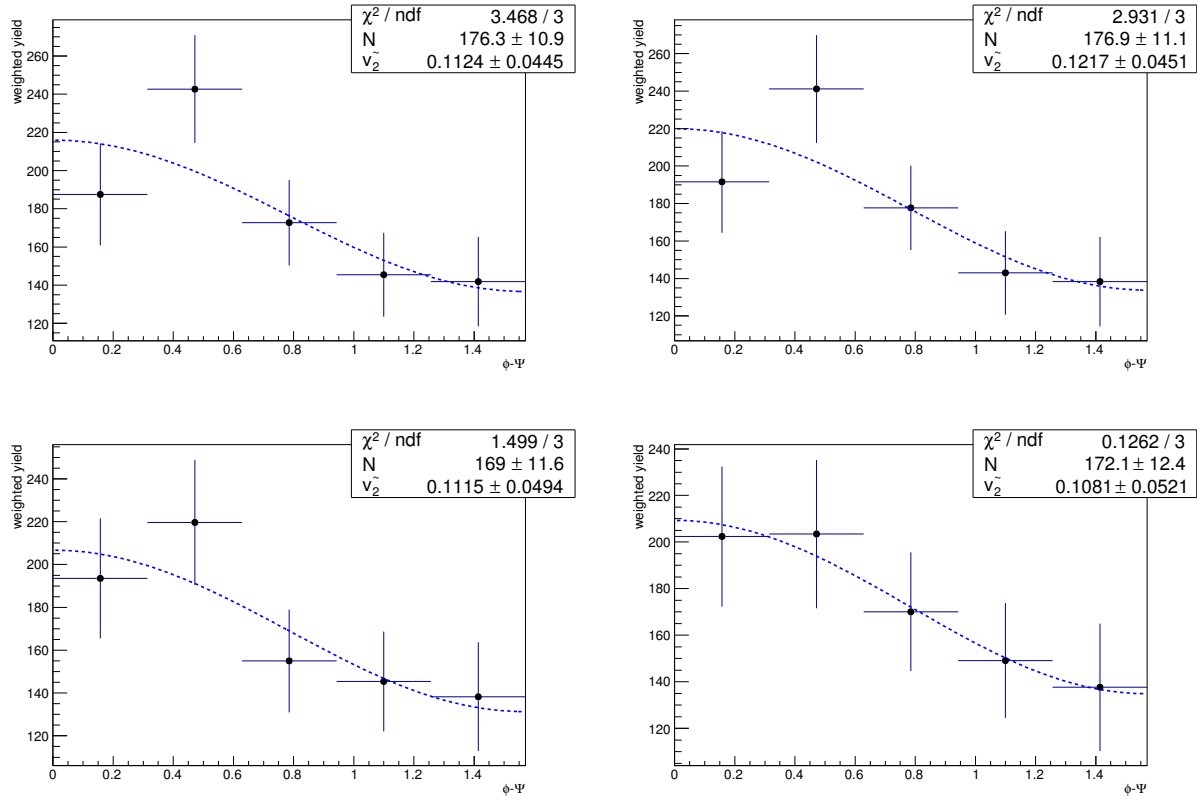


FIG. 165: yield vs. dPhi and $v_{2\text{observe}}$ fit, with yield from fit with standard range (top left), fit from narrower range (top right), side band with standard range (bottom left) and side band with narrower range (bottom right)